PhD Thesis

Signal Processing for Energy-Efficient Burst-Mode RF Transmitters

conducted at the
Signal Processing and Speech Communications Laboratory
Graz University of Technology, Austria

by
Shuli Chi

Supervisors:
Univ.-Prof. Dipl.-Ing. Dr.techn. Gernot Kubin
Priv.-Doz. Dipl.-Ing. Dr.techn. Christian Vogel

Assessors/Examiners:
Univ.-Prof. Dipl.-Ing. Dr.techn. Gernot Kubin
Priv.-Doz. Dipl.-Ing. Dr.techn. Christian Vogel
Adjunct Prof. Sven Mattisson, Lund University, Sweden

Graz, August 2014

Statutory Declaration

I declare that I have authored this thesis independently, that I have not used other than the declared sources/resources, and that I have explicitly marked all material which has been quoted either literally or by content from the used sources.

date

(signature)

Abstract

Modern wireless communication systems utilize complex modulated signals such as OFDM signals to achieve increased data rates and spectral efficiency. These signals are characterized by a high peak-to-average-power ratio (PAPR). Thus, highly linear transmitters are required to provide sufficient transmission signal linearity. Conventional linear PAs, such as Class A or Class AB, produce high efficiency only near or at the peak output power region. As a result, the average efficiency is quite low for high PAPR signals. For non-portable devices such as base stations or mobile devices like mobile phones, low PA efficiency means higher heat dissipation which is often a design criterion. In addition, in mobile devices, a direct consequence of the low PA efficiency is the reduced battery lifetime, especially when the mobile device is required to operate at quite different output power levels. This thesis addresses the challenge of the efficiency enhancement while maintaining the linearity of wireless transmitters for signals with high PAPRs and output powers over a large range of power levels from the signal processing viewpoint.

In the first part of the thesis, the burst-mode RF transmitter that employs pulse-width modulation (PWM) is introduced as an efficiency enhancement transmitter architecture. The PWM is analyzed in detail, where mathematical descriptions of PWM signals of different kinds are provided to explore the possibility of signal processing in burst-mode RF transmitters. In the second part of the thesis, the analysis of continuous-time PWM based burst-mode RF transmitters is carried out. The image problem is addressed when the baseband PWM signal is upconverted to the passband, and image distortion mitigation methods are provided. Furthermore, according to the presented power efficiency analysis, an efficiency optimization procedure is proposed for multilevel burst-mode RF transmitters. By using the efficiency optimization method, the maximum average transmitter efficiency can be achieved by proper choice of the threshold values of the input magnitude according to its probability density function (PDF). In the third and final part of the thesis, the investigation of discrete-time PWM based burst-mode RF transmitters is performed. Discrete-time PWM signals inherently suffer from aliasing distortion due to the sampling of non-bandlimited baseband PWM signals, which degrades the signal quality. To deal with the distortion, the aliasing-free PWM (AFPWM) method is described which allows avoiding the destructive aliasing distortion by limiting the number of harmonics in the generated PWM signals. The power efficiency analysis shows that although the AFPWM method imposes amplitude variation onto the time-domain signal which reduces the PA efficiency, the higher coding efficiency compensates for the RF PA efficiency degradation. An important result obtained is that a good efficiency-linearity trade-off can be achieved for AFPWM based burst-mode RF transmitters by selecting a proper number of harmonics in the generated PWM signals.

Kurzfassung

Moderne drahtlose Kommunikationssysteme nutzen komplex modulierte Signale, wie zum Beispiel OFDM-Signale, um erhöhte Datenraten und größere spektrale Effizienz zu erreichen. Diese Signale kennzeichnet ein hohes Peak-to-Average-Power Ratio (PAPR), wodurch streng lineare Sender notwendig sind. Konventionelle lineare Leistungsverstärker (Power Amplifier, PA), wie zum Beispiel der Klasse A oder AB, arbeiten nur in der Nähe der Spitzenausgangsleistung effizient. Folglich ist die durchschnittliche Effizienz für Signale mit hohem PAPR sehr gering. Eine geringe Effizienz der PAs bedeutet für ortsfeste Sender wie Basisstationen oder mobile Sender wie Handys eine höhere Wärmeabgabe, die oft ein wichtiges Designkriterium ist. Bei mobilen Geräten führt die niedrige PA-Effizienz zusätzlich zu verkürzter Batterielebensdauer, vor allem dann, wenn das mobile Gerät mit sehr unterschiedlichen Ausgangsleistungsstufen umgehen muss. Diese Dissertation befasst sich mit der Effizienzsteigerung von drahtlosen Sendern für Signale mit hohem PAPR und erarbeitet die dafür notwendigen Signalverarbeitungskonzepte. Diese Konzepte versuchen die Effizienz zu steigern ohne die Linearität der Sender substantiell zu verschlechtern.

Im ersten Teil der Arbeit werden Burst-Mode-HF-Sender, welche Pulsweitenmodulation (PWM) verwenden, als eine effizienzsteigernde Senderarchitektur eingeführt. Eine detaillierte Analyse der mathematischen Zusammenhnge von PWM-Signalen zeigt wie Signalverarbeitungsansätze für Burst-Mode-HF-Sender ausgenutzt werden können. Im zweiten Teil der Arbeit wird die Analyse von zeitkontinuierlichen PWM-basierten Burst-Mode-HF-Sendern durchgeführt. Das Abbildungsproblem, welches durch die Modulation von Basisband-PWM-Signalen in das Passband entsteht, wird im Detail besprochen und Möglichkeiten zur Verringerung der resultierenden Verzerrung werden vorgestellt. Ausgehend von einer Analyse der Leistungseffizienz wird ein Effizienzoptimierungsverfahren für Multi-Level-Burst-Mode-HF-Sender vorgeschlagen. Dieses Verfahren erreicht die maximale Sendeeffizienz durch eine Anpassung der Schwellwerte des Multi-Level-Burst-Mode-HF-Senders an die Wahrscheinlichkeitsdichtefunktion des Eingangssignals. Der dritte Teil der Arbeit untersucht zeitdiskrete PWM-basierte Burst-Mode-HF-Sender. Zeitdiskrete Systeme zur PWM-Signalgenerierung erfahren eine inhärente Verzerrung durch Aliasing, die aufgrund der impliziten Abtastung des Systems und der damit verbundenen Abtastung des nicht bandbegrenzten PWM-Basisbandsignals entsteht. Um diese Verzerrung zu vermeiden, wird ein neues PWM Verfahren (AFPWM) beschrieben, welches Aliasing durch eine Begrenzung von Oberschwingungen in den erzeugten PWM-Signalen vermeidet. Eine Analyse der Leistungseffizienz des neuen Verfahrens zeigt, dass die höhere Kodiereffizienz die Effizienzverschlechterung durch die notwendigen Amplitudenvariationen kompensiert. Ein weiteres Ergeb-

nis der Arbeit ist, dass ein guter Kompromiss zwischen Effizienz und Linearität für AFPWM basierende Burst-Mode-HF-Sender getroffen werden kann, indem man eine geeignete Anzahl von Oberschwingungen der erzeugten PWM-Signale wählt.

Contents

Acknowledgment

I would like to express my gratitude to all who have helped and supported me to the completion of the thesis.

First of all, I would like to thank Dr. Christian Vogel, for his support and helpful suggestions. I am deeply grateful for his excellent scientific guidance throughout my research. I am sincerely grateful to my supervisor Prof. Gernot Kubin, for leading me to the signal processing area with his profound knowledge and his support throughout the thesis. I would also like to thank Prof. Sven Mattisson from Lund University, Sweden, for being my examiner for this thesis.

I would like to thank Land Steiermark and the European Union's Seventh Framework Programme, for the funding support for this thesis. I would also like to thank Infineon Technologies for the funding and technical support.

I would like to thank everyone at the signal processing and speech communication laboratory for the interesting technical and non-technical discussions. Special thanks to Katharina Hausmair, Bernhard Geiger, Andreas Pedroß-Engel, Erik Leitinger and Paul Meissner, for our 2 o'clock coffee time and all the fun we had.

Last but not least, my heartfelt thanks to my family for their unconditional support and encouragement. Special thanks to my husband Chao, for being with me through my ups and downs and for his unconditional love and support.

Shuli Chi
Graz, August 2014

List of Figures

List of Tables

List of Acronyms and Abbreviations

3G	Third Generation
ACPR	Adjacent Channel Power Ratio
AFPWM	Aliasing-Free Pulse-Width Modulation
BPF	Bandpass Filter
BPSDM	Bandpass Sigma Delta Modulation
CDF	Cumulative Distribution Function
CDMA	Code Division Multiple Access
DAC	Digital-to-Analog Converter
DE	Double Edge
DEPWM	Double-Edge Pulse-Width Modulation
DLM	Dynamic Load Modulation
DMT	Discrete Multitone
DR	Dynamic Range
DSM	Dynamic Supply Modulation
DVB-T2	Digital Video Broadcasting-Second Generation Terrestrial
EER	Envelope Elimination and Restoration
ET	Envelope Tracking
HP	Highpass
IF	Intermediate Frequency
IQ	Inphase and Quadrature components
LDMOS	Laterally Diffused Metal Oxide Semiconductor
LE	Leading Edge
LINC	Linear Amplification using Nonlinear Components
LP	Lowpass
LPSDM	Lowpass Sigma Delta Modulation
LTE	Long Term Evolution
NMSE	Normalized Mean Square Error

NPWM	Natural Sampling Pulse-Width Modulation
OFDM	Orthogonal Frequency-Division Multiplexing
PA	Power Amplifier
PAE	Power Added Efficiency
PAPR	Peak-to-Average-Power Ratio
PDF	Probability Density Function
PWM	Pulse-Width Modulation
QAM	Quadrature Amplitude Modulation
RF	Radio Frequency
RFPWM	Radio Frequency Pulse-Width Modulation
SAW	Surface Acoustic Wave
SCS	Signal Component Separator
SDM	Sigma Delta Modulation
SEPWM	Single-Edge Pulse-Width Modulation
SMPA	Switched-Mode Power Amplifier
TE	Trailing Edge
TE-NPWM	Trailing-Edge Natural Sampling Pulse-Width Modulation
TE-UPWM	Trailing-Edge Uniform Sampling Pulse-Width Modulation
TL	Transmission Line
UPWM	Uniform Sampling Pulse-Width Modulation
WiMAX	Worldwide Interoperability for Microwave Access

List of Symbols

The list of Symbols is not complete. Any additional symbols will be explained within the context.

General Symbols

t	continuous-time index
n	discrete-time index
f	frequency
c	speed of light in air
λ	wavelength
v	normalized output voltage
B_s	signal bandwidth
M	number of signal paths
m	signal path order index
V_i	threshold values
T_p	period of the reference signal in PWM process
l	time index of the PWM period T_p
f_p	reciprocal of the period T_p or PWM frequency
k	harmonic order index in PWM signals
q	an integer where the qth harmonic is located around the wanted signal at the carrier frequency
$\hat{f}_\mathrm{p}$	a new PWM frequency that can avoid the image peak distortion
f_a	probability density function
$\hat{V}_l$	the optimum threshold values
R_o	load impedance

Operators and Transforms

$\mathcal{F}\{\cdot\}$	Fourier transform
$\mathrm{E}\{\cdot\}$	expectation function
F^{-1}	inverse cumulative distribution function
x^*	complex conjugate of x

Signals and Variables

$x(t)$	continuous-time signal
$x[n]$	discrete-time signal
$a(t)$, $a[n]$	magnitude signal
$\phi(t)$, $\phi[n]$	phase signal
$r(t)$, $r[n]$	reference signal in PWM process
$a_{\mathrm{p}}(t)$, $a_{\mathrm{p}}[n]$	baseband PWM signal
$x_{\mathrm{p}}(t)$, $x_{\mathrm{p}}[n]$	phase modulated baseband PWM signal
$x_{\mathrm{p,PB}}(t)$	upconverted PWM signal or RF burst signal
$x_{\mathrm{PA}}(t)$	amplified RF burst signal
$x_{\mathrm{PB}}(t)$	wanted transmission signal
$X(f)$	frequency-domain signal by Fourier transform
$A(f)$	Fourier transform of the magnitude signal
$X_{\mathrm{p}}(f)$	Fourier transform of the phase modulated baseband PWM signal
$X_{\mathrm{PB}}(f)$	Fourier transform of the transmission signal
$\tilde{X}(f)$	frequency-domain signal by discrete-time Fourier transform
$\tilde{A}(f)$	discrete-time Fourier transform of the magnitude signal
$\tilde{A}_{\mathrm{p}}(f)$	discrete-time Fourier transform of the baseband PWM signal
$\tilde{X}_{\mathrm{p}}(f)$	discrete-time Fourier transform of the phase modulated baseband PWM signal
$a_{\mathrm{p}_m}(t)$	baseband PWM signal in the mth signal path
$x_{\mathrm{p}_m}(t)$	phase modulated baseband PWM signal in the mth signal path
$x_{\mathrm{p,PB}_m}(t)$	RF burst signal in the mth signal path
$r_m(t)$	reference signal in the m-th signal path

Power and Efficiency Related Symbols

General Symbols

P_{s}	power of the transmission signal
P_{tot}	total power of the amplified RF burst signal
P_{dc}	total consumed dc power
η	transmitter efficiency
η_{c}	coding efficiency
η_{PA}	PA drain efficiency

η_EA	envelope amplifier efficiency in EER and ET systems

Specialized Symbols

$P_\mathrm{s}(A)$	transmission signal power for constant input signals
$P_\mathrm{tot}(A)$	total power of the amplified RF burst signal for constant input signals
$P_\mathrm{dc}(A)$	consumed dc power for constant input signals
$\overline{P}_\mathrm{s}$	average power of the transmission signal
$\overline{P}_\mathrm{tot}$	average total power of the amplified RF burst signal
$\overline{P}_\mathrm{dc}$	average total consumed dc power
$P_\mathrm{s}^m(A)$	measured transmission signal power for constant input signals
$P_\mathrm{tot}^m(A,K)$	measured total power of the amplified RF burst signal for constant input signals A with different numbers of harmonics K
$P_\mathrm{dc}^m(A,K)$	measured consumed dc power for constant input signals A with different numbers of harmonics K
$\overline{P}_\mathrm{s}^m$	measured average transmission signal power
$\overline{P}_\mathrm{tot}^m(K)$	measured average total power of the amplified RF burst signal with different numbers of harmonics K
$\overline{P}_\mathrm{dc}^m(K)$	measured average consumed dc power with different numbers of harmonics K
$\eta(A)$	transmitter efficiency for constant input signals A
$\eta_\mathrm{c}(A)$	coding efficiency for constant input signals A
$\eta_\mathrm{tot}(A)$	coding efficiency for constant input signals A
$\overline{\eta}$	average transmitter efficiency
$\overline{\eta}_\mathrm{c}$	average coding efficiency
$\overline{\eta}_\mathrm{PA}$	average RF PA drain efficiency
$\overline{\eta}_\mathrm{max}$	the maximum average transmitter efficiency
$\eta_\mathrm{c}(A,K)$	coding efficiency for constant input signals A with different number of harmonics K
$\overline{\eta}_\mathrm{c}(K)$	average coding efficiency with different number of harmonics K
$\eta^m(A,K)$	measured transmitter efficiency for constant input signals A with different number of harmonics K
$\eta_\mathrm{c}^m(A,K)$	measured coding efficiency for constant input signals A with different number of harmonics K

$\eta_{\mathrm{PA}}^{m}(A, K)$	measured PA drain efficiency for constant input signals A with different number of harmonics K
$\overline{\eta}^{m}(K)$	measured average transmitter efficiency with different number of harmonics K
$\overline{\eta}_{\mathrm{c}}^{m}(K)$	measured average coding efficiency with different number of harmonics K
$\overline{\eta}_{\mathrm{PA}}^{m}(K)$	measured average PA drain efficiency with different number of harmonics K
$\eta_{\mathrm{c}}(A, K, V_i)$	coding efficiency for constant input signals A with different number of harmonics K and threshold values V_i
$\overline{\eta}_{\mathrm{c}}(K, V_i)$	average coding efficiency for a given PDF with different number of harmonics K and threshold values V_i

1

Introduction

1.1 Motivation

Modern wireless communication systems have been developed to provide high data rate services to an increasing number of subscribers. To this end, new standards such as worldwide interoperability for microwave access (WiMAX) [3] and digital video broadcasting - second generation terrestrial (DVB-T2) [4] are utilized, where complex modulated signals such as quadrature amplitude modulation (QAM) modulated orthogonal frequency-division multiplexing (OFDM) [5] signals are employed for increased data rates and spectral efficiency. Nevertheless, complex modulation techniques lead to envelope-varying signals, resulting in high peak-to-average-power ratios (PAPRs) or crest factors [5]. A signal with high PAPR requires the power amplifier (PA) to operate mostly at the rather linear but low-power region, i.e., a large backoff from the maximum transmission power level, where the efficiency of conventional linear PAs, such as Class A or Class AB, is very low [6, 7]. As a result, the average efficiency produced by linearly operated PAs is low for high PAPR signals. The efficiency of the radio frequency (RF) PA is very important in wireless communication systems, especially in mobile devices. The direct consequence of the low RF PA efficiency is reduced battery lifetime. For non-portable applications such as base stations, low RF PA efficiency means higher heat dissipation which is often a design issue.

Besides high PAPRs, the average transmitter efficiency can also be reduced by operating the PA with different average transmission power levels due to the power control strategy [8]. The power control strategy is an important factor in terms of the interference management and energy management. It is used to adjust the transmission power levels of mobile devices and base stations to improve system capacity, providing each user with an acceptable connection while at the same time minimizing the interference to other users and reducing the device's power consumption. The transmission power level is set according to the distance of the mobile device to the base station, and to the neighboring cells. For example, for 3rd generation (3G) systems which adopt the code division multiple access (CDMA) technique, power control is one effective way to avoid the so-called near-far problem, thus increasing system capacity and reducing intra-cell and inter-cell interferences [9]. In Long Term Evolution (LTE) [10, 11] systems, the uplink power control mitigates inter-cell interference, which is the dominant interference source [12]. Due to the power control strategy, it is common for the PA to operate at 10 dB-40 dB backoff from the maximum average transmission power [13]. Consequently, the PA operates mostly in the low-efficiency region, resulting in a low average efficiency.

To enhance the average transmitter efficiency, it is desirable for RF PAs to provide higher efficiency for the low-power input signals. Classical efficiency enhancement techniques can be divided into two categories: the dynamic supply modulation (DSM) and the dynamic load modulation (DLM). The envelope elimination and restoration (EER) [14, 15] technique and the envelope tracking (ET) [15, 16] technique are often treated as DSM technique. The Chireix outphasing amplifier [17, 18] and the Doherty amplifier [19–21] are often referred to as the DLM technique. These techniques can also be categorized depending on the RF PA employed. The ET and the Doherty amplifier techniques are used to boost efficiency for the conventional linear PA operation. The EER and the Chireix outphasing Amplifier techniques are used to enhance efficiency by employing saturated or switched-mode PAs (SMPAs) [6].

The concept of PAs operated in burst mode [22, 23] is another promising approach towards highly efficient RF transmitters. The burst-mode PAs can be SMPAs [6], or conventional PAs driven into the saturated region. In order to drive such burst-mode PAs in an efficient way, appropriate modulation techniques such as sigma delta modulation (SDM) [24, 25] and pulse-width modulation (PWM) [22, 26, 27] are employed to encode the envelope-varying input signal into bursts with constant envelope, where the pulse width varies depending on the magnitude information of the input signal. The transmission signal is retrieved by a band pass filter (BPF) and then sent to the antenna. The burst-mode RF transmitter architecture incorporating PWM will be the focus of this thesis.

1.2 Power Efficiency Enhancement Techniques

In the literature, three most common RF PA efficiency enhancement methods have been proposed and widely discussed [6, 28]. In terms of DSM technique [7, 15, 29], the EER and ET techniques are commonly treated. In terms of DLM technique [7, 18, 21], the Chireix outphasing amplifier and the Doherty amplifier are referred. The pulsed transmitter based on 1-bit modulation schemes of different kinds, such as SDM [30] and PWM [23], has found its way towards RF applications. In this section, these efficiency enhancement techniques will be discussed.

1.2.1 Dynamic Supply Modulation

The concept of the DSM technique is to dynamically adjust the power applied to the RF PA according to the actual power needed by the RF PA so as to reduce the dissipated power [15]. In general, for an EER system, the RF PA amplifies a phase modulated carrier with a constant envelope. Thus a saturated PA like a SMPA can be employed. The envelope of the output signal in EER system is determined by the dynamically modulated supply voltage. The ET technique is used to improve the power efficiency of a linear RF PA. For an ET system, the supply voltage is modulated to track the input signal envelope so as to reduce the dissipated power.

Envelope Elimination and Restoration

The EER technique was originally proposed by Kahn in 1952 [14]. It also has been referred to as Kahn technique [28] or direct polar [15]. A block diagram of the EER system is shown in Figure 1.1. The baseband input signal is first separated into an envelope signal and a phase signal. The envelope signal is amplified by the envelope amplifier and the obtained signal is served as the supply voltage to the RF PA. The phase signal is first modulated to the carrier frequency and then amplified by the RF PA. Thus the input signal to the RF PA is a constant envelope signal containing the phase information. The RF PA is operated in saturation region therefore an SMPA can be employed for this technique.

In an EER system, the envelope of the RF PA output signal is only controlled by the supply voltage, meaning that the linearity responsibility is transferred from the RF PA to the power

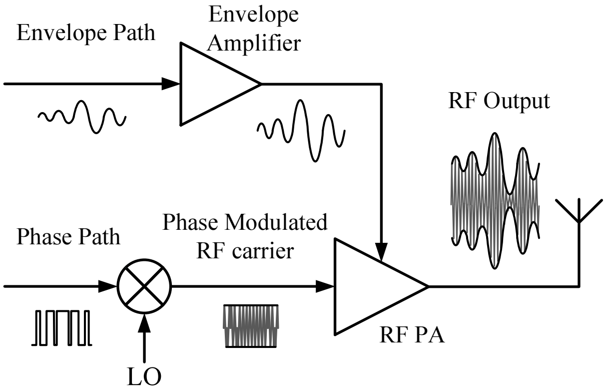

Figure 1.1: Block diagram of an EER system.

supply [15]. Therefore the power supply must be extremely accurate with low noise and distortion. Since the envelope signal is of wider bandwidth compared to the RF output signal, a carefully designed envelope amplifier with sufficiently large bandwidth and high power efficiency is favored. A common rule of thumb of the envelope signal bandwidth is five to seven times of the intended signal bandwidth [15]. The EER scheme potentially provides RF PA peak efficiency even for back-off output power. However, the envelope amplifier with the required bandwidth tends to compromise the power efficiency and reduces the overall transmitter efficiency. The overall transmitter efficiency can be estimated by the product of the individual efficiency by [31]

$$\eta = \eta_{\mathrm{EA}}\eta_{\mathrm{PA}} \tag{1.1}$$

where η_{EA} is the envelope amplifier efficiency and η_{PA} is the RF PA drain efficiency. The efficiency gained by the RF PA can be compromised by the envelope amplifier. There exists many publications which focus on improving the efficiency of envelope amplifier [31]. In [32], dynamic supply circuits using delta modulation and dual-PWM were designed and implemented to achieve a wider bandwidth and higher efficiency for wireless handheld applications. Another issue associated with EER technique is the synchronization between the supply voltage and the RF signal. Since the envelope of the RF PA output signal is determined by the supply voltage, time alignment is critical towards an accurate output. Otherwise, mismatch distortion is required to be compensated [33, 34].

Envelope Tracking

A block diagram of an ET system is shown in Figure 1.2. The ET system shares the similar architecture as the EER system shown in Figure 1.1. The difference is that the RF PA in ET is operated in linear mode, amplifying the upconverted input signal, meaning that the RF PA output signal is defined by the RF PA input signal. Hence, the value of the power supply has a minor effect on the RF output signal envelope compared to the EER scheme [15]. The supply voltage does not have to follow the signal envelope with great accuracy, which is one of the

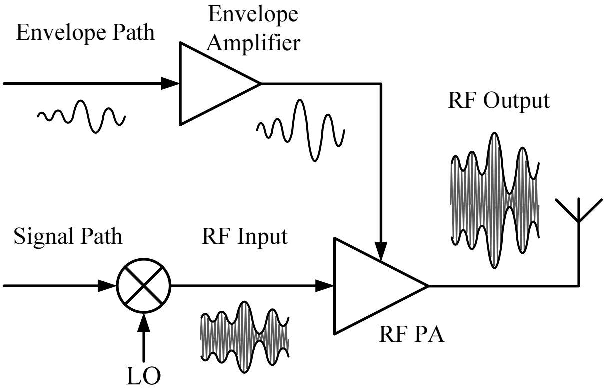

Figure 1.2: Block diagram of an ET system.

appealing aspects of the ET scheme. Although the peak RF PA efficiency in ET architecture is the same as in conventional linear PA with constant supply voltage, the average efficiency is higher [35, 36].

The power efficiency issue of the envelope amplifier in the EER scheme also exists in the ET technique since the transmitter efficiency based on the ET technique depends on the efficiency of the envelope amplifier. Mismatch distortion between the RF input to the PA and the supply voltage is also required to be compensated. There exists many publications which focus on the ET technology [16, 37, 38] or employing hybrid EER and ET schemes to achieve wideband and high efficiency [39]. In [40], wideband ET and hybrid EER structures were proposed. A high efficiency wideband envelope amplifier is designed for EER and ET based wireless LAN applications and an adaptive time-alignment algorithm was proposed to calibrate the time-mismatch in EER and ET systems.

1.2.2 Dynamic Load Modulation

The DLM technique can be used to enhance RF PA efficiency when an envelope-varying signal is employed. The Chireix outphasing amplifier and the Doherty amplifier are commonly referred DLM architectures in the literature. The concept of the DLM technique is that the load impedance seen by the PA varies according to the envelope level of the input signal where the load impedance is selected to provide a good signal linearity and system efficiency [6, 41].

The Chireix Outphasing Amplifier

The Chireix outphasing technique was proposed by Chireix in 1935 [17]. The technique is the origin of the term linear amplification using nonlinear component (LINC), which was first introduced by Cox in 1974 [42]. The outphasing amplifier has been the subject of recent papers in the literature [18, 43–46]. Figure 1.3 shows a block diagram of the Chireix outphasing system.

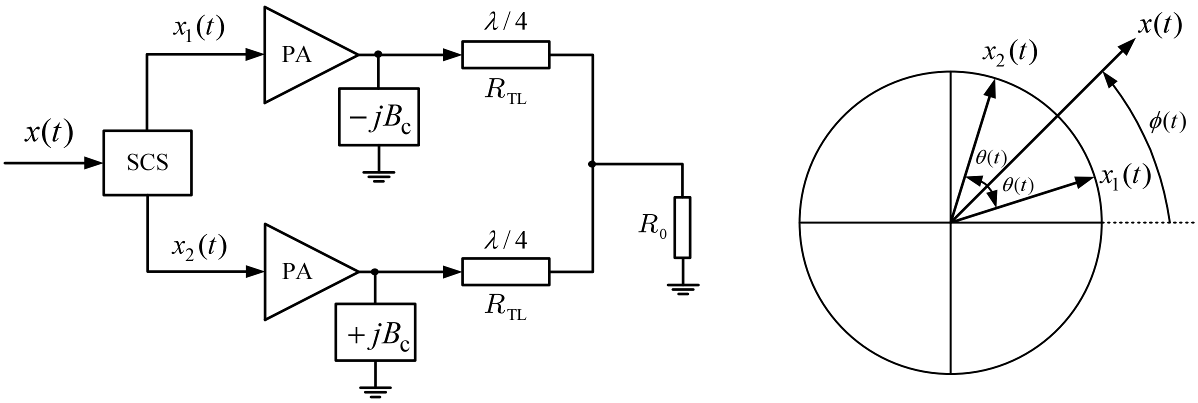

Figure 1.3: Block diagram of a Chireix outphasing system.

The baseband input signal

$$x(t) = a(t)e^{j\phi(t)} \tag{1.2}$$

consisting of the magnitude information $a(t)$ and phase information $\phi(t)$ is separated into two phase modulated constant envelope signals by a signal component separator (SCS). The magnitude signal $a(t)$ can be written in the form

$$a(t)= A_{\max}\cos(\theta(t)) \tag{1.3}$$

where $A_{\max}$ is the maximum value of $a(t)$ and $\theta(t)$ is the outphasing angle which is given by

$$\theta(t) = \arccos\left(\frac{a(t)}{A_{\max}}\right). \tag{1.4}$$

The baseband equivalent expressions of two constant envelope signals are

$$x_1(t)= \frac{A_{\max}}{2}e^{j(\phi(t)+\theta(t))} \tag{1.5}$$

$$x_2(t)= \frac{A_{\max}}{2}e^{j(\phi(t)-\theta(t))}. \tag{1.6}$$

The amplified signals from two RF PAs are combined through a power combiner to retrieve the transmission signal which is ideally a linearly amplified version of the original input signal. These two RF PAs are operated at a fixed input drive level and can be highly nonlinear such as SMPAs [6]. The susceptances B_c and $-B_c$ are added to mitigate the effect of the reactive loads seen by PAs [47] in order to enhance the system efficiency.

The efficiency of the Chireix outphasing amplifier based on ideal Class B PAs for constant

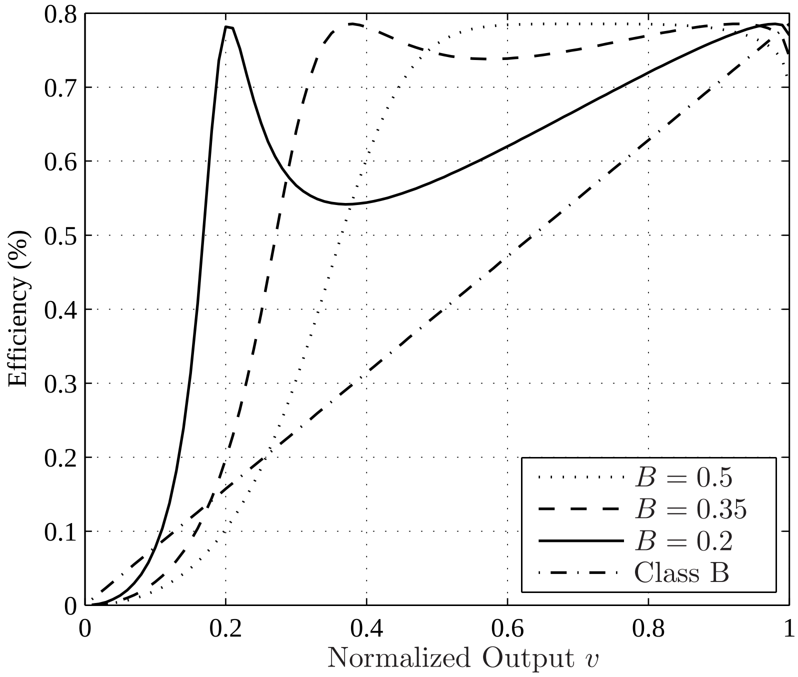

Figure 1.4: Efficiency curves of an ideal Class B based Chireix outphasing PA with different normalized compensation susceptance B.

input signals can be expressed by

$$\eta = \frac{\pi}{4} \frac{v^2}{\sqrt{v^4 + \left(v\sqrt{1-v^2} - B\right)^2}} \tag{1.7}$$

where $v = \cos\theta \in [0,1]$ is the normalized output voltage and $B = B_\mathrm{c} R_\mathrm{TL}^2/(2R_\mathrm{o})$ is the normalized compensation susceptance [47] and R_o is the load impedance. The derivation of (1.7) is shown in Appendix A.1 according to the results obtained in [47]. One case of interest is when $B = 0$, where the resulting efficiency is the same as for an ideal Class B PA. Another interest case occurs when the selection of the B yields a purely resistive load presented at PAs. In this case, the resulting efficiency is the peak efficiency of 78.5% if an ideal Class B PA is considered. Therefore it is possible for the Chireix outphasing amplifier to achieve the maximum efficiency for different output signal levels by choosing an appropriate compensation susceptance. The efficiency curves of the Chireix outphasing amplifier for different normalized B are show in Figure 1.4.

Although the outphasing system is recognized as a highly efficient and linear architecture, some common issues limit its deployment in achieving both high efficiency and linearity. First, the constant envelope signals are required to be generated with two precise phase signals. The linearity of the combined output signal is sensitive to the amplitude and phase mismatch from two branches. In [48], a digital amplitude-to-phase conversion scheme was proposed to implement the converter in digital domain with both accuracy and efficiency. Second, although each branch

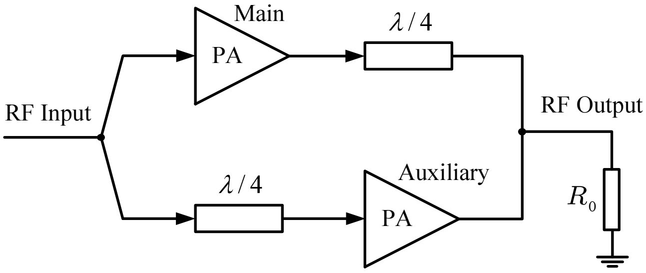

Figure 1.5: Block diagram of a Doherty RF PA.

is able to provide high efficiency by employing an SMPA or a linear PA driven into saturation, the outphasing system as a whole may not preserve this high efficiency. In [18] it is shown that the use of a matched and lossy combiner gives good linearity but decreased efficiency. In case of a nonmatched and lossless combiner, the efficiency is improved, however at the expense of the increased nonlinearity induced from the combining structure.

The Doherty Amplifier

The Doherty amplifier was first proposed in 1936 in [19] and has become one of the most popular efficiency enhancement techniques in recent days [13, 20, 21, 49–51]. The basic concept of a two-stage Doherty amplifier is shown in Figure 1.5. The two amplifiers are termed the main PA and the auxiliary PA[1]. The RF input is split into a low power part and a high power part which go through the main PA and auxiliary PA respectively. The quarter wavelength transmission line on the input to the auxiliary PA is used to compensate for the phase shift of the output signal in the main path. The outputs from the two PAs are then combined through a quarter wavelength transmission line coupler [6]. The output transmission line is used to achieve the load modulation such that the load seen by each PA is varying in different power operation regions in order to maintain high efficiency for power in backoff.

The transition point, denoted as α, is used to divide power operation regions. It is defined as the normalized output voltage level where the auxiliary PA starts to operate. At low output voltage level, which is below the threshold α, the auxiliary PA is cut off and the impedance seen by the auxiliary PA is infinite. The main PA is operated as a linear amplifier with a load impedance of R_o/α^2, where R_o is the output impedance at the load [52]. For output levels above the transition point α, the auxiliary PA starts to operate and the main PA remains saturated and outputs its maximum value.

For an ideal Doherty PA based on ideal Class B PAs, the system efficiency can be expressed as a function of normalized output voltage by

$$\eta = \begin{cases} \dfrac{\pi}{4}\dfrac{v}{\alpha}, & \text{for } v \in [0, \alpha] \\ \dfrac{\pi}{4}\dfrac{v^2}{v(\alpha+1)-\alpha}, & \text{for } v \in (\alpha, 1] \end{cases} \tag{1.8}$$

---

[1] The terms carrier PA and peaking PA are used instead of main PA and auxiliary PA in some literature.

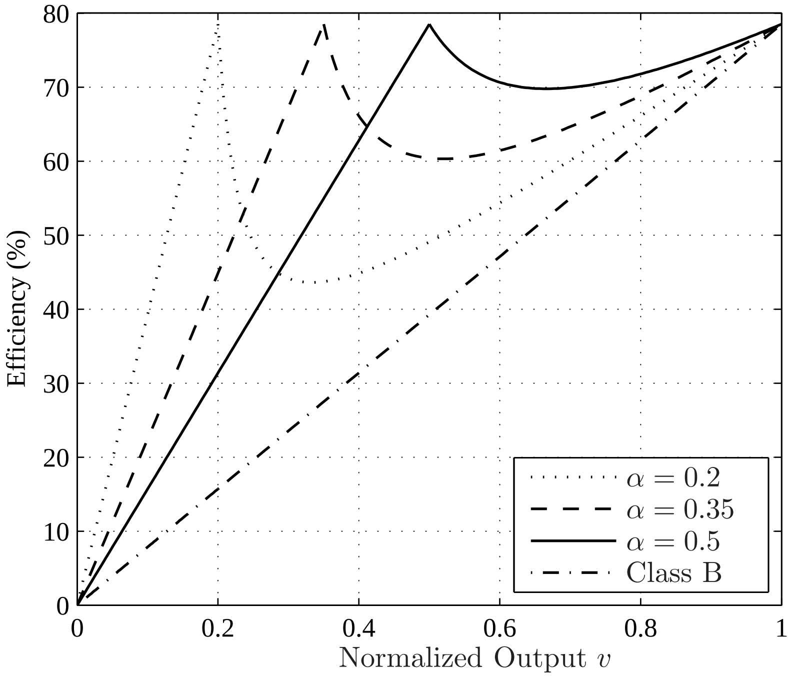

Figure 1.6: Efficiency curves of an ideal Class B based Doherty PA with different transition points α.

where v is the normalized output voltage and $\pi/4$ is the ideal Class B PA peak efficiency. The derivation of (1.8) is given in Appendix A.2 according to [6, 52].

Figure 1.6 shows the efficiency curves according to (1.8) with different values of α. Most conventional PAs with constant load impedance have only one peak power efficiency when applied with peak input level. The example with the ideal Class B PA is illustrated in the figure with dashed-dot line. For the Doherty PA, peak efficiency can be achieved at lower power levels besides the peak level and the efficiency between remains high.

There are several issues related to the practical realization of the Doherty amplifier. Usually the main PA is biased in Class AB mode while the auxiliary PA is biased in Class C mode. The gate biases of the two PA have to be carefully controlled to have the same gain compression characteristics for both of the PAs [21]. The predistortion technique is usually required to compensate the nonlinearity [53–55]. Another issue is the gain fluctuation due to the varying impedances presented at the PA in different power operation regions [21]. Practical methods that mitigate the problem are to divide the input power in an unequal way [51] or to control the main PA and auxiliary PAs separately by digital means [50]. In [56], a digital control strategy was proposed to control the gate bias of the auxiliary amplifier so that the gain variation is mitigated. It is known that the bandwidth of the Doherty amplifier is limited due to the use of the quarter wavelength transmission line as the output combining network, which compromises its capability for wideband/multiband applications [57, 58]. Research effort has been taken into design of wideband Doherty amplifiers [57, 59, 60].

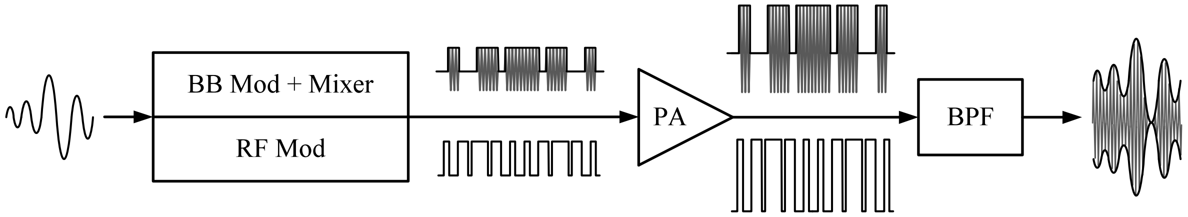

Figure 1.7: Block diagram of a pulsed RF transmitter with baseband and RF modulation schemes.

1.2.3 Pulsed RF Transmitter Architectures

The principle of operation of a pulsed RF transmitter is that a pulsed signal is first generated in the baseband or by an RF modulator, and then amplified by the RF PA. The RF PA is operated in two states: the "on" state and the "off" state. During the "on" state, the RF PA outputs full power and produces the peak efficiency. During the "off" state, the RF PA is completely off and no power is consumed. The transmission signal is then retrieved by means of a BPF before it is sent to the antenna. There are two types of transmitter architectures commonly referred in the literature named after the modulation schemes they employ, namely the SDM based architecture and PWM based architecture. Each transmitter architecture can be divided into two categories: RF or baseband modulation based architecture. Therefore the transmitter employing the respective modulation scheme can be divided into four types: the bandpass sigma-delta modulation (BPSDM) [24,30], the RFPWM [61–64], the lowpass sigma-delta modulation (LPSDM) [25,30,65], the baseband PWM or burst-mode [22,66,67] based RF transmitter architectures. This thesis focuses on the burst-mode RF transmitter architecture. Figure 1.7 shows a simplified block diagram of a pulsed RF transmitter with either a baseband modulation scheme or an RF modulation scheme.

BPSDM based Transmitter Architecture

In BPSDM based transmitters, a pulsed signal at the carrier frequency is generated by the BPSDM modulator. A BPF is required to retrieve the transmission signal to the load since the major drawback of SDM is the large amount of distortion generated by the quantization process [30]. In [68] the application of the BPSDM based transmitter was introduced for the first time where an SMPA was employed as the RF PA. One advantage of the BPSDM transmission is the free of low-frequency noise and distortion [30]. However, when the BPSDM modulator is directly connected to the RF PA, the required clock is four times the carrier frequency, which is not practical [30]. Low intermediate frequency (IF) architectures [69,70] can be used to relax the high clock speed requirement, however, at the expense of the complexity, cost and integration difficulty [30]. Another issue associated with BPSDM is that the required implementation effort of BPSDM is twice of its LPSDM counterpart [30].

RFPWM based Transmitter Architecture

The principle of operation of RFPWM is to vary the pulse width of the generated pulsed train signal at each RF carrier period according to the magnitude of the input signal. The phase information is represented by the timing or the pulse position of the pulses. The unipolar PWM and the bipolar PWM are commonly used RFPWM methods. The harmonics produced by the unipolar PWM are located at multiples of the carrier frequency. While by the bipolar PWM, only harmonics at odd multiples of the carrier frequency are produced. The coding efficiency of RFPWM signals has been addressed in [71]. Since the generated harmonics are far away from the wanted signal located at the carrier frequency, the requirements on the BPF are relaxed. However, the RFPWM method produces pulses with short pulse width especially for signals with high PAPR. It is difficult for the RF PA to correctly and efficiently amplify the narrow pulses. There are studies focus on the novel RF PA topologies design [62,72,73]. Future research from the signal processing point of view is required to look into related issues of the RFPWM scheme.

LPSDM based Transmitter Architecture

LPSDM is a more popular type of SDM used in transmitter architectures in the literature [30,74]. In [74], it was proven that the LPSDM offers the simplest and more efficient architecture compared to its band-pass (BP) and high-pass (HP) counterparts. A quantization noise reduction technique was proposed where a small portion of the out-of-band quantization noise was filtered out such that the SMPA still can be driven by quasi-pulsed signal and provides high efficiency. In [65], a partial quantization noise cancellation method is proposed to suppress the in-band and partial out-of-band quantization noise thus enables the use of a relatively wideband BPF. The baseband magnitude signal is first quantized by the 1-bit LPSDM, producing a binary amplitude signal which includes the desired signal magnitude and the quantization noise. Then the quantization noise is calculated by subtracting the baseband input signal from the quantized signal. A cancellation component is obtained by applying a selected cancellation filter which determines the compensation bandwidth. Afterwards the cancellation component is subtracted from the quantized signal thus the in-band and partial out-of-band quantization noise is eliminated. The selection of the compensation bandwidth needs to be carefully considered. On the one hand, when the compensation bandwidth approaches zero, no noise suppression is performed and the system is a regular LPSDM system with a binary output. On the other hand, when the compensation bandwidth approaches half of the sampling rate of the SDM, meaning that an all pass cancellation filter is used, the system output is identical to the input signal. Therefore the RF PA will be operated in regular linear mode. The author of [65] has investigated signal processing aspects for LPSDM based RF transmitter in [75].

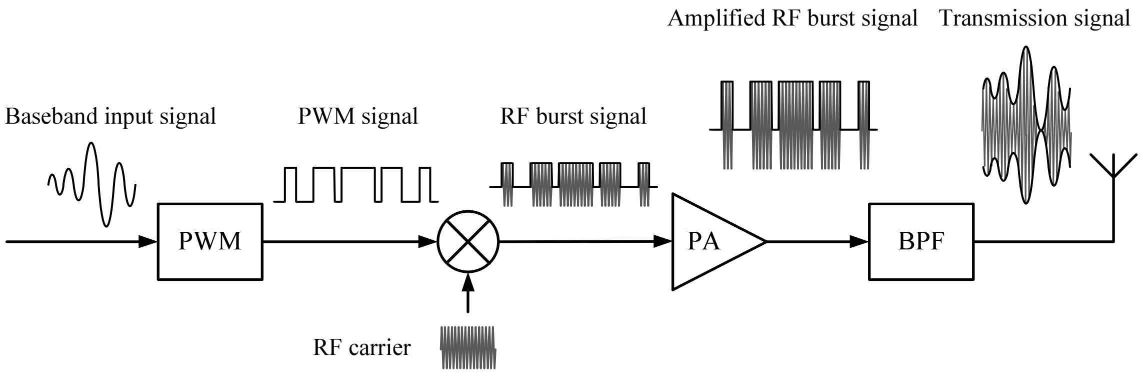

Figure 1.8: Block diagram of a burst-mode RF transmitter architecture.

Burst-Mode Transmitter Architecture

A block diagram of the burst-mode RF transmitter architecture is shown in Figure 1.8. In ideal burst-mode operation [22, 66, 67], a varying-envelope baseband input signal is encoded into a pulsed signal through the pulse-width (PW) modulator. The PWM signal is generated with varying pulse width which depends on the magnitude information of the baseband input signal. The generated PWM signal is then multiplied with the RF carrier to form the RF burst signal. Afterwards, the RF burst signal will be amplified by the RF PA, which is operated in efficient burst mode. Finally, the transmission signal is retrieved by a BPF and sent to the antenna.

An RF PA operated in the burst mode is called a burst-mode RF PA. It can be a linear RF PA [6] driven into saturation or an efficient switched-mode RF PA [6]. The burst-mode RF PA has two operation modes, namely the “on” mode and the “off” mode. During the “on” mode, the RF PA amplifies the applied RF burst signal with non-zero constant envelope. The RF PA thus continuously operates in saturation and generates the amplified RF burst signal with the peak efficiency. During the “off” mode, without applying any input signal, the RF PA is completely off and no power is consumed. Therefore, the burst-mode RF PA operates efficiently in both modes. Thus, high efficiency is possible even with a baseband input signal of high PAPR. A more detailed analysis will be given in Chapter 2.

1.3 Scope of the Thesis

The main objective of this thesis is to use signal processing methods [76, 77] to analyze the efficient burst-mode RF transmitter architecture in order to optimize the transmitter efficiency without compromising the linearity performance.

Numerous methods of design and implementation of the RF PA or transmitter have been reported in the literature, but there are few analytical papers with system-level descriptions of efficient transmitter architectures. In order to investigate the performance of burst-mode RF transmitters, a complete and exact mathematical description of the burst-mode RF transmitter chain is necessity. In a burst-mode RF transmitter, the PW modulator, which encodes the baseband input signal into a pulsed train with varying pulse width, plays an important role. Therefore one focus of the thesis is to develop the analytical description of the baseband PWM signals and extend the results to the passband RF burst signals, amplified RF burst signals and finally the transmission signals. Another focus of the thesis is to analyze and optimize the transmitter efficiency. To this end, the transmitter efficiency is expressed by the multiplication of the maximum RF PA efficiency and the coding efficiency, which evaluates the performance of the PW modulator. An intensive research on the coding efficiency is carried out.

Due to the infinite bandwidth of the PWM signal, problems occur when the PWM is performed digitally. The wanted signal is already severely distorted before the RF PA. To investigate the origin of the distortion, the analytical expressions of discrete-time PWM signals are described accordingly, based on which, an aliasing-free PWM (AFPWM) method is presented. The AFPWM method avoids all destructive distortion originating from the sampling of non-bandlimited signals by limiting the spectral components, in terms of the number of harmonics in the generated PWM signals. The AFPWM method introduces amplitude variations to the generated PWM signals. Hence the RF PA is no longer operated in ideal burst mode. To investigate the transmitter efficiency performance, the efficiency analysis is performed on the discrete-time PWM based burst-mode RF transmitters where it surprisingly shows that the higher coding efficiency compensates for the RF PA efficiency degradation, leading to a transmitter efficiency without degradation. An important result obtained is that good efficiency-linearity trade-off can be achieved by carefully choosing the number of harmonics in AFPWM based burst-mode RF transmitters.

1.4 Outline of the Thesis and Main Contributions

In the following, a chapter by chapter overview will be provided with the main contributions of the author and her publications.

Introduction

In Chapter 1, an introduction of the state-of-the-art efficiency enhancement technology for wireless transmitters is given followed by the introduction of the burst-mode RF transmitter which is the main topic of the thesis.

System Models of Burst-Mode RF Transmitters

In Chapter 2, burst-mode RF transmitter architectures including the two-level and multilevel architectures have been described. The RF PA in a burst-mode RF transmitter is operated in “on” and “off” modes, meaning that when the PA is activated, it is operated in saturation and produces the maximum efficiency, otherwise it is switched off and no power is wasted. This leads to substantially high efficiency of the RF PA.

The efficiency metrics of burst-mode RF transmitters including the PA drain efficiency, the coding efficiency and the transmitter efficiency are given. The coding efficiency is an important figure of merit in the efficiency evaluation of burst-mode RF transmitters. It describes the performance of the PW modulator and the ratio of the transmission power delivered to the antenna to the total power at the output of the RF PA. The transmitter efficiency is ideally the coding efficiency multiplied by the maximum PA drain efficiency.

To investigate the performance of burst-mode RF transmitters, closed-form descriptions of PWM signals of different kinds are provided, such as single-edge PWM (SEPWM), double-edge PWM (DEPWM), two-level PWM and multilevel PWM. The analytical results serve as a basis for the analysis in the rest of the thesis.

[78] S. Chi, C. Vogel and P. Singerl, “The frequency spectrum of polar modulated PWM signals and the image problem,” in *Proceedings of 17th IEEE International Conference on Electronics, Circuits, and Systems (ICECS 2010)*, pp. 679-682, December 2010.

[23] K. Hausmair, S. Chi, P. Singerl and C. Vogel, “Aliasing-free digital pulse-width modulation for burst-mode RF transmitters,” in *IEEE Transactions on Circuits and Systems I: Regular Papers*, pp.415 -427, February 2013.

Continuous-Time PWM Based Burst-Mode RF Transmitters

In Chapter 3, continuous-time PWM based burst-mode RF transmitters are described. In the first part, the image problem that occurs when the non-bandlimited baseband PWM signal is mixed with the carrier frequency to the passband. The wanted signal located around the positive carrier frequency is overlapped with the spectral components of the signal which is modulated to the negative carrier frequency. Thus the wanted signal is distorted already before the RF PA. To deal with the image problem, mathematical expressions of RF burst signals are provided. By using a proper PWM frequency, the image peak distortion in TEPWM signal can be avoided without additional analog component like analog lowpass filter (LPF). The DEPWM method can be treated as a method to reduce the image peak distortion in TEPWM signals.

In the second part, efficiency analysis for continuous-time PWM based burst-mode two-level and multilevel RF transmitters is presented. The efficiency optimization of burst-mode multilevel RF transmitters is investigated. To this end, analytical descriptions of the transmitter efficiency given by the coding efficiency and the maximum PA drain efficiency are presented. The maximum average transmitter efficiency can be achieved by properly choosing the threshold values, which are used to divide the input signal magnitude into several regions, according to the probability density function (PDF) of the input magnitude. Moreover, the efficiency expressions of the burst-mode multilevel transmitters are related to those of the Doherty and multistage Doherty PAs. It shows that the efficiency optimization can also been applied to Doherty and multistage Doherty PAs. Efficiency optimized burst-mode RF transmitters show a great efficiency improvement compared to the non-optimized transmitters, especially for signals with high PAPRs and signals transmitted at a wide range of transmission power levels.

[78] S. Chi, C. Vogel and P. Singerl, “The frequency spectrum of polar modulated PWM

signals and the image problem," in *Proceedings of 17th IEEE International Conference on Electronics, Circuits, and Systems (ICECS)*, pp. 679-682, December 2010.

[79] S. Chi, P. Singerl and C. Vogel, "Coding efficiency optimization for multilevel PWM based switched-mode RF transmitters," in *Proceedings of IEEE 54th International Midwest Symposium on Circuits and Systems (MWSCAS)*, pp. 1-4, August 2011.

[80] S. Chi, P. Singerl and C. Vogel, "Efficiency optimization for burst-mode multilevel radio frequency transmitters," in *EEE Transactions on Circuits and Systems I: Regular Papers*, pp.1901-1914, July 2013.

Discrete-Time PWM based Burst-Mode RF Transmitters

In Chapter 4, discrete-time PWM based burst-mode RF transmitters are described. The discrete-time PWM process is described first and it is shown that the discrete-time PWM signals inherently suffer from aliasing distortion due to the sampling of non-bandlimited baseband PWM signals, resulting in degraded signal quality. To gain a deeper understanding of the discrete-time PWM signals, mathematical expressions of the discrete-time PWM signals are presented. An aliasing-free PWM (AFPWM) method is described to avoid the destructive distortion by limiting the number of harmonics in the generated PWM signals.

AFPWM signals induce small variations on the time-domain signal amplitude, which might affect the RF PA drain efficiency. As has been described before, the transmitter efficiency also depends on the coding efficiency. To investigate the efficiency performance, a thorough analysis on the coding efficiency of the AFPWM based burst-mode RF transmitters is performed. The results show that the higher coding efficiency compensates for the RF PA efficiency degradation leading to a transmitter efficiency without degradation.

An important result obtained is that by properly choosing the number of harmonics used in the generated PWM signals, a good efficiency-linearity trade-off can be achieved for AFPWM based burst-mode RF transmitters.

An analysis of multilevel AFPWM based burst-mode RF transmitters is carried out. The analytical descriptions of multilevel architectures are described from which it is shown that the multilevel architecture can be used to further enhance the transmitter efficiency. Simulation results are used to verify the analytical results. It is also shown that a good efficiency-linearity trade-off can also be achieved by proper choice of the number of harmonics.

[81] S. Chi, K. Hausmair, P. Singerl and C. Vogel, "Coding efficiency of bandlimited PWM based burst-mode RF transmitters," in *Proceedings of 2013 IEEE International Symposium on Circuits and Systems (ISCAS)*, pp.2263 - 2266, May 2013.

[80] S. Chi, P. Singerl and C. Vogel, "Efficiency optimization for burst-mode multilevel radio frequency transmitters," in *EEE Transactions on Circuits and Systems I: Regular Papers*, pp.1901-1914, July 2013.

[23] K. Hausmair, S. Chi, P. Singerl and C. Vogel, "Aliasing-free digital pulse-width modulation for burst-mode RF transmitters," in *IEEE Transactions on Circuits and Systems I: Regular Papers*, pp.415 -427, February 2013.

Summary & Concluding Remarks

In Chapter 5, the scientific work of the thesis is summarized and further research is discussed.

[82] K. Hausmair, S. Chi, P. Singerl and C. Vogel, “How to reach 100% coding efficiency in multilevel burst-mode RF transmitters,” in *Proceedings of 2013 IEEE International Symposium on Circuits and Systems (ISCAS)*, pp.2263 - 2266, May 2013.

2

System Models of Burst-Mode RF Transmitters

In this chapter, different burst-mode RF transmitter architectures will be discussed with detailed information. Then the efficiency metrics that are used to evaluate the performance of burst-mode RF transmitters will be described. Finally the mathematical expressions of PWM signals of different kinds will be derived and analyzed. The analytical results describing the PWM signals are one of the main contributions and will serve as a basis for the analysis in the following chapters.

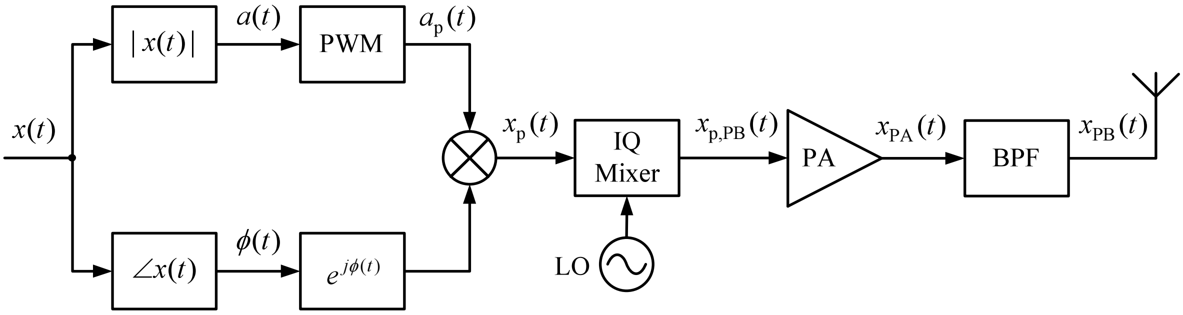

Figure 2.1: Block diagram of a burst-mode two-level RF transmitter architecture.

2.1 Introduction to Burst-Mode RF Transmitters

In burst-mode RF transmitters, the RF PA is ideally operated in "on" and "off" modes, producing the peak efficiency. To drive the RF PA in burst mode, the PWM technique is employed to map the input magnitude into a pulsed train signal. There exists a variety of PWM methods [1] for encoding the baseband input signal into a pulsed signal. The polar modulation based burst-mode transmitter architecture is employed due to its superiority in terms of the efficiency and the lower demand on analog RF components [83]. Depending on the number of PW modulators used, the burst-mode RF transmitters can be categorized into two-level burst-mode RF transmitters, where a single PWM is employed, and multilevel burst-mode RF transmitters, where several PW modulators are incorporated. The multilevel architecture is used to further enhance the overall efficiency [27, 80, 84]. It is known that an ideal PWM signal is of infinite bandwidth. As a result, the RF burst signal and the amplified RF burst signal also have infinite bandwidth. To fulfill the transmission spectral requirements, the BPF is used to filter out the out-of-band spectral content. Consequently, the transmission power is reduced and therefore the efficiency obtained after the burst-mode PA is also reduced. The coding efficiency together with the PA efficiency is used to describe the efficiency for burst-mode RF transmitter.

2.1.1 Burst-Mode Two-Level RF Transmitters

A burst-mode two-level RF transmitter employs a single PWM in baseband processing, where the PW modulator outputs a two-level pulsed signal. A block diagram of the transmitter architecture is shown in Figure 2.1. The complex baseband input signal $x(t)$, which is bandlimited to B_s, can be expressed in polar form as

$$x(t) = a(t)e^{j\phi(t)}. \tag{2.1}$$

The signal $x(t)$ is separated into a magnitude signal $a(t)$ and a phase signal $\phi(t)$. To facilitate the analysis for the rest of the thesis, it is assumed that the magnitude signal is normalized by the maximum magnitude value and thus $a(t) \in [0, 1]$. The magnitude signal $a(t)$ is then encoded into a pulsed signal $a_p(t)$ by the PW modulator. The PWM signal is usually generated

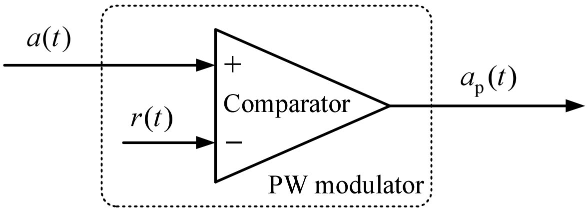

Figure 2.2: Block diagram of a comparator based PW modulator.

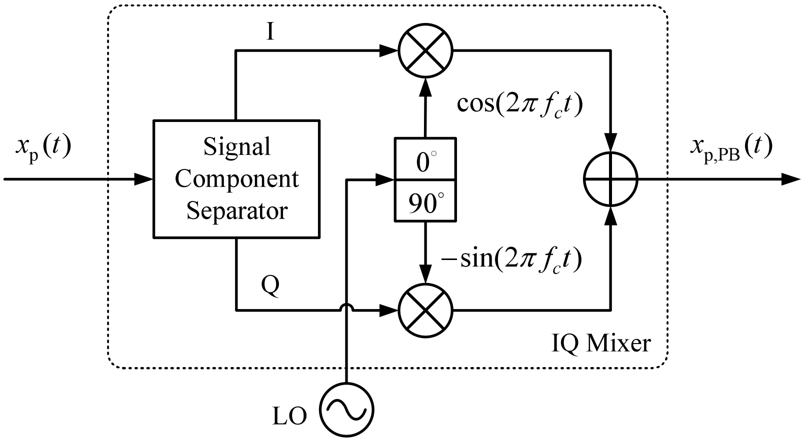

Figure 2.3: Block diagram of an IQ mixer.

by a comparator, comparing the modulating signal $a(t)$ with a reference signal $r(t)$, which has typically the form of a sawtooth waveform or a triangular waveform. A block diagram of the comparator based PW Modulator is shown in 2.2. The generated PWM signal $a_{\mathrm{p}}(t)$ will be multiplied with the phase component $e^{j\phi(t)}$ to form the baseband PWM signal $x_{\mathrm{p}}(t)$. Afterwards, the baseband PWM signal $x_{\mathrm{p}}(t)$ is separated into an in-phase (I) and a quadrature (Q) part and upconverted to the passband by the IQ mixer. A block diagram of the IQ mixer is given in 2.3. The resulting upconverted PWM signal, or the RF burst signal $x_{\mathrm{p,PB}}(t)$ is given by

$$\begin{aligned} x_{\mathrm{p,PB}}(t) &= \mathrm{Re}\left\{x_{\mathrm{p}}(t)e^{j2\pi f_{\mathrm{c}}t}\right\} \\ &= x_{\mathrm{pr}}(t)\cos(2\pi f_{\mathrm{c}}t) - x_{\mathrm{pi}}(t)\sin(2\pi f_{\mathrm{c}}t) \\ &= a_{\mathrm{p}}(t)\cos(2\pi f_{\mathrm{c}}t + \phi(t)) \end{aligned} \tag{2.2}$$

where f_{c} is the carrier frequency and $x_{\mathrm{pr}}(t)$ and $x_{\mathrm{pi}}(t)$ are real part and imaginary part of the signal $x_{\mathrm{p}}(t)$. Then the RF burst signal is amplified by the burst-mode RF PA, producing the amplified RF burst signal $x_{\mathrm{PA}}(t)$. The transmission signal $x_{\mathrm{PB}}(t)$, which is the RF equivalent of $x(t)$, is retrieved from the amplified RF burst signal $x_{\mathrm{PA}}(t)$ by the BPF.

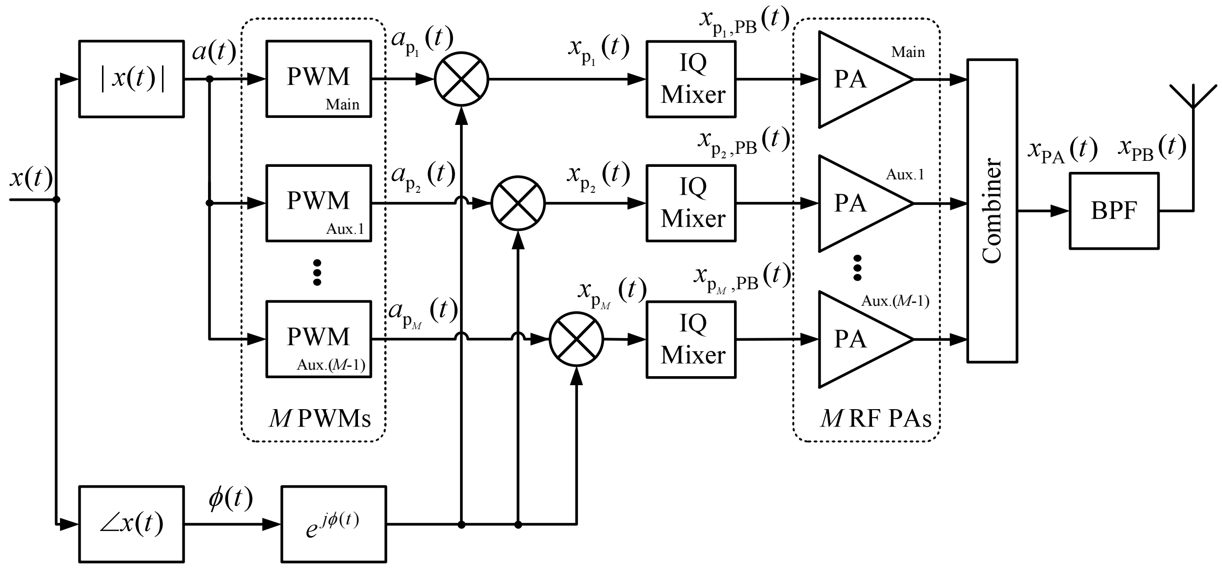

Figure 2.4: Block diagram of a burst-mode multilevel RF transmitter architecture. The transmitter incorporates M signal paths where M PW modulators and M RF PAs are used. The resulting combined output signal is of $(M+1)$ levels.

2.1.2 Burst-Mode Multilevel RF Transmitters

The burst-mode multilevel architecture is used to further enhance the transmitter efficiency for low-valued input signal, or power in backoff, by incorporating more than one PW modulator as well as the RF PA. Figure 2.4 depicts a block diagram of the burst-mode multilevel transmitter architecture consisting of M signal paths, i.e., $(M+1)$ levels in the generated combined signal, where M PW modulators and M RF PAs are employed.

Different from the two-level transmitter architecture, the magnitude signal $a(t)$ in the multilevel transmitter architecture is modulated by the multilevel PWM by comparing $a(t)$ with a series of reference signal $r_m(t)$, where the index m denotes the signal path order with $m \in [1, M], M \geq 2$. The reference signal $r_m(t)$ is defined on the interval $[V_{m-1}, V_m]$, where V_l represents a set of threshold values defined as

$$V_i = \begin{cases} 0, & \text{for} \quad i = 0 \\ \in (0,1), & \text{for} \quad i \in [1, M-1] \\ 1, & \text{for} \quad i = M \end{cases} \tag{2.3}$$

where the index $i \in [0, M]$ denotes the order of the threshold value.

By applying the multilevel PWM to the magnitude signal $a(t)$, a set of PWM signals $a_{p_m}(t)$ is generated. When $a(t)$ is higher than 0 but lower than the threshold value V_1, only the main PW modulator operates and generates the main baseband PWM signal $a_{p_1}(t)$ with the magnitude of V_1 but varying pulse widths. When $a(t)$ exceeds the threshold value V_1, the first auxiliary baseband PWM signal $a_{p_2}(t)$ consisting of pulses with the magnitude of $(V_2 - V_1)$ is generated and the main PW modulator outputs the constant value of V_1, indicating that the duty cycle of the main baseband PWM signal is 100%. The operation of other auxiliary PW modulators follows the same procedure.

A set of RF burst signals $x_{\mathrm{p}_m,\mathrm{PB}}(t)$ is obtained by upconverting the phase modulated PWM signals $x_{\mathrm{p}_m}(t)$ with the IQ mixer. This set of RF burst signals is used to drive a set of burst-mode RF PAs. The main RF PA is driven by the main RF burst signal $x_{\mathrm{p}_1,\mathrm{PB}}(t)$. When the input magnitude exceeds the threshold value V_1, the first auxiliary RF burst signal $x_{\mathrm{p}_2,\mathrm{PB}}(t)$ is generated and drives the first auxiliary RF PA while the main RF PA remains on. When the input magnitude exceeds the threshold value V_2, the second auxiliary PW modulator and the RF PA will be activated and so on. A power combiner is employed to combine the RF PA outputs. After the BPF, the transmission signal $x_{\mathrm{PB}}(t)$ is retrieved from the amplified RF burst signal $x_{\mathrm{PA}}(t)$ and sent to the antenna.

Using the above principle, the burst-mode multilevel transmitter architecture is able to provide higher efficiency for a larger range of output power levels compared to the conventional two-level transmitter architecture, because the multilevel architecture generates less out-of-band power [79, 80]. The analytical description of the PWM signals will be given in the third part of this chapter and the detailed efficiency analysis will be given in the following chapter.

2.2 Efficiency Metrics

Power efficiency is an important factor for the evaluation of the transmitter performance. Since a burst-mode transmitter employs a source encoder such as a PW modulator, out-of-band spectral components are generated. The out-of-band spectral power has to be filtered out to obtain the transmission signal which fulfills the transmission requirements. Hence the transmission power is reduced. The transmitter efficiency, denoted as η, is therefore reduced and is different from the PA drain efficiency, denoted as η_{PA}. Nevertheless, a burst-mode PA ideally provides the peak drain efficiency, which is weighted by the coding efficiency, denoted as η_{c}, to obtain the transmitter efficiency. The coding efficiency is introduced as a figure of merit to evaluate the PW modulator performance,

2.2.1 Power Amplifier Drain Efficiency

PA drain efficiency η_{PA} is defined as the ratio between the delivered total power of the amplified RF burst signal $x_{\mathrm{p,PB}}(t)$ and the consumed dc power,

$$\eta_{\mathrm{PA}} = \frac{P_{\mathrm{tot}}}{P_{\mathrm{dc}}}. \tag{2.4}$$

The efficiency η_{PA} represents the drain efficiency of the RF PA in burst-mode operation. When the RF PA is operated in ideal burst mode it produces the peak drain efficiency. An ideal burst-mode PA operates in two states: “on” and “off”. During the “on” state, the PA is driven into saturation and reaches the peak efficiency η_{PA}. During the “off” state, the PA is completely off and no power is consumed. For example, for Class B or multilevel Class B PAs, the PA efficiency is $\eta_{\mathrm{PA}} = 78.5\%$ [52]. For PAs like Class E and Class F^{-1}, the efficiency η_{PA} is theoretically 100% and measured in the range of $70\% - 80\%$ [85].

2.2.2 Coding Efficiency

Coding efficiency is introduced as a figure of merit to evaluate the source encoder performance such as PW modulator. It is defined as the ratio between the power of the transmission signal $x_{\mathrm{PB}}(t)$ and the total power of the amplified RF burst signal $x_{\mathrm{p,PB}}(t)$ [86],

$$\eta_{\mathrm{c}} = \frac{P_{\mathrm{s}}}{P_{\mathrm{tot}}}. \tag{2.5}$$

Coding efficiency analysis is of great importance in the study of burst-mode transmitter architectures. It is a measure of the PWM performance and the transmitter efficiency.

2.2.3 Transmitter Efficiency

Transmitter efficiency η describes the ratio between the transmission signal power and the consumed dc power [87]. For burst-mode transmitters, the efficiency can also be described by the PA drain efficiency η_{PA} and the coding efficiency η_{c} by [80, 83]

$$\eta = \frac{P_{\mathrm{s}}}{P_{\mathrm{dc}}} = \frac{P_{\mathrm{tot}}}{P_{\mathrm{dc}}}\frac{P_{\mathrm{s}}}{P_{\mathrm{tot}}} = \eta_{\mathrm{PA}}\eta_{\mathrm{c}}. \tag{2.6}$$

In ideal burst-mode operation, the transmitter efficiency η is the coding efficiency η_{c} scaled by the peak PA drain efficiency η_{PA}. Therefore a higher coding efficiency η_{c} leads to a higher transmitter efficiency η.

Note that one should distinguish between two types of efficiencies: the efficiency for constant input signals[2] and the average efficiency for signals with a given PDF. The former one is obtained when the signal is at a certain level, for example shown in Figure 1.4 and Figure 1.6. The average efficiency is obtained by weighting the efficiency curve by the signal PDF. The transmitter performance is best measured by the average efficiency [18]. The average efficiency will be denoted by $\overline{\eta}_{\mathrm{PA}}$, $\overline{\eta}_{\mathrm{c}}$ and $\overline{\eta}$ in the following.

2.3 Pulse-Width Modulation

A PW modulator encodes an input signal, or the modulating signal, into a pulsed signal. The PWM process is usually performed by comparing the modulating signal with a reference signal. Depending on the reference waveforms, PWM process can be categorized into single-edge PWM (SEPWM) process and double-edge PWM (DEPWM) process [1]. The former one employs

---

[2] Also known as instantaneous efficiency in the literature.

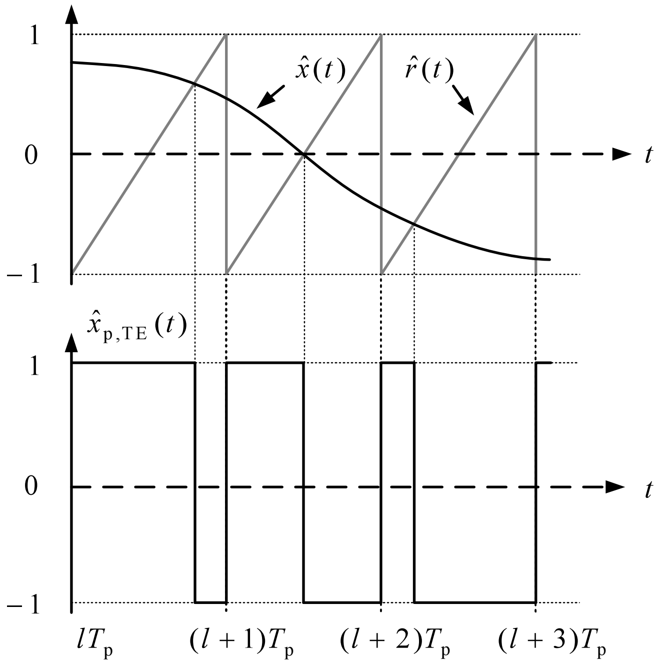

Figure 2.5: An example of the SEPWM process described in [1]. The signals $\hat{x}(t)$, $\hat{r}(t)$ and $\hat{x}_{\mathrm{p,TE}}(t)$ are the modulating signal, reference signal and the generated TEPWM signal, respectively. The period of the reference signal is represented by T_{p}.

a sawtooth reference waveform and the latter one a triangular waveform. Depending on the number of PW modulators used, the PWM process can be categorized into two-level PWM process and multilevel PWM process. The PWM process can also be categorized into uniform-sampling PWM process and natural-sampling PWM process as described in [1]. The generated natural-sampling PWM signal consists of the modulating signal $\hat{x}(t)$ with no distortion in the modulating signal bandwidth except negligible spectral components from higher order harmonics while the generated uniform-sampling PWM signal consists of a distorted form of the modulating signal $\hat{x}(t)$. Therefore, the natural-sampling PWM process concept is adopted in this thesis and hereinafter referred to as the PWM process.

Since PWM plays an important role in burst-mode transmitters, it is desirable to analytically describe the PWM process in order to study the burst-mode technique in depth. In [1], thorough mathematical analysis on the PWM process with different reference signals was carried out, though with Cartesian modulation based PWM process only. An example of such PWM process is illustrated in Figure 2.5, where $\hat{x}(t)$, $\hat{r}(t)$ and T_{p} are the modulating signal, reference signal and the reference signal period, or PWM period, respectively. One drawback of such PWM method is that the coding efficiency is medium. For example, applied with a zero-valued input, the PW modulator still generates a pulsed signal with 50% duty cycle, meaning that the RF PA would still be activated without generating any useful signals. Nevertheless, it provides an analytical approach for the study of the frequency spectra of PWM signals when the modulating signal is an arbitrary bandlimited signal. In this subsection, polar modulation based PWM process will be investigated and closed-form expressions describing the PWM signals of different kinds will be presented.

2.3.1 Two-Level Pulse-Width Modulation

In SEPWM process as illustrated in Figure 2.5 and Figure 2.6, the generated PWM signal will have one edge locate at a fixed time, which is the multiples of the PWM period, while the other edge, trailing-edge (TE) or leading-edge (LE), appears depending on the crossing-points of the input modulating signal and the reference sawtooth signal. The corresponding generated signals are referred to as the TEPWM signal and the LEPWM signal.

In the DEPWM process as illustrated in Figure 2.7, the locations of both edges depend on the crossing-points of the input modulating signal and the reference triangular signal. Since both the TE and the LE of the generated DEPWM signal are determined according to the input modulating signal, the sampling rate is effectively doubled [1].

The analytical approach described in [1] for TEPWM signal will be used as the starting point to deduce the results for polar modulation based TEPWM signal. The results will be transformed to describe LEPWM signal. Afterwards, the expressions of DEPWM signals will be given, which can be decomposed into a sum of a TEPWM signal and a LEPWM signal. Finally, multilevel PWM signals will be described according to the obtained results of SEPWM signals.

Single-Edge PWM Process

Trailing-Edge PWM Process The TEPWM process described in [1] is illustrated in Figure 2.5. The modulating signal is a bounded continuous signal such that $\hat{x}(t) \in [-1, 1]$. A detailed and elaborate analysis leads to the closed-form expression of the TEPWM signal with modulating signal $\hat{x}(t) \in [-1, 1]$ as

$$\hat{x}_{\mathrm{p,TE}}(t) = \hat{x}(t) + \sum_{k=1}^{\infty} \frac{2}{\pi k} \Big[\sin(2\pi k f_{\mathrm{p}} t) - (-1)^k \sin(2\pi k f_{\mathrm{p}} t - \pi k \hat{x}(t)) \Big] \tag{2.7}$$

where k and f_{p} represent the harmonic order and the PWM frequency, $f_{\mathrm{p}} = 1/T_{\mathrm{p}}$, respectively. The subscript “p” denotes the PWM operation.

Assuming that the modulating signal, the reference signal and the generated TEPWM signal in Figure 2.5 are shifted and scaled to be bounded by $[0, 1]$, it is clear that the resulting TEPWM signal is the signal which would be generated by polar modulation based PWM process with modulating signal $a(t)$ as shown in Figure 2.6. Therefore the analytical description of the TEPWM signal produced by polar modulation based PWM process can be deduced accordingly. From Figure 2.5 and Figure 2.6, the modulating signal $a(t)$ can be related to $\hat{x}(t)$ by

$$a(t) = \frac{\hat{x}(t) + 1}{2}. \tag{2.8}$$

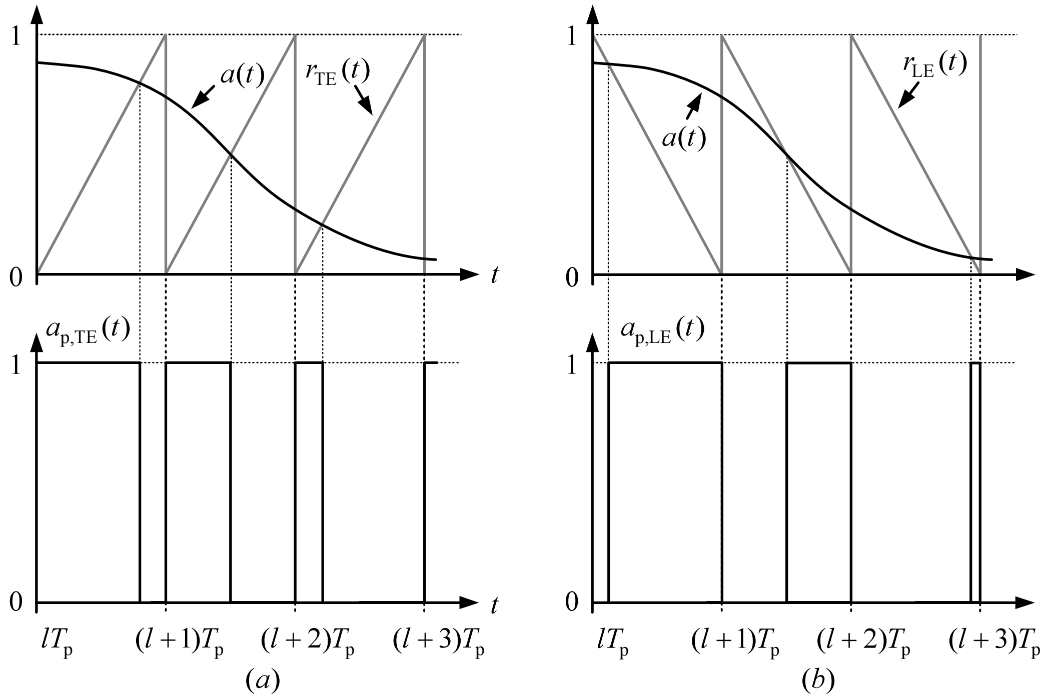

Figure 2.6: SEPWM process: (a) TEPWM process and (b) LEPWM process.

The generated TEPWM signal $a_{\mathrm{p,TE}}(t; a(t))$ with modulating signal $a(t)$ is readily deduced from the TEPWM signal $\hat{x}_{\mathrm{p,TE}}(t)$ with modulating signal $\hat{x}(t)$. It follows that

$$\begin{aligned} a_{\mathrm{p,TE}}(t; a(t)) &= \frac{\hat{x}_{\mathrm{p,TE}}(t; \hat{x}(t)) + 1}{2} \\ &= \frac{\hat{x}_{\mathrm{p,TE}}(t; 2a(t) - 1) + 1}{2}. \end{aligned} \tag{2.9}$$

Note that the modulating signals $a(t)$ and $\hat{x}(t)$ are included as variables to show the transformation steps. Substituting for $\hat{x}_{\mathrm{p,TE}}(t; 2a(t) - 1)$ from (2.7) with modulating signal $(2a(t) - 1)$ gives the description of TEPWM signal $a_{\mathrm{p,TE}}(t)$ by

$$a_{\mathrm{p,TE}}(t) = a(t) + \sum_{k=1}^{\infty} \frac{1}{\pi k} \left[\sin(2\pi k f_{\mathrm{p}} t) - \sin(2\pi k f_{\mathrm{p}} t - 2\pi k a(t))\right] \tag{2.10}$$

where the trigonometric identity

$$\sin(\alpha + \beta) = \sin\alpha \cos\beta + \sin\beta \cos\alpha \tag{2.11}$$

is used. Note that it is not necessary that the modulating signal be a bandlimited function as long as the derivative of the modulating signal is smaller than the PWM frequency [1], such that

$$\left| \frac{da(t)}{dt} \right| < \frac{1}{T_{\mathrm{p}}} = f_{\mathrm{p}}. \tag{2.12}$$

With the phase information, the signal $x_{\mathrm{p,TE}}(t)$ is given by

$$x_{\mathrm{p,TE}}(t)= a_{\mathrm{p,TE}}(t)e^{j\phi(t)} = x(t) + \sum_{k=1}^{\infty} x_{k,\mathrm{TE}}(t) \tag{2.13}$$

where $x_{k,\mathrm{TE}}(t)$ denotes the k-th harmonic component and is given by

$$x_{k,\mathrm{TE}}(t) = \frac{1}{\pi k}\left[\sin(2\pi k f_{\mathrm{p}} t) - \sin(2\pi k f_{\mathrm{p}} t - 2\pi k a(t))\right] e^{j\phi(t)}. \tag{2.14}$$

By using the Fourier transform, the frequency-domain expressions of the TEPWM signal $a_{\mathrm{p,TE}}(t)$ can be derived as

$$A_{\mathrm{p,TE}}(f) = A(f) + \sum_{k=1}^{\infty}\sum_{r=1}^{\infty} \frac{(j2\pi k)^{r-1}}{r!}\left[A_r(f + kf_{\mathrm{p}}) + (-1)^{r-1} A_r(f - kf_{\mathrm{p}})\right] \tag{2.15}$$

where $A(f)$ and $A_r(f)$ are Fourier transforms of $a(t)$ and $a^r(t)$, respectively. The Fourier transform is denoted with $\mathcal{F}\{\cdot\}$ function. The formula

$$\sin\alpha = \frac{e^{j\alpha} - e^{-j\alpha}}{2j} \tag{2.16}$$

and the Taylor series

$$e^{\alpha} - 1 = \sum_{r=1}^{\infty} \frac{\alpha^r}{r!} \tag{2.17}$$

are used to derive the frequency-domain expression of the TEPWM signals. Applying the phase information, the frequency-domain expression of the signal $x_{\mathrm{p,TE}}(t)$ is given by

$$X_{\mathrm{p,TE}}(f) = X(f) + \sum_{k=1}^{\infty} X_{k,\mathrm{TE}}(f) \tag{2.18}$$

where $X(f)$ is the Fourier transform of the signal $x(t)$. The k-th harmonic component in frequency domain is denoted as $X_{k,\mathrm{TE}}(f)$ and is given by

$$X_{\mathrm{k,TE}}(f) = \sum_{r=1}^{\infty} \frac{(j2\pi k)^{r-1}}{r!}\left[A_{r-1}(f + kf_{\mathrm{p}}) + (-1)^{r-1} A_{r-1}(f - kf_{\mathrm{p}})\right] * X(f). \tag{2.19}$$

By having a closer look at the signal $X_{\mathrm{p,TE}}(f)$ it shows that the spectrum consists of the wanted modulating signal component $X(f)$ and a sum of the harmonics which are composed of weighted signal powers located at multiples of the PWM frequency kf_{p}. The PWM signal in general is non-bandlimited since the number of harmonics approaches infinity. An alternative detailed derivation of the TEPWM signal is given in Appendix B.

Leading-Edge PWM Process The LEPWM process is illustrated in Figure 2.6 (b). The description of LEPWM signal $a_{\mathrm{p,LE}}(t)$ can be derived from the results of TEPWM signals $a_{\mathrm{p,TE}}(t)$. The LEPWM signal can be regarded as the signal generated from TEPWM process with modulating signal $(1-a(t))$ and then subtracted from 1,

$$a_{\mathrm{p,LE}}(t;a(t)) = 1 - a_{\mathrm{p,TE}}(t;1-a(t)). \tag{2.20}$$

Substituting for $a_{\mathrm{p,TE}}(t;1-a(t))$ from (2.10) with modulating signal $(1-a(t))$, the expression of the LEPWM signal is given by

$$a_{\mathrm{p,LE}}(t) = a(t) + \sum_{k=1}^{\infty} \frac{1}{\pi k} \left[\sin(2\pi k f_{\mathrm{p}} t + 2\pi k a(t)) - \sin(2\pi k f_{\mathrm{p}} t)\right]. \tag{2.21}$$

The phase modulated LEPWM signal is given by

$$x_{\mathrm{p,LE}}(t) = x(t) + \sum_{k=1}^{\infty} x_{k,\mathrm{LE}}(t) \tag{2.22}$$

where the k-th harmonic component $x_{k,\mathrm{LE}}(t)$ is given by

$$x_{k,\mathrm{LE}}(t) = \frac{1}{\pi k} \left[\sin(2\pi k f_{\mathrm{p}} t + 2\pi k a(t)) - \sin(2\pi k f_{\mathrm{p}} t)\right] e^{j\phi(t)}. \tag{2.23}$$

The spectrum of the TEPWM signal can be expressed by using (2.16) and (2.17) as

$$A_{\mathrm{p,LE}}(f) = A(f) + \sum_{k=1}^{\infty}\sum_{r=1}^{\infty} \frac{(j2\pi k)^{r-1}}{r!} \left[(-1)^{r-1} A_r(f+kf_{\mathrm{p}}) + A_r(f-kf_{\mathrm{p}})\right]. \tag{2.24}$$

With the phase information, the Fourier transform of $x_{\mathrm{p,LE}}(t)$ is given by

$$X_{\mathrm{p,LE}}(f) = X(f) + \sum_{k=1}^{\infty} X_{k,\mathrm{LE}}(f) \tag{2.25}$$

where $X_{k,\mathrm{LE}}(t)$ denotes the k-th harmonic component in frequency domain and is given by

$$X_{\mathrm{k,LE}}(f) = \sum_{r=1}^{\infty} \frac{(j2\pi k)^{r-1}}{r!} \left[(-1)^{r-1} A_{r-1}(f+kf_{\mathrm{p}}) + A_{r-1}(f-kf_{\mathrm{p}})\right] * X(f) \tag{2.26}$$

The properties of the LEPWM signals are similar to those of TEPWM signals. In the following, the DEPWM signal will be mathematically described according to the results of the TEPWM signal and the LTPWM signal.

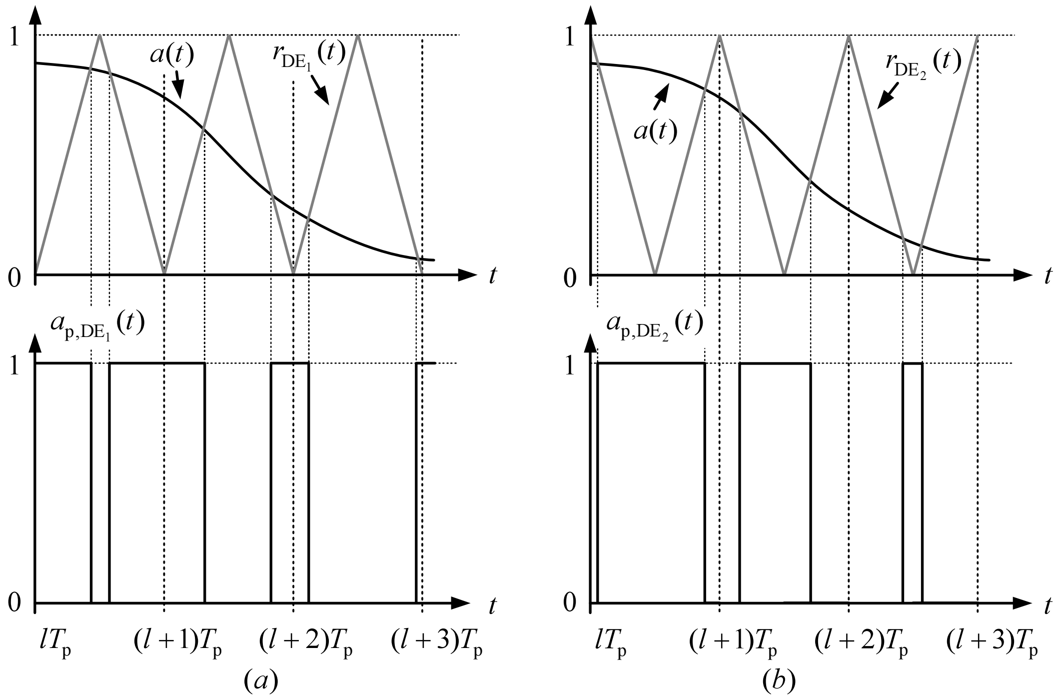

Figure 2.7: DEPWM process. The reference signals $r_{\mathrm{DE}_1}(t)$ and $r_{\mathrm{DE}_2}(t)$ are with a phase difference of 180°.

Double-Edge PWM Process

The DEPWM process is illustrated in Figure 2.7. The reference signals can be phase shifted by 180° as shown in the figure. Unlike SEPWM signals, in one PWM period, each pulse edge location in the DEPWM signal is determined by a different crossing-point of the modulating signal and the reference signal.

The DEPWM signal can be derived from the sum of a TEPWM signal and a LEPWM signal. For the first case when the reference signal is $r_{\mathrm{DE}_1}(t)$ as shown in Figure 2.7 (a), the generated DEPWM signal $a_{\mathrm{p,DE}_1}(t)$ can be obtained as the sum of the TEPWM signal $a_{\mathrm{p,TE}}(t)$ and the LEPWM signal $a_{\mathrm{p,LE}}(t)$ with the modulating signal of $a(t)/2$. It follows that

$$a_{\mathrm{p,DE}_1}(t;a(t)) = a_{\mathrm{p,TE}}(t;\frac{a(t)}{2}) + a_{\mathrm{p,LE}}(t;\frac{a(t)}{2}). \tag{2.27}$$

By applying (2.10) and (2.21) with the modulating signal $a(t)/2$ to (2.27), we obtain

$$\begin{aligned} a_{\mathrm{p,DE}_1}(t) &= a(t) + \sum_{k=1}^{\infty} \frac{1}{\pi k}\left[\sin(2\pi k f_{\mathrm{p}} t + \pi k a(t)) - \sin(2\pi k f_{\mathrm{p}} t - \pi k a(t))\right] \\ &= a(t) + \sum_{k=1}^{\infty} \frac{2}{\pi k} \sin(\pi k a(t)) \cos(2\pi k f_{\mathrm{p}} t) \end{aligned} \tag{2.28}$$

where the trigonometric identity (2.11) is used. The phase modulated signal $x_{\mathrm{p,DE}_1}(t)$ can be expressed by

$$x_{\mathrm{p,DE_1}}(t)= x(t) + \sum_{k=1}^{\infty} x_{k,\mathrm{DE_1}}(t) \tag{2.29}$$

where $x_{k,\mathrm{DE_1}}(t)$ is given by

$$x_{k,\mathrm{DE_1}}(t) = \frac{2}{\pi k}\sin(\pi k a(t))\cos(2\pi k f_{\mathrm{p}} t)e^{j\phi(t)}. \tag{2.30}$$

The frequency-domain expression of the DEPWM signal $a_{\mathrm{p,DE_1}}(t)$ can be derived as

$$A_{\mathrm{p,DE_1}}(f)= A(f) + \sum_{k=1}^{\infty}\sum_{r=0}^{\infty} \frac{(j\pi k)^{2r}}{(2r+1)!}\left[A_{2r+1}(f+kf_{\mathrm{p}}) + A_{2r+1}(f-kf_{\mathrm{p}})\right] \tag{2.31}$$

where the Taylor series

$$\sin\alpha = \sum_{r=0}^{\infty} \frac{(-1)^r \alpha^{2r+1}}{(2r+1)!} \tag{2.32}$$

is used. The frequency-domain expression of the phase modulated signal $x_{\mathrm{p,DE_1}}(t)$ can be derived as

$$X_{\mathrm{p,DE_1}}(f)= X(f) + \sum_{k=1}^{\infty} X_{\mathrm{k,DE_1}}(f) \tag{2.33}$$

where the k-th harmonic content is given by

$$X_{\mathrm{k,DE_1}}(f) = \sum_{r=0}^{\infty} \frac{(j\pi k)^{2r}}{(2r+1)!}\left[A_{2r}(f+kf_{\mathrm{p}}) + A_{2r}(f-kf_{\mathrm{p}})\right] * X(f). \tag{2.34}$$

For the second case when the reference signal is $r_{\mathrm{DE_2}}(t)$ as shown in Figure 2.7 (b), the resulting DEPWM signal $a_{\mathrm{p,DE_2}}(t)$ can be obtained from the sum of the TEPWM signal $a_{\mathrm{p,TE}}(t)$ and the LEPWM signal $a_{\mathrm{p,LE}}(t)$ with the modulating signal of $(1-a(t))/2$,

$$a_{\mathrm{p,DE_2}}(t; a(t)) = 1 - \left[a_{\mathrm{p,TE}}(t; \frac{1-a(t)}{2}) + a_{\mathrm{p,LE}}(t; \frac{1-a(t)}{2})\right] \tag{2.35}$$

Substituting for $a_{\mathrm{p,TE}}(t; \frac{1-a(t)}{2})$ and $a_{\mathrm{p,LE}}(t; \frac{1-a(t)}{2})$ from (2.10) and (2.21), it can be derived that

$$a_{\mathrm{p,DE_2}}(t) = a(t) + \sum_{k=1}^{\infty} \frac{2(-1)^k}{\pi k}\sin(\pi k a(t))\cos(2\pi k f_{\mathrm{p}} t). \tag{2.36}$$

With the phase information, the signal $x_{\mathrm{p,DE}_2}(t)$ is given by

$$x_{\mathrm{p,DE}_2}(t)= x(t) + \sum_{k=1}^{\infty} x_{k,\mathrm{DE}_2}(t) \tag{2.37}$$

where $x_{k,\mathrm{DE}_2}(t)$ is given by

$$x_{k,\mathrm{DE}_2}(t) = \frac{2(-1)^k}{\pi k} \sin(\pi k a(t)) \cos(2\pi k f_\mathrm{p} t) e^{j\phi(t)}. \tag{2.38}$$

The spectrum of the DEPWM signal $a_{\mathrm{p,DE}_2}(t)$ is described by

$$A_{\mathrm{p,DE}_2}(f)= A(f) + \sum_{k=1}^{\infty}\sum_{r=0}^{\infty} \frac{(-1)^k (j\pi k)^{2r}}{(2r+1)!} \left[A_{2r+1}(f + kf_\mathrm{p}) + A_{2r+1}(f - kf_\mathrm{p})\right]. \tag{2.39}$$

The Fourier transform of the phase modulated signal $x_{\mathrm{p,DE}_2}(t)$ is given by

$$X_{\mathrm{p,DE}_2}(f)= X(f) + \sum_{k=1}^{\infty} X_{\mathrm{k,DE}_2}(f) \tag{2.40}$$

where the k-th harmonic content is given by

$$X_{\mathrm{k,DE}_2}(f) = \sum_{r=0}^{\infty} \frac{(-1)^k (j\pi k)^{2r}}{(2r+1)!} \left[A_{2r}(f + kf_\mathrm{p}) + A_{2r}(f - kf_\mathrm{p})\right] * X(f). \tag{2.41}$$

The spectrum of each DEPWM signal consists of the wanted modulating signal component $X(f)$ and harmonics located at kf_p, where the weighting factor is different from that in SEPWM signals in (2.19) and (2.26). Moreover, only the even powers of the modulating signal $A_{2r}(\cdot)$ convoluted with the signal $X(f)$ are included in the spectrum. Each harmonic consisting of the sum of the weighted signal powers is not bandlimited, meaning that the harmonics introduce distortion into the frequency band of the modulating signal, preventing perfect signal recovery. However, by choosing a sufficiently large PWM frequency f_p, the spectral components aliasing into the wanted signal band can be kept negligibly small.

2.3.2 Multilevel Pulse-Width Modulation

The multilevel PWM process is illustrated in Figure 2.8. The example is a three-level DEPWM process with the signal path $M = 2$ and a threshold value of V_1. Assume without loss of generality that only DEPWM is considered in multilevel PWM process analysis. In the figure, two reference signals are given, $r_{\mathrm{DE}_1}(t) \in [0, V_1]$ and $r_{\mathrm{DE}_2}(t) \in [V_1, 1]$. In the multilevel DEPWM process, the adjacent reference signals are required to be phase shifted by 180° to maintain the phase continuity and avoid pulse skipping [88]. The corresponding DEPWM signals $a_{\mathrm{p}_1}(t)$ and $a_{\mathrm{p}_2}(t)$ and the combined three-level DEPWM signal $\sum_{m=1}^{M} a_{\mathrm{p}_m}(t)$ with $M = 2$ are generated accordingly and illustrated in Figure 2.8.

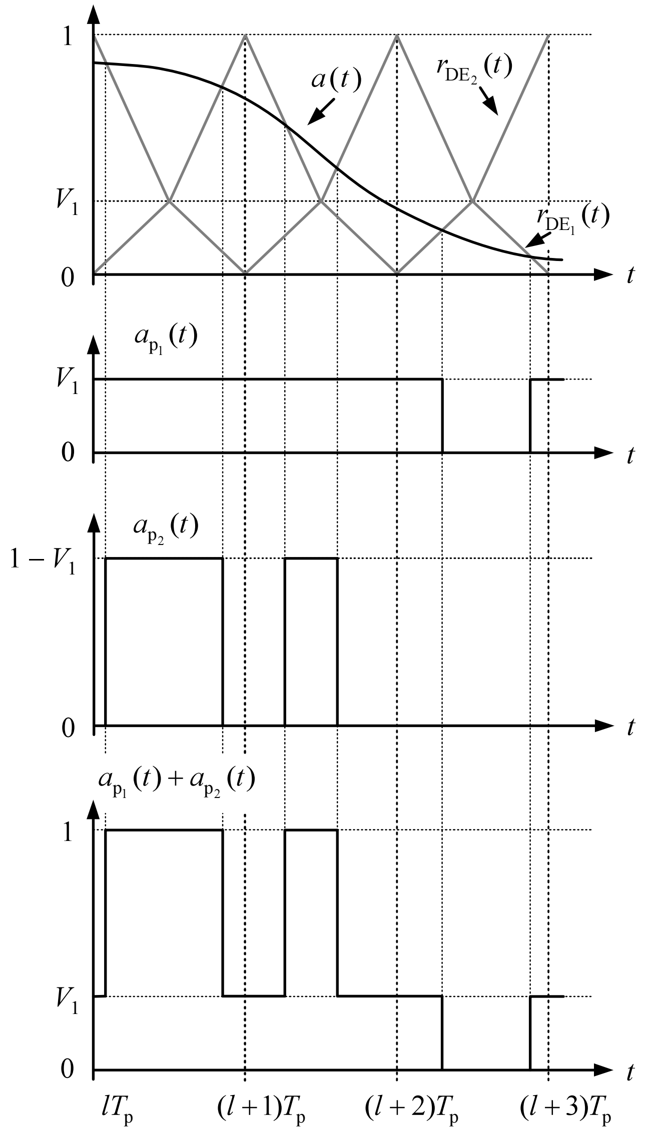

Figure 2.8: A three-level DEPWM process ($M = 2$) as an example of multilevel PWM process. The reference signals $r_{\mathrm{DE}_1}(t)$ and $r_{\mathrm{DE}_2}(t)$ are phase shifted by 180°. The magnitudes of the generated DEPWM signals $a_{\mathrm{p}_1}(t)$ and $a_{\mathrm{p}_2}(t)$ are V_1 and $(1 - V_1)$, respectively, which are determined by the threshold value V_1. The combined signal $\sum_{m=1}^{M} a_{\mathrm{p}_m}(t)$ produces a three-level (multilevel) DEPWM signal.

The results of DEPWM signals obtained above can be used to derive the analytical expressions for multilevel DEPWM signals. First of all, the modulating signal $a(t)$ is divided into M cases depending on the threshold values $V_i, i \in [0, M]$, which is defined in the interval $[0, 1]$ as in (2.3). Note that for the analytical results obtained so far it is assumed that the modulating signal and the ideally generated DEPWM signals are both in the interval of $[0, 1]$. In order to utilize the obtained results for the multilevel DEPWM process, each divided modulating signal $a_m(t) \in [V_{m-1}, V_m]$ needs to be shifted down to the interval of $[0, V_m - V_{m-1}]$ and then scaled up to the interval of $[0,1]$. Then each generated DEPWM signal is scaled down according to the difference of the threshold values $(V_m - V_{m-1})$, and the combined multilevel DEPWM signal $\sum_{m=1}^{M} a_{\mathrm{p}_m}(t)$ will be in the interval of $[0,1]$ as illustrated in Figure 2.8.

For the first case when $a_1(t) \in [0, V_1]$, the DEPWM signal $a_{\mathrm{p}_1}(t)$ is generated with a modulating signal $a_1(t)/V_1$ and then scaled down by the value of V_1. It gives

$$\begin{aligned} a_{\mathrm{p}_1}(t) &= V_1 \left[\frac{a_1(t)}{V_1} + \sum_{k=1}^{\infty} \frac{2}{\pi k} \sin\left(\pi k \frac{a_1(t)}{V_1}\right) \cos(2\pi k f_{\mathrm{p}} t) \right] \\ &= a_1(t) + \sum_{k=1}^{\infty} \frac{2V_1}{\pi k} \sin\left(\pi k \frac{a_1(t)}{V_1}\right) \cos(2\pi k f_{\mathrm{p}} t). \end{aligned} \tag{2.42}$$

For the m-th case when $a(t) \in [V_{m-1}, V_m]$, $m \in [1, M]$, the DEPWM signal $a_{\mathrm{p}_m}(t)$ is generated with a modulating signal $(a_m(t) - V_{m-1})/(V_m - V_{m-1})$ and then scaled down by the value of $(V_m - V_{m-1})$. It follows that

$$a_{\mathrm{p}_m}(t) = a_m(t) - V_{m-1} + \sum_{k=1}^{\infty} \frac{2(-1)^{(m-1)k}(V_m - V_{m-1})}{\pi k} \sin\left(\pi k \frac{a_m(t) - V_{m-1}}{V_m - V_{m-1}}\right) \cos(2\pi k f_{\mathrm{p}} t). \tag{2.43}$$

An example of $a_{\mathrm{p}_m}(t)$ with $m = 1, 2$ is shown in Figure 2.8. After combining M DEPWM signals, the resulting DEPWM signal can be expressed as

$$\begin{aligned} a_{\mathrm{p}}(t) &= \sum_{m=1}^{M} a_{\mathrm{p}_m}(t) \\ &= a(t) + \sum_{m=1}^{M} \sum_{k=1}^{\infty} \frac{2(-1)^{(m-1)k}(V_m - V_{m-1})}{\pi k} \sin\left(\pi k \frac{a_m(t) - V_{m-1}}{V_m - V_{m-1}}\right) \cos(2\pi k f_{\mathrm{p}} t). \end{aligned} \tag{2.44}$$

A special case is when the threshold values are equally spaced, e.g., $V_i = [0, 0.5, 1]$ for $M = 2$, such a PWM based transmitter is called a classic transmitter or non-optimized transmitter. The non-optimized transmitter concept is used in the following chapter when the efficiency optimization is discussed. In a non-optimized PWM process the equally spaced threshold value is given by

$$\dot{V}_i = \frac{i}{M}, \quad i \in [0, M]. \tag{2.45}$$

Using (2.45) in (2.43) gives the expression of the signal generated from a non-optimized PWM process for the m-th case when $a(t) \in (V_{m-1}, V_m]$, $m \in [1, M]$,

$$a_{\mathrm{p}_m}(t) = a_m(t) - \frac{m-1}{M} + \sum_{k=1}^{\infty} \frac{2}{\pi k M} \sin\left(\pi k M a_m(t)\right) \cos(2\pi k f_{\mathrm{p}} t) \tag{2.46}$$

where the trigonometric identity (2.11) is used. The combined DEPWM signal generated from a non-optimized PWM process can be described as

$$\begin{aligned}
a_{\mathrm{p}}(t) &= \sum_{m=1}^{M} a_{\mathrm{p}_m}(t) \\
&= \sum_{m=1}^{M}\left(a_m(t) - \frac{m-1}{M}\right) + \sum_{k=1}^{\infty}\frac{2}{\pi k M}\cos(2\pi k f_{\mathrm{p}} t)\sum_{m=1}^{M}\sin(\pi k M a_m(t)) \\
&= a(t) + \sum_{k=1}^{\infty}\frac{2}{\pi k M}\sin(\pi k M a(t))\cos(2\pi k f_{\mathrm{p}} t) \qquad (2.47)
\end{aligned}$$

where

$$\sum_{m=1}^{M}\sin(\pi k M a_m(t)) = \sin(\pi k M a(t)). \qquad (2.48)$$

At each time index, the signal $a_m(t)$ takes values from $[\frac{m-1}{M}, \frac{m}{M}, a(t) \in (\frac{m-1}{M}, \frac{m}{M})]$. The value of the term $\sin(\pi k M a_m(t))$ in (2.48) takes corresponding values when $a_m(t) = a(t) \in (\frac{m-1}{M}, \frac{m}{M})$ otherwise zero. Hence when the combined signal is considered, the relation (2.48) can be used to obtain (2.47). Applying the phase information to each DEPWM signal $a_{\mathrm{p}_m}(t), m = 1, ..., M$, the phase modulated multilevel DEPWM signal from a non-optimized PWM process is given by

$$x_{\mathrm{p}}(t) = \sum_{m=1}^{M} x_{\mathrm{p}_m}(t) = x(t) + \sum_{k=1}^{\infty} x_k(t) \qquad (2.49)$$

where the k-th harmonic is given by

$$x_k(t) = \frac{2}{\pi k M}\sin(\pi k M a(t))\cos(2\pi k f_{\mathrm{p}} t)e^{j\phi(t)}. \qquad (2.50)$$

The frequency spectrum of the non-optimized multilevel DEPWM signal $a_{\mathrm{p}}(t)$ can be derived as

$$A_{\mathrm{p}}(f) = A(f) + \sum_{k=1}^{\infty}\sum_{r=0}^{\infty}\frac{(j\pi k M)^{2r}}{(2r+1)!}\left[A_{2r+1}(f + k f_{\mathrm{p}}) + A_{2r+1}(f - k f_{\mathrm{p}})\right]. \qquad (2.51)$$

With the phase information, the frequency-domain expression of the signal $x_{\mathrm{p}}(t)$ is described by

$$X_{\mathrm{p}}(f) = X(f) + \sum_{k=1}^{\infty} X_k(f) \qquad (2.52)$$

where $X_k(f)$ is given by

$$X_k(f) = \sum_{r=0}^{\infty}\frac{(j\pi k M)^{2r}}{(2r+1)!}\left[A_{2r}(f + k f_{\mathrm{p}}) + A_{2r}(f - k f_{\mathrm{p}})\right] * X(f). \qquad (2.53)$$

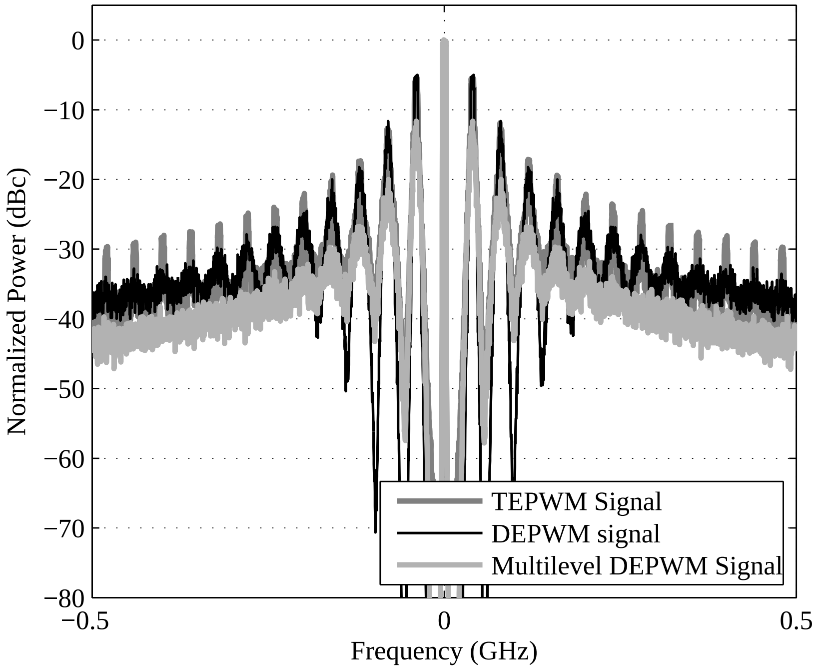

Figure 2.9: Spectra of the TEPWM signal, DEPWM signal and the multilevel DEPWM signal ($M = 2$).

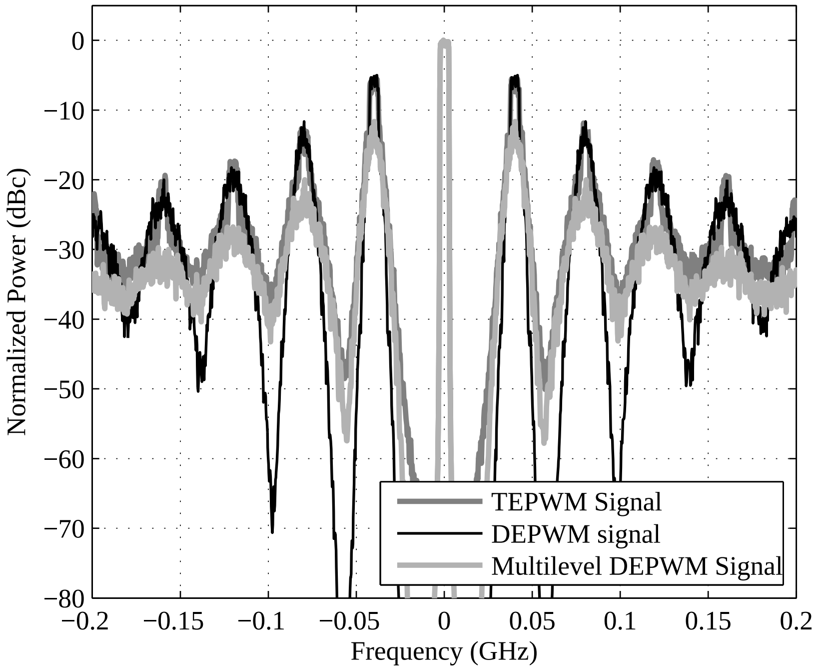

Figure 2.10: A close-up of Figure 2.9.

It can be seen that the harmonics in multilevel DEPWM signals (2.50) are weighted by a smaller factor compared to two-level DEPWM signals (2.30,2.38), meaning that the multilevel DEPWM signal produces less out-of-band spectral components, which can be used to improve the coding efficiency and therefore the transmitter efficiency.

A spectral illustration of the TEPWM signal in (2.13), the DEPWM signal in (2.29) and the multilevel DEPWM signal in (2.49) with $M = 2$ is shown in Figure 2.9. A close-up of Figure 2.9 is shown in Figure 2.10. It can be seen that each spectrum consists of the wanted signal located at the zero frequency and every order of harmonic located at the multiple of the PWM frequency where the harmonics are in a decreasing manner. The multilevel case produces the least out-of-band spectral content.

2.4 Summary and Discussion

In this chapter, burst-mode RF transmitter architectures and efficiency metrics are discussed, and a system-level description of baseband PWM signals is presented.

First, the burst-mode operation is introduced. In burst-mode operation, the modulation signal is first modulated by the PW modulator and then the upconverted RF burst signal is amplified by the burst-mode RF PA. A burst-mode RF PA is operated in "on" and "off" modes, leading to high PA drain efficiency. The PA drain efficiency together with the coding efficiency, which is an important figure of merit to evaluate the performance of the PWM encoder, is used to evaluate the transmitter efficiency. The efficiency metrics are described in the second part of this chapter, and will be further used in the following chapters. In the third part, closed-form descriptions of PWM signals of different kinds are provided. Depending on the reference signals, the PWM process can be categorized into SEPWM process and DEPWM process. Depending on the number of PWMs used, the PWM process can be categorized into two-level PWM process and multilevel PWM process. The analytical results describing the PWM signals are of great importance for the system-level study of burst-mode transmitter architectures and will serve as a basis for the following chapters.

3

Continuous-Time PWM Based Burst-Mode RF Transmitters

In this chapter, continuous-time PWM based burst-mode RF transmitters will be analyzed in terms of the linearity and power efficiency. From the results obtained in Chapter 2 it is clear that the ideally generated PWM signal has infinite bandwidth. For RF applications, when the baseband PWM signal is upconverted to the passband by mixing with the carrier frequency, the out-of-band spectral components will cause distortion to the wanted signal that is located at the carrier frequency. This is called the image problem. The term image here is different from the image from a traditional modulator, where the image is caused by the gain and phase imbalance of the modulator. The image here is part of the desired or generated signal, which is introduced to show that the distortion is inherently produced in the upconverted RF burst signal. Usually the image distortion can be mitigated by using a LPF on the baseband PWM signal to limit the signal bandwidth however at the cost of extra circuit effort. An image distortion mitigation method without extra circuit effort will be described. Then we will show that the DEPWM method can be regarded as one way to mitigate the image distortion in TEPWM signals.

The power efficiency of continuous-time PWM based burst-mode RF transmitters will be analyzed in detail. Both the efficiency for constant input signals and the average efficiency for signals with a given PDF will be described mathematically. We will start with the two-level burst-mode RF transmitter analysis and then proceed to the multilevel transmitter case. For multilevel burst-mode RF transmitters, the transmitter efficiency depends highly on the threshold values which are used to divide the input signal into different levels or to set the upper and lower bounds of the reference signals. For example, the threshold values of the conventional classic multilevel transmitter architecture are equally distributed. We will propose an efficiency optimization procedure which will maximize the transmitter efficiency by using the optimum threshold values according to the signal PDF. It will be shown that the optimized transmitters achieve significantly higher efficiency improvement compared to the conventional classic or non-optimized transmitters as well as the two-level case.

3.1 Image Problem in RF Burst Signals

In the following, the image problem in continuous-time PWM based burst-mode transmitters will be described. First, the spectral analysis of the RF burst signal will be provided followed by the description of the proposed image mitigation method for generating SEPWM signals. Then the spectral comparison of SEPWM and DEPWM signals will be given to show that DEPWM can also be viewed as one method to mitigate the image distortion in TEPWM signals.

3.1.1 Image Problem Analysis

The image problem occurs during the upconversion process when the baseband PWM signal, which has infinite bandwidth, is upconverted to the passband by mixing with the carrier. Figure 3.1(a) shows the spectrum of the baseband TEPWM signal $x_{\mathrm{p,TE}}(t)$. The main power of the input signal $x(t)$ is located around the zero frequency. The PWM harmonics are located at the frequencies that are multiples of the PWM frequency f_{p} and the power of the kth harmonic decreases inversely with k with reference to $x_{\mathrm{p,TE}}(t)$ in (2.13). To find out what causes the image problem, we start with the mathematical expression of the RF burst signal. According to (2.2), the transmission signal $x_{\mathrm{PB}}(t)$ after an ideal BPF can be expressed as

$$\begin{aligned} x_{\mathrm{PB}}(t) &= a(t)\cos(2\pi f_{\mathrm{c}}t + \phi(t)) \\ &= \frac{1}{2}x(t)e^{j2\pi f_{\mathrm{c}}t} + \frac{1}{2}x^*(t)e^{-j2\pi f_{\mathrm{c}}t} \end{aligned} \tag{3.1}$$

where * denotes the complex conjugation. The PA gain is assumed to be 1 to facilitate the analysis. The signal is decomposed to a signal part and its conjugate part to serve the image problem analysis. The frequency-domain expression of the transmission signal can be described by computing the Fourier transform of $x_{\mathrm{PB}}(t)$, which gives

$$\begin{aligned} X_{\mathrm{PB}}(f) &= \frac{1}{2}X(f - f_{\mathrm{c}}) + \frac{1}{2}X^*(-f - f_{\mathrm{c}}) \\ &= X^+_{\mathrm{PB}}(f) + X^-_{\mathrm{PB}}(f) \end{aligned} \tag{3.2}$$

where $X(f)$ is the Fourier transform of the signal $x(t)$. The relation

$$\mathcal{F}\{x^*(t)\} = X^*(-f) \tag{3.3}$$

is used. The superscripts $^+$ and $^-$ in (3.2) denote the corresponding signal components which have been upconverted to the passband by $e^{j2\pi f_{\mathrm{c}}t}$ and $e^{-j2\pi f_{\mathrm{c}}t}$, respectively. From (2.13) the

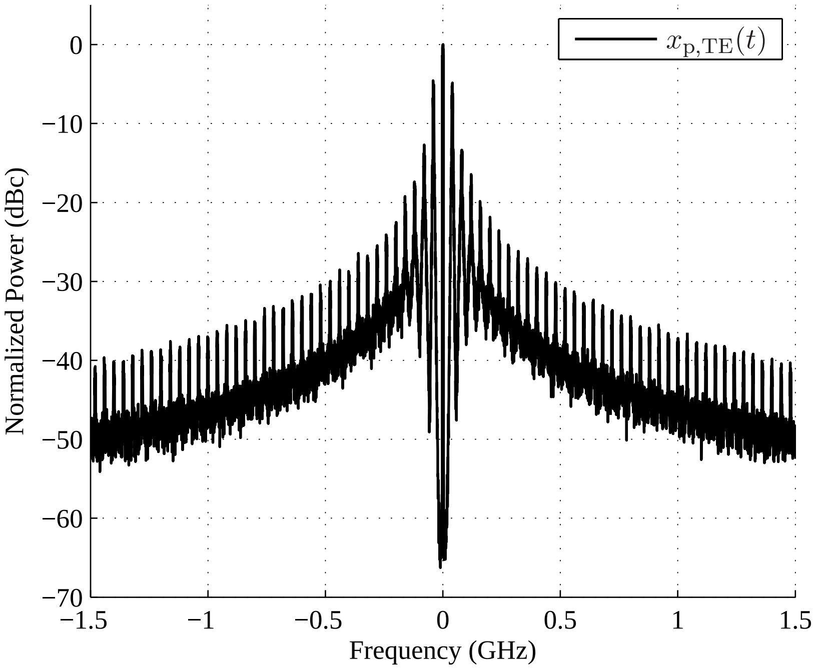

(a) Illustration of the spectrum of the baseband TEPWM signal $x_{\mathrm{p,TE}}(t)$. It includes the spectrum of input signal $x(t)$ and every order of the PWM harmonics. The spacing between adjacent PWM harmonics is equal to the value of f_{p}.

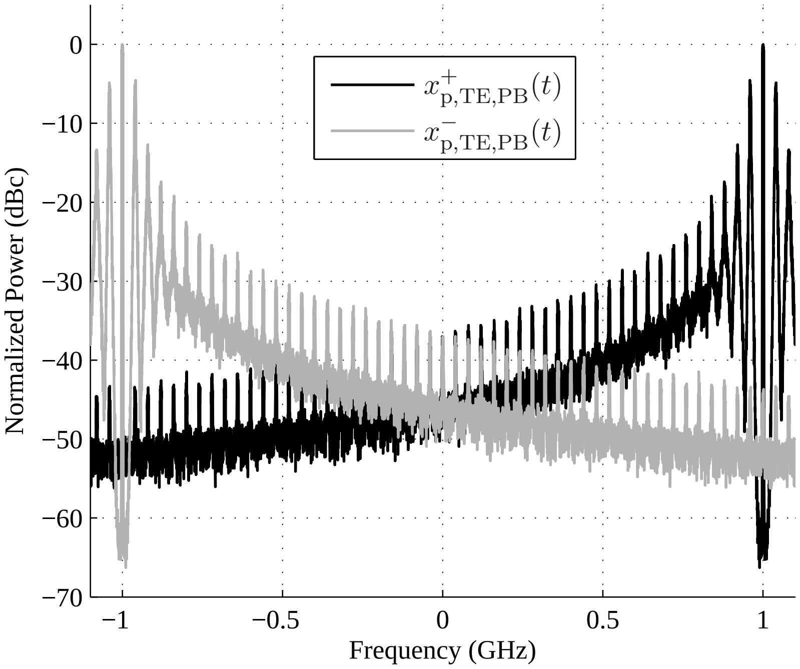

(b) Illustration of the spectrum of the RF burst signal with image problem. The distortion around the wanted signal located at the positive carrier frequency f_{c} is produced by the image spectral components and vice versa.

Figure 3.1: Frequency-domain illustrations of image problem in RF burst signals with TEPWM method.

RF burst signal in time domain is given by

$$\begin{aligned} x_{\mathrm{p,TE,PB}}(t) &= \frac{1}{2}x_{\mathrm{p,TE}}(t)e^{j2\pi f_{\mathrm{c}}t} + \frac{1}{2}x^*_{\mathrm{p,TE}}(t)e^{-j2\pi f_{\mathrm{c}}t} \\ &= x^+_{\mathrm{p,TE,PB}}(t) + x^-_{\mathrm{p,TE,PB}}(t) \end{aligned} \tag{3.4}$$

where the signal components $x^+_{\mathrm{p,TE,PB}}(t)$ and $x^-_{\mathrm{p,TE,PB}}(t)$ are given by

$$x^+_{\mathrm{p,TE,PB}}(t) = \frac{1}{2}x(t)e^{j2\pi f_{\mathrm{c}}t} + \frac{1}{2}\sum_{k=1}^{\infty} x_{k,\mathrm{TE}}(t)e^{j2\pi f_{\mathrm{c}}t} \tag{3.5}$$

and

$$x^-_{\mathrm{p,TE,PB}}(t) = \frac{1}{2}x^*(t)e^{-j2\pi f_{\mathrm{c}}t} + \frac{1}{2}\sum_{k=1}^{\infty} x^*_{k,\mathrm{TE}}(t)e^{-j2\pi f_{\mathrm{c}}t} \tag{3.6}$$

respectively. The signal $x_{k,\mathrm{TE}}(t)$ is given in (2.14) by

$$x_{k,\mathrm{TE}}(t) = \frac{1}{\pi k}\left[\sin(2\pi k f_{\mathrm{p}} t) - \sin(2\pi k f_{\mathrm{p}} t - 2\pi k a(t))\right] e^{j\phi(t)}. \tag{3.7}$$

According to (3.4), the frequency-domain expression of the RF burst signal can be expressed as the sum of a positive and a negative spectrum by

$$X_{\mathrm{p,TE,PB}}(f) = X^+_{\mathrm{p,TE,PB}}(f) + X^-_{\mathrm{p,TE,PB}}(f) \tag{3.8}$$

where according to (3.4) and (2.19) the signal components $X^+_{\mathrm{p,TE,PB}}(f)$ and $X^-_{\mathrm{p,TE,PB}}(f)$ are given by

$$\begin{aligned} X^+_{\mathrm{p,TE,PB}}(f) &= \frac{1}{2}X_{\mathrm{p,TE}}(f - f_{\mathrm{c}}) \\ &= \frac{1}{2}X(f - f_{\mathrm{c}}) + \sum_{k=1}^{\infty}\sum_{r=1}^{\infty}\frac{(j2\pi k)^{r-1}}{2r!}\times \\ &\quad \left[A_{r-1}(f - f_{\mathrm{c}} + kf_{\mathrm{p}}) + (-1)^{r-1}A_{r-1}(f - f_{\mathrm{c}} - kf_{\mathrm{p}})\right] * X(f) \end{aligned} \tag{3.9}$$

and

$$\begin{aligned} X^-_{\mathrm{p,TE,PB}}(f) &= \frac{1}{2}X^*_{\mathrm{p,TE}}(-f - f_{\mathrm{c}}) \\ &= \frac{1}{2}X^*(-f - f_{\mathrm{c}}) + \sum_{k=1}^{\infty}\sum_{r=1}^{\infty}\frac{(j2\pi k)^{r-1}}{2r!}\times \\ &\quad \left[A_{r-1}(f + f_{\mathrm{c}} + kf_{\mathrm{p}}) + (-1)^{r-1}A_{r-1}(f + f_{\mathrm{c}} - kf_{\mathrm{p}})\right] * X^*(-f) \end{aligned} \tag{3.10}$$

respectively. From (3.9) and (3.10) it can be seen that each positive or negative signal component includes the wanted signal or its conjugate and every order of harmonics located at $(\pm f_{\mathrm{c}} \pm k f_{\mathrm{p}})$, which is of infinite bandwidth. The spectrum of the RF burst signal components $x^+_{\mathrm{p,TE,PB}}(t)$

and $x^{-}_{\mathrm{p,TE,PB}}(t)$ are depicted with black and grey lines in Figure 3.1(b), respectively. The image problem discussed is caused by the large bandwidth spectrum of the baseband PWM signal. When the baseband PWM signal is upconverted to the passband, the image spectrum, which is modulated by the negative carrier component $e^{-j2\pi f_c t}$, is overlapped with the spectrum that is modulated with the positive carrier component $e^{j2\pi f_c t}$. As a consequence, when the positive and negative components are combined together to form the real passband signal, the image distortion is induced around the wanted signal located at the positive carrier frequency f_{c} and vice versa, which reduces both in-band and out-of-band signal quality.

3.1.2 Image Distortion Mitigation

From Figure 3.1(b) it can be seen that if the wanted signal located at the carrier frequency f_{c} is not superposed with the image harmonic peak that is produced by the negative spectral component, but in the middle of the adjacent image harmonic peaks, the image peak distortion can be avoided. This can be realized by changing the PWM frequency f_{p} to a proper value. According to Figure 3.1(b), the order of the image harmonic located around the carrier frequency f_{c}, defined as the qth harmonic, is given by

$$q = \mathrm{round}\left(\frac{2f_{\mathrm{c}}}{f_{\mathrm{p}}}\right) \tag{3.11}$$

where q is an integer. The "round" operation is used to find the harmonic that is most close to the carrier frequency f_c, meaning that this harmonic is most likely to induce distortion to the wanted signal at f_c. The worst case is when the qth harmonic is just located at the carrier frequency f_c. The best case is when the wanted signal is located in the middle of the qth harmonic and its adjacent harmonic. Since the carrier frequency f_c is usually fixed, a new PWM frequency $\hat{f}_{\mathrm{p}}$ can be determined for the best case in such a way that

$$-f_{\mathrm{c}} + q\hat{f}_{\mathrm{p}} \pm \frac{1}{2}\hat{f}_{\mathrm{p}} = f_{\mathrm{c}} \tag{3.12}$$

and $\hat{f}_p$ is given by

$$\hat{f}_{\mathrm{p}} = \frac{2f_{\mathrm{c}}}{q \pm \frac{1}{2}}. \tag{3.13}$$

For example, with an input signal of $B_s = 5$ MHz bandwidth, a PWM frequency of $f_{\mathrm{p}} = 40$ MHz and a carrier frequency of $f_{\mathrm{c}} = 1$ GHz, q is given with (3.11) by $q = 50$ and the new PWM frequency is calculated with (3.13) by $\hat{f}_{\mathrm{p}} = 39.6$ MHz and $\hat{f}_{\mathrm{p}} = 40.4$ MHz. By this way, the wanted signal around the carrier frequency is located in the middle of two adjacent image harmonic peaks and the image peak distortion can be avoided. Note that this harmonic distortion mitigation method can avoid the harmonic peak distortion but cannot eliminate all the harmonic distortion.

Besides utilizing the gap between the image harmonic peaks, the DEPWM method can be regarded as one method to mitigate the image problem occurring in TEPWM signals. Since both DEPWM methods have similar properties, the analysis of the first DEPWM is provided. The time-domain representation of the RF burst signal of DEPWM signal $x_{\mathrm{p,DE1,PB}}(t)$ is given by

$$\begin{aligned} x_{\mathrm{p,DE_1,PB}}(t) &= \frac{1}{2}x_{\mathrm{p,DE_1}}(t)e^{j2\pi f_{\mathrm{c}}t} + \frac{1}{2}x^*_{\mathrm{p,DE_1}}(t)e^{-j2\pi f_{\mathrm{c}}t} \\ &= x^+_{\mathrm{p,DE_1,PB}}(t) + x^-_{\mathrm{p,DE_1,PB}}(t) \end{aligned} \tag{3.14}$$

The signal components $x^+_{\mathrm{p,DE_1,PB}}(t)$ and $x^-_{\mathrm{p,DE_1,PB}}(t)$ are given by

$$x^+_{\mathrm{p,DE_1,PB}}(t) = \frac{1}{2}x(t)e^{j2\pi f_{\mathrm{c}}t} + \frac{1}{2}\sum_{k=1}^{\infty} x_{k,\mathrm{DE_1}}(t)e^{j2\pi f_{\mathrm{c}}t} \tag{3.15}$$

and

$$x^-_{\mathrm{p,DE_1,PB}}(t) = \frac{1}{2}x^*(t)e^{-j2\pi f_{\mathrm{c}}t} + \frac{1}{2}\sum_{k=1}^{\infty} x^*_{k,\mathrm{DE_1}}(t)e^{-j2\pi f_{\mathrm{c}}t} \tag{3.16}$$

respectively, where $x_{k,\mathrm{DE_1}}(t)$ is given in (2.30) by

$$\begin{aligned} x_{k,\mathrm{DE_1}}(t) &= \frac{2}{\pi k}\sin(\pi k a(t))\cos(2\pi k f_{\mathrm{p}}t)e^{j\phi(t)}. \\ &= \frac{1}{\pi k}\left[\sin(2\pi k f_{\mathrm{p}}t + \pi k a(t)) - \sin(2\pi k f_{\mathrm{p}}t - \pi k a(t))\right] \end{aligned} \tag{3.17}$$

The Fourier transform of the time-domain signal gives the frequency-domain expression as

$$X_{\mathrm{p,DE_1,PB}}(f) = X^+_{\mathrm{p,DE_1,PB}}(f) + X^-_{\mathrm{p,DE_1,PB}}(f) \tag{3.18}$$

where the positive and negative spectral components $X^+_{\mathrm{p,DE_1,PB}}(f)$ and $X^-_{\mathrm{p,DE_1,PB}}(f)$ are given by

$$\begin{aligned} X^+_{\mathrm{p,DE_1,PB}}(f) =& \frac{1}{2}X_{\mathrm{p,DE_1}}(f - f_{\mathrm{c}}) \\ =& \frac{1}{2}X(f - f_{\mathrm{c}}) + \sum_{k=1}^{\infty}\sum_{r=1}^{\infty}\frac{(j\pi k)^{2r}}{2(2r+1)!}\times \\ & [A_{2r}(f - f_{\mathrm{c}} + kf_{\mathrm{p}}) + A_{2r}(f - f_{\mathrm{c}} - kf_{\mathrm{p}})] * X(f) \end{aligned} \tag{3.19}$$

and

$$\begin{aligned} X^-_{\mathrm{p,DE_1,PB}}(f) =& \frac{1}{2}X^*_{\mathrm{p,DE_1}}(-f - f_{\mathrm{c}}) \\ =& \frac{1}{2}X^*(-f - f_{\mathrm{c}}) + \sum_{k=1}^{\infty}\sum_{r=1}^{\infty}\frac{(j\pi k)^{2r}}{2(2r+1)!}\times \\ & [A_{2r}(f + f_{\mathrm{c}} + kf_{\mathrm{p}}) + A_{2r}(f + f_{\mathrm{c}} - kf_{\mathrm{p}})] * X^*(-f) \end{aligned} \tag{3.20}$$

respectively. For DEPWM signals, the harmonics in (3.17) only contain signal dependent contents $\sin(2\pi k f_\mathrm{p} t \pm \pi k a(t))$ which do not generate harmonic peak distortion as in SEPWM signals. Whereas for the TEPWM signals, the harmonics in (3.7) not only contains the signal dependent content $-\sin(2\pi k f_\mathrm{p} t - 2\pi k a(t))$, but also includes the carrier harmonic content $\sin(2\pi k f_\mathrm{p} t)$ which is the source of the harmonic peak distortion. Therefore in DEPWM signals the image peak distortions can be completely avoided compared to the TEPWM signals. The figure illustration will be shown in the following section.

3.1.3 Simulation Results

The simulations were carried out in Matlab and Simulink environment. The PWM signal is created by a discrete-multitone (DMT) signal with a bandwidth of $B_s = 5\,\mathrm{MHz}$ and a PAPR of 7 dB. The tone spacing is set to 20 kHz. The PWM frequency f_p is set to 40 MHz and the carrier frequency f_c is set to 1 GHz. The simulation time step is set to 0.1 ns to capture sufficient out-of-band spectrum of the RF burst signal due to the large bandwidth of the PWM signal.

The normalized mean square error (NMSE) and the dynamic range (DR) are used to measure in-band error and out-of-band error before and after the image distortion mitigation. The NMSE in dB is defined by

$$\mathrm{NMSE} = 10\log_{10}\left(\frac{\mathrm{E}\left\{|\tilde{x}(t) - x(t)|^2\right\}}{\mathrm{E}\left\{|\tilde{x}(t)|^2\right\}}\right) \tag{3.21}$$

where $\mathrm{E}\{\cdot\}$ is the expectation function. The signal $\tilde{x}(t)$ is the demodulated in-band signal in $B_s = 5\,\mathrm{MHz}$ from the passband signal $x_{\mathrm{p,PB}}(t)$ for instance $x_{\mathrm{p,TE,PB}}(t)$ in (3.4) or $x_{\mathrm{p,DE_1,PB}}(t)$ in (3.14). The DR of the signal in dB is defined in frequency domain as

$$\mathrm{DR} = 10\log_{10}\left(\frac{\max_{f\in f_\mathrm{in}} X_{\mathrm{p,PB}}(t)}{\max_{f\in f_\mathrm{out}} X_{\mathrm{p,PB}}(t)}\right) \tag{3.22}$$

where $f \in f_\mathrm{in}$ denotes that the evaluation bandwidth is $f \in [-B_s/2, B_s/2]$ which is the same as performing a lowpass filter with a bandwidth of $B_s/2$ and $f \in f_\mathrm{out}$ denotes that f is bounded by $B_s/2 \le |f| \le 2B_s$. The signal $X_{\mathrm{p,PB}}(t)$ denotes the spectrum of the RF burst signal such as $x_{\mathrm{p,TE,PB}}(t)$ in (3.4) or $x_{\mathrm{p,DE_1,PB}}(t)$ in (3.14).

Figure 3.2 shows the spectrum of the RF burst signal with TEPWM method. It is a close-up of Figure 3.1(b). The positive and negative spectral components of signals $x^{+}_{\mathrm{p,TE,PB}}(t)$ and $x^{-}_{\mathrm{p,TE,PB}}(t)$ are illustrated with black and grey lines, respectively. The PWM frequency is set to $f_\mathrm{p} = 40$ MHz. Hence the image harmonic peak that introduces the image peak distortion to the wanted signal is located around the carrier frequency $f_\mathrm{c} = 1$ GHz. The NMSE and DR are -40.8 dB and 48.8 dB, respectively.

Figure 3.3 shows the spectrum of the RF burst signal with TEPWM method with image distortion mitigation. The new PWM frequency $\hat{f}_\mathrm{p}$ is set to 39.6 MHz according to (3.13). It can be seen that the wanted signal located at carrier frequency f_c is in the middle of adjacent

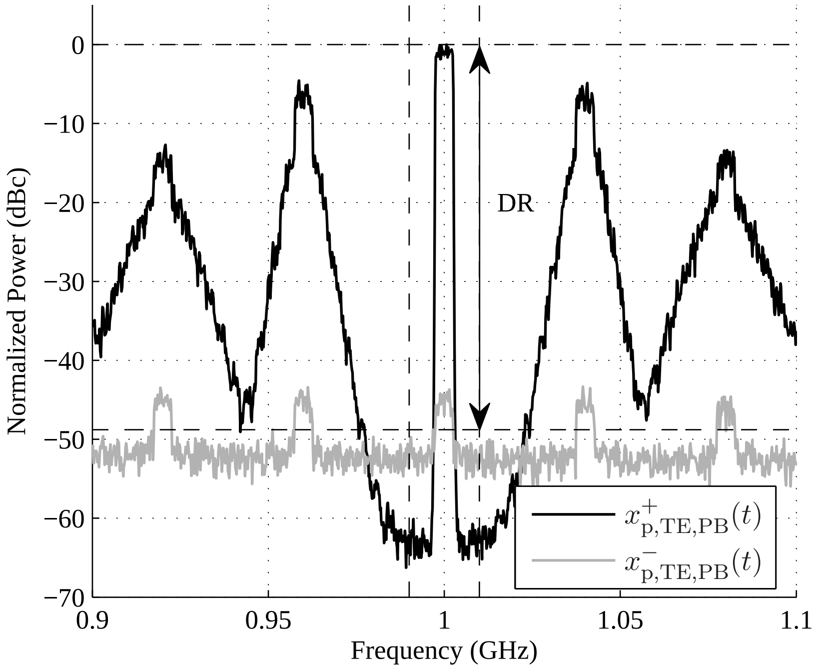

Figure 3.2: Spectrum of TEPWM generated RF burst signal with image peak distortion. This figure is a close-up of Figure 3.1(b). The image harmonic peak distortion (grey line) is located around the wanted signal at positive carrier frequency f_c. The NMSE and DR are −40.8 dB and 48.8 dB, respectively.

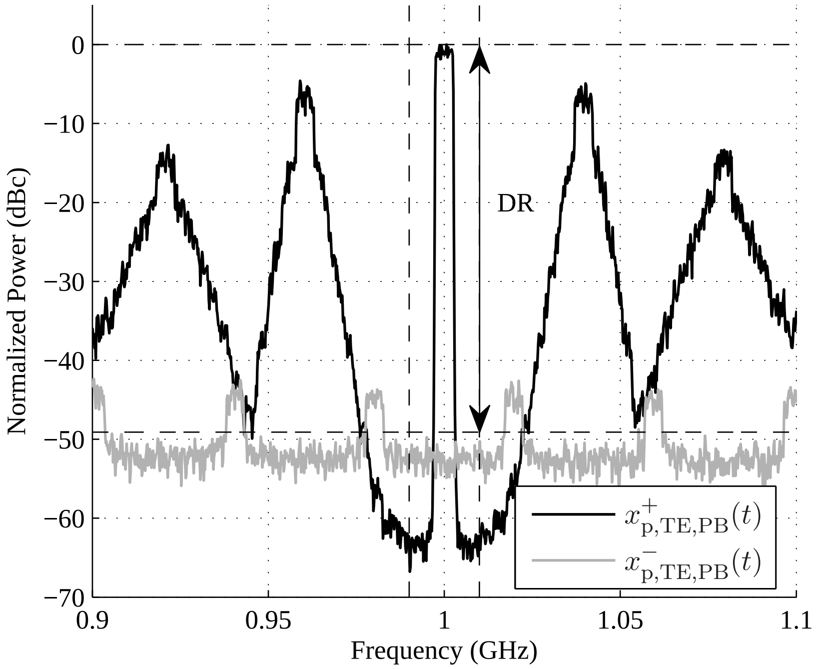

Figure 3.3: Spectrum of TEPWM generated RF burst signal with image distortion mitigation. With a new PWM frequency of $\hat{f}_{\mathrm{p}} = 39.6$ MHz, the image peak distortion can be avoided. The NMSE and DR are −46.9 dB and 49.1 dB, respectively.

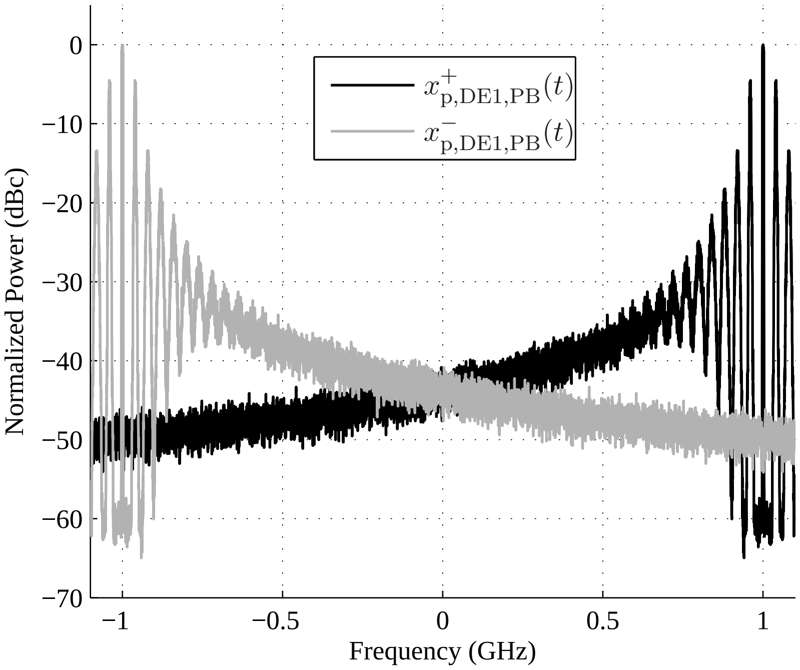

(a) Spectrum of DEPWM generated RF burst signal.

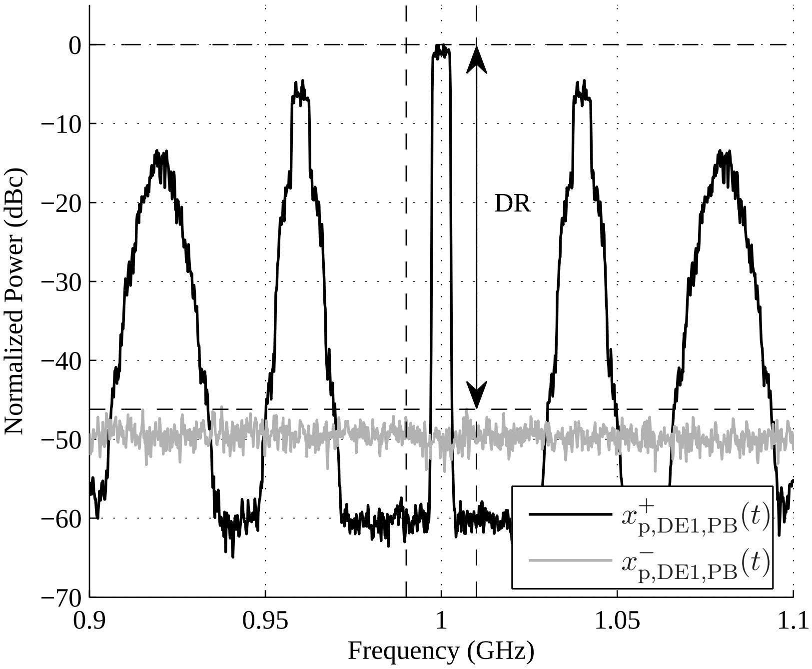

(b) Close-up of the spectrum of DEPWM generated RF burst signal.

Figure 3.4: Spectrum of DEPWM generated RF burst signal. The PWM frequency is $f_{\mathrm{p}} = 40$ MHz. The NMSE and DR are -48.3 dB and 46.2 dB, respectively.

	NMSE (dB)	DR (dB)
TEPWM with $f_\mathrm{p} = 40$ MHz	-40.8	48.8
TEPWM with $\hat{f}_\mathrm{p} = 39.6$ MHz	-46.9	49.1
DEPWM with $f_\mathrm{p} = 40$ MHz	-48.3	46.2

Table 3.1: Image mitigation performance for the given simulation setup.

image harmonic peaks and therefore the image peak distortion is avoided. By this approach, the NMSE and DR are -46.9 dB and 49.1 dB, respectively. The NMSE is improved by 6.1 dB and the DR is slightly increased.

Figure 3.4 shows the spectra of the RF burst signal with DEPWM method. The positive and negative spectral components of signals $x^{+}_{\mathrm{p,DE_1,PB}}(t)$ and $x^{-}_{\mathrm{p,DE_1,PB}}(t)$ are illustrated with black and grey lines, respectively. From Figure 3.4(a) it can be seen that there are no image peak distortions around the wanted signal in the DEPWM generated RF signal. A close-up of Figure 3.4(a) is shown in Figure 3.4(b). The NMSE and DR are -48.3 dB and 46.2 dB, respectively. The NMSE is improved by 7.5 dB compared to the TEPWM generated RF burst without image distortion mitigation though the DR is decreased by 2.6 dB.

The image mitigation performance is summarized in Table 3.1. Since DEPWM signals are generated without image peak distortions around the wanted signals, and the performance metrics are comparable to those of TEPWM signals with image distortion mitigation, the DEPWM signals will be the focus of investigation in the following.

3.2 Power Efficiency Analysis

Power efficiency is very important in burst-mode RF transmitters. In this section the power efficiency analysis for burst-mode RF transmitters will be carried out. First, the efficiency analysis for constant input signals will be given. Then the analysis of the average efficiency is presented. The average efficiency is represented by the PDF of the input magnitude, where the input signal can be a signal at the maximum average transmission power level as well as a combination of signals at different average transmission power levels. Afterwards, the average efficiency optimization is performed for burst-mode multilevel transmitters. Finally, the efficiency relation between burst-mode multilevel transmitters and (multistage) Doherty PAs is investigated. Simulation results will be presented to show that the optimized burst-mode multilevel transmitters outperform two-level as well as non-optimized burst-mode multilevel transmitters.

3.2.1 Efficiency for Constant Input Signals

According to the definitions of power efficiencies in Section 2.2, the coding efficiency for constant input signals $x(t) = A, A \in [0,1]$, denoted as $\eta_{\mathrm{c}}(A)$, is defined by

$$\eta_{\mathrm{c}}(A) = \begin{cases} \dfrac{P_{\mathrm{s}}(A)}{P_{\mathrm{tot}}(A)}, & \text{for } |x(t)| = A, \quad A \in (0,1] \\ 0, & \text{for } |x(t)| = A, \quad A = 0. \end{cases} \tag{3.23}$$

The transmitter efficiency for constant input signals, denoted as $\eta(A)$, is given by

$$\eta(A) = \frac{P_{\mathrm{s}}(A)}{P_{\mathrm{dc}}(A)} = \eta_{\mathrm{PA}}\eta_{\mathrm{c}}(A). \tag{3.24}$$

Since an RF PA operated in burst mode produces the maximum PA efficiency, the analysis of the coding efficiency will be the focus. To compute the signal power $P_{\mathrm{s}}(A)$, the transmission signal for a constant input signal can be expressed by

$$x_{\mathrm{PB}}(t) = A\cos(2\pi f_{\mathrm{c}} t). \tag{3.25}$$

Assuming that the input signal is sufficiently long and the carrier frequency f_{c} is much higher than the PWM frequency f_{p}, the signal power $P_{\mathrm{s}}(A)$ is closely approximated by

$$P_{\mathrm{s}}(A) = \frac{1}{T_{\mathrm{p}}} \int_0^{T_{\mathrm{p}}} x_{\mathrm{PB}}^2(t)dt = \frac{1}{2}A^2 \tag{3.26}$$

with a normalized load value of $1\,\Omega$. The assumed load value makes no difference for the efficiency calculation because the ratio between the signal power and the total power is of interest. Note that the signal power $P_{\mathrm{s}}(A)$ depends on the input magnitude A. The total power $P_{\mathrm{tot}}(A)$, on the other hand, changes according to the employed transmitter architectures.

Burst-Mode Two-Level Transmitters ($M = 1$)

A burst-mode two-level transmitter contains only one signal path. The coding efficiency for a two-level transmitter, which has been investigated in [83], is briefly introduced here for comparison.

A block diagram of the burst-mode two-level RF transmitter is illustrated in Figure 2.1 in Section 2.1.1. Fig. 3.5 shows the time domain signals of a burst-mode two-level transmitter. The total power of the amplified RF burst signal $x_{\mathrm{PA}}(t)$ is calculated as

$$\begin{aligned} P_{\mathrm{tot}}(A) &= \frac{1}{T_{\mathrm{p}}} \int_0^{D(A)T_{\mathrm{p}}} (\cos 2\pi f_{\mathrm{c}} t)^2 dt \\ &= \frac{1}{2}A, \quad A \in [0,1] \end{aligned} \tag{3.27}$$

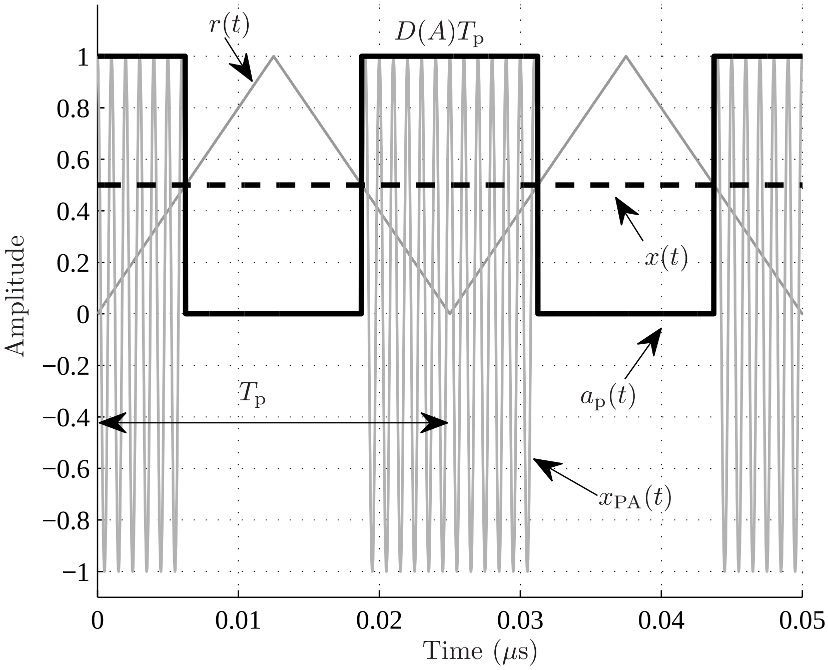

Figure 3.5: Time-domain signals of the burst-mode two-level RF transmitter. The period of the reference signal $r(t)$ is denoted by T_p. The duty-cycle is denoted as $D(A)$ which is the ratio of the pulse width to the period T_p. The constant input signal, PWM signal and the amplified RF burst signal are represented by $x(t)$, $a_\mathrm{p}(t)$ and $x_\mathrm{PA}(t)$, respectively.

where $D(A)$ describes the duty-cycle of the PW modulator output and is described by

$$D(A) = A, \quad A \in [0,1]. \tag{3.28}$$

Therefore, according to (3.23) with (3.26) and (3.27), the coding efficiency for the two-level transmitter is given by

$$\eta_\mathrm{c}(A) = \frac{\frac{1}{2}A^2}{\frac{1}{2}A} = A, \quad A \in [0,1]. \tag{3.29}$$

It can be seen that the coding efficiency linearly depends on the input magnitude and it reaches the maximum efficiency of 100% at the maximum input value $A = 1$.

Burst-Mode Multilevel Transmitters ($M \geq 2$)

A block diagram of a burst-mode multilevel RF transmitter is illustrated in Figure 2.4 in Section 2.1.2. The coding efficiency for constant signals is categorized into M cases depending on the input magnitude as

$$x(t) = A \quad \text{for} \quad A \in (V_{m-1}, V_m] \tag{3.30}$$

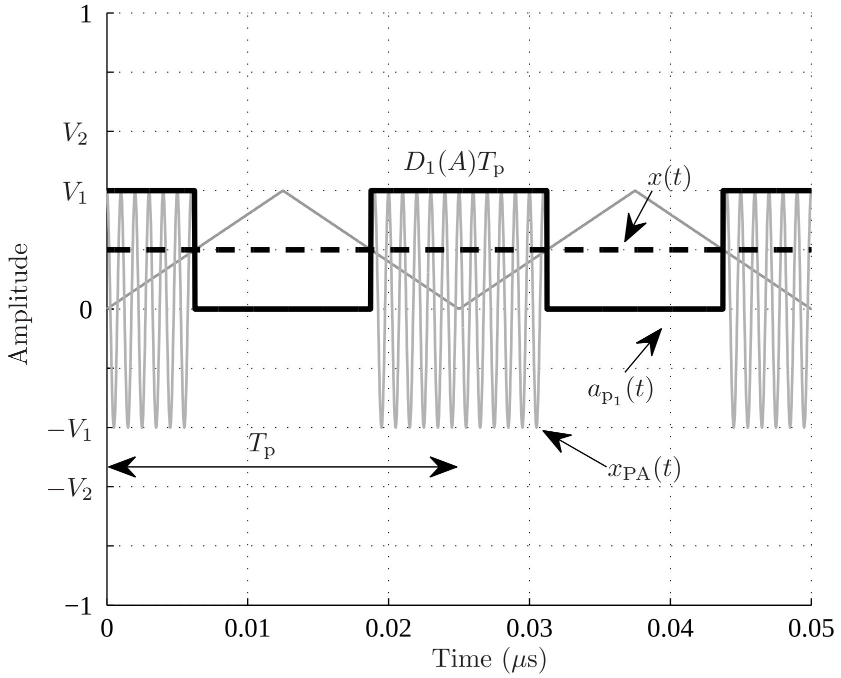

(a) Time-domain signals with constant input signal $x(t) = A \in (0, V_1]$.

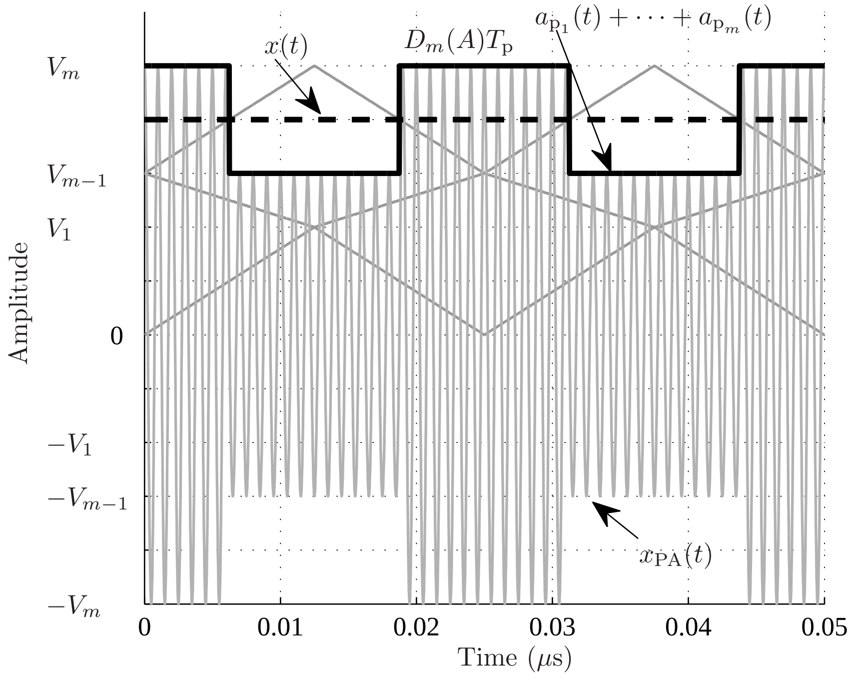

(b) Time-domain signals with constant input signal $x(t) = A \in (V_{m-1}, V_m]$.

Figure 3.6: Time-domain signals of the burst-mode multilevel RF transmitters with constant input signals.

where the threshold value $V_i, i \in [0, M]$ is defined in (2.3) in Section 2.1.2.

For the first case ($m = 1$) when $x(t) = A \in (0, V_1]$, which is illustrated in Figure 3.6(a), the total power of the amplified RF burst signal can be obtained by

$$\begin{aligned} P_{\mathrm{tot}_1}(A) &= \frac{1}{T_\mathrm{p}} \int_0^{D_1(A)T_\mathrm{p}} (V_1 \cos 2\pi f_\mathrm{c} t)^2 dt \\ &= \frac{1}{2} A V_1, \quad A \in (0, V_1] \end{aligned} \tag{3.31}$$

where $D_1(A)$ describes the duty-cycle of the main PW modulator output and is given by

$$D_1(A) = \frac{A}{V_1}, \quad A \in (0, V_1]. \tag{3.32}$$

Therefore, for the first case, the coding efficiency is calculated according to (3.23) with (3.26) and (3.31) as

$$\eta_{\mathrm{c}_1}(A) = \frac{\frac{1}{2}A^2}{\frac{1}{2}AV_1} = \frac{A}{V_1}, \quad A \in (0, V_1]. \tag{3.33}$$

It is clear that the coding efficiency for this case also linearly depends on the input magnitude with the efficiency peak obtained at $A = V_1$.

For the mth case when $x(t) = A \in (V_{m-1}, V_m]$, which is illustrated in Figure 3.6(b), the total power of the amplified RF burst signal can be calculated as

$$\begin{aligned} P_{\mathrm{tot}_m}(A) &= \frac{1}{T_\mathrm{p}} \left(\int_0^{D_m(A)T_\mathrm{p}} (V_m \cos 2\pi f_c t)^2 dt + \int_0^{(1-D_{m-1}(A))T_p} (V_{m-1} \cos 2\pi f_c t)^2 dt \right) \\ &= \frac{1}{2} \left(A(V_{m-1} + V_m) - V_{m-1} V_m \right), \quad A \in (V_{m-1}, V_m] \end{aligned} \tag{3.34}$$

where $D_m(A)$ represents the duty-cycle of the $(m-1)$th auxiliary PW modulator output and is given by

$$D_m(A) = \frac{A - V_{m-1}}{V_m - V_{m-1}}, \quad A \in (V_{m-1}, V_m]. \tag{3.35}$$

Therefore, for the mth case, the coding efficiency is given according to (3.23) with (3.26) and (3.34) by

$$\eta_{c_m}(A) = \frac{A^2}{A(V_{m-1} + V_m) - V_{m-1} V_m}, \quad A \in (V_{m-1}, V_m] \tag{3.36}$$

which gives the maximum coding efficiency with $A = V_m$.

As a result, the coding efficiency for burst-mode multilevel transmitters for constant input

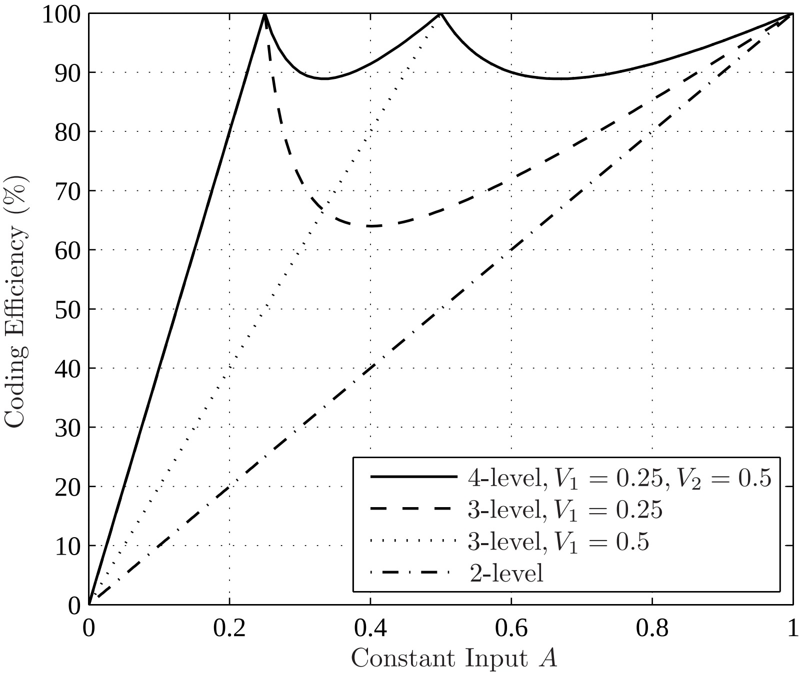

Figure 3.7: Coding efficiency with constant input signals for burst-mode $(M + 1)$-level RF transmitters $(M = 1, 2, 3)$.

signals $x(t) = A, A \in [0, 1]$ can be represented in general as

$$\eta_c(A) = \begin{cases} 0, & \text{for } \ A = 0 \\ \dfrac{A^2}{A(V_{m-1} + V_m) - V_{m-1}V_m}, & \text{for } \ A \in (V_{m-1}, V_m], \ \ m \in [1, M]. \end{cases} \tag{3.37}$$

where M represents the total number of paths of the burst-mode transmitter, and V_i is the threshold value defined in (2.3).

Fig. 3.7 illustrates coding efficiency curves of different burst-mode transmitters for constant input signals. For a $(M+1)$-level transmitter, there will be M efficiency peaks. The dash-dotted line shows the efficiency curve for the two-level transmitter. As shown, the coding efficiency of multilevel transmitters is better than the two-level case for all input values. Consequently, multilevel transmitters are able to provide higher efficiency compared to the two-level case.

3.2.2 Average Efficiency for Arbitrary Input Signals

The average efficiency is defined as the ratio of the average desired RF inband power $\overline{P}_\mathrm{s}$ to the average consumed power $\overline{P}_\mathrm{dc}$ and is given by [52]

$$\overline{\eta} = \frac{\overline{P}_\mathrm{s}}{\overline{P}_\mathrm{dc}} = \eta_\mathrm{PA}\overline{\eta}_\mathrm{c} \tag{3.38}$$

where $\overline{\eta}_\mathrm{c}$ describes the average coding efficiency by [79]

$$\overline{\eta}_\mathrm{c} = \frac{\overline{P}_\mathrm{s}}{\overline{P}_\mathrm{tot}} = \frac{\int_0^1 A^2 f_a(A) dA}{\int_0^1 \frac{A^2}{\eta_\mathrm{c}(A)} f_a(A) dA}, \quad A \in [0,1] \tag{3.39}$$

where $f_a(A)$ is the PDF of the input magnitude and $\eta_\mathrm{c}(A)$ represents the coding efficiency for constant input signals given in (3.37).

Note that the PDF $f_a(A)$ is not limited to representing the distribution of the input magnitude at the maximum average transmit power level, i.e., with input magnitude bounded by $[0, 1]$. It can also describe the magnitude distribution of signals at different average transmission power levels, or a combination of the above-mentioned signals due to the power control. For example, two sets of signals with the same PAPR are considered, where the average transmit power levels are the maximum and 20 dB backoff from the maximum. Therefore, the signals are described within intervals of $[0, 1]$ and $[0, 0.1]$, respectively. The resulting PDF of the combined signal will have more occurrences at the lower magnitude values, which leads to a higher overall PAPR than the given PAPR. A detailed example of signals at variable average transmit power levels will be given by the end of the following subsection.

The average transmitter efficiency is given by combining (3.38) and (3.39)

$$\overline{\eta} = \eta_\mathrm{PA} \frac{\int_0^1 A^2 f_a(A) dA}{\int_0^1 \frac{A^2}{\eta_c(A)} f_a(A) dA}, \quad A \in [0,1]. \tag{3.40}$$

We can thus calculate the average efficiency using the PDF $f_a(A)$, the PA efficiency η_PA, and the coding efficiency $\eta_c(A)$.

For example, the average transmitter efficiency for a two-level transmitter is

$$\overline{\eta} = \eta_\mathrm{PA} \frac{\int_0^1 A^2 f_a(A) dA}{\int_0^1 A f_a(A) dA}, \quad A \in [0,1] \tag{3.41}$$

obtained from (3.40) with (3.29). Note that, for the generic $(M + 1)$-level $(M \geq 2)$ case, the coding efficiency $\eta_\mathrm{c}(A)$ in (3.40) depends on the threshold value V_i. Consequently, the choice of V_i has an impact on the average efficiency $\overline{\eta}$. This will be investigated in the following subsection, leading to the optimization concept for burst-mode multilevel transmitters.

3.2.3 Efficiency Optimization

In order to study the impact of the threshold values on the average efficiency, first we expand the expression for the average efficiency (3.40) with the coding efficiency (3.37). We will then show that it is possible to find a set of threshold values maximizing the average efficiency. We will begin with the efficiency optimization of a burst-mode three-level transmitter and then extend the concept to general multilevel burst-mode transmitters.

Burst-Mode Three-level Transmitters ($M = 2$)

For a burst-mode three-level transmitter, according to (3.37), the coding efficiency is given as

$$\eta_{\mathrm{c}}(A) = \begin{cases} \dfrac{A}{V_1}, & \text{for } A \in [0, V_1] \\ \dfrac{A^2}{A(V_1+1)-V_1}, & \text{for } A \in (V_1, 1]. \end{cases} \tag{3.42}$$

Substituting (3.42) for $\eta_{\mathrm{c}}(A)$ in (3.40), the average efficiency for the burst-mode three-level transmitter can be expressed by

$$\overline{\eta} = \eta_{\mathrm{PA}} \frac{\int_0^1 A^2 f_a(A) dA}{G(V_1)}, \quad A \in [0, 1] \tag{3.43}$$

where $G(V_1)$ describes the total power of the amplified RF burst signal as

$$G(V_1) = V_1 \int_0^1 A f_a(A) dA + \int_{V_1}^1 A f_a(A) dA - V_1 \int_{V_1}^1 f_a(A) dA. \tag{3.44}$$

Note that in (3.43), the average signal power ($\int_0^1 A^2 f_a(A) dA$) is independent of the threshold values. We can thus obtain the maximum average efficiency by finding the minimum of $G(V_1)$. To this end, the first-order and second-order derivatives of $G(V_1)$ with respect to V_1 are derived

$$\frac{\partial G}{\partial V_1} = \int_0^1 A f_a(A) dA - \int_{V_1}^1 f_a(A) dA \tag{3.45}$$

and

$$\frac{\partial^2 G}{\partial V_1^2} = f_a(V_1). \tag{3.46}$$

where we used the relation

$$\frac{\partial}{\partial V_1} \int_{V_1}^1 y(\xi) d\xi = -y(V_1). \tag{3.47}$$

It is assumed that the PDF $f_a(\cdot)$ is smooth and is non-zero over the definition domain. Hence it follows from (3.46) that $f_a(V_1) > 0$, and (3.44) can provide the minimum of $G(V_1)$ if there exists a $\hat{V}_1$ in (3.45) such that

$$\int_{\hat{V}_1}^1 f_a(A) dA = \int_0^1 A f_a(A) dA. \tag{3.48}$$

This value is given by [79, 80]

$$\hat{V}_1 = F^{-1}(1 - E(A)) \tag{3.49}$$

where $E(\cdot)$ is the expectation operator and $F^{-1}(\cdot)$ is the inverse cumulative distribution function (CDF). With (3.43), (3.44), (3.48) and (3.49), the maximum average efficiency is given by

$$\begin{aligned}\overline{\eta}_{\max} &= \eta_{\mathrm{PA}} \frac{\int_0^1 A^2 f_a(A)dA}{\int_{\hat{V}_1}^1 A f_a(A)dA} \\ &= \eta_{\mathrm{PA}} \frac{\int_0^1 A^2 f_a(A)dA}{\int_{F^{-1}(1-E(A))}^1 A f_a(A)dA}.\end{aligned} \tag{3.50}$$

Thus the optimum threshold value V_1 of three-level transmitters can be analytically determined from the input magnitude PDF according to (3.49). Using this threshold, the maximum average efficiency is reached as in (3.50).

Burst-Mode ($M+1$)-level Transmitters ($M \geq 3$)

In this case, the average efficiency can be expressed by (3.40) with (3.37) as

$$\overline{\eta} = \eta_{\mathrm{PA}} \frac{\int_0^1 A^2 f_a(A)dA}{G(V_1, ..., V_{M-1})}, \quad A \in [0,1] \tag{3.51}$$

where $G(V_1, ..., V_{M-1})$ describes the total power of the amplified RF burst signal as

$$\begin{aligned}&G(V_1, ..., V_{M-1}) \\ &= \sum_{m=1}^{M} \int_{V_{m-1}}^{V_m} \left(A(V_{m-1}+V_m) - V_{m-1}V_m\right) f_a(A)dA.\end{aligned} \tag{3.52}$$

The maximum average efficiency can be obtained by finding a set of optimum threshold values $(\hat{V}_1, ..., \hat{V}_{M-1})$ leading to the minimum of (3.52). The maximum efficiency is given by

$$\overline{\eta}_{\max} = \eta_{\mathrm{PA}} \frac{\int_0^1 A^2 f_a(A)dA}{G(\hat{V}_1, ..., \hat{V}_{M-1})}, \quad A \in [0,1]. \tag{3.53}$$

For uniformly distributed signals, the optimum threshold values and the maximum efficiency can be analytically determined as

$$\hat{V}_l = \frac{l}{M}, \quad l = 0, ..., M \tag{3.54}$$

and

$$\overline{\eta}_{\max} = \eta_{\mathrm{PA}} \frac{1}{1 + \frac{1}{2M^2}}. \tag{3.55}$$

The obtained optimum threshold values according to the uniform distribution are the same as the typically chosen non-optimized threshold values. Therefore the non-optimized transmitter only gives the maximum efficiency for uniformly distributed input magnitudes. Typical com-

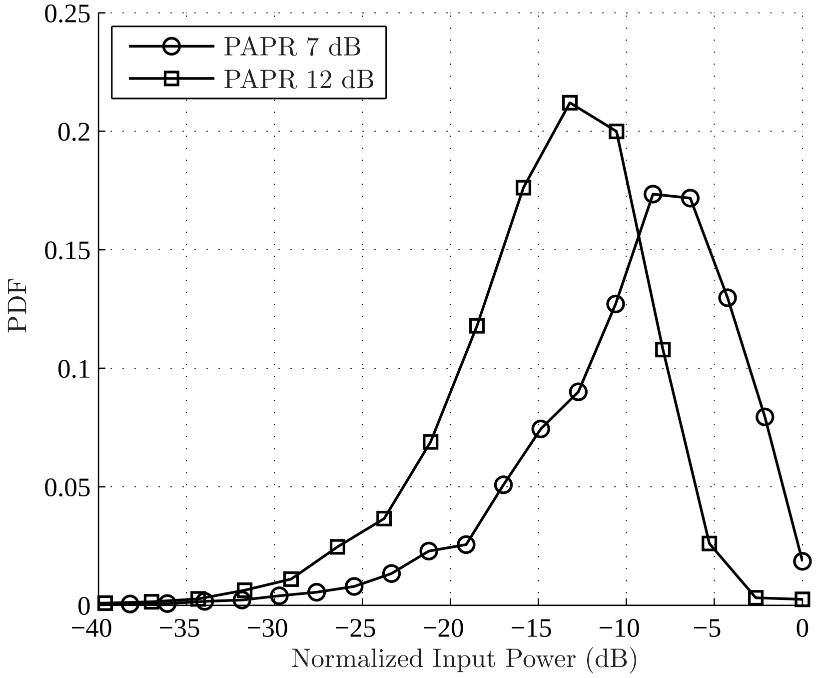

Figure 3.8: PDFs of the input signal power of DMT signals with PAPRs of 7 dB and 12 dB.

PAPR (dB)		7	8	9	10	11	12
3-level	$\hat{V}_1$	0.42	0.40	0.38	0.35	0.33	0.30
4-level	$\hat{V}_1$	0.30	0.27	0.25	0.23	0.21	0.20
	$\hat{V}_2$	0.57	0.53	0.50	0.46	0.44	0.41

Table 3.2: Optimum threshold values for DMT signals with different PAPRs when $a(t) \in [0, 1]$.

PAPR (dB)		7	8	9	10	11	12
$\overline{\eta}$ (%)	2-level	39.7	35.4	31.6	28.4	25.5	22.5
	3-level (non-optimized)	64.4	61.3	57.6	53.0	48.9	44.1
	3-level (optimized)	65.5	63.5	61.7	60.2	58.4	57.2
	4-level (non-optimized)	71.6	70.0	68.1	65.9	62.9	59.3
	4-level (optimized)	72.3	71.5	70.8	69.9	69.1	68.9

Table 3.3: Average transmitter efficiency for DMT signals with different PAPRs when $a(t) \in [0, 1]$.

	$\hat{V}_1$	$\hat{V}_2$
3-level	0.16	-
4-level	0.08	0.31

Table 3.4: Optimum threshold values for the given power profile.

	2-level	3-level (non-optimized)	3-level (optimized)	4-level (non-optimized)	4-level (optimized)
$\overline{\eta}$ (%)	12.2	23.6	41.0	33.2	57.5

Table 3.5: Average transmitter efficiency for the given power profile.

munication signals have different distributions, which require to solve the optimization problem numerically, where optimization methods such as line searching [89] can be used.

The PDFs of the input power of DMT signals with 7 dB and 12 dB PAPR are shown in Fig 3.8. A high PAPR leads to more occurrences at low input power. Table 3.2 gives the optimum threshold values of three-level and four-level transmitters for DMT signals with different PAPRs when $a(t) \in [0, 1]$. The optimum threshold value $\hat{V}_1$ of the three-level transmitter is obtained according to (3.49), and the optimum threshold values $(\hat{V}_1, \hat{V}_2)$ of the four-level transmitter are obtained by finding the minimum of (3.52). For the DMT signal with the same PAPR but a different $a(t)_{\max}$, the optimum threshold values can be calculated by scaling the values in the Table 3.2 with $a(t)_{\max}$.

Table 3.3 presents the average efficiency for two-level, non-optimized and optimized three-level and four-level transmitters. The PAs are assumed in ideal Class B operation and the PA efficiency is therefore $\eta_{\mathrm{PA}} = 78.5\%$. For two-level transmitters the average efficiency is calculated from (3.41). For non-optimized transmitters the average efficiency is obtained by (3.51) with equally spaced threshold values. For optimized three-level and four-level transmitters the average efficiency is calculated according to (3.50) and (3.53) with the optimum threshold values given in Table 3.2, respectively. It is shown that the efficiency of the optimized transmitters outperforms two-level and non-optimized transmitters, especially for signals with high PAPRs. For the signal with 12 dB PAPR, the optimized three-level transmitter achieves an efficiency improvement of 13.1 percentage points compared to the non-optimized case, and 34.7 percentage points compared to the two-level case. For the four-level case, the improvements are 9.6 and 46.4 percentage points, respectively.

Fig. 3.9(a) shows the power profile of a representative CDMA mobile transmitter average transmission power levels according to [13, 90]. In order to perform the efficiency optimization for signals at variable average transmission power levels, it is assumed that the transmission power changes linearly with the input power [49], and the power profile describes a combination

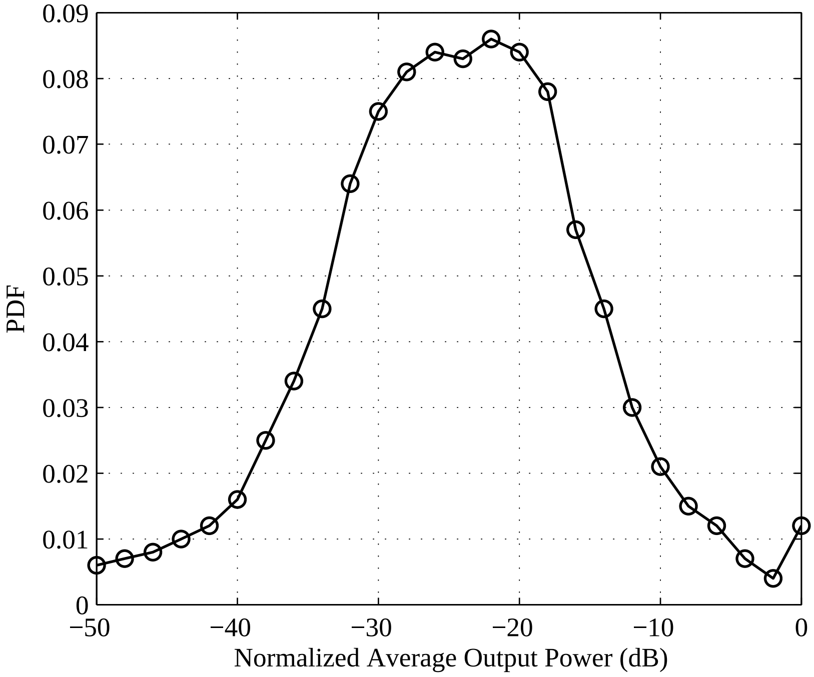

(a) PDF, or power profile, of the normalized average transmission power levels of a representative CDMA mobile transmitter.

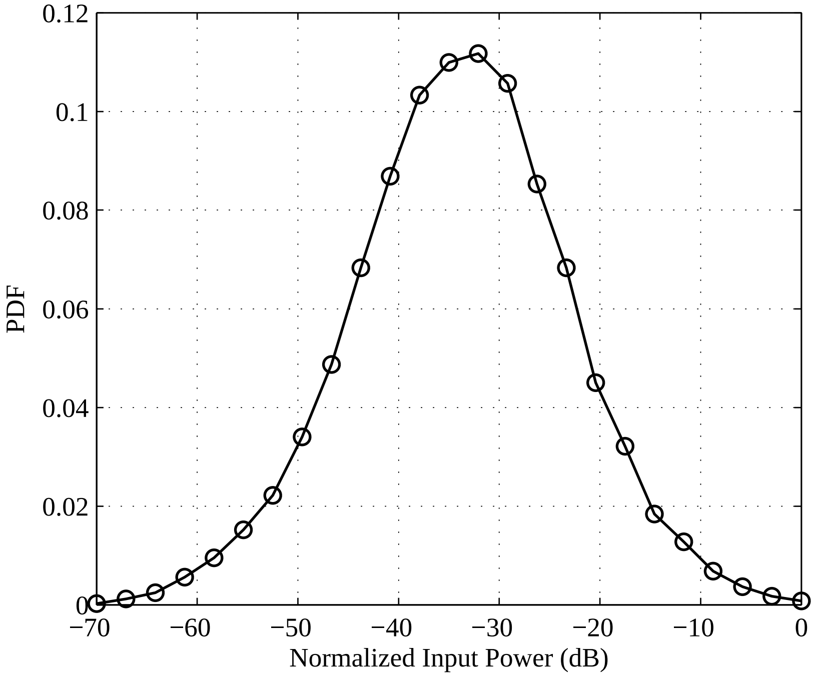

(b) PDF of the input power of the combined DMT signals with different average transmission power levels according to (a).

Figure 3.9: PDFs of (a) the normalized average transmission power levels of a representative CDMA mobile transmitter and (b) the input power of the combined DMT signals with different average transmission power levels.

of DMT signals with the same PAPR of 7 dB but different average transmission power levels, i.e., different input magnitude intervals. The occurrence of the DMT signal at a certain average transmission power level can be found in Fig. 3.9(a). Therefore a PDF describing the distribution of overall input magnitudes of the combined DMT signals can be obtained, denoted as $f_a(A)$, and is used for the efficiency optimization. Fig. 3.9(b) gives the PDF of the input power of the combined DMT signals with different average transmission power levels according to Fig. 3.9(a). The PAPR of the combined signals is 22 dB. The corresponding optimum threshold values and average efficiency are shown in Table 3.4 and Table 3.5. The ideal Class B operation efficiency is assumed for the calculation. The efficiency improvement obtained by the optimized three-level transmitter is 17.4 percentage points compared to the non-optimized case and 28.8 percentage points compared to the two-level case. For the four-level case, the improvements are 24.3 and 45.3 percentage points, respectively.

3.2.4 Efficiency Relation to the Doherty PA

The Doherty PA is well known for its potential to deliver high efficiency [19, 49]. Many publications have investigated extended Doherty PAs [13, 91] and multistage Doherty PAs [21, 92] to further enhance the efficiency over classic Doherty PAs.

For an ideal Doherty PA based on ideal Class B PAs, according to [52], the Doherty PA efficiency for a constant output voltage v_o is

$$\eta_{\mathrm{DPA}}(v_o) = \begin{cases} \eta_{\mathrm{PA}} \dfrac{1}{\alpha} \dfrac{v_o}{v_{\max}}, & \text{for } \; v_o \in [0, \alpha v_{\max}] \\ \eta_{\mathrm{PA}} \dfrac{(\frac{v_o}{v_{\max}})^2}{\frac{v_o}{v_{\max}}(\alpha+1)-\alpha}, & \text{for } \; v_o \in (\alpha v_{\max}, v_{\max}] \end{cases} \tag{3.56}$$

where $v_{\max}$ is the maximum output voltage level, and the PA efficiency is $\eta_{\mathrm{PA}} = 78.5\%$. The design parameter α represents the voltage division ratio. This ratio determines the contribution of the main PA and the auxiliary PA to the output power of the Doherty PA.

When a Doherty PA is backed off from full power to lower power output levels, it is assumed that the output power changes linearly with the input power [49]. Therefore, according to (3.56), the output voltage v_o can be first normalized to the maximum output voltage $v_{\max}$, and then related to the normalized input voltage A. This leads to the Doherty PA efficiency for constant input signals $x(t) = A$, $A \in [0, 1]$ of

$$\eta_{\mathrm{DPA}}(A) = \begin{cases} \eta_{\mathrm{PA}} \dfrac{A}{\alpha}, & \text{for } \; A \in [0, \alpha] \\ \eta_{\mathrm{PA}} \dfrac{A^2}{A(\alpha+1)-\alpha}, & \text{for } \; A \in (\alpha, 1] \end{cases} \tag{3.57}$$

where $\eta_{\mathrm{DPA}}(A)$ represents the efficiency for the Doherty PA. For a classic Doherty PA, the ratio α is set to 0.5. If α is set to values lower than 0.5, the main amplifier reaches saturation at a lower power level. This extended Doherty PA has been used for efficiency enhancement for transmission power over a wide range of power levels [13].

In order to show the efficiency relation between the burst-mode multilevel transmitters and the Doherty PAs, the efficiency for a three-level burst-mode transmitter is given according to (3.24) and (3.37) as

$$\eta(A) = \begin{cases} \eta_{\mathrm{PA}} \dfrac{A}{V_1}, & \text{for } A \in [0, V_1] \\ \eta_{\mathrm{PA}} \dfrac{A^2}{A(V_1+1) - V_1}, & \text{for } A \in (V_1, 1]. \end{cases} \tag{3.58}$$

Based on the analysis before, we know that the threshold value V_1 also determines the input power to the main and auxiliary PAs. Therefore, the design parameter α in Doherty PAs and the threshold value V_1 in burst-mode multilevel transmitters is considered to have the same functionality. Comparing (3.57) with (3.58), it is clear that the efficiency expressions of the Doherty PA and the burst-mode three-level transmitter are identical for constant input signals. For a three-stage Doherty PA, the efficiency curve can be described as [92]

$$\eta_{\mathrm{DPA}}(A) = \begin{cases} \eta_{\mathrm{PA}} \dfrac{A}{\alpha}, & \text{for } A \in [0, \alpha] \\ \eta_{\mathrm{PA}} \dfrac{A^2}{A(\alpha+\beta) - \alpha\beta}, & \text{for } A \in (\alpha, \beta] \\ \eta_{\mathrm{PA}} \dfrac{A^2}{A(\beta+1) - \beta}, & \text{for } A \in (\beta, 1] \end{cases} \tag{3.59}$$

where α and β, which are the inverse of γ_2 and γ_1 in [92], determine the contribution of the PAs to the overall output power, and the transition where the auxiliary PAs are turned on. Note that in (3.59) the output voltage is already related to the normalized input. The efficiency expressions for the three-stage Doherty PA and the four-level burst-mode transmitter are the same when we compare (3.59) to (3.37) with $M = 3$, and with the knowledge of α, β having the same functionality with V_1, V_2. This relation can be generalized for other multistage Doherty PAs and burst-mode multilevel transmitters.

3.2.5 Simulation Results

Simulation Setup

Simulations were carried out in Matlab and Simulink environment using the SimPowerSystems toolbox. The SimPowerSystems toolbox is designed for simulating and modeling electrical power systems [93].

Fig. 3.10 illustrates the setup of the simulated burst-mode three-level transmitter. The main and the auxiliary PA are in Class B operation. The transistors of the PAs are modeled as voltage driven current sources including the nonlinear knee effect. The capacitors are ideally modeled. The inductors connected with the supply voltage are modeled with a small ohmic loss mainly to guarantee the simulator convergence. The output signals from the main and auxiliary PAs are

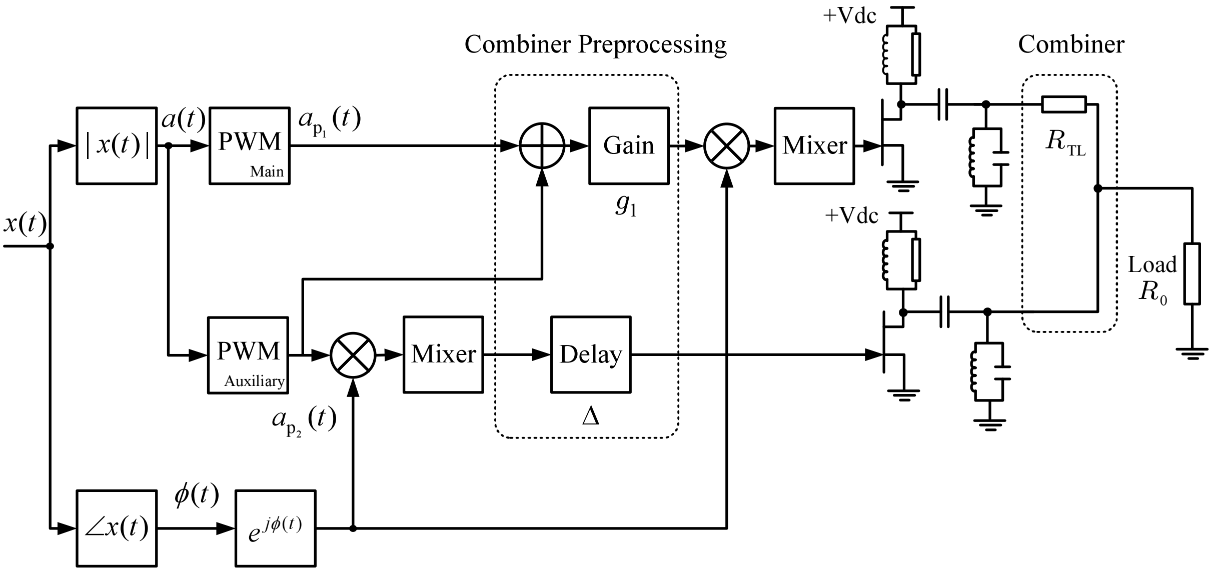

Figure 3.10: Simulation setup of a burst-mode three-level RF transmitter.

combined through a lossless quarter wavelength transmission line to achieve load modulation. The characteristic impedance of the transmission line is

$$R_{\mathrm{TL}} = \frac{R_0}{V_1} \tag{3.60}$$

where $R_0 = 25\,\Omega$ is the load impedance used in the simulations, and V_1 is the threshold value. In the low-power operation when only the main PA is turned on, the impedance seen by the main PA is

$$R^{\mathrm{l}}_{\mathrm{main}} = \frac{R_0}{V_1^2}. \tag{3.61}$$

In the high-power operation when both PAs are on, the impedances seen by the main PA and the auxiliary PA are

$$R^{\mathrm{h}}_{\mathrm{main}} = \frac{R_0}{V_1}, \quad R^{\mathrm{h}}_{\mathrm{aux}} = \frac{R_0}{(1 - V_1)}. \tag{3.62}$$

The varying impedances result in the gain fluctuation and the efficiency degradation as described in [21, 50, 51]. A practical method to improve the gain flatness is to divide the input power in an unequal way [13, 51]. For burst-mode transmitters, the reduction of the input magnitude to the PWM will not decrease the burst magnitude to the PA as required but the burst duration. Therefore the method introduced in [94], indicated by dashed boxes, is used to achieve the unequal input voltage division in each operation region, leading to proper power combining. The gain inside the combiner preprocessing block is set to

$$g_1 = V_1 \tag{3.63}$$

according to the currents from PAs in different power operation regions, which are inversely proportional to the impedances. When only the main PA is turned on, the magnitude of the signal after the combiner preprocessing block in the main path is V_1^2. When both PAs are turned on, the magnitudes of the signals in the main and auxiliary paths are V_1 and $(1-V_1)$, respectively. By doing so, the gain flatness and efficiency for burst-mode transmitters are improved. A delay block in the auxiliary path is used to compensate the delay (phase shifting) between the PA outputs, where the delay value is calculated as

$$\Delta = \frac{\frac{\lambda}{4}}{c} = \frac{1}{4f_\mathrm{c}} \tag{3.64}$$

where λ is the wavelength of the radio wave at the carrier frequency $f_\mathrm{c} = 1\,\mathrm{GHz}$, and c is the speed of light, set to $3 \times 10^8\,\mathrm{m/s}$. The desired signal is retrieved later on by ideal bandpass filtering.

The simulation setup for other burst-mode multilevel transmitters can be generalized from this burst-mode three-level transmitter architecture. For a 4-level burst-mode transmitter, the impedance of the transmission line that connects the main PA and the first auxiliary PA, and the impedance of the transmission line that connects two auxiliary PAs and the load R_0 are [92]

$$R_{\mathrm{TL}_1} = \frac{R_0}{V_1 V_2}, \quad R_{\mathrm{TL}_2} = \frac{R_0}{V_2} \tag{3.65}$$

where (V_1, V_2) are the threshold values of four-level burst-mode transmitters and $R_0 = 16.7\ \Omega$. In the low-power operation, the impedance seen by the main PA is

$$R^{\mathrm{l}}_{\mathrm{main}} = \frac{R_0}{V_1^2}. \tag{3.66}$$

In the medium-power operation, the impedances seen by the main PA and the first auxiliary PA are

$$R^{\mathrm{m}}_{\mathrm{main}} = \frac{R_0}{V_1 V_2}, \quad R^{\mathrm{m}}_{\mathrm{aux}_1} = \frac{R_0}{V_2(V_2 - V_1)}. \tag{3.67}$$

In the high-power operation, the impedances seen by the main PA and two auxiliary PAs are

$$R^{\mathrm{h}}_{\mathrm{main}} = \frac{R_0}{V_1 V_2}, \quad R^{\mathrm{h}}_{\mathrm{aux}_1} = \frac{R_0}{V_2(1 - V_1)}, \quad R^{\mathrm{h}}_{\mathrm{aux}_2} = \frac{R_0}{1 - V_2}. \tag{3.68}$$

The combiner preprocessing is performed according to the different impedances seen by the PAs, where the gain in the main path and the first auxiliary path is set to V_1 and V_2, respectively. The delays in the first and the second auxiliary paths are Δ and 2Δ, respectively. The transmitter efficiency for constant input signals is

$$\eta(A) = \frac{P_\mathrm{s}(A)}{P_\mathrm{dc}(A)} \tag{3.69}$$

where $P_{\mathrm{s}}(A)$ is the signal power of $x_{\mathrm{p,PB}}(t)$ at the load inside the 5 MHz signal. The average efficiency for the DMT signal at the maximum average transmission power level is

$$\overline{\eta} = \frac{\overline{P}_{\mathrm{s}}}{\overline{P}_{\mathrm{dc}}}. \tag{3.70}$$

A complex bandwidth of $B_{\mathrm{s}} = 5\,\mathrm{MHz}$ is used for the DMT signal, therefore $\overline{P}_{\mathrm{s}}$ is the signal power of $x_{\mathrm{p,PB}}(t)$ at the load inside the 5 MHz signal. For signals at variable average transmission power levels, the average efficiency is evaluated by

$$\overline{\eta} = \frac{\int_0^1 A^2 f_a(A) dA}{\int_0^1 \frac{A^2}{\eta(A)} f_a(A) dA} \tag{3.71}$$

where $\eta(A)$ represents the simulated transmitter efficiency for constant input signals with different threshold values.

Efficiency for Constant Input Signals

Fig. 3.11 and Fig. 3.12 show the simulated efficiency curves of two-level, three-level, and four-level burst-mode transmitters with different threshold values for constant input signals. The dashed lines depict the efficiency curves for the non-optimized transmitters. The solid lines depict the efficiency curves of the optimized transmitters for DMT signals with different PAPRs. The optimum threshold values are given in Table 3.2. In the figures, it is shown that the efficiencies of the optimized and non-optimized multilevel transmitters are considerably higher than the two-level case. It is also shown that the efficiency curves of the optimized transmitters reach the initial peaks at lower input compared to the non-optimized cases. Therefore, the optimized transmitters can provide higher efficiency for signals with high PAPRs, which will be demonstrated in the following subsection.

Average Efficiency for DMT Signals with Different PAPRs

Fig. 3.13 and Fig. 3.14 show the simulated average efficiency for three-level and four-level burst-mode transmitters with different threshold values for signals with different PAPRs. In Fig. 3.13, the markers represent the average efficiency obtained with the calculated optimum threshold values $\hat{V}_1$. The non-optimized cases are shown with $V_1 = 0.5$, and the two-level cases are included with $V_1 = 1$ for the comparison purpose. For the DMT signal with 12 dB PAPR, an improvement of 11.5 percentage points is obtained with the optimized three-level transmitter compared to the non-optimized case. Compared to the two-level case, an improvement of 32.2 percentage points can be achieved. In Fig. 3.14, contour levels of $25\% - 60\%$ with an interval of 5%, and 63.5% are shown. The average efficiency of 63.5% is obtained with the calculated optimum threshold values of $(0.20, 0.41)$. For the DMT signal with 12 dB PAPR, an improvement of 7.6 percentage points can be obtained compared to the non-optimized case, and 42 percentage points compared to the two-level case. The results are summarized in Table 3.6. The difference

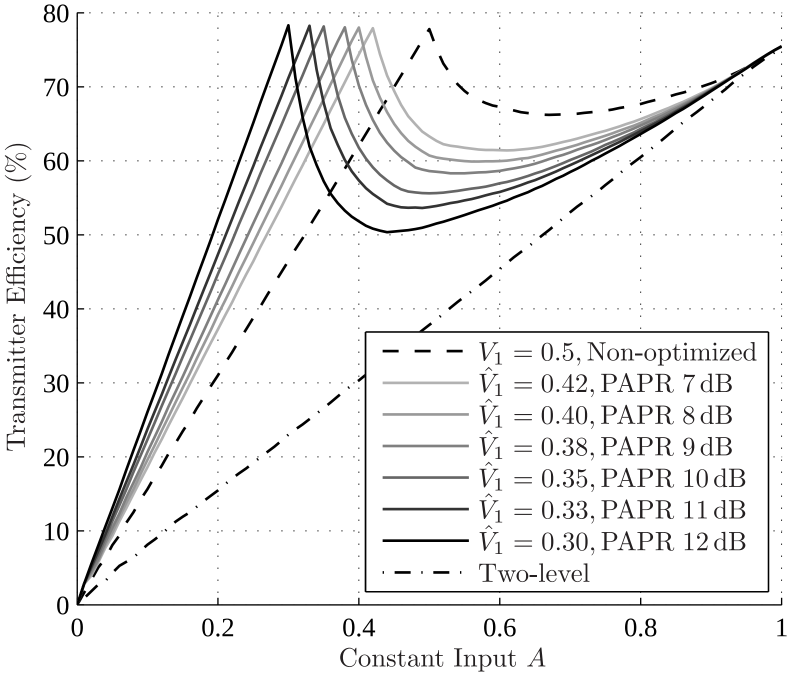

Figure 3.11: Simulated efficiency curves of two-level and three-level transmitters with different threshold values for constant input signals.

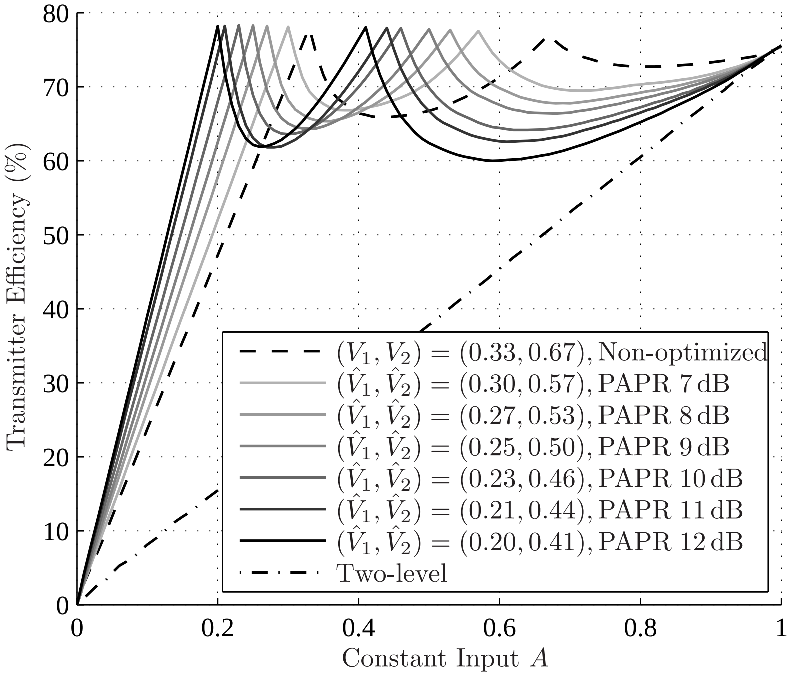

Figure 3.12: Simulated efficiency curves of two-level and four-level transmitters with different threshold values for constant input signals.

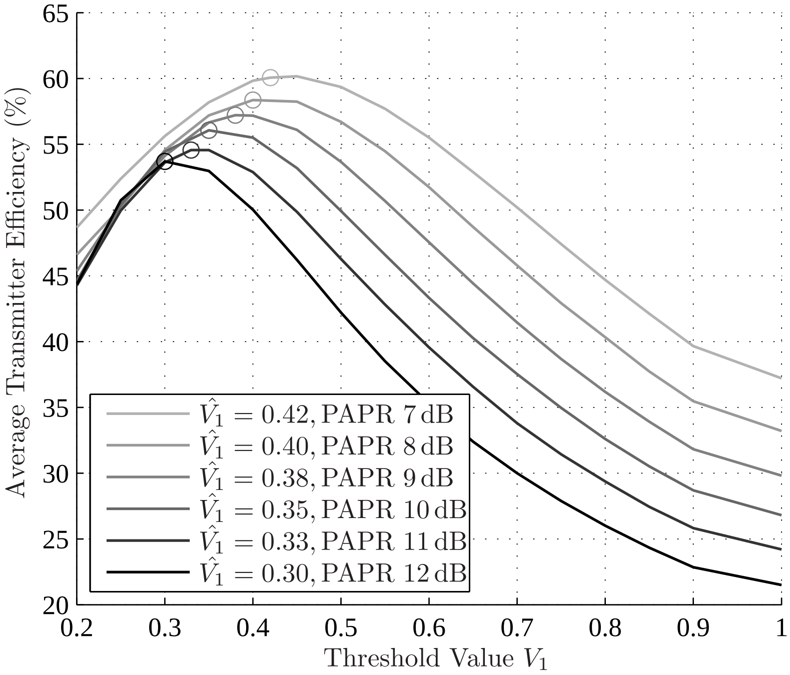

Figure 3.13: Average transmitter efficiency of three-level burst-mode transmitters for DMT signals with different PAPRs. Markers represent the average efficiency obtained with the calculated optimum threshold value $\hat{V}_1$. The non-optimized cases are shown with $V_1 = 0.5$, and the two-level cases are included with $V_1 = 1$ for the comparison purpose.

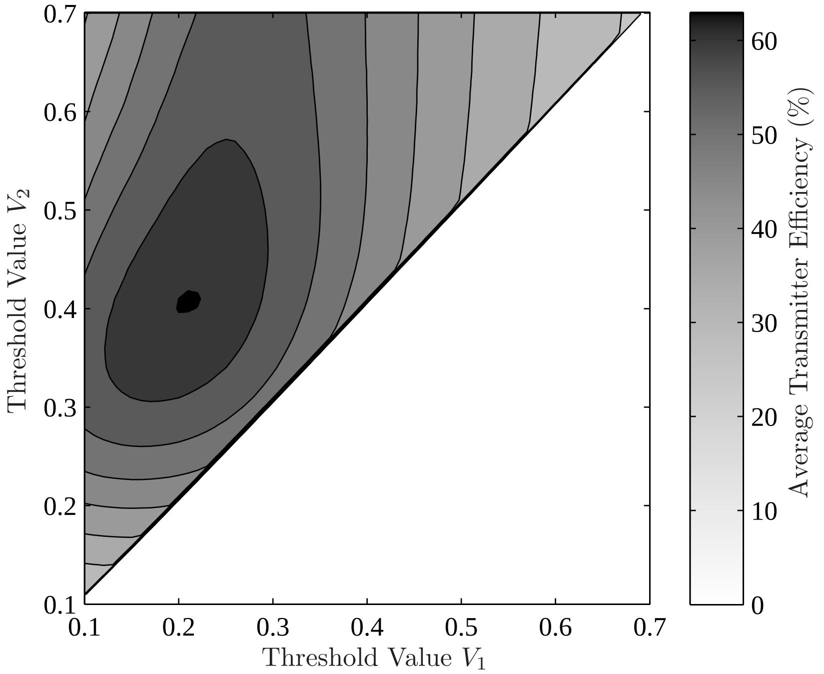

Figure 3.14: Average transmitter efficiency of four-level burst-mode transmitters for the DMT signal with 12 dB PAPR. Contour levels of $25\% - 60\%$ with an interval of 5%, and 63.5% are shown in the figure. The average efficiency of 63.5% is obtained with the optimum threshold value $(\hat{V}_1, \hat{V}_2) = (0.20, 0.41)$.

PAPR (dB)		7	8	9	10	11	12
	2-level	37.2	33.2	29.8	26.8	24.2	21.5
$\overline{\eta}$ (%)	3-level (non-optimized)	59.4	56.7	53.7	49.9	46.3	42.2
	3-level (optimized)	60.1	58.4	57.2	56.1	54.6	53.7
	4-level (non-optimized)	64.8	63.7	62.6	61.1	58.8	55.9
	4-level (optimized)	65.3	64.4	64.4	63.9	63.5	63.5

Table 3.6: Simulated average transmitter efficiency for DMT signals with different PAPRs when $a(t) \in [0, 1]$.

between the simulation results in Table 3.6 and the calculated results in Table 3.3 is due to the PA losses.

Fig. 3.15 shows the frequency spectra $X_{\mathrm{p,PB}}(f)$ with the 12 dB PAPR DMT signal of the two-level, non-optimized and optimized three-level transmitters. Note that signals to be transmitted to the antenna require bandpass filtering of the shown signals in the figures. It can be seen that the DRs of the non-optimized and optimized transmitter output signals are comparable, which are around 30 dB. After using delay and gain corrections, NMSEs of the two-level, non-optimized and optimized three-level transmitters are -31.9 dB, -33.2 dB and -29.4 dB, respectively. With the same signal applied to the four-level transmitters, the non-optimized and optimized transmitters give the DRs of around 30 dB as shown in Fig 3.16. In general, as observed from the simulations, DRs of the PA output from non-optimized and optimized transmitters are in the same range for the signal with the same PAPR. NMSEs of the non-optimized and optimized four-level transmitters are -29.4 dB and -30.6 dB, respectively. Linearization techniques such as feed-forward or digital predistortion can be applied to further improve the linearity [6, 91, 95–97]. It can be seen from the figures that the optimized transmitters produce fewer out-of-band spectral components, which improve the coding efficiency and therefore the overall efficiency. Moreover, the use of the optimized transmitters can relax the requirements of the BPF. With more levels, the out-of-band spectral components can be further reduced, however, at the cost of an increased hardware complexity.

Average Efficiency for Average Transmission Power over a Wide Range of Power Levels

The power profile and the generated PDF of the combined signals with different average transmission power levels used in this subsection are shown in Fig. 3.9. The simulated efficiency curves $\eta(A)$ for constant input signals are shown in Fig. 3.17. It can be seen that the first efficiency peak for the four-level case is slightly lower due to the lower PA efficiency for low-power input signals with small threshold values.

Table 3.7 shows the average efficiency for two-level, non-optimized and optimized three-level and four-level transmitters according to (3.71). It is shown that the efficiency of the optimized

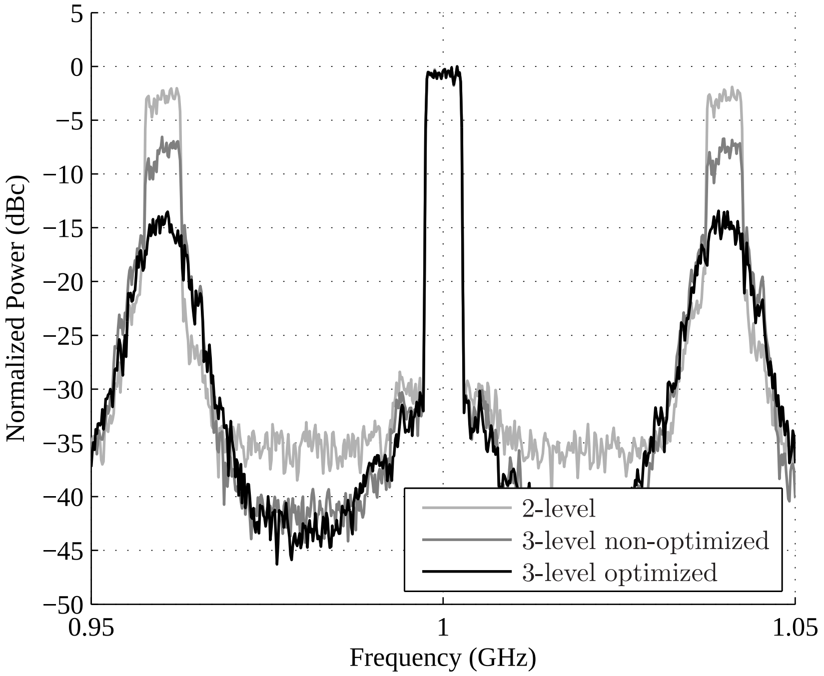

Figure 3.15: Spectra of the two-level, non-optimized and optimized three-level transmitters with the DMT signal of 12 dB PAPR. DRs of the three-level transmitters are in the same range of around 30 dB. The out-of-band spectral content of the optimized transmitter is greatly reduced compared to the two-level and the non-optimized case.

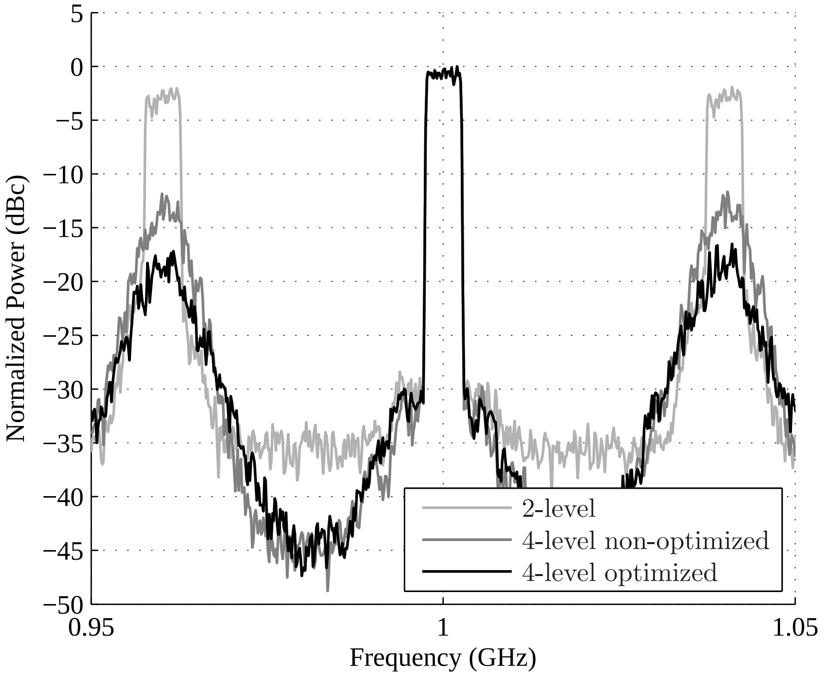

Figure 3.16: Spectra of the non-optimized and optimized four-level transmitters with the DMT signal of 12 dB PAPR. The DRs are in the same range of around 30 dB.

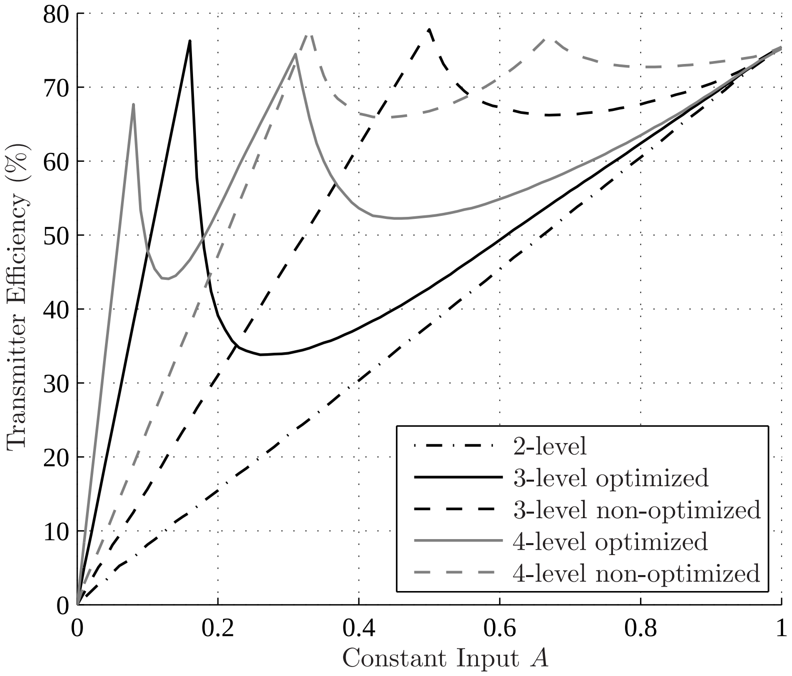

Figure 3.17: Simulated efficiency curves of two-level, three-level and four-level transmitters with constant input signals for the given power profile.

	2-level	3-level (non-optimized)	3-level (optimized)	4-level (non-optimized)	4-level (optimized)
$\overline{\eta}$ (%)	12.0	23.1	38.6	32.6	51.9

Table 3.7: Evaluated average transmitter efficiency for the given power profile.

three-level transmitter gives an improvement of 15.5 percentage points compared to the non-optimized case. Compared to the two-level case, the optimized three-level transmitter achieves an improvement of 26.6 percentage points. With the optimized four-level transmitter, the efficiency improvement is 19.3 percentage points compared to the non-optimized case, and 39.9 percentage points compared to the two-level case. Note that the optimized three-level transmitter outperforms the non-optimized four-level transmitter, where the use of the three-level transmitter will circumvent the design complexity and cost compared to the four-level case.

The optimum threshold values $(V_1, V_2) = (0.08, 0.31)$ will result in a higher impedance seen by the main PA in the low-power operation than in the high-power operation. It is known that too large impedance ratios should be avoided since they will lead to efficiency degradation in power backoff as discussed in [50]. A possible way to mitigate this problem is to obtain a new set of threshold values that gives a higher value of V_1. For example, with $(V_1, V_2) = (0.1, 0.34)$, the obtained average transmitter efficiency is 52.7%, which is higher than the average transmitter efficiency with the optimum threshold values due to a higher transmitter efficiency in the power backoff. If the value of V_1 is further increased, the average transmitter efficiency may decrease due to a lower average coding efficiency because the threshold values are far away from the optimum threshold values. For example, with $(V_1, V_2) = (0.15, 0.4)$ and $(V_1, V_2) = (0.2, 0.45)$, the obtained average efficiencies are 49.6% and 44.8%, respectively, which still have 17 and 12.2 percentage points efficiency improvements compared to the non-optimized cases, 37.6 and 32.8 percentage points efficiency improvements compared to the two-level cases.

3.2.6 Practical Implementation Considerations

From the analysis in Section 3.2.1, Section 3.2.2 and Section 3.2.5, it can be seen that the threshold value has a very important impact on the transmitter design for efficiency enhancement. First, it determines when the auxiliary PA is activated. Accordingly, the coding efficiency and the transmitter efficiency can be evaluated. Second, it determines the impedances seen by PAs and therefore the gain property of the transmitter. The gain fluctuation in burst-mode transmitters can be mitigated by delivering unequal input voltage to each PA at different power operation regions as described in Section 3.2.5. Third, the threshold value determines the transistor periphery ratio of the main PA and the auxiliary PAs [92]. For example, the transistor periphery ratio is $V_1 : (1 - V_1)$ for a three-level case and $V_1V_2 : (1 - V_1)V_2 : (1 - V_2)$ for a four-level case. Note that the use of too large transistor ratios should be avoided since the efficiency in the low-power region would be decreased due to the device parasitics, matching and combining losses [50]. A possible way to mitigate this problem is to penalize small magnitudes and therefore increase the threshold values.

The PA design is also important for burst-mode transmitters. Switched-mode PAs and harmonics-tuned PAs [6], e.g., in Class F mode, can be used to further improve the peak efficiency for constant input signals as well as the average efficiency for statistical signals without degrading the linearity performance. To operate the PA in a highly efficient way, burst-mode operation requires the input matching network to provide a relatively large bandwidth to ensure an approximately rectangular envelope at the transistor gate. The design of such wideband matching network is challenging especially if a high gain is required. Packaged transistors with partly built-in matching networks would be preferred to achieve a large bandwidth as well as a high efficiency [98].

Another important aspect in the optimization is the number of signal paths M used in burst-mode transmitters. On the one hand, as shown in the efficiency analysis in this section, a large M leads to a higher possible average efficiency for statistical signals. On the other hand, a large M results in an increased hardware complexity including the required signal processing, additional PAs and a more complex power combiner. From the analytical and simulation results, optimized transmitters with a small M can achieve a significant improvement over non-optimized transmitters for signals with high PAPRs and signals over a wide range of power levels. They can even achieve a higher efficiency compared to non-optimized transmitters with a larger M as shown in Section 3.2.5 and therefore circumvent the hardware complexity.

3.3 Summary and Discussion

In this chapter, continuous-time PWM based burst-mode RF transmitters have been analyzed. In the first part, the image problem is illustrated when a baseband PWM signal is upconverted to the passband. To deal with the image distortion, spectral analysis of RF burst signals are provided and image distortion mitigation methods are described. By proper choice the PWM frequency f_p, the image peak distortion in TEPWM generated RF burst signals can be avoided. The DEPWM method can be regarded as image distortion mitigation method to reduce the image peak distortion in TEPWM generated RF burst signals. In simulations the image distortion mitigation methods show promising results in image peak distortion reduction evaluated in NMSE and DR. The NMSE is improved by 6.1 dB and 7.5 dB and the DR is slightly increased and decreased by 2.6 dB by the image gap method and the DEPWM method, respectively. Since DEPWM signals are generated without image peak distortions around the wanted signals, and the performance metrics are comparable to those of TEPWM signals with image distortion mitigation, the DEPWM signals have been the focus of investigation in this chapter.

In the second part, power efficiency analysis has been described where efficiency optimization of burst-mode multilevel transmitters has been investigated. For this purpose, detailed mathematical descriptions of the transmitter efficiency utilizing the PA efficiency and the coding efficiency have been presented. The maximum average efficiency can be achieved by changing the threshold values according to input magnitude statistics. The efficiency expressions of the burst-mode multilevel transmitters have been related to those of the Doherty PA and the multistage Doherty PA. It has been shown that functionality of the threshold values in burst-mode multilevel transmitters and the design parameters in (multistage) Doherty PAs is the same. This result makes the presented optimization procedure also suitable for the efficiency optimization of (multistage) Doherty PAs. Simulations of burst-mode multilevel transmitters have been performed to verify the analytical results. For signals with high PAPRs and signals at variable average transmission power levels, the optimized burst-mode multilevel transmitters show a major efficiency improvement compared to the non-optimized and the two-level cases. For example, for the DMT signal with 12 dB PAPR, an improvement of 11.5 percentage points is obtained with the optimized three-level transmitter compared to the non-optimized case. Compared to the two-level case, an improvement of 32.2 percentage points can be achieved. An improvement of 7.6 percentage points can be obtained with the optimized four-level transmitter compared to the non-optimized case, and 42 percentage points compared to the two-level case. An approach is provided to obtain the optimum thresholds and the optimized efficiency, which will allow the designers to estimate and predict the efficiency of the optimized transmitter in an early design stage before great effort is put into the complete design prototype. The increasing need of higher efficiency for signals with high PAPRs and signals at variable average transmission power levels makes the optimized burst-mode multilevel transmitter a promising candidate for future wireless communication networks.

4

Discrete-Time PWM based Burst-Mode RF Transmitters

The advantages of digital circuits have opened opportunities for digitally enhanced analog systems [99]. A digital implementation of the PWM is advantageous. However, the digital realization of PWM can be challenging since an ideal PWM signal is of infinite bandwidth. If the signal is generated digitally at a finite sampling rate, a large amount of distortion is introduced and the signal quality is degraded.

In this chapter, a thorough analysis of discrete-time PWM based burst-mode RF transmitters will be provided. Problems of the discrete-time PWM such as bandwidth, signal quality, and efficiency will be addressed. In digitally generated PWM signals, due to the sampling with finite sampling frequency, the aliasing distortion inherently exists and reduces the wanted signal quality. An aliasing-free PWM method will be presented to limit the number of harmonics in the generated PWM signals and thus eliminate all destructive aliasing distortion.

Amplitude variation is induced onto the amplitude of the AFPWM signals. When driven by such signals, the RF PA is operated over a wider range of power regions. The efficiency provided by the RF PA is reduced. However, we will show that although the PA efficiency is decreased, a higher coding efficiency is able to compensate for the efficiency loss, leading to a transmitter efficiency without degradation. An efficiency-linearity trade-off for AFPWM based burst-mode RF transmitters will be shown according to the chosen number of harmonics in the generated AFPWM signals.

In this chapter you will find the answer to the question: how to make a discrete-time PWM based burst-mode RF transmitter a competent candidate for energy-efficient transmitter architectures.

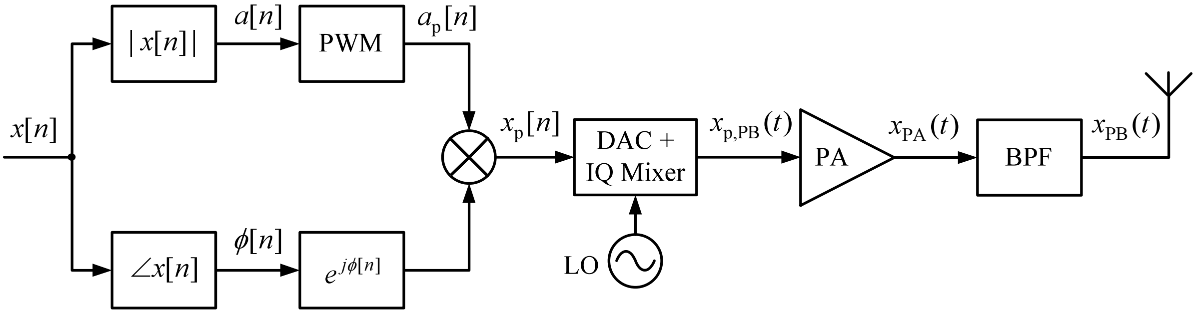

Figure 4.1: Block diagram of a burst-mode two-level RF transmitter architecture with discrete-time PWM process.

4.1 Discrete-Time PWM Process

A block diagram of the burst-mode two-level RF transmitter architecture with discrete-time baseband processing blocks is shown in Figure 4.1. The baseband signal processing is performed digitally. A digital-to-analog converter (DAC) is used to convert digital signals into analog signals. In order to gain insight into the signal characteristics in discrete-time PWM based transmitter architectures, it is necessary to develop the discrete-time equivalent of the continuous-time signals that have been derived before, both in time domain and frequency domain.

A discrete-time signal can often arise from periodic sampling of a continuous-time signal [76]. The value of discrete-time signal at index n, is equal to the value of the continuous-time signal $x(t)$ at time nT_s,

$$x[n] = x(nT_\mathrm{s}) \tag{4.1}$$

where T_s is the sampling period and $f_\mathrm{s} = 1/T_\mathrm{s}$ is the sampling frequency. The discrete-time signals corresponding to $a(t)$ and $\phi(t)$ can be expressed as $a[n]$ and $\phi[n]$, respectively.

A comparator based discrete-time PW modulator is shown in Figure 4.2. A discrete-time modulating signal $a[n]$ is compared with a reference signal $r[n]$ and outputs a discrete-time PWM signal $a_\mathrm{p}[n]$. The triangular waveform is considered as the reference signal. Thus, a DEPWM signal is generated. Since both DEPWM signals have similar properties, only one of the DEPWM processes and the resulting signals will be described.

The discrete-time signals in the baseband processing can be described based on the analytical results obtained for continuous-time signals given in Section 2.3. According to (2.28), the discrete-time PWM signal $a_\mathrm{p}[n]$ is given by

$$a_\mathrm{p}[n]= a[n] + \sum_{k=1}^{\infty} \frac{2}{\pi k} \sin(\pi k a[n]) \cos(2\pi k f_\mathrm{p} n T_\mathrm{s}). \tag{4.2}$$

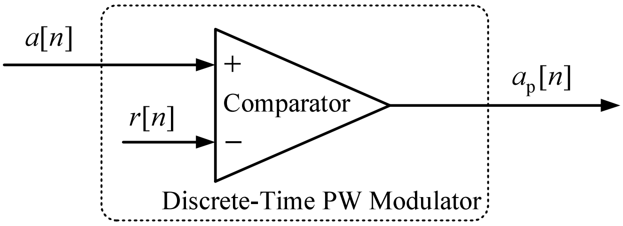

Figure 4.2: Block diagram of a comparator based discrete-time PW modulator.

With the phase information $e^{j\phi[n]}$, the phase modulated signal $x_{\mathrm{p}}[n]$ can be expressed by

$$x_{\mathrm{p}}[n]= x[n] + \sum_{k=1}^{\infty} x_k[n] \tag{4.3}$$

where $x_k[n]$ is given by

$$x_k[n] = \frac{2}{\pi k} \sin(\pi k a[n]) \cos(2\pi k f_{\mathrm{p}} n T_{\mathrm{s}}) e^{j\phi[n]}. \tag{4.4}$$

The frequency-domain expression of the PWM signal $a_{\mathrm{p}}[n]$ can be derived by using the discrete-time Fourier transform (DTFT), which gives

$$\tilde{A}_{\mathrm{p}}(f)= \frac{1}{T_{\mathrm{s}}} \sum_{\zeta=-\infty}^{\infty} A_{\mathrm{p}}(f - \zeta f_{\mathrm{s}}) \tag{4.5}$$

where the signal $A_{\mathrm{p}}(f)$ is the Fourier transform of the continuous-time PWM signal $a_{\mathrm{p}}(t)$ and is given in (2.31). The frequency-domain expression of the phase modulated signal $x_{\mathrm{p}}(t)$ can be derived as

$$\tilde{X}_{\mathrm{p}}(f)= \frac{1}{T_{\mathrm{s}}} \sum_{\zeta=-\infty}^{\infty} X_{\mathrm{p}}(f - \zeta f_{\mathrm{s}}) \tag{4.6}$$

where $X_{\mathrm{p}}(f)$ is given in (2.33) which is the Fourier transform of the phase modulated signal $x_{\mathrm{p}}(t)$. Sampling of continuous-time signals causes spectral copies of the continuous-time signal at each integer multiple of the sampling frequency ζf_{s} as can be seen in (4.5) and (4.6). Since the continuous-time PWM signal and the phase modulated PWM signal are of infinite bandwidth, the spectral copies overlap with each other and induce aliasing distortion to the original continuous-time signal [76]. In consequence, the in-band and out-of band signal quality of the discrete-time PWM signals are degraded.

A discrete-time PWM process is illustrated in Figure 4.3. Since both of the discrete-time signals $a[n]$ and $r[n]$ are only defined at integer values of n, the trailing edges and the leading edges of the resulting discrete-time PWM signal $a_{\mathrm{p}}[n]$ only occur at the time instances nT_{s}. When compared to the continuous-time PWM signal $a_{\mathrm{p}}(t)$, which is depicted in grey line, the switching time instants of the trailing and leading edges in $a_{\mathrm{p}}[n]$ and $a_{\mathrm{p}}(t)$ are most likely

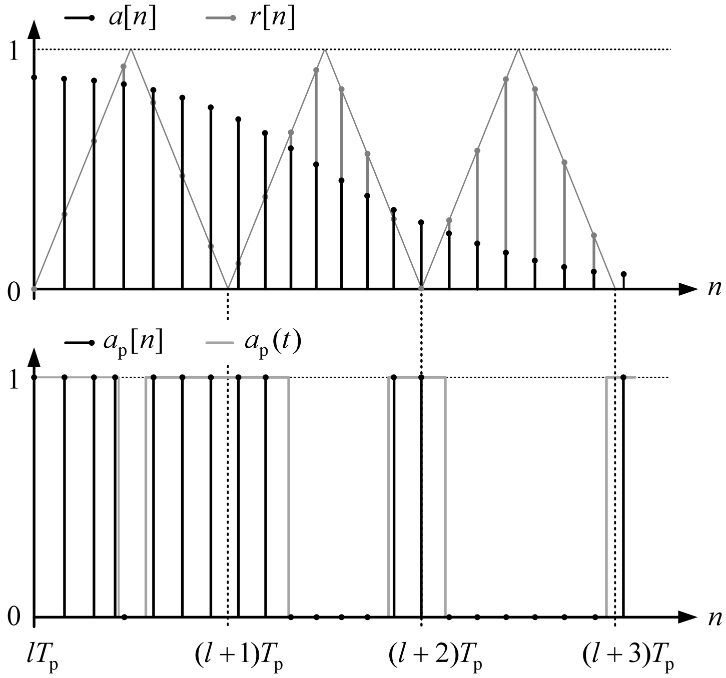

Figure 4.3: Time-domain illustration of a discrete-time PWM process.

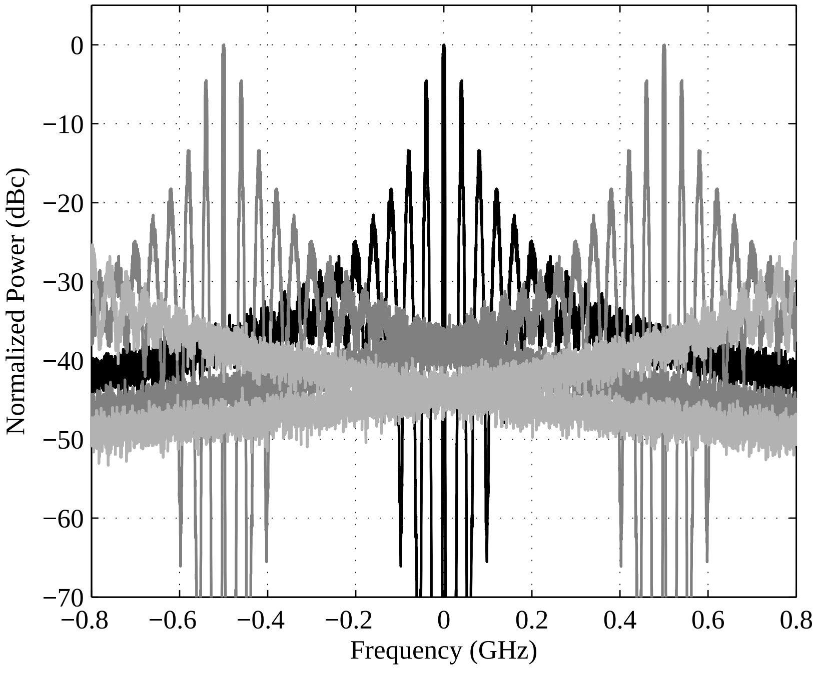

Figure 4.4: Frequency-domain illustration of a discrete-time PWM signal.

not the same. The mismatch of the switching time instants induce the aliasing distortion into the discrete-time PWM signal $a_{\mathrm{p}}[n]$, which reduces the in-band and out-of-band signal quality. Frequency-domain illustration is shown in Figure 4.4 since the concept of the aliasing distortion is most easily understood in the frequency domain. The input signal $x[n]$ is a complex DMT signal with $B_{\mathrm{s}} = 5$ MHz bandwidth. A PWM frequency $f_{\mathrm{p}} = 40$ MHz and a sampling frequency $f_{\mathrm{s}} = 500$ MHz are used. The spectrum of the original continuous-time phase modulated PWM signal is depicted in black line and the spectral copies of the original signal are illustrated in grey lines. The spectral copies and the spectrum of the original signal are added together to form the spectrum of the discrete-time PWM signal. It is shown that the aliasing distortion is introduced to the signal in the band-of-interest, i.e., 5 MHz around the zero frequency, which reduces the in-band and out-of band signal quality such as NMSE and DR.

Note that the aliasing in the discrete-time PWM signal cannot be eliminated by commonly used anti-aliasing filter. The reason is that when generated digitally, the PWM signal $a_{\mathrm{p}}[n]$ is already distorted by aliasing and a filter cannot remove it. Hence, aliasing is generated inherently within the discrete-time PWM process. Although by using a higher sampling frequency f_{s}, the amount of the aliasing distortion can be reduced, however, it is desirable to keep the sampling frequency f_{s} as low as possible towards a feasible hardware realization and a reduced power consumption. In the following, it is shown how to limit the spectral components that are generated by the PWM process. Based on the analysis presented before, the representation of the PWM signal such as in (4.2) can be slightly modified to limit the generated spectral content and therefore reduces the signal bandwidth.

4.2 Digital Aliasing-Free PWM

4.2.1 Digital Aliasing-Free PWM Analysis

According to (4.5) and (2.31), the frequency-domain expression of the digital aliasing-free PWM (AFPWM) signal is given by

$$\begin{aligned}\tilde{A}_{\mathrm{p}}(f) &= \frac{1}{T_{\mathrm{s}}} \sum_{\zeta=-\infty}^{\infty} A_{\mathrm{p}}(f - \zeta f_{\mathrm{s}}) \\ &= \frac{1}{T_{\mathrm{s}}} \sum_{\zeta=-\infty}^{\infty} A(f - \zeta f_{\mathrm{s}}) + \frac{1}{T_{\mathrm{s}}} \sum_{\zeta=-\infty}^{\infty} \sum_{k=1}^{K} A_k(f - \zeta f_{\mathrm{s}}) \qquad (4.7)\end{aligned}$$

where $A_k(f)$ is given by

$$A_k(f) = \sum_{r=0}^{\infty} \frac{(j\pi k)^{2r}}{(2r+1)!} \left[A_{2r+1}(f + kf_{\mathrm{p}}) + A_{2r+1}(f - kf_{\mathrm{p}})\right] \qquad (4.8)$$

The number of harmonics has been limited to a finite integer K and therefore the bandwidth of the PWM signal is limited. The same procedure can be applied to the phase modulated signal.

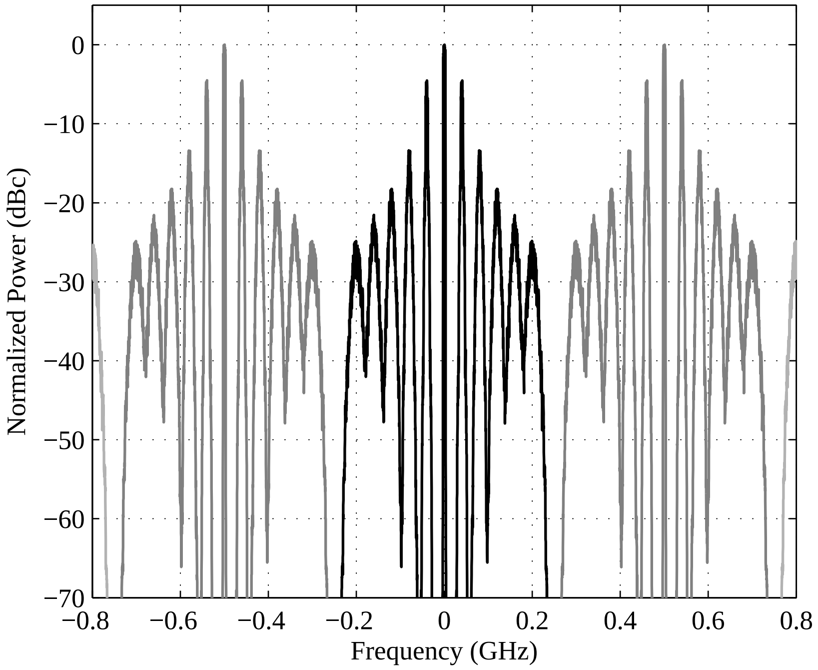

Figure 4.5: Frequency-domain illustration of an AFPWM signal.

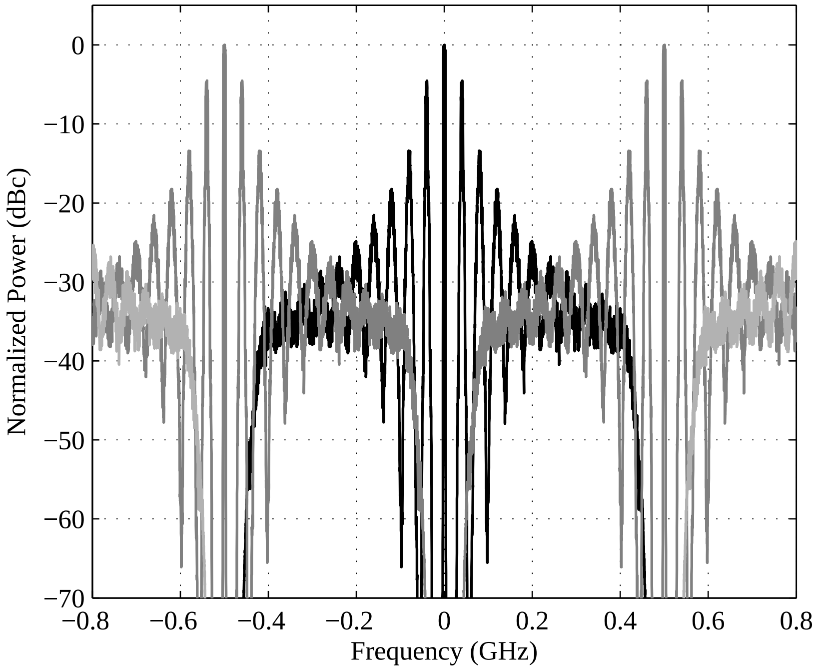

Figure 4.6: Frequency-domain illustration of the AFPWM signal with a higher number of harmonics compared to Figure 4.5. More harmonics are included to mitigate the amplitude variation in the time-domain signal.

The frequency-domain expression of the digital AFPWM signal with the phase information is given by

$$\begin{aligned}\tilde{X}_{\mathrm{p}}(f) &= \frac{1}{T_{\mathrm{s}}}\sum_{\zeta=-\infty}^{\infty} X_{\mathrm{p}}(f-\zeta f_{\mathrm{s}}) \\ &= \frac{1}{T_{\mathrm{s}}}\sum_{\zeta=-\infty}^{\infty} X(f-\zeta f_{\mathrm{s}}) + \frac{1}{T_{\mathrm{s}}}\sum_{\zeta=-\infty}^{\infty}\sum_{k=1}^{K} X_k(f-\zeta f_{\mathrm{s}})\end{aligned} \tag{4.9}$$

where $X_k(f)$ is given in (2.34). Since only the number of harmonics is changed in the equations, the time-domain signals can also be described according to the results obtained before in (2.28) and (2.29). The time-domain expression of the digital AFPWM signal is given by

$$a_{\mathrm{p}}[n] = a[n] + \sum_{k=1}^{K} a_k[n] \tag{4.10}$$

where $a_k[n]$ is given by

$$a_k[n] = \frac{2}{\pi k}\sin(\pi k a[n])\cos(2\pi k f_{\mathrm{p}} n T_{\mathrm{s}}). \tag{4.11}$$

The phase modulated signal $x_{\mathrm{p}}[n]$ can be expressed by

$$x_{\mathrm{p}}[n] = x[n] + \sum_{k=1}^{K} x_k[n] \tag{4.12}$$

where $x_k[n]$ is given by (4.4).

The spectrum of the phase modulated signal $x_{\mathrm{p}}[n]$ is illustrated in Figure 4.5. It can be seen that the PWM signal contains a finite number of harmonics and there exists no aliasing-distortion between spectral copies in the observation range. The digital AFPWM method also eliminates the image distortion that described in Section 3.1.

Limiting the number of harmonics in the generated PWM signals is a simple and effective method. But a side effect comes along with this method. A bandlimited PWM signal introduces ripples in the ideal switching signal amplitude, which requires a multi-bit DAC to convert sufficient amplitude information from digital domain to analog domain. Also the limited bandwidth changes the switching properties of the PWM signals. The PWM signals no longer hold ideal switching properties which only have “on” and “off” states. If the RF PA is driven into saturation, clipping of the signal amplitude can happen. The amplitude variation together with the RF PA nonlinearity result in nonlinear distortion on the PA output signal [65].

To reduce the amplitude variation, spectral aliasing might be accepted as long as there is no aliasing-distortion present in the wanted signal located around the zero frequency. A spectral illustration is shown in Figure 4.6. By setting the number of harmonics K to an appropriate higher value, proper amount of spectral aliasing is introduced. The number of harmonics K can be chosen as the highest possible integer that does not induce aliasing-distortion to the wanted signal around the zero frequency.

4.2.2 Simulation and Measurement Results

Simulations and measurements are performed to evaluate the performance of the AFPWM method. The baseband input signal $x[n]$ is generated by a DMT signal with a bandwidth of $B_s = 5\,\mathrm{MHz}$ and a PAPR of 7 dB. The sampling frequency is set to $f_\mathrm{s} = 500\,\mathrm{MHz}$ and the tone spacing is set to $\Delta f = 20\,\mathrm{KHz}$. The PWM frequency f_p is set to 40 MHz and the carrier frequency f_c is set to 900 MHz.

Simulation Results

Simulations are carried out in Matlab and Simulink environment. Figure 4.7 shows a spectral comparison of the frequency-domain signals of a conventional digital PWM signal and the signal generated by the AFPWM method. The conventional digital PWM signal is generated by comparing the modulating signal $a[n]$ with the triangular reference signal $r[n]$. As described before, the conventional digital PWM signal includes every order of harmonic. The aliasing distortion due to the infinite signal bandwidth decreases the quality of the wanted signal in the band of interest in term of NMSE. The grey line plots the spectrum of the conventional digital PWM signal which has a DR of around 30 dB while the DR of the AFPWM signal is more than 80 dB. The number of harmonics K of the AFPWM signal is set to $K = 8$ because it is an appropriate number that induces negligible aliasing distortion to the wanted signal while keeping tolerable time-domain amplitude variation. The time-domain PWM signals are shown in Figure 4.8, from where the amplitude variation of AFPWM signal can be observed. Because of this amplitude variation, the realization of AFPWM method requires a multi-bit DAC to convert sufficient amplitude information to analog domain. The amplitude variation together with the RF PA nonlinearity causes nonlinear distortion on the PA output signal.

Measurement Results

Measurements are carried out to verify the theoretical and the simulation results. A block diagram of the measurement setup is shown in Figure 4.9. The PWM signal is generated in Matlab and Simulink with a PWM frequency of $f_\mathrm{p} = 40\,\mathrm{MHz}$ and a sampling frequency of $f_\mathrm{s} = 500\,\mathrm{MHz}$. The generated PWM signal is then sent to a pattern generator FPGA board which is connected to a dual-channel 16 bit, 1 GSPS DAC evaluation module. The I and Q parts of the PWM signal are converted to analog domain by the DAC with a sampling frequency of 500 MHz, respectively. The DAC output is transformer coupled, where the transformer is designed for a frequency range of 9 MHz-625 MHz [100]. Thus the baseband PWM signal is digitally modulated to an intermediate frequency in Matlab and Simulink before it is fed to the pattern generator and DAC evaluation module. Then the DAC output is upconverted to the carrier frequency of $f_c = 900\,\mathrm{MHz}$ by a vector signal generator used as an IQ-mixer, where the suppression of the unwanted image up to ±10 MHz is 60 dB and up to ±60 MHz is 48 dB [101].

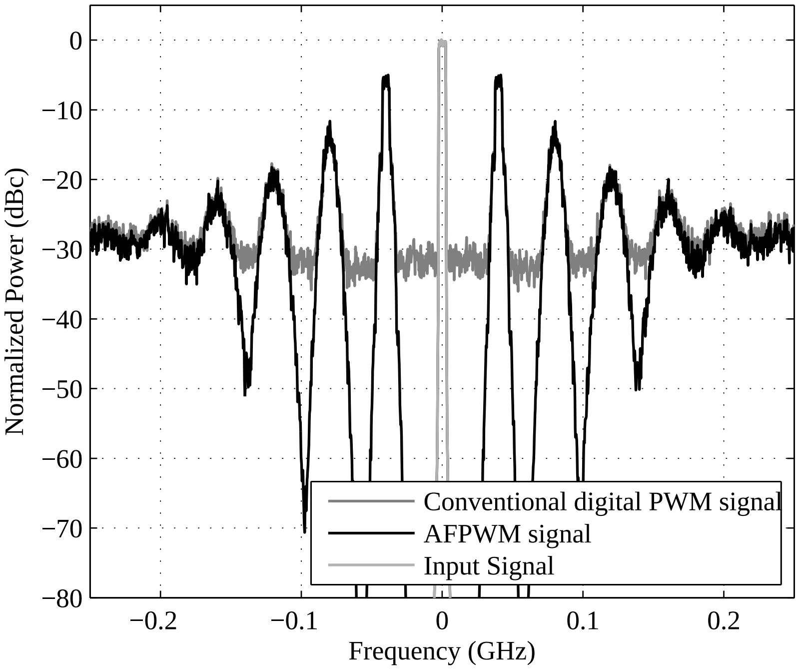

Figure 4.7: A comparison of the frequency-domain conventional digitally generated PWM signal and the AFPWM signal.

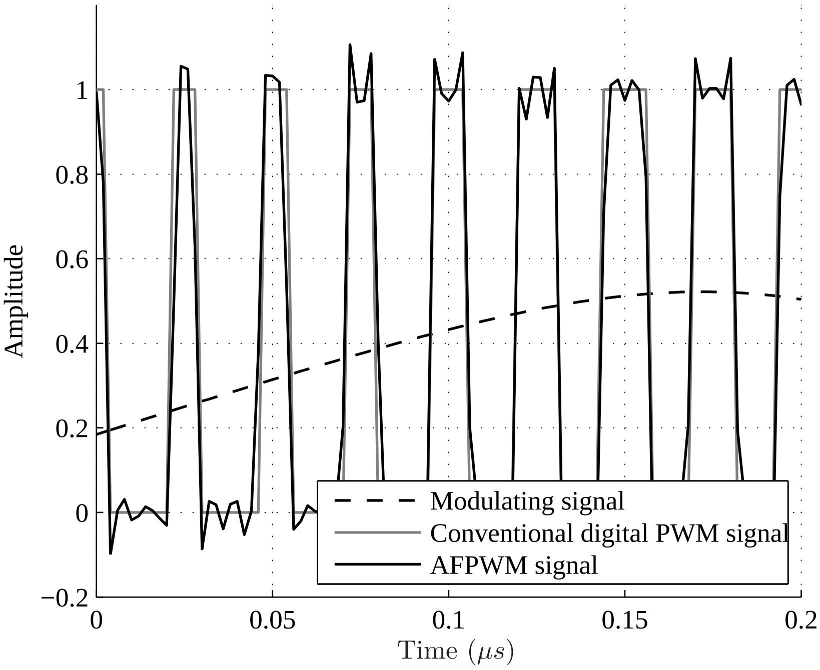

Figure 4.8: A comparison of the time-domain conventional digitally generated PWM signal and the AFPWM signal.

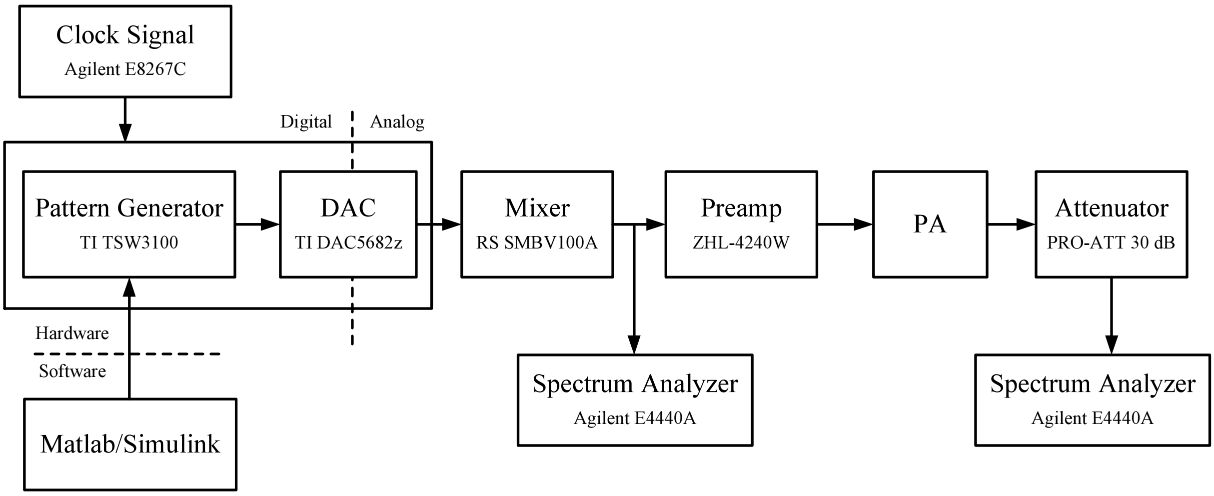

Figure 4.9: Measurement setup.

The RF burst signal $x_{\mathrm{p,PB}}(t)$ at the mixer output is first connected to the spectrum analyzer and the performance of RF burst signals generated with different methods are evaluated.

Furthermore, in order to evaluate the performance of the AFPWM signal applied to an RF PA, a linear Class-AB RF PA is included in the demonstrator. After the mixer, the RF burst signal is first pre-amplified, and then amplified by the Class-AB RF PA. The RF PA is an 8 W, 1 GHz Class-AB PA with transmission line based input/output matching, fabricated on a Rogers 4530B substrate with an Infineon 30 V laterally diffused metal oxide semiconductor (LDMOS) transistor (engineering sample). The basic properties of the PA are a power added efficiency (PAE) of more than 72% over 200 MHz bandwidth, a gain of 18 dB over 200 MHz bandwidth, and peak power of 8 W over 125 MHz bandwidth, all at $f_c = 900\,\mathrm{MHz}$ center frequency [23]. The utilized peak output power is slightly below the P-1 dB point of the PA to allow a certain amount of amplitude variations [65]. The amplified RF burst signal $x_{\mathrm{PA}}(t)$ is attenuated first and then measured by the spectrum analyzer.

Figure 4.10 and Figure 4.11 show the measured RF burst signals $x_{\mathrm{p,PB}}(t)$ generated by the conventional digital PWM and the AFPWM method, respectively. It can be seen that with the AFPWM method, the achieved DR of the PWM signal is around 58 dB, which has an improvement of more than 30 dB compared to the PWM signal generated with the conventional digital PWM method, which has a DR around 27 dB.

Figure 4.12 and Figure 4.13 show the measured amplified RF burst signal $x_{\mathrm{PA}}(t)$ after the attenuator. It can be seen that with conventional digital PWM method, the DR stays approximately the same as the RF burst signal before the amplification. Though the matching network and PA itself may include nonlinear distortion to the RF burst signal, it is likely that the nonlinearity is not observable in this case. However, on the other hand, the matching network and the PA induces a great amount of nonlinear distortion to the RF burst signal generated by the AFPWM method. As shown in Figure 4.13, the DR of the amplified RF burst signal is around 34 dB. The nonlinear distortion produced is likely due the amplitude variation together with the

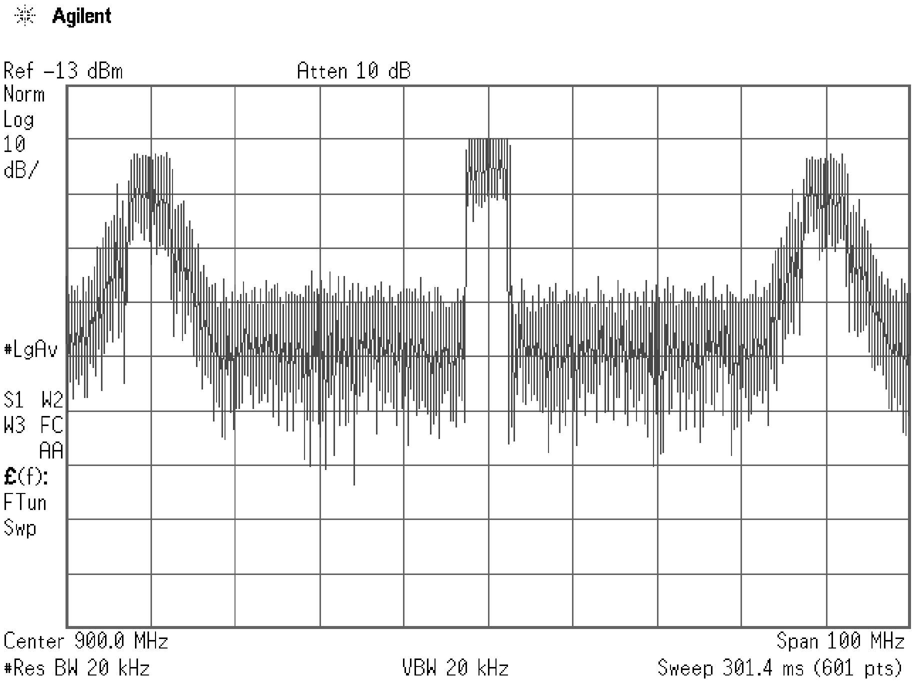

Figure 4.10: Measurement result of the RF burst signal $x_{\mathrm{p,PB}}(t)$ generated from the conventional digital PWM method.

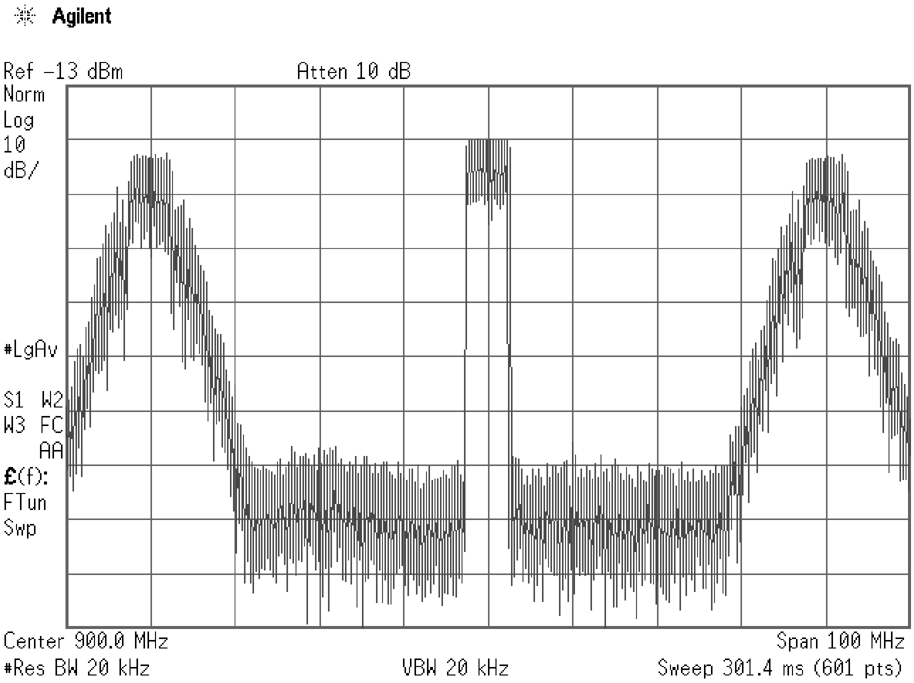

Figure 4.11: Measurement result of the RF burst signal $x_{\mathrm{p,PB}}(t)$ generated from the AFPWM method.

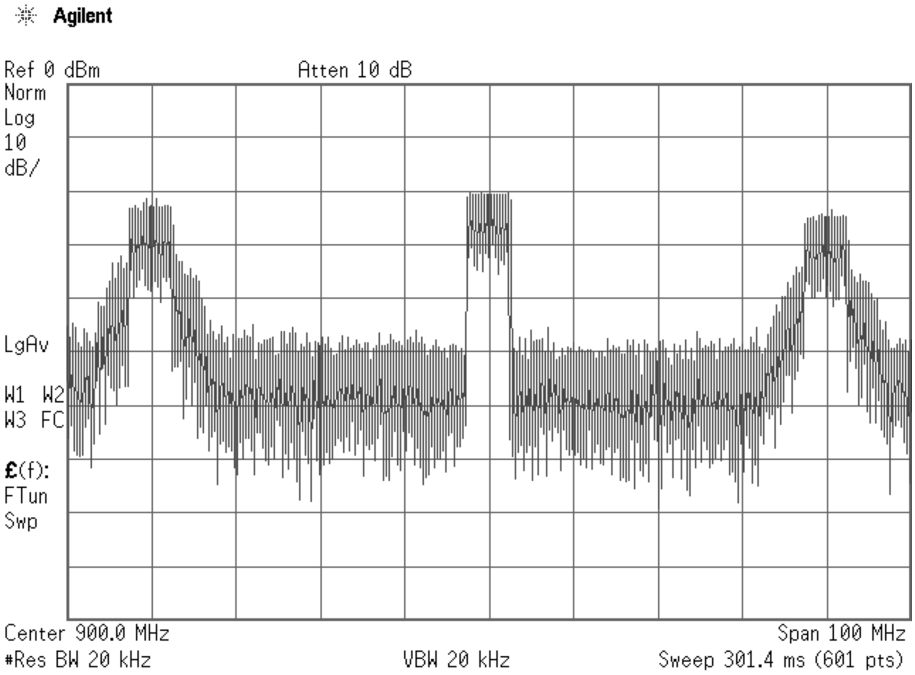

Figure 4.12: Measurement result of the amplified RF burst signal $x_{\mathrm{PA}}(t)$ generated from the conventional digital PWM method.

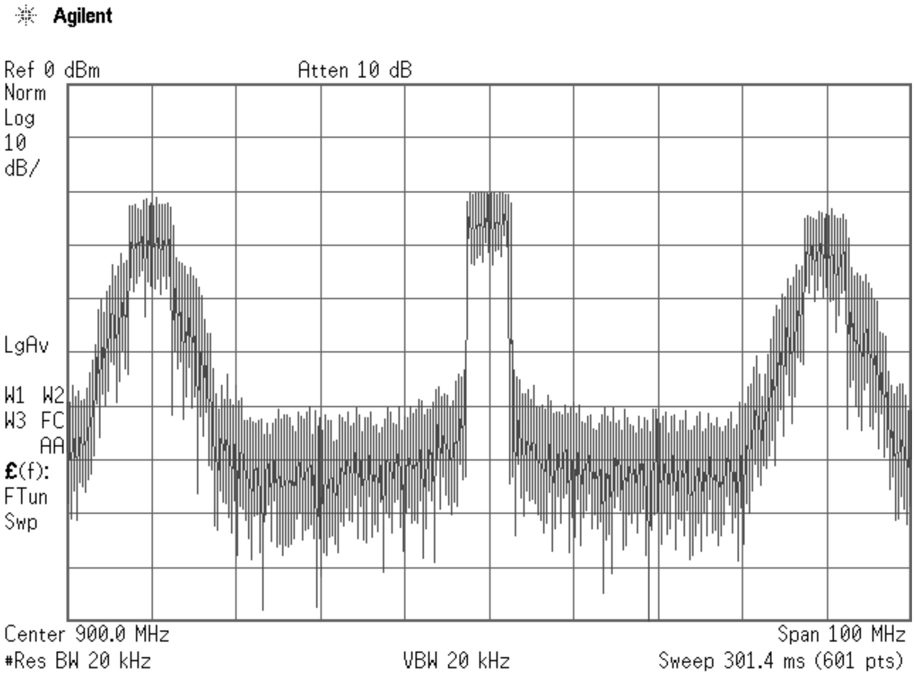

Figure 4.13: Measurement result of the amplified RF burst signal $x_{\mathrm{PA}}(t)$ generated from the AFPWM method.

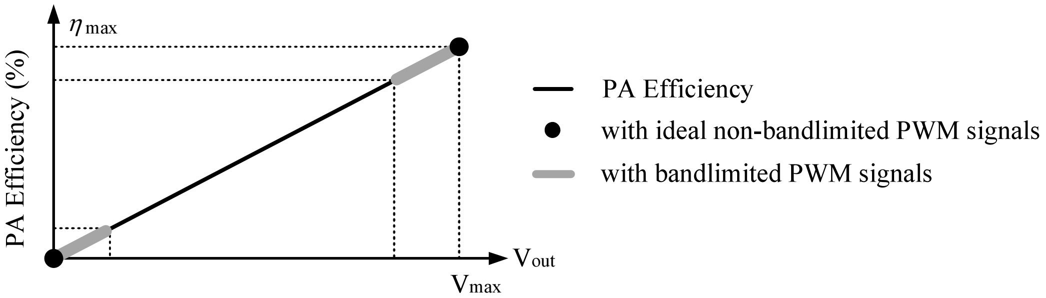

Figure 4.14: Illustration of applied input signal regions and the PA efficiency.

PA nonlinearity. Nevertheless, with the AFPWM method, the DR of the amplified RF burst is still improved by 7 dB compared to the case with conventional digital PWM method.

4.3 Power Efficiency Analysis

The burst-mode concept is proposed for its potentially high PA efficiency for signals with high PAPR. This is based on the requirement that the envelope of the signal driving the PA only consists of two levels or states, “on” and “off”, to produce the maximum efficiency when the PA is activated. Since an AFPWM signal is bandlimited and it intrinsically introduces ripples in the ideal switching signal amplitude as shown in Figure 4.8, the resulting PA efficiency might be decreased. However, the transmitter efficiency, which not only depends on the PA efficiency but also the coding efficiency, is of interest. It is important to investigate the transmitter efficiency, especially the coding efficiency, to seek the viability of the described AFPWM method.

The illustration of the applied input signal regions and the output voltage versus the PA efficiency is shown in Figure 4.14. With the AFPWM signal, the PA is operated over a slightly wider range of efficiency regions, depicted by the grey lines, instead of operating just at saturation and in cut-off as in the ideal burst-mode operation with non-bandlimited PWM signals, depicted by black solid circle. The large amplitude variation results in PA efficiency reduction. However, the degraded PA efficiency does not necessarily result in a degraded transmitter efficiency because there is another contributing factor, the coding efficiency, needs to be considered. If the coding efficiency is higher and can compensate for the PA efficiency loss, the transmitter efficiency will not suffer from degradation. The bias points of the PA operation for the ideal and bandlimited cases are not shown in the figure, but should be considered. For example, when a Class B PA is used for the ideal non-bandlimited PWM signal, the PA should be biased into Class AB mode when bandlimited PWM signal is applied. At the same time, the utilized peak output power should be slightly lower to allow a certain amount of amplitude variation [65].

In the following, the coding efficiency of AFPWM signals with different harmonics is described mathematically. Then measurements are performed and the measurement results are used to verify the simulation results and show that the transmitter efficiency is not degraded by using the AFPWM method.

4.3.1 Coding Efficiency for Constant Input Signals

According to the definition of the coding efficiency in Section 2.2, similar to the coding efficiency defined for continuous-time constant input signals in (4.13), the coding efficiency for constant input signal $x[n] = A, A \in [0, 1]$ can be expressed by

$$\eta_{\mathrm{c}}(A) = \begin{cases} \dfrac{P_{\mathrm{s}}(A)}{P_{\mathrm{tot}}(A)}, & \text{for } |x[n]| = A, \quad A \in (0, 1] \\ 0, & \text{for } |x[n]| = A, \quad A = 0. \end{cases} \tag{4.13}$$

According to (3.25) and (3.26), the signal power $P_s(A)$ can be described by

$$P_s(A) = \frac{A^2}{2} \tag{4.14}$$

with a normalized load value of $1\,\Omega$. According to (4.12) and (4.4), the phase modulated baseband PWM signal $x_{\mathrm{p,DE}_1}[n]$ with constant input signal $x[n] = A$ is given by

$$x_{\mathrm{p,DE}_1}[n] = A + \sum_{k=1}^{K} x_{k,\mathrm{DE}_1}[n] \tag{4.15}$$

where $x_{k,\mathrm{DE}_1}[n]$ with constant input signal $x[n] = A$ is given by

$$x_{k,\mathrm{DE}_1}[n] = \frac{2}{\pi k} \sin(\pi k A) \cos(2\pi k f_{\mathrm{p}} n T_{\mathrm{s}}). \tag{4.16}$$

The phase information $e^{j\phi[n]}$ in this case is a constant of 1. Since the PWM signal $x_{\mathrm{p,DE}_1}(t)$ is the baseband equivalent of the ideally amplified RF burst signal $x_{\mathrm{p,PB}}(t)$, the passband signal $x_{\mathrm{PA}}(t)$ can be described by

$$x_{\mathrm{PA}}(t) = \left(A + \sum_{k=1}^{K} x_{k,\mathrm{DE}_1}(t) \right) \cos(2\pi f_{\mathrm{c}} t). \tag{4.17}$$

where $x_{k,\mathrm{DE}_1}(t)$ with constant input signal $x[n] = A$ is given by

$$x_{k,\mathrm{DE}_1}(t) = \frac{2}{\pi k} \sin(\pi k A) \cos(2\pi k f_{\mathrm{p}} t). \tag{4.18}$$

By using the trigonometric identities and the multinomial theorem, with $f_c \gg f_p$, according to (4.17) and (4.18), the total power of the amplified RF burst signal $x_{\mathrm{PA}}(t)$ with constant input signal $x[n] = A$ can be closely approximated by

$$\begin{aligned} P_{\mathrm{tot}}(A, K) &= \frac{1}{T_{\mathrm{p}}} \int_0^{T_{\mathrm{p}}} x_{\mathrm{PA}}^2(t) dt \\ &= \frac{1}{2T_{\mathrm{p}}} \int_0^{T_{\mathrm{p}}} \left[\left(A + \sum_{k=1}^{K} a_k(t) \right)^2 + \left(A + \sum_{k=1}^{K} a_k(t) \right)^2 \cos(4\pi f_c t) \right] dt \end{aligned}$$

$$
\begin{aligned}
&\approx \frac{1}{2T_p}\int_0^{T_p}\left(A+\sum_{k=1}^{K}a_k(t)\right)^2 dt\\
&=\frac{1}{2T_p}\int_0^{T_p}\left(A^2+\sum_{k=1}^{K}a_k^2(t)\right) dt\\
&=\frac{A^2}{2}\left(1+2\sum_{k=1}^{K}\operatorname{sinc}^2(kA)\right)
\end{aligned}
\tag{4.19}
$$

where

$$
\operatorname{sinc}(kA)=\frac{\sin(\pi kA)}{\pi kA} \tag{4.20}
$$

is used. Therefore, according to (4.13), (4.14) and (4.19), the coding efficiency for constant input signal $x[n]=A$ with K harmonics in the generated PWM signals is given by

$$
\eta_{\mathrm{c}}(A,K)=\begin{cases}\dfrac{1}{1+2\sum_{k=1}^{K}\operatorname{sinc}^2(kA)}, & A\in(0,1]\\ 0, & A=0.\end{cases} \tag{4.21}
$$

Figure 4.15(a) shows the coding efficiency $\eta_c(A,K)$ for constant input signal $x[n]=A$ with different numbers of harmonics K. Figure 4.15(b) depicts an example with $A=0.5$. Note that for $A=0.5$, the coding efficiency $\eta_c(A,K)$ in (4.21) for an even K is the same as for the odd $(K-1)$, because the even harmonics are located at the zeros of the spectral envelope of the generated PWM signal. It can be seen from Figure 4.15 that, for a fixed K, the coding efficiency increases as the input A increases. The upper and lower bounds for this case are

$$
\eta_{\mathrm{c}}(A=1,K)=1 \quad \text{and} \quad \eta_{\mathrm{c}}(A=0,K)=0. \tag{4.22}
$$

For a certain A, the coding efficiency decreases as K increases, where the lower bound of the coding efficiency can be obtained by $K\to\infty$, i.e., with the ideal non-bandlimited PWM [79], and the upper bound is given by $K\to 0$, i.e., without PWM. With $K\to\infty$, the coding efficiency can be obtained according to (3.29). Hence, the lower bound and the upper bound of the coding efficiency with K harmonics are given by

$$
\eta_{\mathrm{c}}(A,K=\infty)=A \quad \text{and} \quad \eta_{\mathrm{c}}(A,K=0)=1. \tag{4.23}
$$

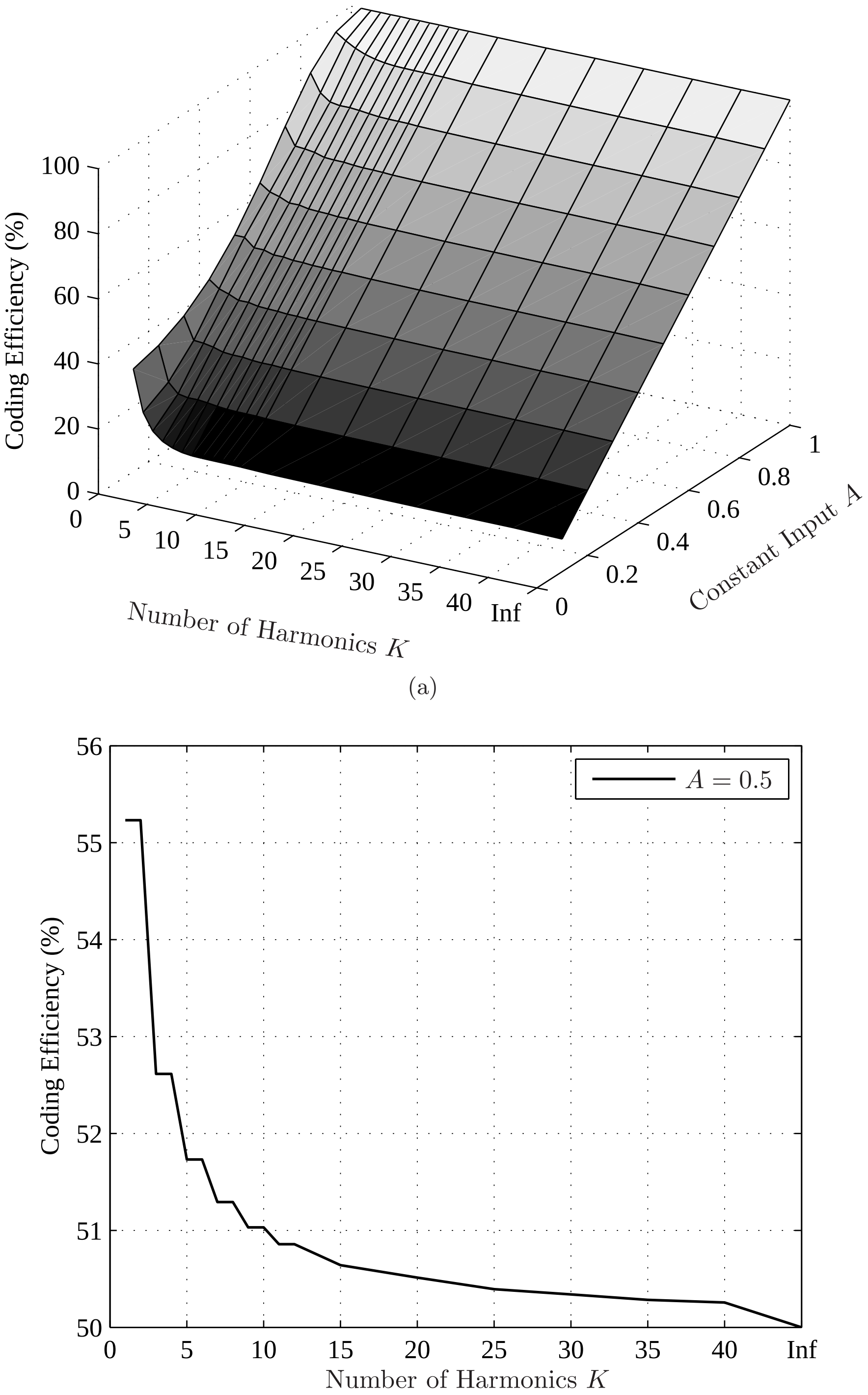

(a)

(b)

Figure 4.15: (a) Coding efficiency $\eta_c(A, K)$ as a function of the constant input $x[n] = A$ and the number of harmonics K. (b) The example with $A = 0.5$.

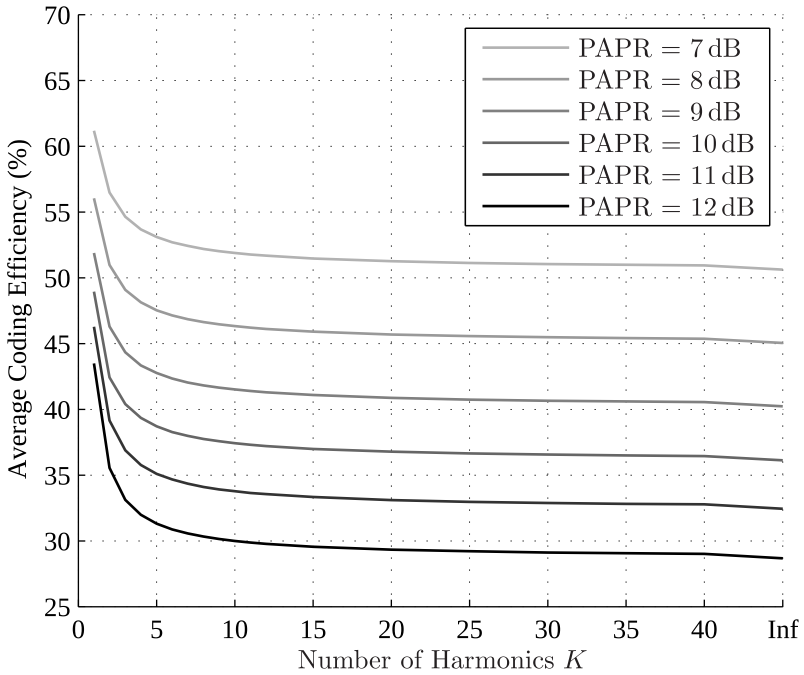

Figure 4.16: Average coding efficiency $\overline{\eta}_c(K)$ for DMT signals with different PAPRs and different numbers of harmonics K.

4.3.2 Average Coding Efficiency for Arbitrary Input Signals

The average coding efficiency is defined as the ratio of the average transmission signal power to the average total power of the amplified RF burst signal

$$\overline{\eta}_c(K)= \frac{\frac{1}{N}\sum_{n=1}^{N} A^2 f_a(A)}{\frac{1}{N}\sum_{n=1}^{N} \frac{A^2}{\eta_c(A,K)} f_a(A)} \tag{4.24}$$

where N is the number of samples and $f_a(A)$ describes the PDF of the input magnitude. The term $\eta_c(A,K)$ represents the coding efficiency for constant input signal $x[n]=A$ with different numbers of harmonics K given in (4.21).

Figure 4.16 shows the average coding efficiency $\overline{\eta}_c(K)$ of DMT signals with different PAPRs and different numbers of harmonics K. For a certain PAPR, the average coding efficiency decreases as K increases. The lower bound and the upper bound can also be obtained by $K \to \infty$ and $K \to 0$, respectively. The lower bound is also with the ideally generated non-bandlimited PWM signals.

Although the coding efficiency is higher for a smaller number of harmonics K, the signal quality after the amplification might be deteriorated. With a smaller K, there will be stronger amplitude variation, which in combination with the PA nonlinearity, leads to more nonlinear distortion on the output signals [65]. Hence, a sufficiently large K is needed to reduce the amplitude variation and therefore obtain an acceptable linearity. Also, for $K = 0$, the PA is operated in linear mode where the average PA efficiencty is very low. In contrast, the coding efficiency, which is a measure of the transmitter efficiency, decreases as K increases. This efficiency-linearity trade-off requires the proper choice of K. This trade-off will be demonstrated through measurements.

4.3.3 Measurement Results

Measurements are carried out to verify the efficiency performance of AFPWM signals. The coding efficiency, the PA efficiency as well as the transmitter efficiency are measured and analyzed with different test signals.

Measurement Setup

The block diagram of the measurement setup is similar to the one shown in Figure 4.9. The difference is that the RS ZVL3 is used in spectrum analyzer mode to measure the signal power and the adjacent channel power ratio (ACPR). The efficiency performance is evaluated after the attenuator. The other devices and analog components like the DAC, the mixer and the PA are the same as used in the measurement setup in Section 4.2.2.

The general test settings are as follows: constant input signal $x[n] = A, A \in [0, 1]$ with a step size of 0.1 is used. DMT signals of 5 MHz complex bandwidth and PAPR of $7 - 12\,\mathrm{dB}$ are used for the average efficiency test. The PWM signal is generated in Matlab and Simulink with a sampling frequency of $f_s = 500\,\mathrm{MHz}$ and a PWM frequency of 40.1 MHz which is slightly different from $f_\mathrm{p} = 40\,\mathrm{MHz}$ to avoid harmonics exactly overlapping the signal in the band of interest especially for the constant input signal test. The number of harmonics K is set to $K \in [1, 40]$. The conventional generated digital PWM signal, by comparing the modulating signal with the reference signal, includes every order of harmonic and is denoted with $K = \mathrm{Inf}$.

Efficiency Metrics for Measurement

The measured coding efficiency η_c^m, the PA efficiency η_PA^m and the transmitter efficiency η^m for constant input signals are evaluated by

$$\begin{aligned}\eta_\mathrm{c}^m(A,K) &= \frac{P_\mathrm{s}^m(A)}{P_\mathrm{tot}^m(A,K)}\\ \eta_\mathrm{PA}^m(A,K) &= \frac{P_\mathrm{tot}^m(A,K)}{P_\mathrm{dc}^m(A,K)}\\ \eta^m(A,K) &= \frac{P_\mathrm{s}^m(A)}{P_\mathrm{dc}^m(A,K)}\end{aligned} \tag{4.25}$$

and for DMT signals by

$$\overline{\eta}_\mathrm{c}^m(K) = \frac{\overline{P}_\mathrm{s}^m}{\overline{P}_\mathrm{tot}^m(K)}$$

$$\begin{aligned}\overline{\eta}_{\mathrm{PA}}^{m}(K) &= \frac{\overline{P}_{\mathrm{tot}}^{m}(K)}{\overline{P}_{\mathrm{dc}}^{m}(K)} \\ \overline{\eta}^{m}(K) &= \frac{\overline{P}_{\mathrm{s}}^{m}}{\overline{P}_{\mathrm{dc}}^{m}(K)}.\end{aligned} \tag{4.26}$$

For constant input signals, the power $P_s^m(A)$ is the measured single-tone power at the carrier frequency. For the DMT signal, the power $\overline{P}_{\mathrm{s}}^{m}$ is the signal power measured in the band of interest [85], i.e., 5 MHz bandwidth around the carrier frequency f_{c}. The total power for both cases is the measured power within 1 GHz bandwidth around f_{c}, and dc power is the overall power consumption.

Measurement Results

For Constant Input Signals Figure 4.17(a) shows the measured coding efficiency $\eta_{\mathrm{c}}^{m}(A, K)$ for constant input signals $x[n] = A$ with different numbers of harmonics K. The efficiency curve has a similar shape compared to the one representing the simulation results in Figure 4.15(a). Figure 4.17(b) shows the efficiency curves for $A = 0.5$ as an example. It can be seen that the coding efficiency curve obtained according to (4.21) agrees with the measured result where the difference is less than two percentage points.

Figure 4.18 shows the measured PA efficiency $\eta_{\mathrm{PA}}^{m}(A, K)$, the transmitter efficiency $\eta^{m}(A, K)$, and the comparison of the measured coding efficiency $\eta_{\mathrm{c}}^{m}(A, K)$ and the calculated coding efficiency $\eta_{\mathrm{c}}(A, K)$ according to (4.21) for input signal of $A = 0.5$. It shows that the actual RF PA efficiency slightly affect the transmitter efficiency in AFPWM based transmitter architectures especially for small number of harmonics K. As shown in the figure, for a small K, the PA efficiency is decreased but the coding efficiency is rather high, which compensates for the PA efficiency degradation. Therefore, for constant signal test, AFPWM signals lead to a transmitter efficiency without efficiency degradation.

For DMT Signals with Different PAPRs Figure 4.19 shows the comparison between the measured average coding efficiency $\overline{\eta}_{\mathrm{c}}^{m}(K)$ and the calculated average coding efficiency $\overline{\eta}_{\mathrm{c}}(K)$ according to (4.24) for the 5 MHz, 7 dB PAPR DMT signal. The efficiency curves agree with each other. Figure 4.20 shows the measured average PA efficiency $\overline{\eta}_{\mathrm{PA}}^{m}(K)$, the average transmitter efficiency $\overline{\eta}^{m}(K)$, and the comparison of the measured average coding efficiency $\overline{\eta}_{\mathrm{c}}^{m}(K)$ and the calculated average coding efficiency $\overline{\eta}_{\mathrm{c}}(K)$. It can be seen that for a small K, the high average coding efficiency compensates for the average PA efficiency degradation, resulting in an average transmitter efficiency without degradation.

From the measurements it can be seen that the AFPWM method, although it induces amplitude variation, produces a transmitter efficiency without degradation compared to the conventional digital PWM method.

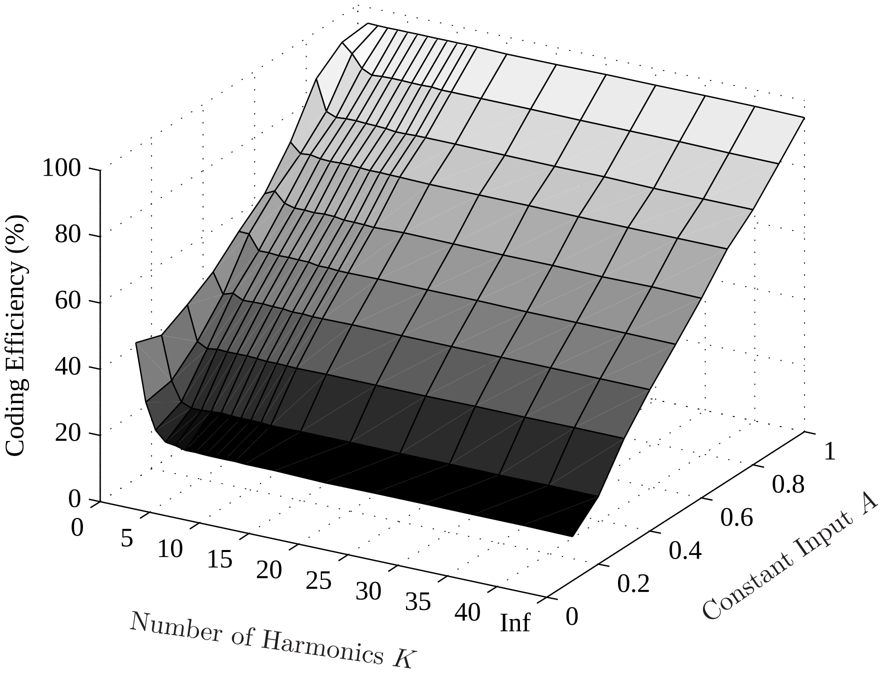

(a)

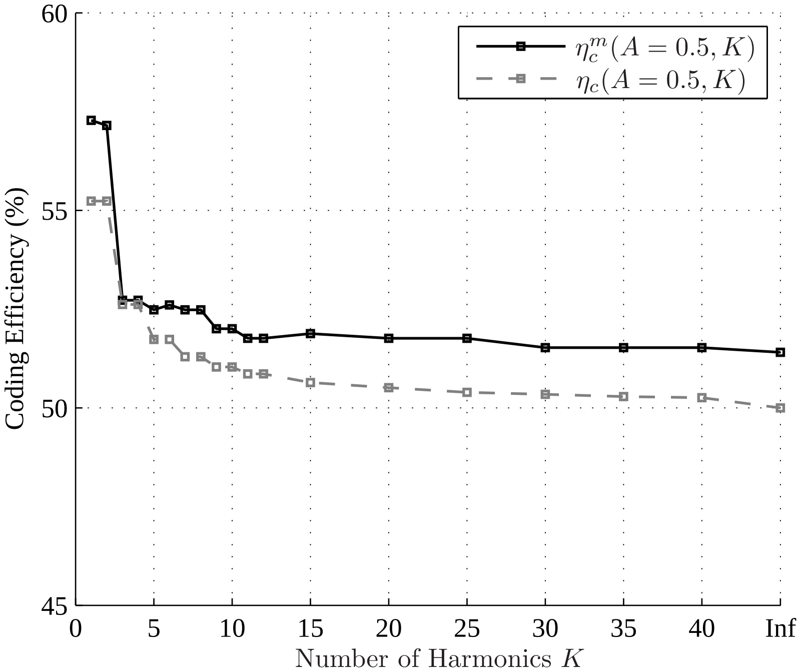

(b)

Figure 4.17: (a) Measured coding efficiency $\eta_c^m(A,K)$ as a function of the constant input signal $x[n]=A$ and the number of harmonics K. (b) The example with $A=0.5$. The coding efficiency $\eta_c(A=0.5,K)$ is obtained according to (4.21).

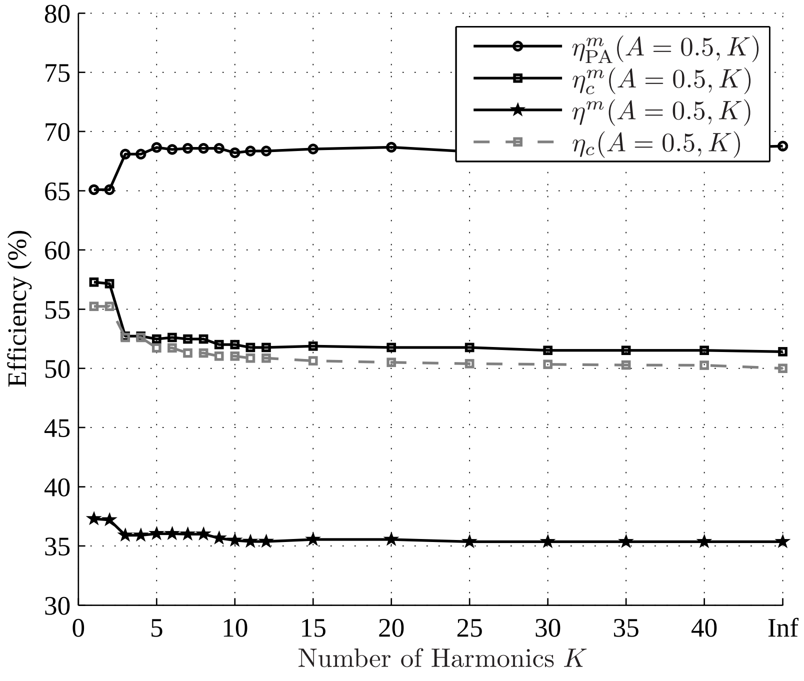

(a)

Figure 4.18: Measured PA efficiency $\eta_{\mathrm{PA}}^{m}(A,K)$, coding efficiency $\eta_{c}^{m}(A,K)$ and transmitter efficiency $\eta^{m}(A,K)$ for $A = 0.5$.

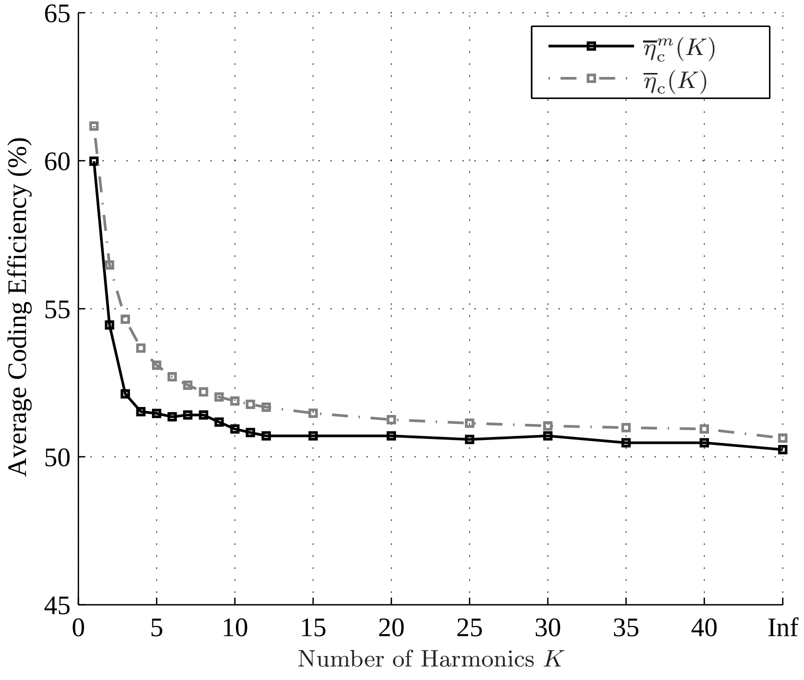

Figure 4.19: Measured and calculated average coding efficiency for the DMT signal of 5 MHz, 7 dB PAPR with different numbers of harmonics K. The average coding efficiency $\overline{\eta}_{c}(K)$ is obtained according to (4.24).

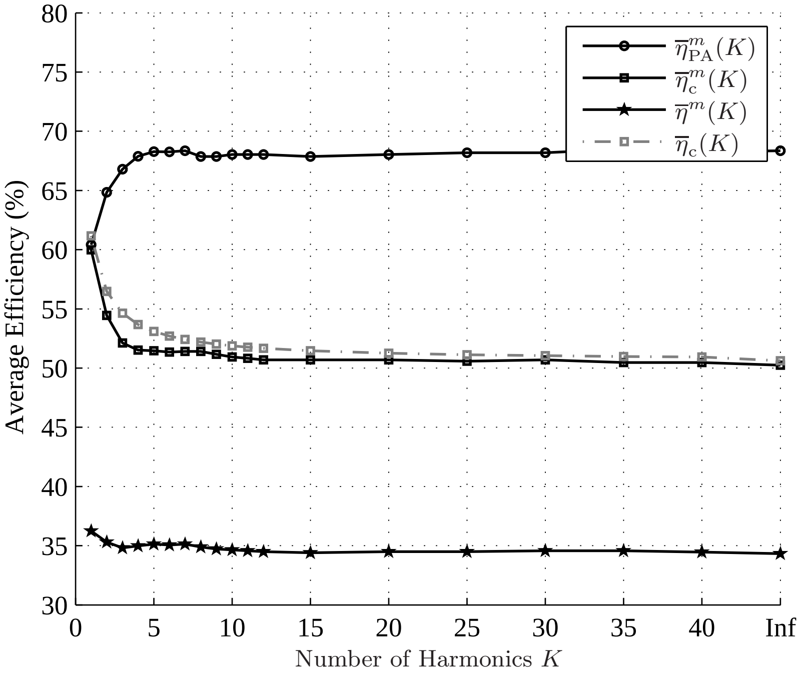

Figure 4.20: Measured average PA efficiency $\eta^m_{\mathrm{PA}}(K)$, coding efficiency $\eta^m_c(K)$ and transmitter efficiency $\eta^m(K)$ with different numbers of harmonics K. $\overline{\eta}_c(K)$ is obtained according to (4.24).

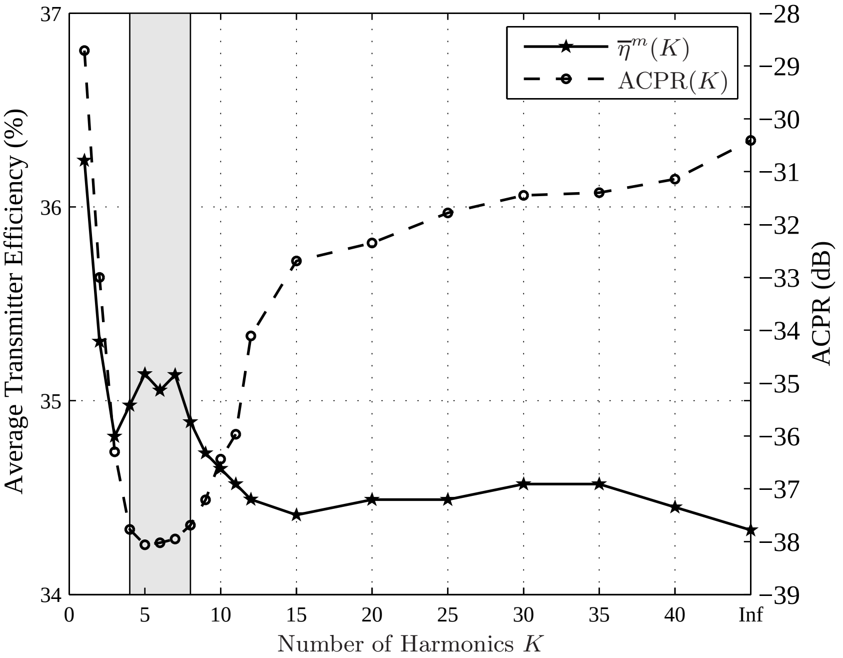

Figure 4.21: Efficiency-linearity trade-off: an appropriate number of harmonics can be determined from the measured transmitter efficiency $\overline{\eta}^m(K)$ and the ACPR. The 5 MHz, 7 dB PAPR DMT signal is used as the test signal.

4.4 Efficiency-Linearity Trade-Off

On the one hand, from the results obtained above, it has been shown that a higher average transmitter efficiency can be obtained with a smaller number of harmonics K due to the higher average coding efficiency. Therefore, from the efficiency perspective, it is desirable to keep K as small as possible to achieve a high average transmitter efficiency. On the other hand, when it comes to the linearity of the transmission signal, a small K results in large variation in the signal amplitude, deteriorating the quality of the amplified signal due to the clipping of the signal amplitude in combination with the PA nonlinearity [65]. Consequently, it is desirable to keep K as large as possible to obtain a flat signal amplitude and thus a good transmission signal quality. With the AFPWM method, however, the number of harmonics K should be small enough to prevent aliasing distortion caused by the sampling process which has been analyzed in Section 4.2. [23]. Therefore, from the linearity perspective, the number of harmonics K should be sufficiently large to prevent large amplitude variation and at the same time small enough without introducing aliasing distortion.

To illustrate the efficiency-linearity trade-off, Figure 4.21 depicts the measured average transmitter efficiency as well as the measured ACPR for the 5 MHz, 7 dB PAPR DMT signal with different number of harmonics K. As can be observed from the figure, for the used measurement setup, the number of harmonics can be chosen between $K \in [4, 8]$ (grey area) to provide a good efficiency-linearity trade-off. The average transmitter efficiency can be achieved is around 35% and the ACPR is around $-38\,\mathrm{dB}$.

In conclusion, by properly choosing the system parameters, AFPWM signals outperform the conventional digital PWM signals in terms of the signal quality, evaluated by DR or ACPR, without degrading the transmitter efficiency.

4.5 Multilevel Aliasing-Free PWM based Burst-Mode RF Transmitters

The transmitter architecture of a digital PWM based burst-mode two-level transmitter, illustrated in Figure 4.1, can be extended to a digital PWM based burst-mode multilevel transmitter as shown in Figure 4.22. Similar to the continuous-time multilevel PWM based transmitter architecture described in Section 2.1.2, the digital PWM based multilevel transmitter incorporates M PW modulators and M RF PAs. Each PWM process is performed digitally and the AFPWM method is applied. Then each phase modulated AFPWM signal is converted to an analog signal and upconverted to the passband. Afterwards the RF burst signal is amplified by the RF PA and the transmission signal is retrieved by the BPF from the combined amplified RF burst signal.

Multilevel transmitter architectures are employed to further improve the transmitter efficiency. The analysis of continuous-time PWM based multilevel transmitter architecture has been described in Section 3.2. From the analysis and results obtained, it can be seen that the

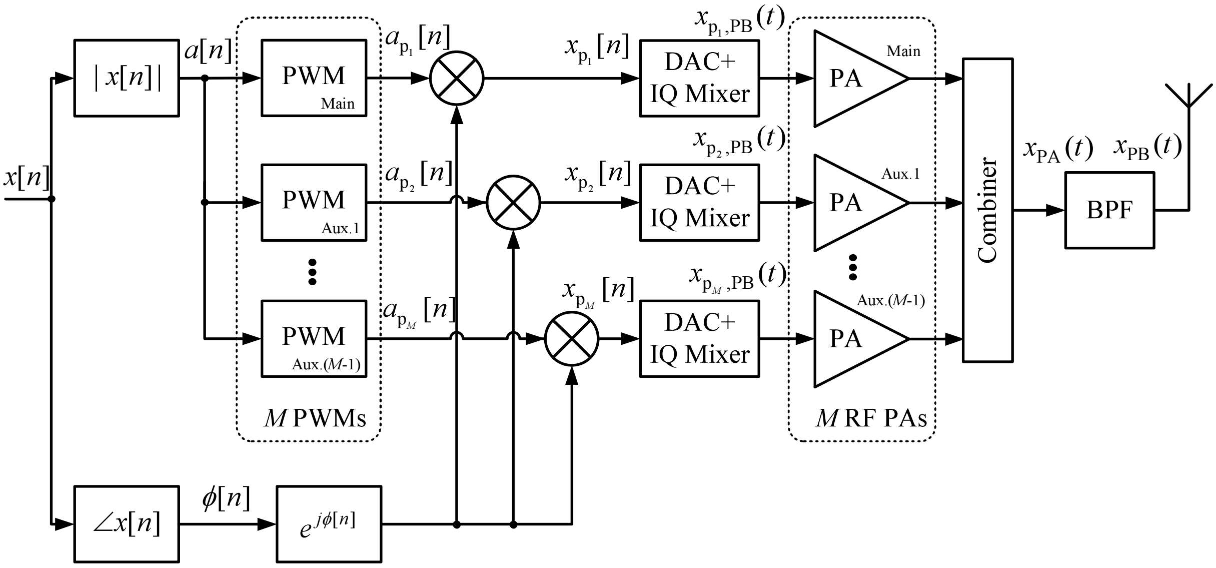

Figure 4.22: Block diagram of a burst-mode multilevel RF transmitter architecture with digital AFPWM process.

multilevel transmitter architecture provides a higher transmitter efficiency while maintaining good transmission signal quality. The optimized transmitter architecture can further improve the transmitter efficiency especially for signals with high PAPRs. In this section, the digital AFPWM based multilevel transmitter architectures will be analyzed and the performance metrics such as signal linearity and power efficiency as well as efficiency-linearity trade-off will be described. Also, the efficiency optimization will be applied to enhance the transmitter efficiency.

4.5.1 Multilevel Aliasing-Free PWM Analysis

The modulating signal $a[n]$ is divided into M cases depending on the threshold values V_i defined in (2.3). Each divided modulating signal $a_m[n] \in [V_{m-1}, V_m]$, $m \in [1, M]$ is modulated by the AFPWM method. Based on the analytical results obtained for continuous-time multilevel PWM signals in Section 2.3.2, the generated digital AFPWM signals can be described accordingly. For the general m-th case when $a[n] \in [V_{m-1}, V_m]$, acording to (2.43), the generated digital AFPWM signal is given by

$$a_{p_m}[n] = a_m[n] - V_{m-1} + \sum_{k=1}^{K} \frac{2(-1)^{(m-1)k}(V_m - V_{m-1})}{\pi k} \sin\left(\pi k \frac{a_m[n] - V_{m-1}}{V_m - V_{m-1}}\right) \cos(2\pi k f_p n T_s) \tag{4.27}$$

where the number of harmonics is limited to K. Thus the generated out-of-band spectral content is reduced. The combined AFPWM signal can be expressed by

$$\begin{aligned} a_{\mathrm{p}}[n] &= \sum_{m=1}^{M} a_{\mathrm{p}_m}[n] \\ &= a[n] + \sum_{m=1}^{M}\sum_{k=1}^{K} \frac{2(-1)^{(m-1)k}(V_m - V_{m-1})}{\pi k} \sin\left(\pi k \frac{a_m[n] - V_{m-1}}{V_m - V_{m-1}}\right) \cos(2\pi k f_{\mathrm{p}} n T_{\mathrm{s}}). \end{aligned} \tag{4.28}$$

With the phase information $e^{j\phi[n]}$, the phase modulated multilevel AFPWM signal is given by

$$x_{\mathrm{p}}[n] = \sum_{m=1}^{M} x_{\mathrm{p}_m}[n] = x[n] + \sum_{m=1}^{M}\sum_{k=1}^{K} x_{m,k}[n] \tag{4.29}$$

where the m-th path, k-th harmonic is given by

$$x_{m,k}[n] = \frac{2(-1)^{(m-1)k}(V_m - V_{m-1})}{\pi k} \sin\left(\pi k \frac{a_m[n] - V_{m-1}}{V_m - V_{m-1}}\right) \cos(2\pi k f_{\mathrm{p}} n T_{\mathrm{s}}) e^{j\phi[n]}. \tag{4.30}$$

A special case of the multilevel AFPWM signal is the non-optimized AFPWM signal with equally spaced threshold values. The phase modulated non-optimized AFPWM signal is given by

$$x_{\mathrm{p}}[n] = x[n] + \sum_{k=1}^{K} x_k[n] \tag{4.31}$$

where the k-th harmonic is given by

$$x_k[n] = \frac{2}{\pi k M} \sin(\pi k M a[n]) \cos(2\pi k f_{\mathrm{p}} n T_{\mathrm{s}}) e^{j\phi[n]}. \tag{4.32}$$

The frequency-domain expression of the combined AFPWM signal $x_{\mathrm{p}}[n]$ is described by

$$\tilde{X}_{\mathrm{p}}(f) = \frac{1}{T_{\mathrm{s}}} \sum_{\zeta=-\infty}^{\infty} X_{\mathrm{p}}(f - \zeta f_{\mathrm{s}}) \tag{4.33}$$

where $X_{\mathrm{p}}(f)$ is given by

$$X_{\mathrm{p}}(f) = X(f) + \sum_{k=1}^{K}\sum_{r=0}^{\infty} \frac{(j\pi k M)^{2r}}{(2r+1)!} \left[A_{2r}(f + k f_{\mathrm{p}}) + A_{2r}(f - k f_{\mathrm{p}})\right] * X(f) \tag{4.34}$$

where $X(f)$ is the Fourier transform of the continuous-time signal $x(t)$.

Figure 4.23 shows the spectral comparison of the conventional digitally generated PWM signal and three-level AFPWM signal with the number of harmonics $K = 8$. The test signal is of 7 dB PAPR and the threshold value is of $V_1 = 0.42$ which is the optimum threshold value of the 7 dB PAPR signal. It can be seen that, similar to the two-level case which has been described in Section 4.2, the multilevel AFPWM signal outperforms the conventional digitally generated PWM signal in terms of the signal linearity. The DR of the conventional digitally generated PWM signal is around 38 dB whereas the DR of AFPWM signal is more than 80 dB.

The corresponding time-domain signals and the modulating signal are shown in Figure 4.24. The PWM signals shown are the combined signals from the corresponding main and auxiliary PWM signals. As expected, with limited number of harmonics, the amplitude variation is superimposed on the AFPWM signal amplitude.

4.5.2 Power Efficiency Analysis

Since the multilevel transmitter architecture is employed to further improve the transmitter efficiency, it is interesting to see the performance metrics of the digital AFPWM based multilevel transmitter architecture. The coding efficiency for AFPWM based multilevel burst-mode RF transmitters will be described first and the transmitter efficiency and the linearity performance will be evaluated through simulations.

Coding Efficiency for Constant Input Signals

According to (4.28), the AFPWM signal $x_{\mathrm{p}}[n]$ for constant input signal $x[n] = A \in (0, V_1]$ is expressed by

$$x_{\mathrm{p}}[n]= A + \sum_{k=1}^{K} \frac{2V_1}{\pi k} \sin(\pi k \frac{A}{V_1}) \cos(2\pi k f_{\mathrm{p}} n T_{\mathrm{s}}). \tag{4.35}$$

Following the same procedure described in Section 4.3.1, the total power of the amplified RF burst signal is

$$P_{\mathrm{tot}_1}(A, K) = \frac{A^2}{2} \left(1 + 2\sum_{k=1}^{K} \mathrm{sinc}^2(k\frac{A}{V_1}) \right). \tag{4.36}$$

Thus for the first case when input signal $x[n] = A \in (0, V_1]$, the coding efficiency is given by

$$\eta_{\mathrm{c}}(A, K) = \frac{1}{1 + 2\sum_{k=1}^{K} \mathrm{sinc}^2(kA)}, \quad A \in (0, V_1]. \tag{4.37}$$

$$\tag{4.38}$$

When $x[n] = A \in (V_{m-1}, V_m], m \in [1, M]$, the AFPWM signal is given by

$$x_{\mathrm{p}}[n]= A + \sum_{k=1}^{K} \frac{2(-1)^{(m-1)k}(V_m - V_{m-1})}{\pi k} \sin(\pi k \frac{A - V_{m-1}}{V_m - V_{m-1}}) \cos(2\pi k f_p n T_s) \tag{4.39}$$

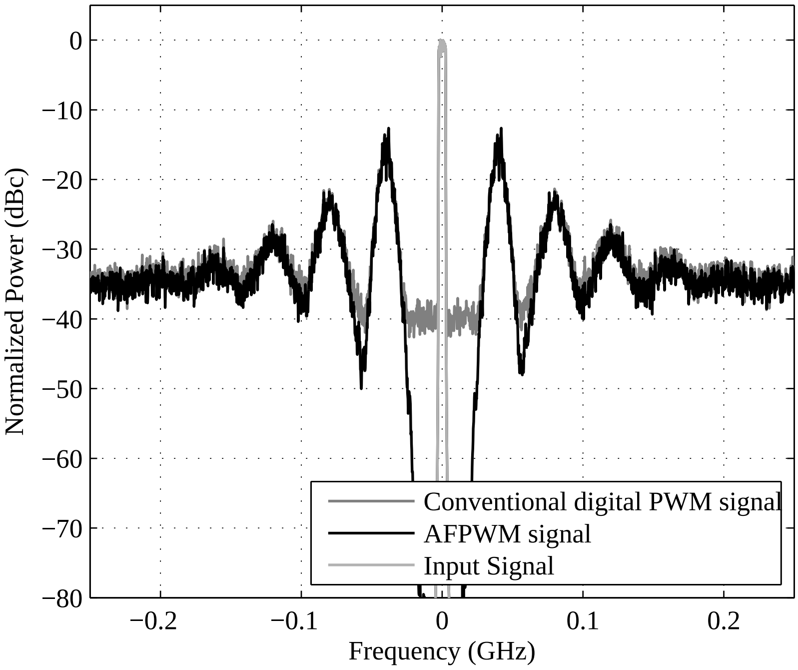

Figure 4.23: A comparison of the frequency-domain conventional digitally generated PWM signal and the three-level AFPWM signal.

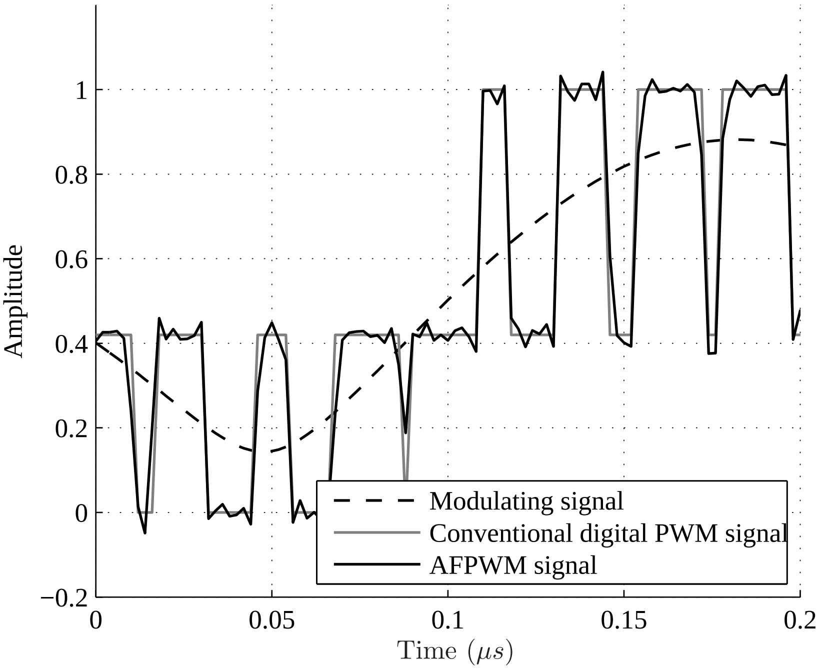

Figure 4.24: A comparison of the time-domain conventional digitally generated PWM signal and the three-level AFPWM signal.

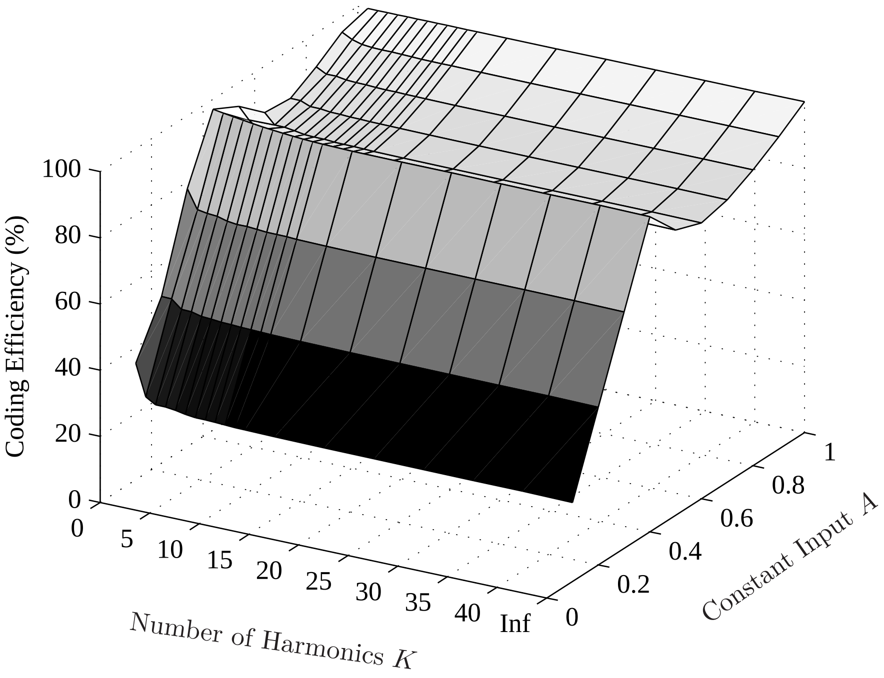

(a)

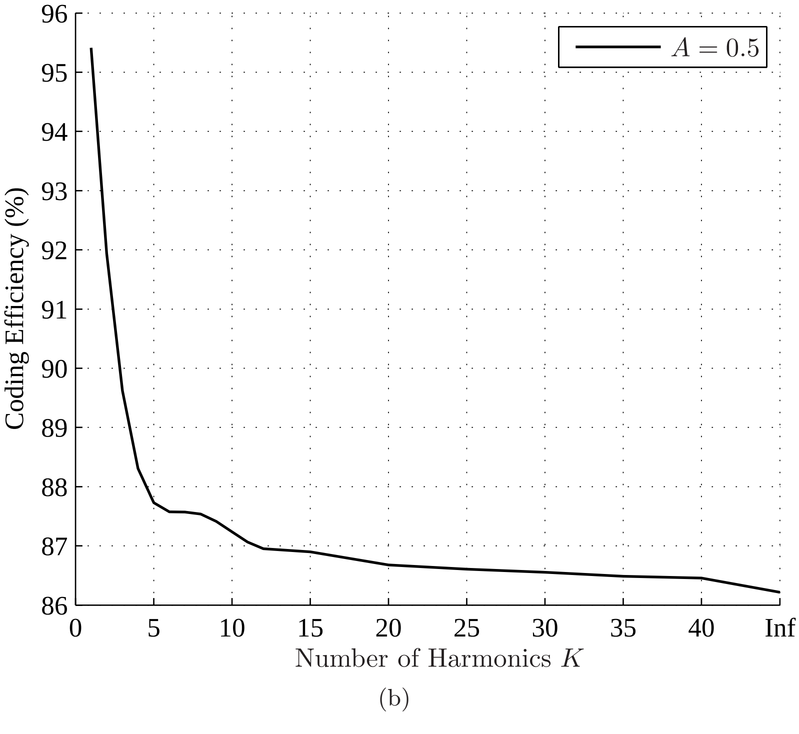

(b)

Figure 4.25: (a) Coding efficiency $\eta_c(A, K)$ as a function of the constant input $x[n] = A$ and the number of harmonics K of the optimized three-level transmitter. (b) The example with $A = 0.5$.

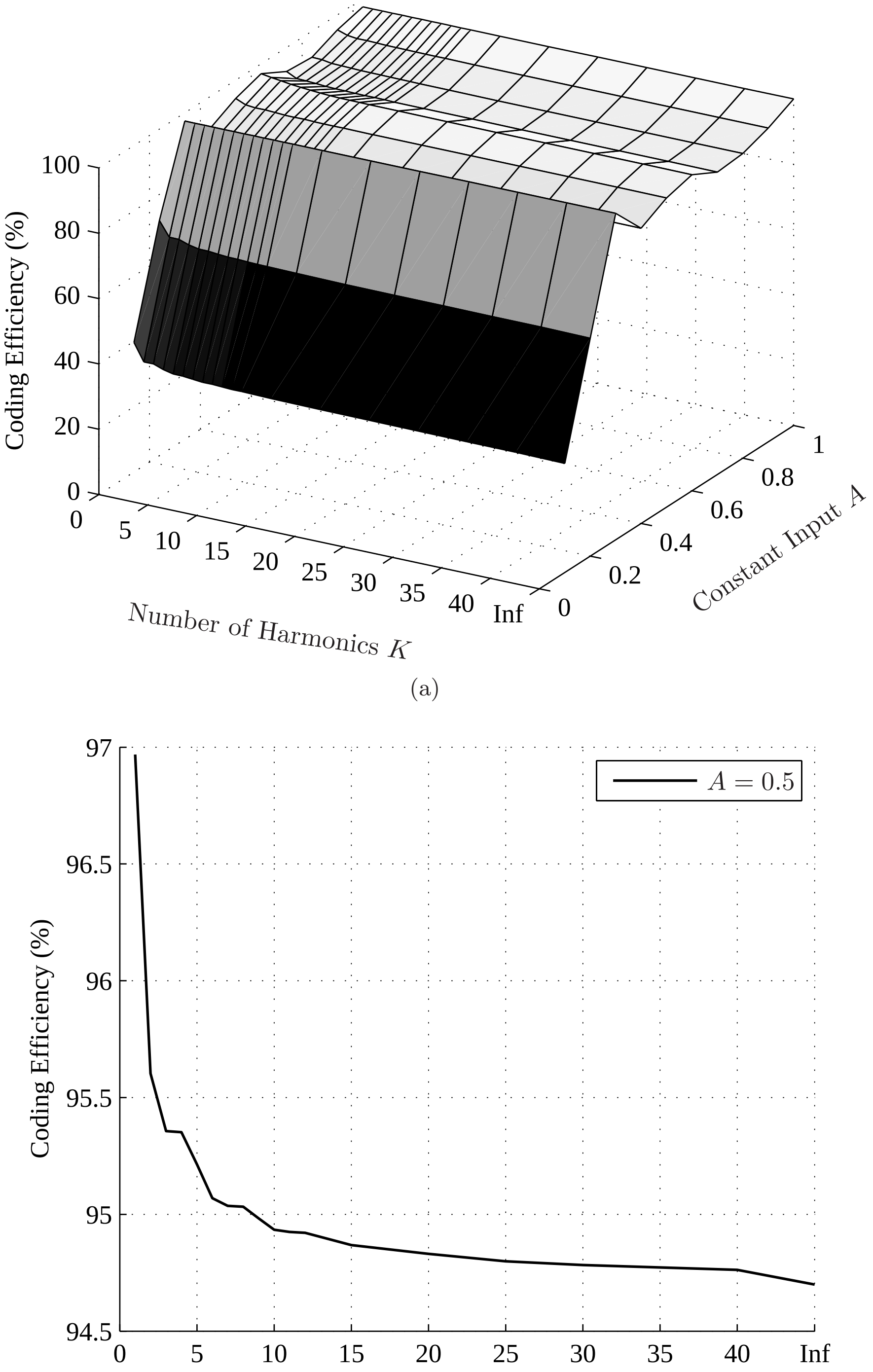

(a)

(b)

Figure 4.26: (a) Coding efficiency $\eta_c(A, K)$ as a function of the constant input $x[n] = A$ and the number of harmonics K of the optimized four-level transmitter. (b) The example with $A = 0.5$.

The total power of the amplified RF burst signal is

$$\eta_{\mathrm{c}}(A,K)=\frac{1}{2}A^2+(A-V_{m-1})^2\sum_{k=1}^{K}\mathrm{sinc}^2(k\frac{A-V_{m-1}}{V_m-V_{m-1}}),\quad A\in(V_{m-1},V_m]. \tag{4.40}$$

$$\tag{4.41}$$

Therefore, the coding efficiency for AFPWM based burst-mode multilevel RF transmitters is given by

$$\eta_c(A,K,V_i)=\begin{cases}0, & \text{for } A=0\\ \dfrac{A^2}{A^2+2(A-V_{m-1})^2\sum_{k=1}^{K}\mathrm{sinc}^2(k\frac{A-V_{m-1}}{V_m-V_{m-1}})}, & \text{for } A\in(V_{m-1},V_m],\\ & m\in[1,M],V_i\in[0,1],i\in[0,M].\end{cases} \tag{4.42}$$

For a fixed input A, the upper bound of the coding effiicency is given by $K\to 0$ and $\eta_{\mathrm{c}}(A,K=0)=1$. With $K\to\infty$, the lower bound of the coding efficiency is by using the conventioanl PWM method and can be obtained according to (3.37) which depends on the threshold values.

A special case of the multilevel transmitter architectures is the non-optimized transmitter architecture, according to (4.31) and (4.32), the AFPWM signal with constant input signal $x[n]=A$ is given by

$$x_{\mathrm{p}}[n]=A+\sum_{k=1}^{K}\frac{2}{\pi kM}\sin(\pi kMA)\cos(2\pi kf_pT_sn). \tag{4.43}$$

The coding efficiency for AFPWM based non-optimized burst-mode multilevel RF transmitters can be described as

$$\eta_c(A,K)=\frac{1}{1+2\sum_{k=1}^{K}\mathrm{sinc}^2(kMA)},\quad A\in(0,1]. \tag{4.44}$$

Note that in the non-optimized transmitter case, the threshold value is not included as one of the variables as in the general case in (4.42) because the threshold value is equally distributed and this information is already taken into consideration.

Figure 4.25(a) shows the coding efficiency curve of the optimized three-level transmitter from (4.42) with the threshold value $V_i=[0,0.42,1]$ for different constant input signal $x[n]=A$ with different number of harmonics K. An example with $x[n]=0.5$ is illustrated in Figure 4.25(b). The coding efficiency decreases as K increases, similar to the two-level case which is shown in Figure 4.15(b), moreover, the coding efficiency is greatly improved in the optimized three-level case.

Figure 4.26(a) depicts the coding efficiency curve of the optimized four-level transmitter with $V_i=[0,0.3,0.57,1]$ for different constant input signal $x[n]=A$ with different number of harmonics K. From the example with $x[n]=0.5$ in Figure 4.26(b), it can be seen that the coding efficiency is further improved compared to the two-level case.

Average Coding Efficiency for Signals with a Given PDF

The average coding efficiency is defined as the ratio of the average transmission signal power to the average total power of the amplified RF burst signal

$$\overline{\eta}_c(K,V_i)=\frac{\frac{1}{N}\sum_{n=1}^{N}A^2 f_a(A)}{\frac{1}{N}\sum_{n=1}^{N}\frac{A^2}{\eta_{\mathrm{c}}(A,K,V_i)}f_a(A)} \tag{4.45}$$

where the coding efficiency $\eta_{\mathrm{c}}(A,K,V_i)$ is given in (4.42).

Figure 4.27 shows the average coding efficiency of the optimized three-level transmitter obtained from (4.45) with $V_i=[0,0.42,1]$ and Figure 4.28 shows the average coding efficiency of the optimized four-level case with $V_i=[0,0.3,0.57,1]$. It can be seen that for a certain PAPR, the average coding efficiency is decreased as K increases. The average coding efficiency of the optimized three-level and four-level transmitters are greatly improved compared to the two-level case. With the four-level case, the coding efficiency can be further improved compared to the three-level case.

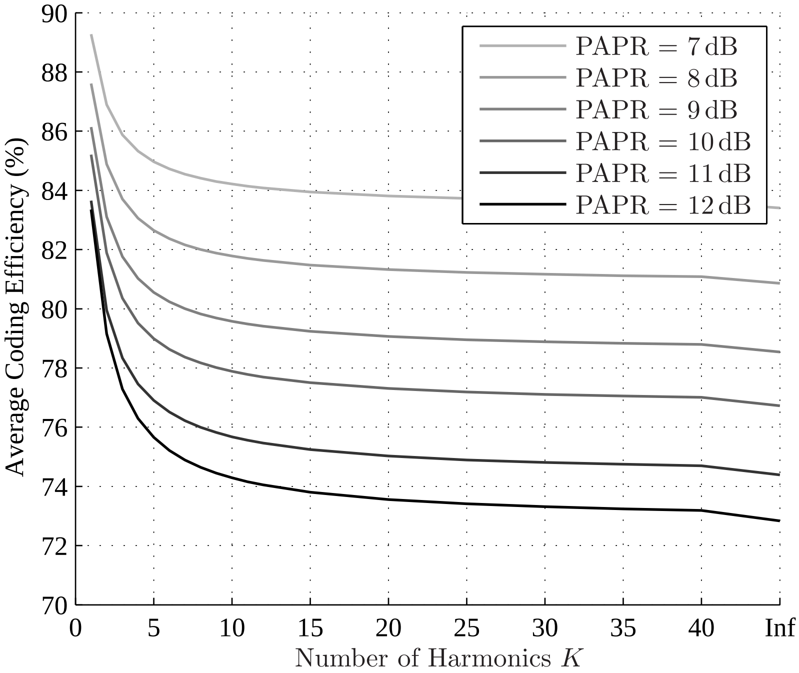

Figure 4.27: Average coding efficiency $\overline{\eta}_c(K)$ for DMT signals with different PAPRs and different numbers of harmonics K of the optimized three-level transmitter.

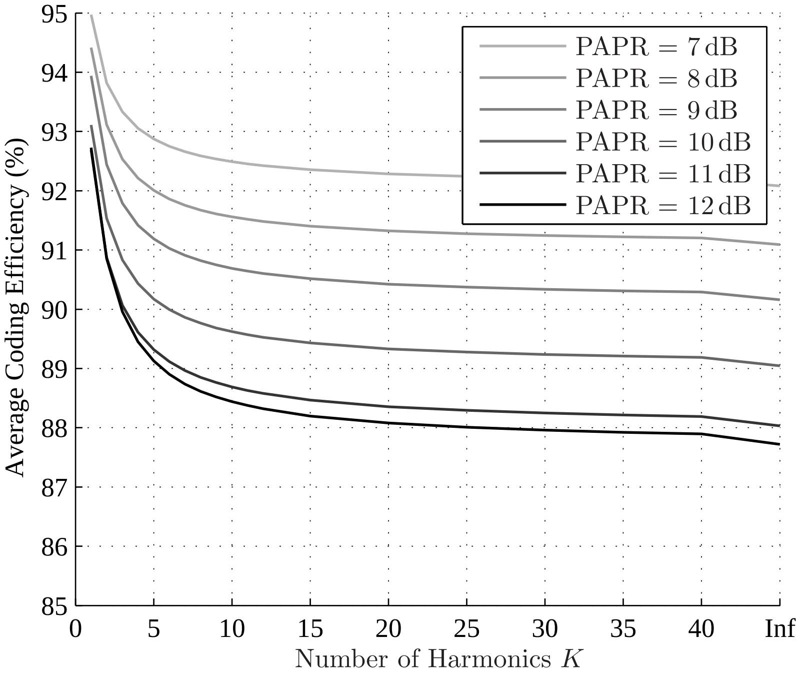

Figure 4.28: Average coding efficiency $\overline{\eta}_c(K)$ for DMT signals with different PAPRs and different numbers of harmonics K of the optimized four-level transmitter.

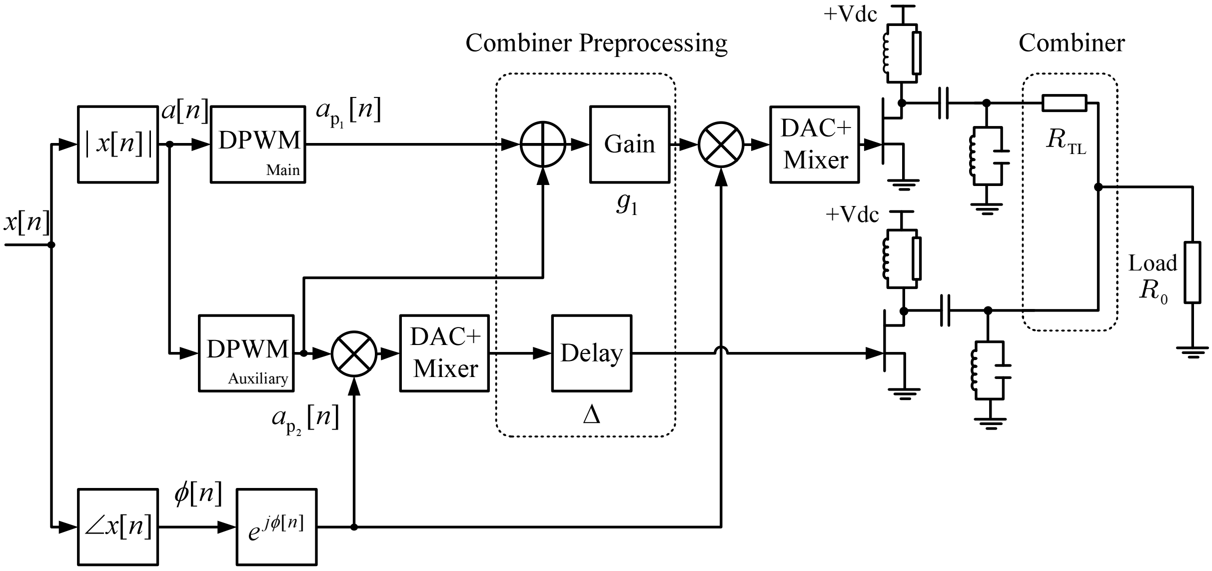

Figure 4.29: Simulation setup of a burst-mode three-level RF transmitter with digital PWM process.

4.5.3 Simulation Results

Simulation results are used to verify the results from the multilevel transmitter architecture analysis obtained before. The simulation setup of a burst-mode three-level transmitter with digital PWM process is shown in Figure 4.29. The function blocks of the combiner preprocess, the PA and the combiner are the same as described in Section 3.2.5. The difference is in the baseband digital signal processing blocks. The digital PWM process consists of conventional digital PWM process and the AFPWM process with different number of harmonics.

Efficiency for Constant Input Signals

Measured average PA efficiency η_{PA}^m, coding efficiency η_c^m and transmitter efficiency η^m with different numbers of harmonics K.

The simulated coding efficiency of the optimized three-level and four-level transmitters with different constant input signals and different number of harmonics are shown in Figure 4.30(a) and Figure 4.31(a). The corresponding examples with $x[n] = 0.5$ are shown in Figure 4.30(b) and Figure 4.31(b). Additionally, the theoretical results obtained from (4.42) with $x[n] = 0.5$ are also shown in dashed grey lines for comparison. It can be seen that the simulated coding efficiency agrees with the theoretical result. Although the PA efficiency is lower with a smaller number of harmonics K, the coding efficiency is higher which compensates for the efficiency degradation, leading to a transmitter efficiency which is not degraded.

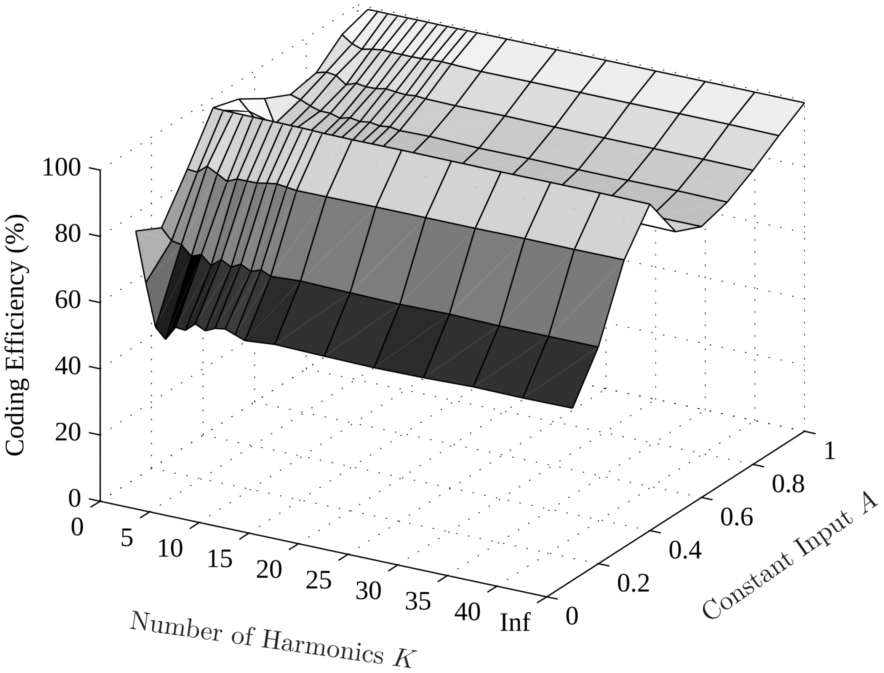

(a)

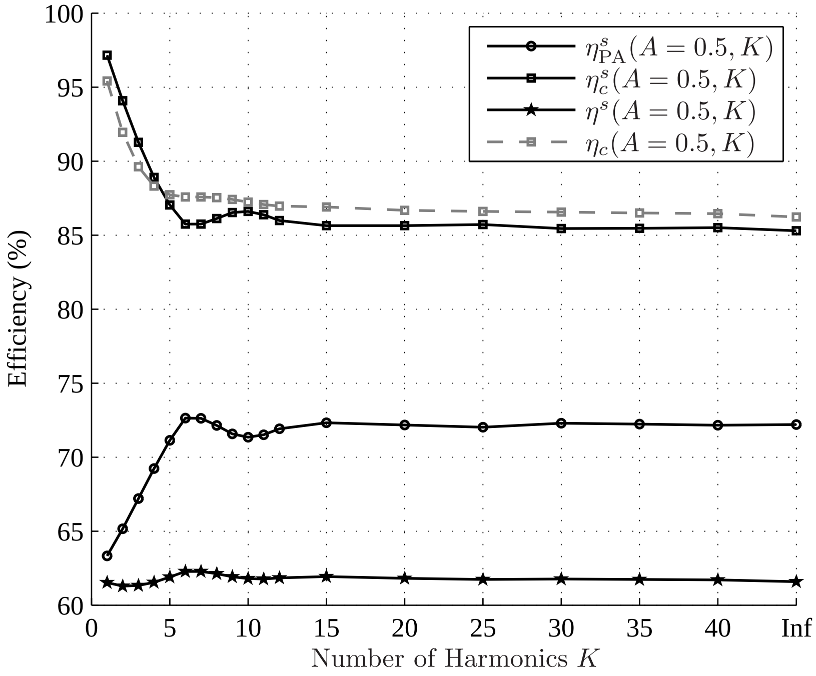

(b)

Figure 4.30: (a) Simulated coding efficiency $\eta^s_c(A, K)$ as a function of the constant input signal $x[n] = A$ and the number of harmonics K of the optimized three-level transmitter. (b) Simulated PA efficiency $\eta^s_{\mathrm{PA}}(A, K)$, coding efficiency $\eta^s_c(A, K)$ and transmitter efficiency $\eta^s(A, K)$ for $A = 0.5$. The coding efficiency $\eta_c(A = 0.5, K)$ is obtained according to (4.42).

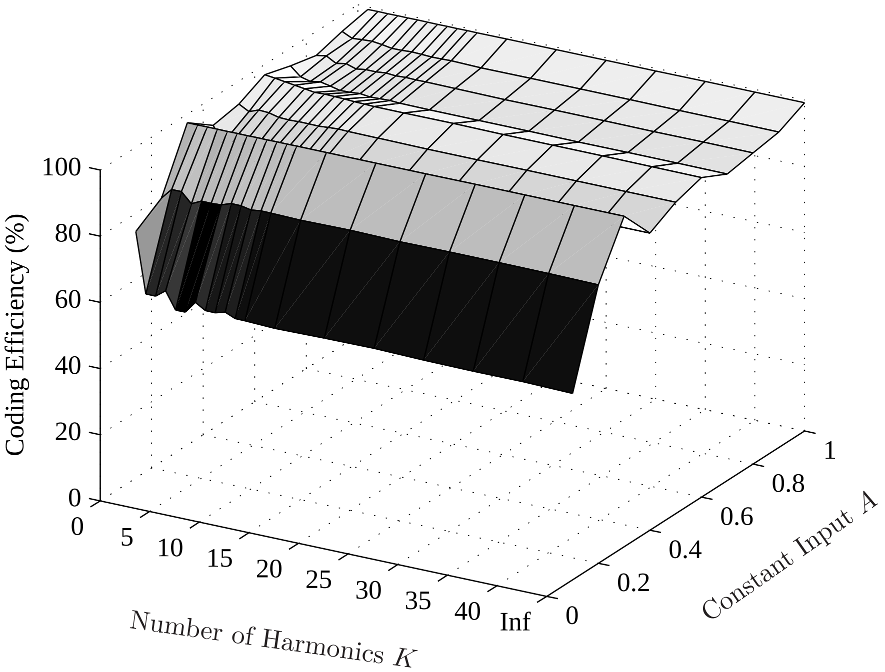

(a)

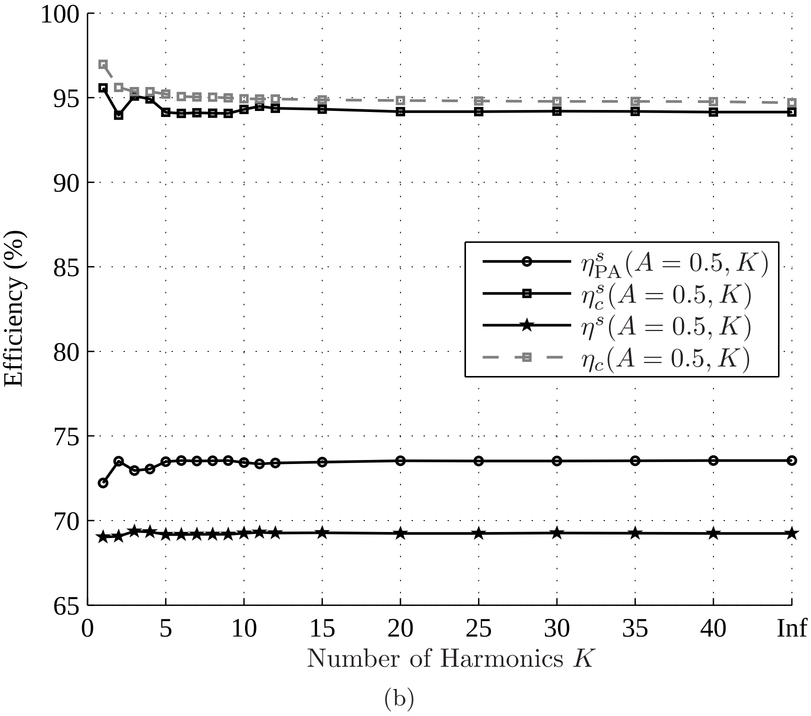

(b)

Figure 4.31: (a) Simulated coding efficiency $\eta^s_c(A,K)$ as a function of the constant input signal $x[n]=A$ and the number of harmonics K of the optimized four-level transmitter. (b) Simulated PA efficiency $\eta^s_{\mathrm{PA}}(A,K)$, coding efficiency $\eta^s_c(A,K)$ and transmitter efficiency $\eta^s(A,K)$ for $A=0.5$. The coding efficiency $\eta_c(A=0.5,K)$ is obtained according to (4.42).

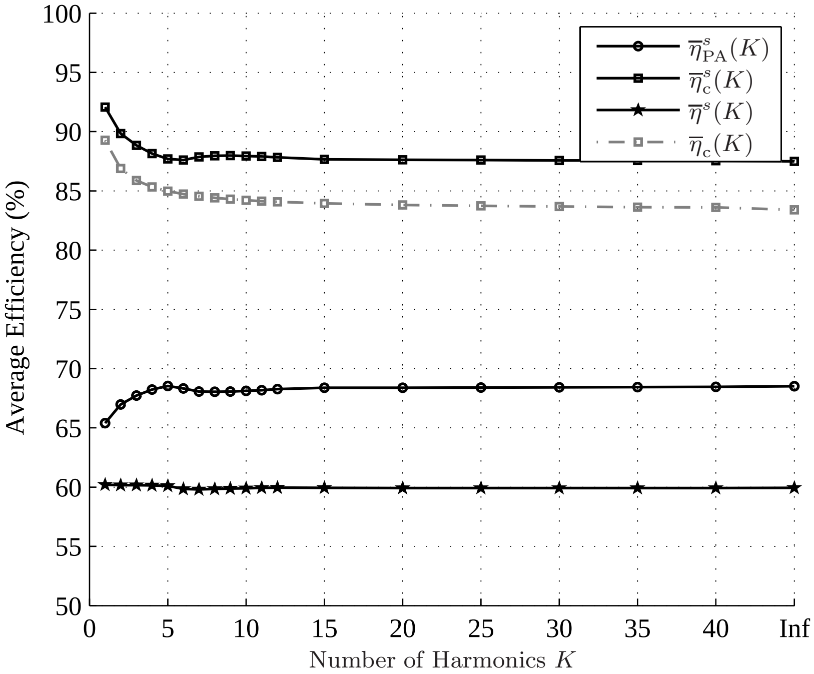

Figure 4.32: Simulated average PA efficiency $\eta^s_{\mathrm{PA}}(K)$, coding efficiency $\eta^s_c(K)$ and transmitter efficiency $\eta^s(K)$ with different numbers of harmonics K for the DMT signal of 5 MHz, 7 dB PAPR of the optimized three-level transmitter. The average coding efficiency $\overline{\eta}_c(K)$ is obtained according to (4.45).

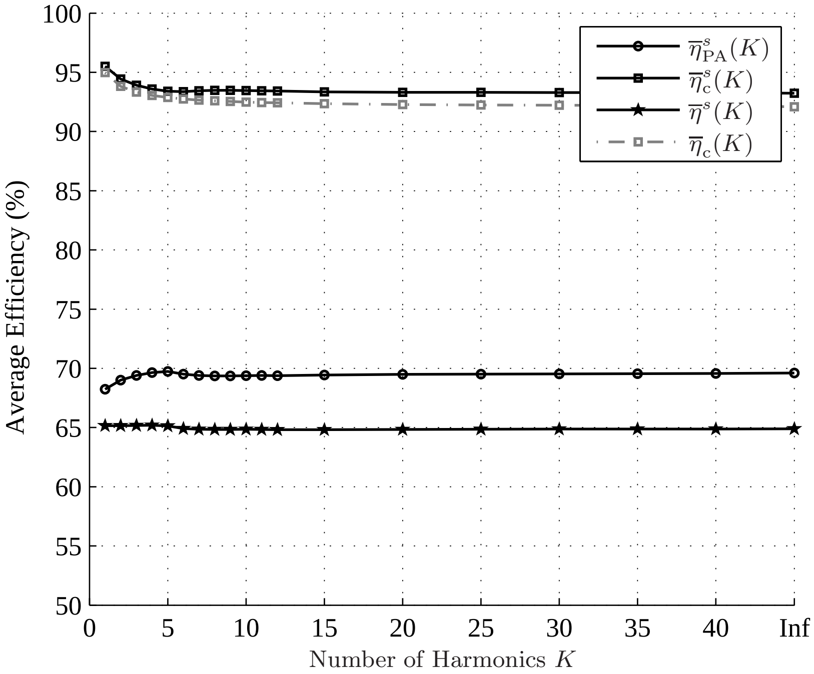

Figure 4.33: Simulated average PA efficiency $\eta^s_{\mathrm{PA}}(K)$, coding efficiency $\eta^s_c(K)$ and transmitter efficiency $\eta^s(K)$ with different numbers of harmonics K for the DMT signal of 5 MHz, 7 dB PAPR of the optimized four-level transmitter. The average coding efficiency $\overline{\eta}_c(K)$ is obtained according to (4.45).

PAPR (dB)		7	8	9	10	11	12
$\overline{\eta}$ (%)	2-level	36.2	33.2	29.2	26.4	23.8	21.4
	3-level (non-optimized)	59.3	56.2	53.1	49.2	45.6	41.4
	3-level (optimized)	60.1	57.7	56.3	55.2	53.3	52.5
	4-level (non-optimized)	64.8	63.2	61.4	60.2	57.8	55.1
	4-level (optimized)	65.1	63.7	63.2	63.0	63.0	62.9

Table 4.1: Simulated average transmitter efficiency for DMT signals with different PAPRs with $K = 5$ when $a(t) \in [0, 1]$.

Average Efficiency for DMT Signals with Different PAPRs

The simulated average coding efficiency of the optimized three-level and four-level transmitters with the DMT signal of 7 dB PAPR are shown in Figure 4.32 and Figure 4.33. Again, the higher average coding efficiency compensates for the lower PA efficiency resulting in a transmitter efficiency without degradation. The simulated average coding efficiency also agrees with the theoretical results. Note that the difference between the simulated average coding efficiency and the theoretical result of the three-level transmitter is slightly larger than the four-level case. The possible explanation is that the DMT signal into the PA is bandlimited by the PA matching networks, where the out-of-band components are attenuated. Because the four-level case generates less out-of-band spectral components, the coding efficiency is less affected by the PA matching networks.

Efficiency-Linearity Trade-Off

The average transmitter efficiency, ACPR and NMSE of the optimized three-level and four-level transmitters are shown in Figure 4.34 and Figure 4.35. It can be seen that there also exists the sweet spot of the number of harmonics K for each case where a good efficiency-linearity trade-off can be achieved. As has been described in Section 4.4, a smaller K mostly leads to a higher average transmitter efficiency, at the same time, the number K should be large enough but not too large to induce aliasing distortion to obtain a good transmission signal quality.

In the considered simulation setup where the bandwidth of the PA is around 300 MHz, the number of harmonics can be chosen between $K \in [4, 6]$ to obtain a satisfying transmitter efficiency as well as the signal linearity in terms of ACPR and NMSE. Table 4.1 shows the simulated average transmitter efficiency for DMT signals with different PAPRs with harmonics $K = 5$ when $a(t) \in [0, 1]$. It can be seen that the efficiency of the optimized three-level and four-level transmitters outperforms two-level and non-optimized transmitters, especially for signals with high PAPRs. To further improve the transmitter performance, linearization techniques such as predistortion can be employed.

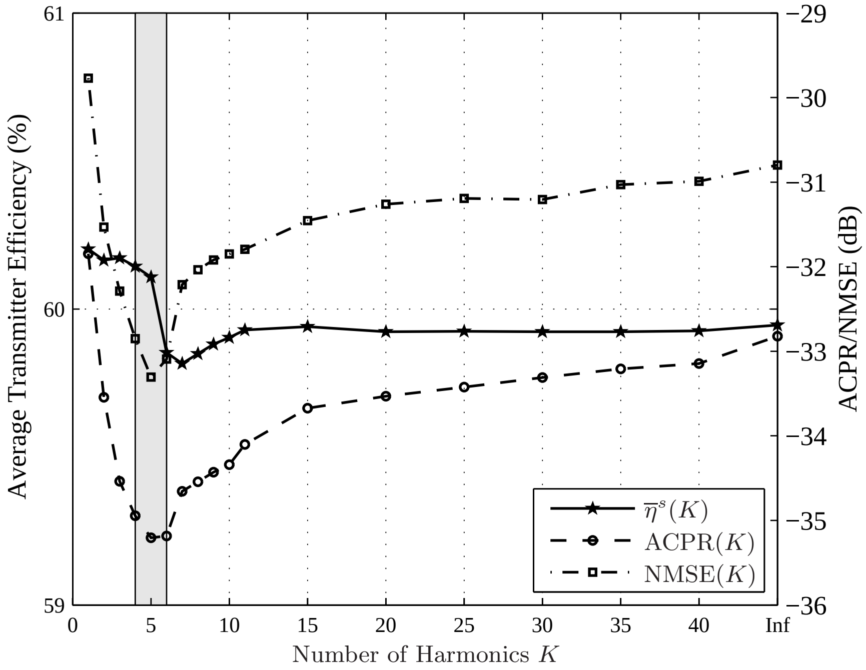

Figure 4.34: Efficiency-linearity trade-off for the optimized three-level transmitter: an appropriate number of harmonics can be determined from the simulated transmitter efficiency, ACPR and NMSE. The 5 MHz, 7 dB PAPR DMT signal is used as the test signal.

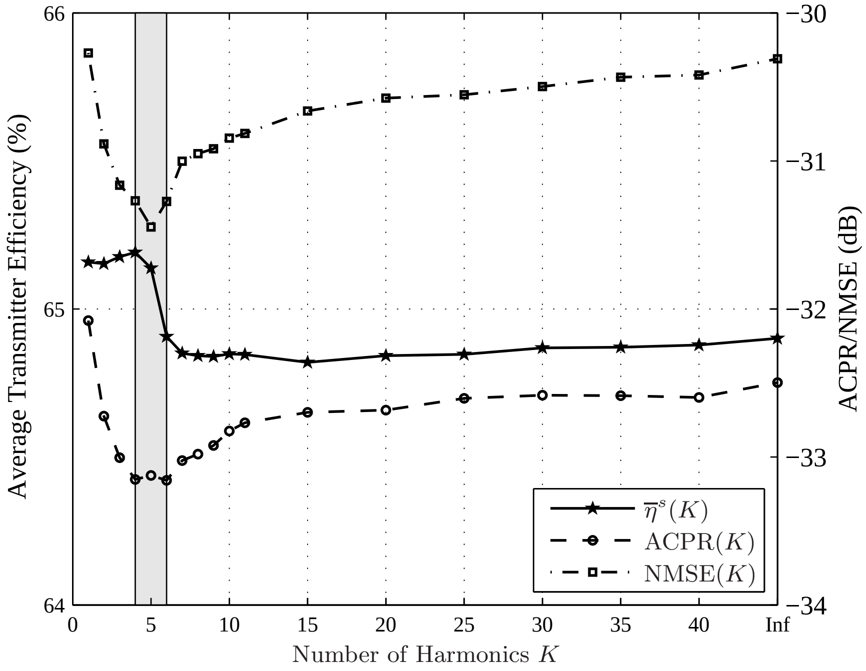

Figure 4.35: Efficiency-linearity trade-off for the optimized four-level transmitter: an appropriate number of harmonics can be determined from the simulated transmitter efficiency, ACPR and NMSE. The 5 MHz, 7 dB PAPR DMT signal is used as the test signal.

4.6 Summary and Discussion

In this chapter, a thorough analysis on the discrete-time PWM based burst-mode RF transmitters has been carried out. Mathematical analysis of discrete-time PWM signals has been described. Discrete-time PWM process inherently suffers from aliasing distortion which degrades the signal quality. Aliasing-free PWM method has been described, which limits the number of harmonics in the generated PWM signals. Simulation and measurement results have been used to verify the superior performance of AFPWM based burst-mode RF transmitter over the conventional comparator PWM based burst-mode RF transmitter.

AFPWM signals introduce variation onto the time-domain signal amplitude, which might affect the RF PA efficiency. However, the transmitter efficiency is also influenced by the coding efficiency. A thorough analysis on the coding efficiency of the AFPWM based burst-mode RF transmitter has been performed. The results show that the higher coding efficiency compensates for the RF PA efficiency degradation. The measurement results have been used to verify the results that the resulting transmitter efficiency is not degraded owning to the higher coding efficiency.

An important conclusion obtained from the measurements is that by choosing an appropriate number of harmonics, a good efficiency-linearity trade-off can be achieved for the AFPWM based burst-mode RF transmitters.

In this chapter, the multilevel AFPWM based burst-mode RF transmitters have been investigated. Analytical descriptions of the multilevel AFPWM signals as well as the coding efficiency have been shown. The multilevel architecture can be used to further enhance the transmitter efficiency through the improved coding efficiency. Simulation results of three-level and four-level transmitters have shown that the optimized transmitter architectures outperform the non-optimized and two-level cases. A good efficiency-linearity trade-off can also be achieved by proper choice of number of harmonics.

5

Summary and Concluding Remarks

5.1 Summary of Scientific Results

In this thesis, the signal processing for energy-efficient burst-mode RF transmitters has been presented. In Chapter 1, this thesis was motivated by the development and technology trends of efficient transmitter architectures where the signal processing can be used to analyze the transmitter architecture and further enhance the transmitter efficiency. In modern wireless communication systems, the new standards, such as LTE, DVB-T2, utilize signals with high PAPR. For these signals, conventional RF PAs operated in linear mode produce only moderate average efficiency. This reduces the battery lifetime for mobile devices and comes with an increases design cost for non-portable applications. An introduction to the common efficiency enhancement transmitter architectures has been provided. The burst-mode RF transmitters which utilize binary source encoders such as a PW modulator together with the RF PA operated in burst mode, which is in saturation or in cutoff, has been considered as one candidate for the high efficiency transmitters.

In Chapter 2, an introduction to burst-mode RF transmitters has been presented where the principle of operation of two-level and multilevel burst-mode RF transmitters has been described. The efficiency metrics including the RF PA drain efficiency, the coding efficiency as well as the transmitter efficiency are given, where the transmitter efficiency can be ideally expressed as the multiplication of the peak RF PA efficiency with the coding efficiency. Therefore the coding efficiency is an important measure in burst-mode RF transmitters. To investigate the possibility of signal processing in burst-mode RF transmitters, a mathematical framework of the transmitter architecture is required. To this end, mathematical descriptions of burst-mode RF transmitters both in time-domain and frequency-domain have been introduced. These models serve as basis and are used through out the thesis for system performance evaluation, efficiency analysis and signal processing method development to optimize the transmitter efficiency and enhance the system performance.

In Chapter 3, the analysis of continuous-time PWM based burst-mode RF transmitters has been carried out. First, the image problem has been addressed, which occurs when the baseband PWM signal is upconverted to the passband. To understand the problem, an analysis of the upconverted signals is given based on the mathematical description of the passband signals. The wanted signal located around the positive carrier frequency overlaps with the spectral components of the signal which is modulated to the negative carrier frequency. Thus the wanted signal is distorted already before the RF PA. By using a proper PWM frequency, without using additional analog components like analog LPFs, the image peak distortion in the TEPWM signal can be avoided. From the analysis, it can be seen that the DEPWM method can be treated as a method to reduce the image peak distortion in TEPWM signals. In the second part of the chapter, efficiency analysis of the two-level and multilevel burst-mode RF transmitters has been presented. First of all, the efficiency expression for constant input signals is given followed by the efficiency expression with a given PDF of amplitude-varying input signals. According to the analytical results obtained, the efficiency optimization method of the multilevel burst-mode RF transmitters is presented. The maximum average transmitter efficiency can be achieved by properly choosing the threshold values, which are used to divide the input signal magnitude, according to its PDF. Moreover, the efficiency expressions of the burst-mode multilevel transmitters have been related to those of the Doherty and multistage Doherty PAs. It is shown that the efficiency optimization can also been applied to Doherty and multistage Doherty PAs. The analytical and simulation results show that the efficiency optimized burst-mode RF transmitters provide a great efficiency improvement compared to the non-optimized transmitters especially for signals with high PAPRs and signals transmitted at a wide range of transmission power levels.

In Chapter 4, the investigation of the discrete-time PWM based burst-mode RF transmitters has been performed. When the PWM signal is generated digitally, the wanted signal is severely distorted compared to the ideally generated continuous-time PWM signal. To explore the origin of this distortion, the discrete-time PWM process has been described mathematically where it can be seen that the discrete-time PWM signals inherently suffer from aliasing distortion due to the sampling of non-bandlimited baseband PWM signals which degrades the signal quality. To deal with the distortion, the AFPWM method is described to avoid the destructive aliasing distortion by limiting the number of harmonics in the generated PWM signals. One drawback is that the AFPWM method induces amplitude variation onto the time-domain signal. Since the RF PA is not operated only in saturation or in cutoff, but at a wider range of power levels, the PA efficiency might be degraded. According to the transmitter efficiency expression, the transmitter efficiency depends not only on the PA efficiency but also on the coding efficiency. Hence, a thorough analysis of the coding efficiency of the AFPWM based burst-mode RF transmitters has been performed. The results show that the higher coding efficiency compensates for the RF PA efficiency degradation. An important result obtained from the measurements is that by properly choosing the number of harmonics used in the generated PWM signals, a good efficiency-linearity trade-off can be achieved for the AFPWM based burst-mode RF transmitters. The simulation and measurement results have demonstrated the superiority of the AFPWM method over the conventional digital PWM method. The analysis of multilevel AFPWM based burst-mode RF transmitters has been carried out. It is shown that the multilevel transmitter architectures can be used to further enhance the transmitter efficiency.

5.2 Future Research

For burst-mode transmitters, a BPF is required to remove the out-of-band spectral components [66]. This is often achieved by using a surface acoustic wave (SAW) BPF [26]. By using the BPF, the out-of-band spectral components are filtered away, meaning that the transmission power is reduced, thus the transmitter efficiency is degraded. The coding efficiency has been used to describe the ratio of transmission power to the total power at the input of the BPF under the assumption that only the inband wanted signal is transmitted and all the out-of-band power is wasted. To utilize the out-of-band power in an efficient way, efficient signal reconstruction methods have been suggested in [102, 103]. To keep a low PWM switching frequency and thus a low RF PA switching loss, a narrow BPF is required for signal reconstruction. However, narrow bandwidth BPF at RF suffers from large insertion loss which may reduce the efficiency of the transmitter [104]. To relax the requirements on the BPF is an important direction in the future research.

In a recent work [82], to which the author has contributed, a multilevel multiphase AFPWM based burst-mode RF transmitter with 100% coding efficiency has been described. Thus the requirements of the BPF can be greatly reduced. The principle of operation of the multilevel multiphase PWM method [27, 84] is that the input signal is compared with M PWM reference waveforms with the same magnitude but equally distributed phases, where M is the number of signal paths employed in the transmitter architecture. By doing so, the harmonics close to the wanted signal, from $K = 1$ to $K = M - 1$, can be removed and the requirements on the BPF can be eased. The theory behind this harmonic cancellation is the polyphase multipath theory which was proposed in [105]. The basic principle of the polyphase multipath technique is shown in Appendix C. Applying this theory to AFPWM method, by carefully choosing the number of harmonics K in the generated PWM signal and the number of signal paths M, the out-of-band spectral components can be completely removed. Thus, the coding efficiency can achieve 100% and the need for a BPF is potentially eliminated. Future research shall include a deeper analysis on the combining system and the realization of the transmitter.

Highly efficient transmitter architectures are desirable in many applications in wireless communication systems. It is expected that, with the fast developing technology solving the implementation challenges, attention and interest in burst-mode RF transmitter architectures will continue to grow. The research work presented in this thesis should provide a solid basis for further research in academia as well as in industry in the focused field.

A

Efficiency of the State-of-the-Art Amplifiers

A.1 Efficiency of the Chireix Outphasing Amplifier

A block diagram of a Chireix outphasing system is shown in Figure A.1 [47]. The constant baseband input signals $x(t) = A \in [0, 1]$ can be expressed in polar form as

$$x(t) = A = A_{\max} e^{j\theta} = \cos\theta \tag{A.1}$$

where $A_{\max} = 1$ is the maximum value of A. Two RF outphasing signals are given in the baseband equivalent forms by

$$x_1 = \frac{1}{2} e^{j\theta} \tag{A.2}$$

$$x_2 = \frac{1}{2} e^{-j\theta} \tag{A.3}$$

where θ describes the outphasing angle between two branches. It gives

$$\theta = \arccos \frac{A}{A_{\max}} = A. \tag{A.4}$$

To compute the efficiency, the output power P_{o} and the total consumed dc power P_{dc} are required where the efficiency is described as

$$\eta = \frac{P_{\mathrm{o}}}{P_{\mathrm{dc}}} = \frac{V_{\mathrm{o}}^2/(2R_{\mathrm{o}})}{2V_{\mathrm{dd}} I_{\mathrm{dc}}}. \tag{A.5}$$

The operation of the system can be described from the load signal and backwards to the PA signals. The output current and voltage going through the load R_o can be expressed in polar

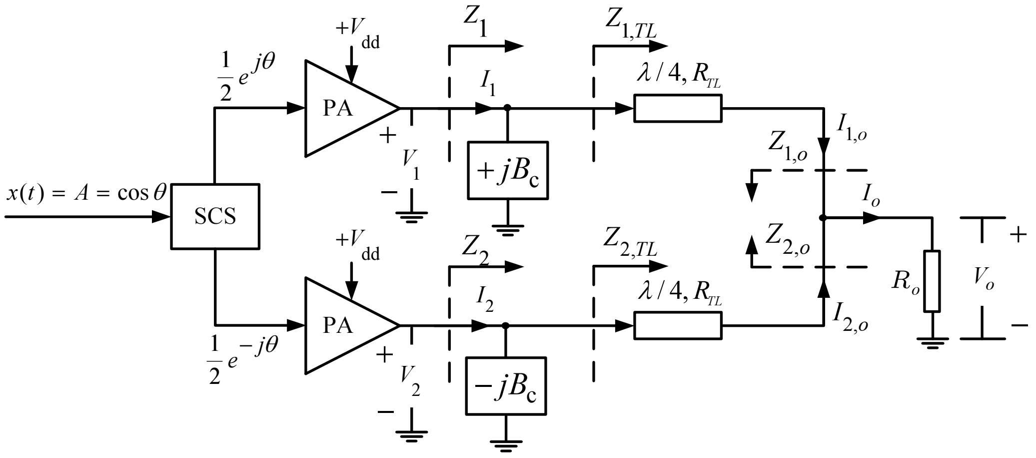

Figure A.1: Block diagram of a Chireix outphasing amplifier system.

form as

$$I_\mathrm{o} = I_\mathrm{max}\cos\theta \tag{A.6}$$

$$V_\mathrm{o} = V_\mathrm{max}\cos\theta \tag{A.7}$$

where I_max and V_max are the peak current and peak voltage, respectively. According to (A.6), the output currents from the transmission lines are

$$I_\mathrm{1,o} = \frac{I_\mathrm{max}}{2}e^{j\theta} \tag{A.8}$$

$$I_\mathrm{2,o} = \frac{I_\mathrm{max}}{2}e^{-j\theta} \tag{A.9}$$

respectively. The impedances presented at the transmission line outputs are

$$Z_\mathrm{1,o} = \frac{V_\mathrm{o}}{I_\mathrm{1,o}} = 2R_\mathrm{o}\frac{V_\mathrm{o}}{V_\mathrm{max}}e^{-j\theta} \tag{A.10}$$

$$Z_\mathrm{2,o} = \frac{V_\mathrm{o}}{I_\mathrm{2,o}} = 2R_\mathrm{o}\frac{V_\mathrm{o}}{V_\mathrm{max}}e^{j\theta} \tag{A.11}$$

where $I_\mathrm{max} = V_\mathrm{max}/R_\mathrm{o}$ is used. The quarter wavelength lossless transmission line has the following input-output properties

$$\text{impedance relation} \quad Z_\mathrm{in}Z_\mathrm{out} = R_\mathrm{TL}^2 \tag{A.12}$$

$$\text{voltage relation} \quad V_\mathrm{in} = \frac{R_\mathrm{TL}}{Z_\mathrm{out}}V_\mathrm{out} \tag{A.13}$$

$$\text{current relation} \quad I_\mathrm{in} = \frac{Z_\mathrm{out}}{R_\mathrm{TL}}I_\mathrm{out} \tag{A.14}$$

According to (A.12) the impedances presented at the input of transmission lines are

$$Z_{1,\mathrm{TL}}= \frac{R_{\mathrm{TL}}^2}{Z_{1,\mathrm{o}}} = \frac{R_{\mathrm{TL}}^2}{2R_{\mathrm{o}}}\frac{V_{\max}}{V_{\mathrm{o}}}e^{j\theta} \tag{A.15}$$

$$Z_{1,\mathrm{TL}}= \frac{R_{\mathrm{TL}}^2}{Z_{1,\mathrm{o}}} = \frac{R_{\mathrm{TL}}^2}{2R_{\mathrm{o}}}\frac{V_{\max}}{V_{\mathrm{o}}}e^{-j\theta}. \tag{A.16}$$

The susceptance B_{c} is added in each branch to mitigate the effect of the reactive load presented at the RF PA output. The admittances at the RF PA outputs can be expressed by

$$Y_1= \frac{1}{Z_{1,\mathrm{TL}}} + jB_{\mathrm{c}} = \frac{2R_{\mathrm{o}}}{R_{\mathrm{TL}}^2}\frac{V_{\mathrm{o}}}{V_{\max}}\cos\theta + j\left(-\frac{2R_{\mathrm{o}}}{R_{\mathrm{TL}}^2}\frac{V_o}{V_{\max}}\sin\theta + B_{\mathrm{c}}\right) \tag{A.17}$$

$$Y_1= \frac{1}{Z_{2,\mathrm{TL}}} - jB_{\mathrm{c}} = \frac{2R_{\mathrm{o}}}{R_{\mathrm{TL}}^2}\frac{V_{\mathrm{o}}}{V_{\max}}\cos\theta + j\left(\frac{2R_{\mathrm{o}}}{R_{\mathrm{TL}}^2}\frac{V_{\mathrm{o}}}{V_{\max}}\sin\theta - B_{\mathrm{c}}\right). \tag{A.18}$$

According to (A.13) the output voltages of RF PAs are

$$V_1= \frac{R_{\mathrm{TL}}}{Z_{1,\mathrm{o}}}V_{\mathrm{o}} = \frac{R_{\mathrm{TL}}}{2R_{\mathrm{o}}}V_{\max}e^{j\theta} \tag{A.19}$$

$$V_2= \frac{R_{\mathrm{TL}}}{Z_{2,\mathrm{o}}}V_{\mathrm{o}} = \frac{R_{\mathrm{TL}}}{2R_{\mathrm{o}}}V_{\max}e^{-j\theta}. \tag{A.20}$$

For saturated Class B, the maximum output voltage is the supply voltage V_{dd}, leading to

$$V_{\mathrm{dd}} = \frac{R_{\mathrm{TL}}}{2R_{\mathrm{o}}}V_{\max} \tag{A.21}$$

The output currents from RF PAs are

$$I_1= V_1Y_1 \tag{A.22}$$

$$I_2= V_2Y_2. \tag{A.23}$$

For an ideal Class B PA, the dc current is [6]

$$I_{\mathrm{dc}}= \frac{2}{\pi}|I_1| = \frac{2}{\pi}|I_2| = \frac{2}{\pi}|V_1||Y_1| \tag{A.24}$$

The efficiency of Class B PA based Chireix outphasing amplifier for constant input signals can be expressed by

$$\begin{aligned}\eta =& \frac{P_\mathrm{o}}{P_\mathrm{dc}} = \frac{V_\mathrm{o}^2/(2R_\mathrm{o})}{2V_\mathrm{dd}I_\mathrm{dc}} \\ =& \frac{\pi}{4}\frac{\left(\frac{V_\mathrm{o}}{V_\mathrm{max}}\right)^2}{\sqrt{\left(\frac{V_\mathrm{o}}{V_\mathrm{max}}\right)^4 + \left(\frac{V_\mathrm{o}}{V_\mathrm{max}}\sqrt{1-\left(\frac{V_\mathrm{o}}{V_\mathrm{max}}\right)^2} - \frac{R_\mathrm{TL}^2}{2R_\mathrm{o}}B_\mathrm{c}\right)^2}} \\ =& \frac{\pi}{4}\frac{v^2}{\sqrt{v^4 + \left(v\sqrt{1-v^2} - B\right)^2}}\end{aligned} \tag{A.25}$$

where $v = V_\mathrm{o}/V_\mathrm{max}$ is normalized output voltage and $B = B_\mathrm{c}R_\mathrm{TL}^2/(2R_\mathrm{o})$ is the normalized susceptance. When $R_\mathrm{o} = 1, R_\mathrm{TL} = 2$ the susceptance $B = 2B_\mathrm{c}$. With $B = 0$ the efficiency expression of (A.25) is given by

$$\eta = \frac{\pi}{4}\frac{v^2}{\sqrt{v^4 + \left(v\sqrt{1-v^2}\right)^2}} = \frac{\pi}{4}v \tag{A.26}$$

which is the same as an ideal Class B PA operated in linear mode. With $B = v\sqrt{1-v^2}$ meaning that the impedance presented at the PA is purely resistive, the efficiency expression can be described as

$$\eta = \frac{\pi}{4}\frac{v^2}{\sqrt{v^4}} = \frac{\pi}{4} \tag{A.27}$$

which gives the maximum efficiency. Therefore it is possible for the Chireix outphasing amplifier to achieve the maximum efficiency for different output signal level by choosing an appropriate compensation susceptance.

A.2 Efficiency of the Doherty Amplifier

A block diagram of a Doherty amplifier system is shown in Figure A.2 [52]. The quarter wavelength transmission line at the input to the auxiliary PA is used to compensate for the $\pi/2$ phase shift caused by the quarter wavelength transmission line at the output of the main PA. Since only the impedance of the latter transmission line is used, in the following analysis, the transmission line referred to is the one at the output of the main PA.

The Doherty amplifier operation can be divided into two operation regions with corresponding

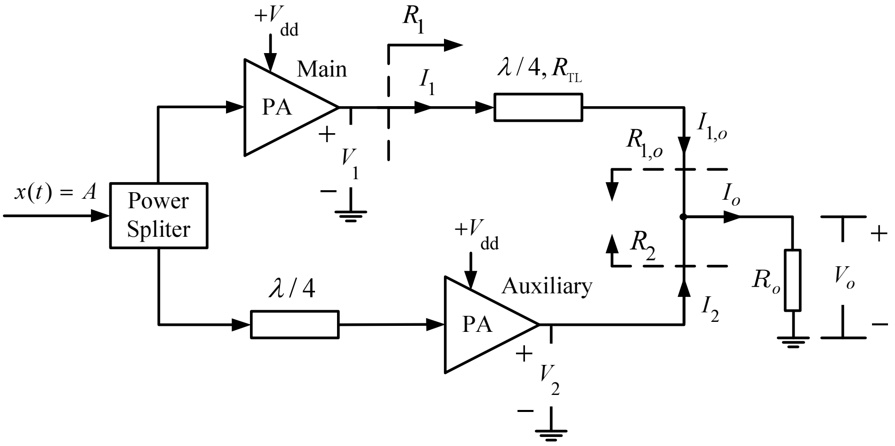

Figure A.2: Block diagram of a Doherty amplifier system.

constant baseband input signal by

$$x(t) = A, A \in [0, \alpha] \tag{A.28}$$

$$x(t) = A, A \in (\alpha, 1] \tag{A.29}$$

where α is the transition point above which the auxiliary PA starts to operate. The transition point is defined as the division ratio such that at the peak output power [52]

$$I_{1,\mathrm{o}} = \alpha I_{\max} \tag{A.30}$$

$$I_2 = (1-\alpha) I_{\max} \tag{A.31}$$

where $I_{\max}$ is the maximum output current through the load R_{o}. It gives

$$I_{\max} = \frac{V_{\mathrm{dd}}}{R_{\mathrm{o}}} \tag{A.32}$$

where V_{dd} is the supply voltage. The input-output relations of the quarter wavelength lossless transmission line described in (A.14) are listed here again to serve the following analysis

$$\text{impedance relation} \quad R_{\mathrm{in}} R_{\mathrm{out}} = R_{\mathrm{TL}}^2 \tag{A.33}$$

$$\text{voltage relation} \quad V_{\mathrm{in}} = \frac{R_{\mathrm{TL}}}{R_{\mathrm{out}}} V_{\mathrm{out}} \tag{A.34}$$

$$\text{current relation} \quad I_{\mathrm{in}} = \frac{R_{\mathrm{out}}}{R_{\mathrm{TL}}} I_{\mathrm{out}}. \tag{A.35}$$

In peak-power operation, with the main PA output voltage $V_1 = V_{\mathrm{dd}}$, according to (A.34), it gives

$$V_1 = \frac{R_{\mathrm{TL}}}{R_{1,\mathrm{o}}} V_{\mathrm{dd}} = V_{\mathrm{dd}} \tag{A.36}$$

thus

$$R_{\mathrm{TL}} = R_{1,\mathrm{o}}. \tag{A.37}$$

With (A.30) and (A.32), the impedance presented at the transmission line output is

$$R_{1,\mathrm{o}} = \frac{V_{\mathrm{dd}}}{I_{1,\mathrm{o}}} = \frac{R_{\mathrm{o}}}{\alpha}. \tag{A.38}$$

Accordingly, it gives

$$R_{\mathrm{TL}} = R_{1,\mathrm{o}} = \frac{R_{\mathrm{o}}}{\alpha}. \tag{A.39}$$

The efficiency expression for the Doherty amplifier can be described by

$$\eta = \frac{P_{\mathrm{o}}}{P_{\mathrm{dc}}} = \frac{V_{\mathrm{o}}^2/(2R_{\mathrm{o}})}{V_{\mathrm{dd}} I_{\mathrm{dc}}} \tag{A.40}$$

where V_{dd} is the supply voltage and I_{dc} is the dc current. Given R_{o} and V_{dd} it is necessary to derive the expression of I_{dc} in terms of V_{o} to obtain the efficiency expression in relation with the output voltage.

In the low-power operation where $x(t) = A, A \in [0, \alpha]$, the auxiliary PA is cut off and only the main PA is operated. According to (A.35), (A.39) and $I_{\mathrm{o}} = V_{\mathrm{o}}/R_{\mathrm{o}}$, the current at the main PA output is given by

$$I_1 = \frac{R_{\mathrm{o}}}{R_{\mathrm{TL}}} I_{\mathrm{o}} = \alpha \frac{V_{\mathrm{o}}}{R_{\mathrm{o}}}. \tag{A.41}$$

For an ideal Class B PA, the dc current I_{dc} is given by

$$I_{\mathrm{dc}} = \frac{2}{\pi} I_1 = \frac{2}{\pi} \frac{\alpha V_{\mathrm{o}}}{R_{\mathrm{o}}}. \tag{A.42}$$

Therefore in the low-power region, according to (A.40) and (A.42), the efficiency of the Doherty PA is given by

$$\begin{aligned} \eta &= \frac{P_{\mathrm{o}}}{P_{\mathrm{dc}}} = \frac{\frac{V_{\mathrm{o}}^2}{2R_{\mathrm{o}}}}{\frac{2}{\pi} V_{\mathrm{dd}} \frac{\alpha V_{\mathrm{o}}}{R_{\mathrm{o}}}} \\ &= \frac{\pi}{4} \frac{v}{\alpha} \end{aligned} \tag{A.43}$$

where $v = (V_{\mathrm{o}}/V_{\mathrm{dd}})$ is the normalized output voltage.

In the high-power operation where $x(t) = A, A \in (\alpha, 1]$, both of the main PA and the auxiliary PA are operated. The main PA is operated in saturation and outputs the maximum voltage of

$V_1 = V_{\mathrm{dd}}$. According to (A.34), (A.33) and (A.39)

$$\begin{aligned} I_1 &= \frac{V_1}{R_1} = \frac{V_1}{\frac{R_{\mathrm{TL}}^2}{R_{1,\mathrm{o}}}} = \frac{V_1}{R_{\mathrm{TL}}}\frac{V_\mathrm{o}}{V_{\mathrm{dd}}} = \frac{V_{\mathrm{dd}}}{\frac{R_\mathrm{o}}{\alpha}}\frac{V_\mathrm{o}}{V_{\mathrm{dd}}} \\ &= \frac{\alpha V_\mathrm{o}}{R_\mathrm{o}} \end{aligned} \tag{A.44}$$

the dc current of the main PA can be described by

$$I_{\mathrm{dc1}} = \frac{2}{\pi} I_1 = \frac{2}{\pi}\frac{\alpha V_\mathrm{o}}{R_\mathrm{o}}. \tag{A.45}$$

The current at the output of the transmission line is given according to (A.35), (A.34) and (A.44) by

$$\begin{aligned} I_{1,\mathrm{o}} &= \frac{R_{\mathrm{TL}}}{R_{1,\mathrm{o}}} I_1 = \frac{V_{\mathrm{dd}}}{V_\mathrm{o}}\frac{\alpha V_\mathrm{o}}{R_\mathrm{o}} \\ &= \frac{\alpha V_{\mathrm{dd}}}{R_\mathrm{o}}. \end{aligned} \tag{A.46}$$

From Figure A.2 it can be seen that the current at the output of the auxiliary PA can be obtained by subtracting the current at the load from the current at the output of the transmission line in (A.46)

$$\begin{aligned} I_2 &= I_\mathrm{o} - I_{1,\mathrm{o}} \\ &= \frac{V_\mathrm{o} - \alpha V_{\mathrm{dd}}}{R_\mathrm{o}}. \end{aligned} \tag{A.47}$$

Thus, the dc current of the auxiliary PA is given by

$$I_{\mathrm{dc2}} = \frac{2}{\pi} I_2 = \frac{2}{\pi}\frac{(V_\mathrm{o} - \alpha V_{\mathrm{dd}})}{R_\mathrm{o}}. \tag{A.48}$$

Therefore in the high-power region, according to (A.40), (A.45) and (A.48), the efficiency of the Doherty PA is given by

$$\begin{aligned} \eta &= \frac{P_\mathrm{o}}{P_{\mathrm{dc}}} = \frac{P_\mathrm{o}}{V_{\mathrm{dd}}\left(I_{\mathrm{dc1}} + I_{\mathrm{dc2}}\right)} = \frac{\pi}{4}\frac{\left(\frac{V_\mathrm{o}}{V_{\mathrm{dd}}}\right)^2}{\frac{V_\mathrm{o}}{V_{\mathrm{dd}}}(\alpha+1) - \alpha} \\ &= \frac{\pi}{4}\frac{v^2}{v(\alpha+1) - \alpha}. \end{aligned} \tag{A.49}$$

where v is the normalized output voltage. According to (A.43) and (A.49), the efficiency expression of the Doherty amplifier can be described by

$$\eta = \begin{cases} \dfrac{\pi}{4}\dfrac{v}{\alpha}, & \text{for } \ v \in [0, \alpha] \\ \dfrac{\pi}{4}\dfrac{v^2}{v(\alpha+1)-\alpha}, & \text{for } \ v \in (\alpha, 1] \end{cases} \tag{A.50}$$

where the normalized output voltage v is linearly related to the constant input $x(t) = A$.

B

A Detailed Derivation of PWM Signals

The derivation provided in the following gives a complete procedure of determining the mathematical expressions of the TEPWM signal, the results of which can be extended to other types of PWM signals. The obtained results are the same as described in Section 2.3.1. This procedure is according to the reference [1] and the results have been published in [78].

All the PWM signals considered so far are from the natural-sampling PWM (NPWM) process with an input signal of continuous magnitude. To obtain the analytical expressions of the NPWM signals, the uniform-sampling PWM (UPWM) is introduced where the input signal of UPWM process holds the same value in each PWM period T_p. Figure B.1 illustrats TE-UPWM process and TE-NPWM process.

B.1 General Expressions of PWM Signals

For the input signal $x(t)$, where $|x(t)| \leq 1$ for all t, it gives

$$x(t) = a(t)e^{j\phi(t)} \tag{B.1}$$

where $a(t)$ is the magnitude signal and $\phi(t)$ is the phase signal. A PWM modulator compares the input signal $a(t)$ to a reference sawtooth signal with a period of T_p. During the lth pulse interval $[lT_\mathrm{p}, (l+1)T_\mathrm{p})$, the sawtooth signal can be expressed as

$$r(t) = \frac{t}{T_\mathrm{p}} - l. \tag{B.2}$$

For TE-UPWM signal, the leading edge of the lth pulse occurs at time $t = lT_\mathrm{p}$ while the trailing edge occurs at the solution to the lth crossing-point equation when uniform-sampled

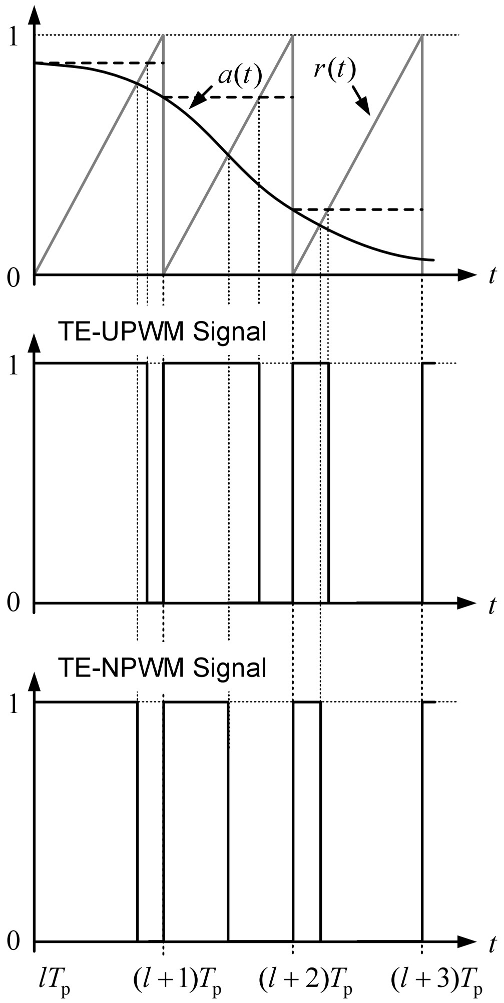

Figure B.1: UPWM process versus NPWM process.

input signal equals to the sawtooth signal. It gives

$$a(lT_\mathrm{p}) = \frac{t_\mathrm{l,U}}{T_\mathrm{p}} - l \tag{B.3}$$

where

$$t_\mathrm{l,U} = lT_\mathrm{p} + T_\mathrm{p} a(lT_\mathrm{p}) \tag{B.4}$$

and the lth pulse width $\tau_\mathrm{l,U}$ can be expressed as

$$\tau_\mathrm{l,U} = T_\mathrm{p} a(lT_\mathrm{p}). \tag{B.5}$$

For TE-NPWM signal, the leading edge of the lth pulse occurs at time $t = lT_\mathrm{p}$ while the trailing edge occurs at the time instant $t_\mathrm{l,N}$, which is the solution to the lth crossing-point equation when natural-sampled input signal equals to the sawtooth signal. It gives

$$a(t_{\mathrm{l,N}}) = \frac{t_{\mathrm{l,N}}}{T_{\mathrm{p}}} - l \tag{B.6}$$

where we can get

$$t_{\mathrm{l,N}} = lT_{\mathrm{p}} + T_{\mathrm{p}}a(t_{\mathrm{l,N}}) \tag{B.7}$$

and the lth pulse width $\tau_{\mathrm{l,N}}$ can be expressed as

$$\tau_{\mathrm{l,N}} = T_{\mathrm{p}}a(t_{\mathrm{l,N}}). \tag{B.8}$$

Therefore, a generic TEPWM signal can be expressed as

$$a_{\mathrm{p}}(t;\tau_{\mathrm{l}}) = \sum_{l=-\infty}^{\infty} u(t - lT_{\mathrm{p}}) - u(t - lT_{\mathrm{p}} - \tau_{\mathrm{l}}), \tag{B.9}$$

where the lth pulse width τ_{l} depends on the magnitude signal $a(t)$. For TE-UPWM, $\tau_{\mathrm{l}} = T_{\mathrm{p}}a(lT_{\mathrm{p}})$ as given in (B.5) and for TE-NPWM $\tau_{\mathrm{l}} = T_{\mathrm{p}}a(t_{\mathrm{l,N}})$ as given in (B.8).

B.2 For TE-UPWM Signals

For TE-UPWM signals, according to (B.5), the expression (B.9) can be described by

$$a_{\mathrm{p,U}}(t) = \sum_{l=-\infty}^{\infty} u(t - lT_{\mathrm{p}}) - u(t - lT_{\mathrm{p}} - T_{\mathrm{p}}a(lT_{\mathrm{p}})). \tag{B.10}$$

The Fourier transform of (B.10) is given by

$$\begin{aligned}
A_{\mathrm{p,U}}(f) &= \sum_{l=-\infty}^{\infty} \frac{e^{-j2\pi f lT_{\mathrm{p}}}}{j2\pi f} + \pi\delta(2\pi f)e^{-j2\pi f lT_{\mathrm{p}}} - \frac{e^{-j2\pi f(lT_{\mathrm{p}}+T_{\mathrm{p}}a(lT_{\mathrm{p}}))}}{j2\pi f} - \pi\delta(2\pi f)e^{-j2\pi f(lT_{\mathrm{p}}+T_{\mathrm{p}}a(lT_{\mathrm{p}}))} \\
&= \sum_{l=-\infty}^{\infty} \frac{e^{-j2\pi f lT_{\mathrm{p}}}\left(1 - e^{-j2\pi f T_{\mathrm{p}}a(lT_{\mathrm{p}})}\right)}{j2\pi f} \\
&= \sum_{l=-\infty}^{\infty} \frac{e^{-j2\pi f lT_{\mathrm{p}}}}{j2\pi f} \sum_{r=1}^{\infty} -\frac{(-j2\pi f T_{\mathrm{p}}a(lT_{\mathrm{p}}))^r}{r!} \\
&= \sum_{r=1}^{\infty} \frac{-1}{j2\pi f}\frac{(-j2\pi f T_{\mathrm{p}})^r}{r!}\frac{1}{T_{\mathrm{p}}} \sum_{l=-\infty}^{\infty} T_{\mathrm{p}}a^r(lT_{\mathrm{p}})e^{-j2\pi f lT_{\mathrm{p}}} \\
&= \sum_{r=1}^{\infty} \frac{(-j2\pi f T_{\mathrm{p}})^{r-1}}{r!} \sum_{k=-\infty}^{\infty} A_r(f - kf_{\mathrm{p}})
\end{aligned} \tag{B.11}$$

where $A_r(f)$ is the Fourier transforms of $(a(t))^r$ and the Taylor series

$$e^{\xi} - 1 = \sum_{r=1}^{\infty} \frac{\xi^r}{r!} \tag{B.12}$$

is used. Let

$$A_{\mathrm{p,U}}(f) = A_{\mathrm{U}}(f) + \sum_{k=1}^{\infty} A_{\mathrm{k,U}}(f) \tag{B.13}$$

where

$$A_{\mathrm{U}}(f) = \sum_{r=1}^{\infty} \frac{(-j2\pi f T_{\mathrm{p}})^{r-1}}{r!} A_r(f) = A(f) + \sum_{r=2}^{\infty} \frac{(-j2\pi f T_{\mathrm{p}})^{r-1}}{r!} A_r(f) \tag{B.14}$$

and

$$A_{\mathrm{k,U}}(f) = \sum_{k=1}^{\infty} \frac{(-j2\pi f T_{\mathrm{p}})^{r-1}}{r!} [A_r(f + kf_{\mathrm{p}}) + A_r(f - kf_{\mathrm{p}})]. \tag{B.15}$$

The Inverse Fourier transform of (B.14) is

$$a_{\mathrm{U}}(t) = a(t) + \sum_{r=2}^{\infty} \frac{1}{r!} (-T_{\mathrm{p}})^{r-1} \frac{d^{r-1}[a^r(t)]}{dt^{r-1}} \tag{B.16}$$

where the relation

$$\mathcal{F}^{-1}\left\{(j2\pi f)^r H(f)\right\} = \frac{d^r[h(t)]}{dt^r} \tag{B.17}$$

is used and $\mathcal{F}^{-1}$ denotes the inverse Fourier transform. The Fourier transform of (B.15) is

$$a_{\mathrm{k,U}}(t) = \sum_{r=1}^{\infty} \frac{1}{r!} (-T_{\mathrm{p}})^{r-1} \frac{d^{r-1}[2a^r(t)\cos(2\pi f_{\mathrm{p}} kt)]}{dt^{r-1}}. \tag{B.18}$$

Therefore the TE-UPWM signal can be expressed as

$$\begin{aligned} a_{\mathrm{p,U}}(t) &= a_{\mathrm{U}}(t) + a_{\mathrm{k,U}}(t) \\ &= a_{\mathrm{U}}(t) + \sum_{k=1}^{\infty} \frac{1}{k\pi} \left[\sin(2\pi k f_{\mathrm{p}} t) - \sin(2\pi k f_{\mathrm{p}} t - 2\pi k a_{\mathrm{U}}(t)) \right] \end{aligned} \tag{B.19}$$

where the proof is similar to that of TE-NPWM signal which is of more interest and given in (B.31).

B.3 For TE-NPWM Signals

The TE-NPWM signal obtained from the natural sampling of $a(t)$ can be regarded as the TE-UPWM signal obtained from the uniform sampling of $\hat{a}(t)$, where $\hat{a}(t)$ is a distorted form of $a(t)$ [1]. The results of TE-UPWM signals can then be applied to obtain the expressions of TE-NPWM signals. In order to determine $\hat{a}(t)$, a generalized crossing-point equation is given by

$$\hat{t} = t + T_{\mathrm{p}} a(\hat{t}), \qquad \hat{t} \in [lT_{\mathrm{p}}, (l+1)T_{\mathrm{p}}] \tag{B.20}$$

where it gives $\hat{t} = t_{\mathrm{l,N}}$ if $t = lT_{\mathrm{p}}$ as in (B.7). The slope of the modulating signal $a(t)$ should be smaller than the reference signal so that the solution to the crossing-point equation (B.20) $\hat{t}$ is unique for each choice of t [1]. Thus $\hat{a}(t)$ can be defined by

$$\hat{a}(t) = a(\hat{t}), \qquad -\infty < t < \infty. \tag{B.21}$$

According to (B.5), (B.8), (B.20) and (B.21), the lth TE-NPWM pulse width $\tau_{\mathrm{l,N}} = T_{\mathrm{p}} a(t_{\mathrm{l,N}})$ for the singal $a(t)$ is the same as the pulse width $T_{\mathrm{p}}\hat{a}(lT_{\mathrm{p}})$, that is the lth TE-UPWM pulse width for the signal $\hat{a}(t)$. Therefore the TE-NPWM signal from $a(t)$ is the same as the TE-UPWM signal from $\hat{a}(t)$. The TE-NPWM signal obtained from $a(t)$ is given by

$$a_{\mathrm{p,N}}(t) = a_{\mathrm{N}}(t) + a_{\mathrm{k,N}}(t) \tag{B.22}$$

where according to (B.16) it gives

$$a_{\mathrm{N}}(t; a(t)) = a_{\mathrm{N}}(t; \hat{a}(t)) = \hat{a}(t) + \sum_{r=2}^{\infty} \frac{1}{r!}(-T_{\mathrm{p}})^{r-1} \frac{d^{r-1}[\hat{a}^r(t)]}{dt^{r-1}} \tag{B.23}$$

with the frequency-domain expression by

$$A_{\mathrm{N}}(f) = \hat{A}(f) + \sum_{r=2}^{\infty} \frac{(-j2\pi f T_{\mathrm{p}})^{r-1}}{r!} \hat{A}_r(f) \tag{B.24}$$

where $\hat{A}_r(f)$ is the Fourier transform of the signal $(\hat{a}(t))^r$. The signal $a_{\mathrm{k,N}}(t)$ is given by

$$a_{\mathrm{k,N}}(t) = \sum_{r=1}^{\infty} \frac{1}{r!}(-T_{\mathrm{p}})^{r-1} \frac{d^{r-1}[2\hat{a}^r(t)\cos(2\pi f_{\mathrm{p}} k t)]}{dt^{r-1}} \tag{B.25}$$

with the frequency-domain expression by

$$A_{\mathrm{k,N}}(f) = \sum_{r=1}^{\infty} \frac{(-j2\pi f T_{\mathrm{p}})^{r-1}}{r!} [\hat{A}_r(f + kf_{\mathrm{p}}) + \hat{A}_r(f - kf_{\mathrm{p}})]. \tag{B.26}$$

It has been shown in [1] that according to the Lagrange theorem it gives

$$a_{\mathrm{N}}(t) = a(t) \tag{B.27}$$

meaning that when natural sampling is used, the generated PWM signal consists of the wanted modulating signal $a(t)$. To express the signal in (B.25) in terms of $a(t)$, the following formular

$$\frac{d^r}{dt^r}(u \cdot v) = \sum_{i=0}^{r} \binom{r}{i} \left(\frac{d^{r-i}u}{dt^{r-i}}\right) \left(\frac{d^i v}{dt^i}\right) \tag{B.28}$$

where

$$\binom{r}{i} = \frac{r!}{i!(r-i)!} \tag{B.29}$$

and the formula [1]

$$(a(t))^i = \sum_{m=0}^{\infty} \frac{1}{m!}(-T_{\mathrm{p}})^m \left(\frac{i}{i+m}\right) \frac{d^m}{dt^m}(\hat{a}(t))^{m+i} \tag{B.30}$$

are applied to (B.25). It gives

$$\begin{aligned}
a_{\mathrm{k,N}}(t) =& \sum_{r=1}^{\infty} \frac{1}{r!}(-T_{\mathrm{p}})^{r-1} \frac{d^{r-1}}{dt^{r-1}} \left[2\hat{a}^r(t)\cos(2\pi f_{\mathrm{p}} k t)\right] \\
=& \sum_{r=1}^{\infty} \frac{1}{r!}(-T_{\mathrm{p}})^{r-1} \frac{d^{r-1}}{dt^{r-1}} \left[\hat{a}^r(t)\left(e^{j2\pi k f_{\mathrm{p}} t} + e^{-j2\pi k f_{\mathrm{p}} t}\right)\right] \\
=& \sum_{r=1}^{\infty} \frac{1}{r!}(-T_{\mathrm{p}})^{r-1} \sum_{i=0}^{r-1} \binom{r-1}{i} \left(\frac{d^{r-1-i}\hat{a}^r(t)}{dt^{r-1-i}}\right) \left(\frac{d^i\left(e^{j2\pi k f_{\mathrm{p}} t} + e^{-j2\pi k f_{\mathrm{p}} t}\right)}{dt^i}\right) \\
=& \sum_{r=1}^{\infty} \frac{1}{r!}(-T_{\mathrm{p}})^{r-1} \sum_{i=0}^{r-1} \frac{(r-1)!}{i!(r-1-i)!}(j2\pi k f_{\mathrm{p}})^i \left(e^{j2\pi k f_{\mathrm{p}} t} + (-1)^i e^{-j2\pi k f_{\mathrm{p}} t}\right) \left(\frac{d^{r-1-i}\hat{a}^r(t)}{dt^{r-1-i}}\right) \\
=& \sum_{r=1}^{\infty} \sum_{i=0}^{r-1} \frac{(r-1)!}{r!}(-T_{\mathrm{p}})^{r-1-i} \left(\frac{-1}{f_{\mathrm{p}}}\right)^i \frac{(j2\pi k)^i (f_{\mathrm{p}})^i}{i!(r-1-i)!} \left(e^{j2\pi k f_{\mathrm{p}} t} + (-1)^i e^{-j2\pi k f_{\mathrm{p}} t}\right) \left(\frac{d^{r-1-i}\hat{a}^r(t)}{dt^{r-1-i}}\right) \\
=& \sum_{r=1}^{\infty} \sum_{i=0}^{r-1} \frac{1}{r}(-T_{\mathrm{p}})^{r-1-i}(-1)^i \frac{(j2\pi k)^i}{i!(r-1-i)!} \left(e^{j2\pi k f_{\mathrm{p}} t} + (-1)^i e^{-j2\pi k f_{\mathrm{p}} t}\right) \left(\frac{d^{r-1-i}\hat{a}^r(t)}{dt^{r-1-i}}\right) \\
=& \sum_{i=0}^{\infty} \frac{(j2\pi k)^i}{i!} \left(e^{-j2\pi k f_{\mathrm{p}} t} + (-1)^i e^{j2\pi k f_{\mathrm{p}} t}\right) \sum_{m=0}^{\infty} \left(\frac{1}{m+i+1}\right) \frac{1}{m!}(-T_{\mathrm{p}})^m \frac{d^m}{dt^m}(\hat{a}(t))^{m+i+1} \\
=& \sum_{i=0}^{\infty} \frac{(j2\pi k)^i}{(i+1)!} \left(e^{-j2\pi k f_{\mathrm{p}} t} + (-1)^i e^{j2\pi k f_{\mathrm{p}} t}\right)(a(t))^{i+1} \\
=& \sum_{i=0}^{\infty} \frac{1}{j2\pi k} \left(\frac{(j2\pi k a(t))^{i+1}}{(i+1)!} e^{-j2\pi k f_{\mathrm{p}} t} - \frac{(-j2\pi k a(t))^{i+1}}{(i+1)!} e^{j2\pi k f_{\mathrm{p}} t}\right)
\end{aligned}$$

$$
\begin{aligned}
&=\frac{1}{j2\pi k}\Big[\Big(e^{j2\pi k a(t)}-1\Big)e^{-j2\pi k f_{\mathrm{p}}t}-\Big(e^{-j2\pi k a(t)}-1\Big)e^{j2\pi k f_{\mathrm{p}}t}\Big]\\
&=\frac{1}{k\pi}\big[\sin(2\pi k f_{\mathrm{p}}t)-\sin(2\pi k f_{\mathrm{p}}t-2\pi k a(t))\big] \qquad \text{(B.31)}
\end{aligned}
$$

where the Taylor series (B.12) is used and $m = r - i - 1$ is applied. Therefore according to (B.22), (B.27) and (B.31), the time-domain TE-NPWM signal with magnitude input $a(t) \in [0, 1]$ is given by

$$a_{\mathrm{p,N}}(t)= a(t)+\sum_{k=1}^{\infty}\frac{1}{k\pi}\big[\sin(2\pi k f_{\mathrm{p}}t)-\sin(2\pi k f_{\mathrm{p}}t-2\pi k a(t))\big]. \qquad \text{(B.32)}$$

The frequency-domain signal can be expressed by

$$A_{\mathrm{p,N}}(f)= A(f)+\sum_{k=1}^{\infty}\sum_{r=1}^{\infty}\frac{(j2\pi k)^{r-1}}{r!}\big[A_r(f+kf_{\mathrm{p}})+(-1)^{r-1}A_r(f-kf_{\mathrm{p}})\big]. \qquad \text{(B.33)}$$

The analytical results describing other types of PWM signals can be extended from the results obtained for TE-NPWM signals and are given in Section 2.3.

C

Basic Principle of Polyphase Multipath technique

The aim of the polyphase multipath technique lies in two aspects [2, 105]. First, each desired signal after the nonlinear system in each path should have the same phase, such that the desired signals can be constructively combined to form the wanted signal. Second, undesired signals after the nonlinear system in each path should have different phases, such that the unwanted signals are canceled out.

A block diagram of the polyphase multipath system is shown in Figure C.1. The nonlinear system is assumed to be memoryless and weakly nonlinear [105]. With an input signal of $x(t) = A\cos(2\pi ft)$, the output of the nonlinear system in the mth path will be

$$z_m(t) = b_0 + \sum_{k=1}^{\infty} b_k(\cos 2\pi ft + (m-1)k\phi) \tag{C.1}$$

where m denotes the order of the signal path and b_k are weighting constants. The phase shift ϕ satisfies

$$\phi = \frac{2\pi}{M} \tag{C.2}$$

where M is the number of signal paths. After the phase compensation, it gives

$$\begin{aligned} y_m(t) &= b_0 + \sum_{k=1}^{\infty} b_k \cos\left(2\pi ift + (m-1)(k-1)\phi\right) \\ &= b_0 + b_1 \cos\left(2\pi ft\right) + \sum_{k=2}^{\infty} b_k \cos\left(2\pi ift + (m-1)(k-1)\phi\right) \end{aligned} \tag{C.3}$$

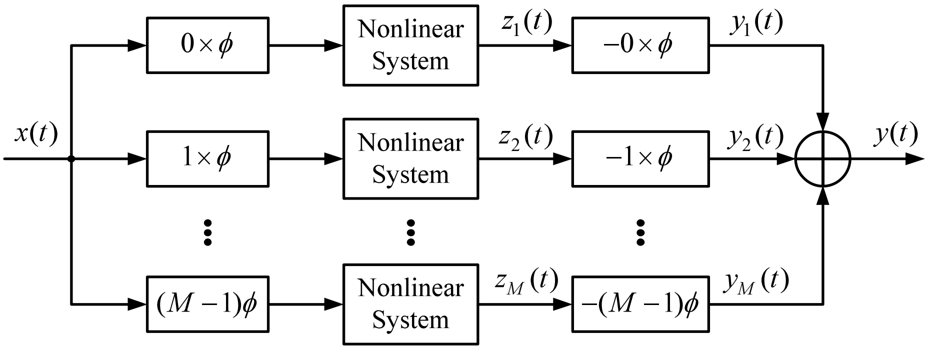

Figure C.1: Block diagram of a polyphase multipath (M path) system according to [2].

It can be seen that the desired signal $b_1 \cos(2\pi f t)$ from each path is with the same phase and can be added constructively. When the harmonics from different paths are added, for the kth harmonic, $k \geq 2$, it gives

$$y_k(t) = \sum_{m=1}^{M} b_k \cos\left(2\pi i f t + (m-1)(k-1)\phi\right). \tag{C.4}$$

It can be seen that when $M = 1$ the harmonics cannot be canceled out. Thus to cancel the harmonics the signal paths is required to be $M \geq 2$. By use of the term $\sin((k-1)\phi/2)$, the harmonics in (C.4) can be expressed by

$$\begin{aligned} y_k(t) &= \frac{\sum_{m=1}^{M} b_k \cos\left(2\pi i f t + (m-1)(k-1)\phi\right) \sin((k-1)\frac{\phi}{2})}{\sin((k-1)\frac{\phi}{2})} \\ &= b_k \sin\left(2\pi i f t + \frac{(2M-1)(k-1)\phi}{2}\right) - b_k \sin\left(2\pi i f t - \frac{(k-1)\phi}{2}\right) \\ &= \frac{b_k \cos\left(2\pi i f t + \frac{(M-1)(k-1)\phi}{2}\right) \sin\left(\frac{M(k-1)\phi}{2}\right)}{\sin\left((k-1)\frac{\phi}{2}\right)} \\ &= \frac{b_k \cos\left(2\pi i f t + \frac{(M-1)(k-1)\pi}{M}\right) \sin((k-1)\pi)}{\sin\left(\frac{(k-1)\pi}{M}\right)} \\ &= 0 \end{aligned} \tag{C.5}$$

where (C.2) is applied and the trigonometric identities

$$\cos\alpha \sin\beta = \frac{\sin(\alpha+\beta) - \sin(\alpha-\beta)}{2} \tag{C.6}$$

$$\sin\alpha - \sin\beta = 2\cos\left(\frac{\alpha+\beta}{2}\right)\sin\left(\frac{\alpha-\beta}{2}\right) \tag{C.7}$$

are used. Note that (C.5) requires $\sin((k-1)\phi/2) \neq 0$, meaning that $k \neq qM + 1, q = 1, 2, \cdots$.

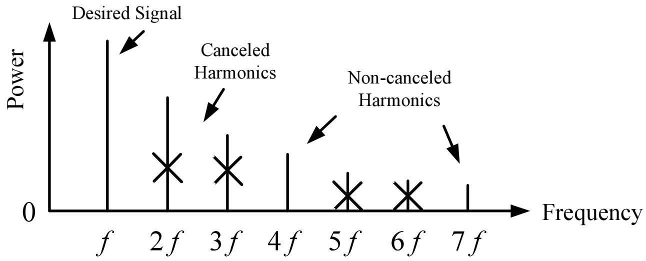

Figure C.2: Spectral illustration of a polyphase multipath system with $M = 3$ according to [2].

Otherwise for $k = qM + 1$ the harmonics are not canceled out. An illustration of the harmonic cancelation in frequency domain is shown in Figure C.2.

The polyphase multipath technique can be applied to the PWM system in order to cancel the nearest harmonics around the desired signal or cancel all the harmonics. Note that the nonlinear system here is referred to the PWM operator. Since the PW modulator generates the wanted signal together with the harmonics, it is not necessary to use phase compensation after the PWM modulator. The phase shift for each path is applied to the reference signal during the PWM process.

For the AFPWM method, according to (4.2), the signals generated by the reference signals with equally distributed phases can be expressed by

$$a_{\mathrm{p}_m}[n]= \frac{1}{M}a[n] + \sum_{k=1}^{K} \frac{2}{\pi k M} \sin(\pi k a[n]) \cos\left(2\pi k f_{\mathrm{p}} n T_{\mathrm{s}} - \frac{2\pi k(m-1)}{M}\right). \tag{C.8}$$

When signals from different paths are added up, the desired signals are constructively combined to form the wanted signal $a[n]$. The harmonics are partly or all canceled depending on the relation between the total number of harmonics K and the number of paths M. If $k \leq (M-1)$, by using AFPWM method, all of the harmonics can be canceled out after a constructive combining. Thus a coding efficiency of 100% can be achieved for such multiphase multilevel PWM based burst-mode RF transmitters [82].

Bibliography

[1] Z. Song and D. V. Sarwate, "The frequency spectrum of pulse width modulated signals," *Signal Processing*, vol. 83, no. 10, pp. 2227–2258, October 2003. (document), 2.1, 2.3, 2.5, 2.3.1, 2.3.1, B, B.3

[2] R. Shrestha, E. Klumperink, E. Mensink, G. Wienk, and B. Nauta, "A polyphase multipath technique for software-defined radio transmitters," *IEEE Journal of Solid-State Circuits*, vol. 41, no. 12, pp. 2681–2692, 2006. (document), C, C.1, C.2

[3] D. Pareit, B. Lannoo, I. Moerman, and P. Demeester, "The history of WiMAX: A complete survey of the evolution in certification and standardization for IEEE 802.16 and WiMAX," *IEEE Communications Surveys Tutorials*, vol. 14, no. 4, pp. 1183–1211, 2012. 1.1

[4] "Digital Video Broadcasting (DVB) – Frame structure channel coding and modulation for a second generation digital terrestrial television broadcasting system (DVB-T2)," European Standard (Telecommunications series) ETSI EN 302 755 V1.1.1, Sept. 2009. 1.1

[5] Y. Li and G. Stüber, *Orthogonal Frequency Division Multiplexing for Wireless Communications*. Springer, 2010. 1.1

[6] S. C. Cripps, *RF Power Amplifiers for Wireless Communications*, 2nd ed. Norwood, MA: Artech House, 2006. 1.1, 1.2, 1.2.2, 1.2.2, 1.2.2, 1.2.2, 1.2.3, 3.2.5, 3.2.6, A.1

[7] P. Lavrador, T. Cunha, P. Cabral, and J. Pedro, "The linearity-efficiency compromise," *IEEE Microwave Magazine*, vol. 11, no. 5, pp. 44 –58, August 2010. 1.1, 1.2

[8] M. Chiang, P. Hande, T. Lan, and C. W. Tee, *Power Control in Wireless Cellular Networks*. Foundations Trends Networking, 2008. 1.1

[9] A. Yener, R. Yates, and S. Ulukus, "Interference management for CDMA systems through power control, multiuser detection, and beamforming," *IEEE Transactions on Communications*, vol. 49, no. 7, pp. 1227–1239, July 2001. 1.1

[10] "Evolved Universal Terrestrial Radio Access (E-UTRA) – User Equipment (UE) radio transmission and reception," LTE Technical Specification Release 10 3GPP TS 36.101 V10.0.0, Oct. 2010. 1.1

[11] H. G. Myung and D. J. Goodman, *Single Carrier FDMA: A New Air Interface for Long Term Evolution*. John Wiley & Sons, Ltd., 2008. 1.1

[12] A. Simonsson and A. Furuskar, “Uplink power control in LTE - overview and performance, subtitle: Principles and benefits of utilizing rather than compensating for SINR variations,” in *IEEE 68th Vehicular Technology Conference (VTC 2008-Fall)*, September 2008, pp. 1–5. 1.1

[13] M. Iwamoto, A. Williams, P.-F. Chen, A. Metzger, L. Larson, and P. Asbeck, “An extended Doherty amplifier with high efficiency over a wide power range,” *IEEE Transactions on Microwave Theory and Techniques*, vol. 49, no. 12, pp. 2472–2479, December 2001. 1.1, 1.2.2, 3.2.3, 3.2.4, 3.2.5

[14] L. Kahn, “Single-sideband transmission by envelope elimination and restoration,” *Proceedings of the IRE*, vol. 40, no. 7, pp. 803 –806, july 1952. 1.1, 1.2.1

[15] E. McCune, “Envelope tracking or polar-which is it?” *IEEE Microwave Magazine*, vol. 13, no. 4, pp. 34–56, May-June 2012. 1.1, 1.2, 1.2.1, 1.2.1, 1.2.1

[16] F. Wang, A. Yang, D. Kimball, L. Larson, and P. Asbeck, “Design of wide-bandwidth envelope-tracking power amplifiers for OFDM applications,” *Microwave Theory and Techniques, IEEE Transactions on*, vol. 53, no. 4, pp. 1244–1255, April 2005. 1.1, 1.2.1

[17] H. Chireix, “High power outphasing modulation,” *Proceedings of the Institute of Radio Engineers*, vol. 23, no. 11, pp. 1370 – 1392, nov. 1935. 1.1, 1.2.2

[18] A. Birafane, M. El-Asmar, A. B. Kouki, M. Helaoui, and F. M. Ghannouchi, “Analyzing LINC systems,” *Microwave Magazine, IEEE*, vol. 11, no. 5, pp. 59–71, August 2010. 1.1, 1.2, 1.2.2, 1.2.2, 2.2.3

[19] W. Doherty, “A new high efficiency power amplifier for modulated waves,” *Proceedings of the Institute of Radio Engineers*, vol. 24, no. 9, pp. 1163 – 1182, Sept. 1936. 1.1, 1.2.2, 3.2.4

[20] B. Kim, J. Kim, I. Kim, and J. Cha, “The Doherty power amplifier,” *IEEE Microwave Magazine*, vol. 7, no. 5, pp. 42–50, October. 1.1, 1.2.2

[21] B. Kim, I. Kim, and J. Moon, “Advanced Doherty architecture,” *IEEE Microwave Magazine*, vol. 11, no. 5, pp. 72–86, August 2010. 1.1, 1.2, 1.2.2, 1.2.2, 3.2.4, 3.2.5

[22] B. François, E. Kaymaksut, and P. Reynaert, “Burst mode operation as an efficiency enhancement technique for RF power amplifiers,” in *in Proceedings of General Assembly and Scientific Symposium (URSI)*, August 2011, pp. 1–4. 1.1, 1.2.3, 1.2.3

[23] K. Hausmair, S. Chi, P. Singerl, and C. Vogel, “Aliasing-free digital pulse-width modulation for burst-mode RF transmitters,” *IEEE Transactions on Circuits and Systems I: Regular Papers*, vol. 60, no. 2, pp. 415 –427, February 2013. 1.1, 1.2, 1.4, 1.4, 4.2.2, 4.4

[24] R. Schreier and G. C. Temes, *Understanding Delta-Sigma Data Converters*, ieee press, john wiley & sons, inc. ed., 445 Hoes Lane Piscataway, NJ 08854, 2005. 1.1, 1.2.3

[25] U. Gustavsson, T. Eriksson, and C. Fager, “Quantization noise minimization in $\Sigma\Delta$ modulation based RF transmitter architectures,” *IEEE Transactions on Circuits and Systems I: Regular Papers*, vol. 57, no. 11, pp. 1–10, 2010. 1.1, 1.2.3

[26] J.-H. Chen, H.-S. Yang, and Y.-J. Chen, “A multi-level pulse modulated polar transmitter using digital pulse-width modulation,” *IEEE Microwave and Wireless Components Letters*, vol. 20, no. 5, pp. 295–297, May 2010. 1.1, 5.2

[27] J.-H. Chen, H.-S. Yang, H.-C. Lin, and Y.-J. Chen, “A polar-transmitter architecture using multiphase pulsewidth modulation,” *IEEE Transactions on Circuits and Systems I: Regular Papers*, vol. 58, no. 2, pp. 244–252, February 2011. 1.1, 2.1, 5.2

[28] F. Raab, P. Asbeck, S. Cripps, P. Kenington, Z. Popovic, N. Pothecary, J. Sevic, and N. Sokal, “Power amplifiers and transmitters for RF and microwave,” *IEEE Transactions on Microwave Theory and Techniques*, vol. 50, no. 3, pp. 814 –826, March 2002. 1.2, 1.2.1

[29] B. Kim, M. Junghwan, and K. Ildu, “Efficiently amplified,” *IEEE Microwave Magazine*, vol. 11, no. 5, pp. 87–100, 2010. 1.2

[30] M. Ebrahimi, M. Helaoui, and F. Ghannouchi, “Delta-sigma-based transmitters: Advantages and disadvantages,” *IEEE Microwave Magazine*, vol. 14, no. 1, pp. 68 –78, January/February 2013. 1.2, 1.2.3, 1.2.3, 1.2.3

[31] F. Wang, D. Kimball, J. Popp, A. Yang, D.-C. Lie, P. Asbeck, and L. Larson, “Wideband envelope elimination and restoration power amplifier with high efficiency wideband envelope amplifier for WLAN 802.11g applications,” in *2005 IEEE MTT-S International Microwave Symposium Digest*, 2005, pp. 1–4. 1.2.1

[32] J.-H. Chen, *Wideband Dynamic Biasing of Power Amplifiers for Wireless Handheld Applications.* Georgia Institute of Technology, 2011. 1.2.1

[33] J. Pedro, J. Garcia, and P. Cabral, “Nonlinear distortion analysis of polar transmitters,” *IEEE Transactions on Microwave Theory and Techniques*, vol. 55, no. 12, pp. 2757–2765, Dec 2007. 1.2.1

[34] A. Diet, C. Berland, M. Villegas, and G. Baudoin, “EER architecture specifications for OFDM transmitter using a class E amplifier,” *IEEE Microwave and Wireless Components Letters*, vol. 14, no. 8, pp. 389–391, 2004. 1.2.1

[35] “An introduction to envelope tracking for RF amplifiers,” White Paper, OpenET Alliance Limited, November 2011. 1.2.1

[36] “Envelope tracking PA characterisation,” White Paper, OpenET Alliance Limited, November 2011. 1.2.1

[37] D. Kimball, J. Jeong, C. Hsia, P. Draxler, S. Lanfranco, W. Nagy, K. Linthicum, L. Larson, and P. Asbeck, "High-efficiency envelope-tracking W-CDMA base-station amplifier using GaN HFETs," *IEEE Transactions on Microwave Theory and Techniques*, vol. 54, no. 11, pp. 3848–3856, Nov 2006. 1.2.1

[38] Y. Li, J. Lopez, D. Lie, K. Chen, S. Wu, T.-Y. Yang, and G.-K. Ma, "Circuits and system design of RF polar transmitters using envelope-tracking and SiGe power amplifiers for mobile WiMAX," *Circuits and Systems I: Regular Papers, IEEE Transactions on*, vol. 58, no. 5, pp. 893–901, may 2011. 1.2.1

[39] F. Wang, D. Kimball, J. Popp, A. Yang, D. Lie, P. Asbeck, and L. Larson, "An improved power-added efficiency 19-dBm hybrid envelope elimination and restoration power amplifier for 802.11g WLAN applications," *IEEE Transactions on Microwave Theory and Techniques*, vol. 54, no. 12, pp. 4086–4099, December 2006. 1.2.1

[40] F. Wang, *High Efficiency Linear Envelope Tracking and Envelope Elimination and Restoration Power Amplifier for WLAN OFDM Applications.* Georgia Institute of Technology, 2011. 1.2.1

[41] F. Raab, "High-efficiency linear amplification by dynamic load modulation," in *2003 IEEE MTT-S International Microwave Symposium Digest*, vol. 3, 2003, pp. 1717–1720. 1.2.2

[42] D. Cox, "Linear amplification with nonlinear components," *IEEE Transactions on Communications*, vol. 22, no. 12, pp. 1942–1945, 1974. 1.2.2

[43] A. Birafane and A. Kouki, "On the linearity and efficiency of outphasing microwave amplifiers," *IEEE Transactions on Microwave Theory and Techniques*, vol. 52, no. 7, pp. 1702–1708, 2004. 1.2.2

[44] M. Helaoui, S. Boumaiza, F. Ghannouchi, A. Kouki, and A. Ghazel, "A new mode-multiplexing LINC architecture to boost the efficiency of WiMAX up-link transmitters," *IEEE Transactions on Microwave Theory and Techniques*, vol. 55, no. 2, pp. 248–253, 2007. 1.2.2

[45] D. Perreault, "A new power combining and outphasing modulation system for high-efficiency power amplification," *IEEE Transactions on Circuits and Systems I: Regular Papers*, vol. 58, no. 8, pp. 1713 –1726, August 2011. 1.2.2

[46] M. Heidari, M. Lee, and A. Abidi, "All-digital outphasing modulator for a software-defined transmitter," *IEEE Journal of Solid-State Circuits*, vol. 44, no. 4, pp. 1260–1271, 2009. 1.2.2

[47] F. Raab, "Efficiency of outphasing RF power-amplifier systems," *IEEE Transactions on Communications*, vol. 33, no. 10, pp. 1094–1099, 1985. 1.2.2, 1.2.2, A.1

[48] A. D. Pham, *Outphase Power Amplifiers in OFDM Systems.* Massachusetts Institute of Technology, 2005. 1.2.2

[49] W. C. E. Neo, J. Qureshi, M. J. Pelk, J. R. Gajadharsing, and L. C. N. de Vreede, “A mixed-signal approach towards linear and efficient N-way Doherty amplifiers,” *IEEE Transactions on Microwave Theory and Techniques*, vol. 55, no. 5, pp. 866–879, May 2007. 1.2.2, 3.2.3, 3.2.4

[50] M. Pelk, W. Neo, J. Gajadharsing, R. Pengelly, and L. de Vreede, “A high-efficiency 100-w GaN three-way Doherty amplifier for base-station applications,” *IEEE Transactions on Microwave Theory and Techniques*, vol. 56, no. 7, pp. 1582–1591, July 2008. 1.2.2, 1.2.2, 3.2.5, 3.2.5, 3.2.6

[51] J. Kim, J. Cha, I. Kim, and B. Kim, “Optimum operation of asymmetrical-cells-based linear Doherty power amplifiers-uneven power drive and power matching,” *IEEE Transactions on Microwave Theory and Techniques*, vol. 53, no. 5, pp. 1802–1809, May 2005. 1.2.2, 1.2.2, 3.2.5

[52] F. Raab, “Efficiency of doherty RF power-amplifier systems,” *IEEE Transactions on Broadcasting*, vol. BC-33, no. 3, pp. 77–83, September 1987. 1.2.2, 1.2.2, 2.2.1, 3.2.2, 3.2.4, A.2

[53] Y.-S. Lee, S.-Y. Lee, and Y.-H. Jeong, “Linearity improvement of Doherty amplifier with analog predistorter for WCDMA applications,” in *36th European Microwave Conference, 2006.*, Sept 2006, pp. 1205–1208. 1.2.2

[54] S. chan Jung, O. Hammi, and F. Ghannouchi, “Design optimization and DPD linearization of GaN-based unsymmetrical Doherty power amplifiers for 3G multicarrier applications,” *IEEE Transactions on Microwave Theory and Techniques*, vol. 57, no. 9, pp. 2105–2113, Sept 2009. 1.2.2

[55] J. Moon, J. Kim, I. Kim, J. Kim, and B. Kim, “Highly efficient three-way saturated Doherty amplifier with digital feedback predistortion,” *IEEE Microwave and Wireless Components Letters*, vol. 18, no. 8, pp. 539–541, Aug 2008. 1.2.2

[56] Y. Zhao, *High Efficiency and High Linearity Doherty Amplifiers for Portable Wireless Communications.* University of California, San Diego, 2006. 1.2.2

[57] R. Darraji and F. Ghannouchi, “Digital Doherty amplifier with enhanced efficiency and extended range,” *IEEE Transactions on Microwave Theory and Techniques*, vol. 59, no. 11, pp. 2898–2909, 2011. 1.2.2

[58] Y.-T. D. Wu, *A Doherty Power Amplifier with Extended Bandwidth and Reconfigurable Back-off Level.* University of Waterloo, 2013. 1.2.2

[59] R. Darraji, F. Ghannouchi, and M. Helaoui, “Mitigation of bandwidth limitation in wireless Doherty amplifiers with substantial bandwidth enhancement using digital techniques,” *IEEE Transactions on Microwave Theory and Techniques*, vol. 60, no. 9, pp. 2875–2885, 2012. 1.2.2

[60] W. Chen, S. Bassam, X. Li, Y. Liu, K. Rawat, M. Helaoui, F. Ghannouchi, and Z. Feng, "Design and linearization of concurrent dual-band Doherty power amplifier with frequency-dependent power ranges," *IEEE Transactions on Microwave Theory and Techniques*, vol. 59, no. 10, pp. 2537–2546, 2011. 1.2.2

[61] F. Raab, "Radio frequency pulsewidth modulation," *IEEE Transactions on Communications*, vol. 21, no. 8, pp. 958–966, 1973. 1.2.3

[62] J. Walling and D. Allstot, "Pulse-width modulated CMOS power amplifiers," *IEEE Microwave Magazine*, vol. 12, no. 1, pp. 52–60, Feb 2011. 1.2.3

[63] M. Nielsen and T. Larsen, "An RF pulse width modulator for switch-mode power amplification of varying envelope signals," in *2007 Topical Meeting on Silicon Monolithic Integrated Circuits in RF Systems*, 2007, pp. 277–280. 1.2.3

[64] S. Rosnell and J. Varis, "Bandpass pulse-width modulation (BP-PWM)," in *2005 IEEE MTT-S International Microwave Symposium Digest*, 2005, pp. 731–734. 1.2.3

[65] U. Gustavsson, T. Eriksson, H. Mashad Nemati, P. Saad, P. Singerl, and C. Fager, "An RF carrier bursting system using partial quantization noise cancellation," *IEEE Transactions on Circuits and Systems I: Regular Papers,*, vol. 59, no. 3, pp. 515 –528, March 2012. 1.2.3, 1.2.3, 4.2.1, 4.2.2, 4.3, 4.3.2, 4.4

[66] P. Reynaert, "Polar modulation," *IEEE Microwave Magazine*, vol. 12, no. 1, pp. 46–51, February 2011. 1.2.3, 1.2.3, 5.2

[67] D. Parveg, P. Singerl, A. Wiesbauer, H. Mashad Nemati, and C. Fager, "A broadband, efficient, overdriven class-J RF power amplifier for burst mode operation," in *Proceedings of European Microwave Conference (EuMC)*, September 2010, pp. 1666–1669. 1.2.3, 1.2.3

[68] A. Jayaraman, P. Chen, G. Hanington, L. Larson, and P. Asbeck, "Linear high-efficiency microwave power amplifiers using bandpass delta-sigma modulators," *IEEE Microwave and Guided Wave Letters*, vol. 8, no. 3, pp. 121–123, 1998. 1.2.3

[69] S.-R. Yoon and S.-C. Park, "All-digital transmitter architecture based on bandpass delta-sigma modulator," in *9th International Symposium on Communications and Information Technology, 2009. ISCIT 2009.*, 2009, pp. 703–706. 1.2.3

[70] P.-I. Mak, S.-P. U, and R. Martins, "Transceiver architecture selection: Review, state-of-the-art survey and case study," *IEEE Circuits and Systems Magazine*, vol. 7, no. 2, pp. 6–25, 2007. 1.2.3

[71] D. Markert, C. Haslach, G. Fischer, and A. Pascht, "Coding efficiency of RF pulse-width-modulation for mobile communications," in *2012 International Symposium on Signals, Systems, and Electronics (ISSSE)*, 2012, pp. 1–5. 1.2.3

[72] M. Ozen, R. Jos, C. Andersson, M. Acar, and C. Fager, “High-efficiency rf pulsewidth modulation of class-e power amplifiers,” *IEEE Transactions on Microwave Theory and Techniques*, vol. 59, no. 11, pp. 2931–2942, 2011. 1.2.3

[73] J. Walling, H. Lakdawala, Y. Palaskas, A. Ravi, O. Degani, K. Soumyanath, and D. Allstot, “A class-E PA with pulse-width and pulse-position modulation in 65 nm cmos,” *IEEE Journal of Solid-State Circuits*, vol. 44, no. 6, pp. 1668–1678, 2009. 1.2.3

[74] M. M. Ebrahimi, *Delta-Sigma Based Transmitters for GHz Wireless Radio Systems*. Georgia Institute of Technology, 2011. 1.2.3

[75] U. Gustavsson, *From Noise-Shaped Coding to Energy Efficiency - One bit at the time*. Chalmers University of Technology, 2011. 1.2.3

[76] A. V. Oppenheim, R. W. Schafer, and J. R. Buck, *Discrete-time signal processing*, 2nd ed. Upper Saddle River, NJ, USA: Prentice-Hall, Inc., 1999. 1.3, 4.1, 4.1

[77] A. V. Oppenheim, A. S. Willsky, and N. S. Hamid, *Signal and System*, 2nd ed. Upper Saddle River, NJ, USA: Prentice-Hall, Inc., 1996. 1.3

[78] S. Chi, C. Vogel, and P. Singerl, “The frequency spectrum of polar modulated PWM signals and the image problem,” in *2010 17th IEEE International Conference on Electronics, Circuits, and Systems (ICECS).*, December 2010, pp. 679–682. 1.4, 1.4, B

[79] S. Chi, P. Singerl, and C. Vogel, “Coding efficiency optimization for multilevel PWM based switched-mode RF transmitters,” in *in Proceedings of IEEE International Midwest Symposium on Circuits and Systems (MWSCAS)*, August 2011, pp. 1–4. 1.4, 2.1.2, 3.2.2, 3.2.3, 4.3.1

[80] ——, “Efficiency optimization for burst-mode multilevel radio frequency transmitters,” *IEEE Transactions on Circuits and Systems I: Regular Papers*, vol. PP, no. 99, pp. 1–14. 1.4, 1.4, 2.1, 2.1.2, 2.2.3, 3.2.3

[81] S. Chi, K. Hausmair, and C. Vogel, “Coding efficiency of bandlimited PWM based burst-mode RF transmitters,” in *2013 IEEE International Symposium on Circuits and Systems (ISCAS)*, May 2013, pp. 2263–2266. 1.4

[82] K. Hausmair, S. Chi, and C. Vogel, “How to reach 100% coding efficiency in multilevel burst-mode RF transmitters,” in *2013 IEEE International Symposium on Circuits and Systems (ISCAS)*, 2013, pp. 2255–2258. 1.4, 5.2, C

[83] T. Blocher and P. Singerl, “Coding efficiency for different switched-mode RF transmitter architectures,” in *in Proceedings of IEEE International Midwest Symposium on Circuits and Systems (MWSCAS)*, August 2009, pp. 276–279. 2.1, 2.2.3, 3.2.1

[84] H.-S. Yang, J.-H. Chen, and Y. J. Emery Chen, "A polar transmitter using interleaving pulse modulation for multimode handsets," *IEEE Transactions on Microwave Theory and Techniques*, vol. 59, no. 8, pp. 2083–2090, August 2011. 2.1, 5.2

[85] F. Ghannouchi, S. Hatami, P. Aflaki, M. Helaoui, and R. Negra, "Accurate power efficiency estimation of GHz wireless delta-sigma transmitters for different classes of switching mode power amplifiers," *IEEE Transactions on Microwave Theory and Techniques*, vol. 58, no. 11, pp. 2812–2819, November 2010. 2.2.1, 4.3.3

[86] T. Johnson and S. P. Stapleton, "RF class-D amplification with bandpass sigma delta modulator drive signals," *IEEE Transactions on Circuits and Systems I: Regular Papers*, vol. 53, no. 12, pp. 2507–2520, December 2006. 2.2.2

[87] F. Raab, P. Asbeck, S. Cripps, P. Kenington, Z. Popovic, N. Pothecary, J. Sevic, and N. Sokal, "RF and microwave power amplifier and transmitter technologies - part 1," *High Freq. Electron.*, pp. 22–36, May 2003. 2.2.3

[88] A. Garcia i Tormo, A. Poveda, E. Alarcoandn, H. Bergveld, B. Buter, and R. Karadi, "An enhanced switching policy for buck-derived multi-level switching power amplifiers," in *Proceedings of IEEE International Symposium on Circuits and Systems (ISCAS)*, June 2010, pp. 3196–3199. 2.3.2

[89] R. Fletcher, *Practical Methods of Optimization*, 2nd ed. New York, USA: Wiley-Interscience, 1987. 3.2.3

[90] G. Hanington, P.-F. Chen, P. Asbeck, and L. Larson, "High-efficiency power amplifier using dynamic power-supply voltage for CDMA applications," *IEEE Transactions on Microwave Theory and Techniques*, vol. 47, no. 8, pp. 1471–1476, August 1999. 3.2.3

[91] J. Kim, B. Fehri, S. Boumaiza, and J. Wood, "Power efficiency and linearity enhancement using optimized asymmetrical Doherty power amplifiers," *IEEE Transactions on Microwave Theory and Techniques*, vol. 59, no. 2, pp. 425–434, February 2011. 3.2.4, 3.2.5

[92] N. Srirattana, A. Raghavan, D. Heo, P. Allen, and J. Laskar, "Analysis and Design of a High-Efficiency Multistage Doherty Power Amplifier for Wireless Communications," *IEEE Transactions on Microwave Theory and Techniques*, vol. 53, no. 3, pp. 852–860, March 2005. 3.2.4, 3.2.5, 3.2.6

[93] G. Sybille, "SimPowerSystems User's Guide, Version 4," *published under sublicense from Hydro-Quebec, and The MathWorks, Inc.*, October 2004. 3.2.5

[94] J. Sjostrom, "Multi-level pulse width modulation power amplifier method and apparatus," U.S. Patent US 2010/0 054 325 A1, March 4, 2010. 3.2.5

[95] Y. Y. Woo, J. Kim, J. Yi, S. Hong, I. Kim, J. Moon, and B. Kim, "Adaptive digital feedback predistortion technique for linearizing power amplifiers," *Microwave Theory and Techniques, IEEE Transactions on*, vol. 55, no. 5, pp. 932 –940, May 2007. 3.2.5

[96] S. Afsardoost, T. Eriksson, and C. Fager, “Digital predistortion using a vector-switched model,” *IEEE Transactions on Microwave Theory and Techniques*, vol. 60, no. 4, pp. 1166–1174, 2012. 3.2.5

[97] A. Zhu, P. Draxler, C. Hsia, T. Brazil, D. Kimball, and P. Asbeck, “Digital predistortion for envelope-tracking power amplifiers using decomposed piecewise volterra series,” *IEEE Transactions on Microwave Theory and Techniques*, vol. 56, no. 10, pp. 2237–2247, 2008. 3.2.5

[98] P. Aaen, J. A. Plá, and J. Wood, *Modeling and Characterization of RF and Microwave Power FETs.* Cambridge University Press, 2007. 3.2.6

[99] F. Dielacher, C. Vogel, P. Singerl, S. Mendel, and A. Wiesbauer, “A holistic design approach for systems on chip,” September 2009, pp. 301 –306. 4

[100] “Mini-Circuits RF Transformer datasheet ADT4-1T,” Mini-Circuits. 4.2.2

[101] “R&S SMBV100A Vector Signal Generator Specifications,” Rohde & Schwarz, Version 03.00, March 2011. 4.2.2

[102] B. François, P. Reynaert, A. Wiesbauer, and P. Singerl, “Analysis of burst-mode RF PA with direct filter connection,” in *European Microwave Conference (EuMC)*, September 2010, pp. 974–977. 5.2

[103] S. Liao and Y. E. Wang, “A high efficiency WCDMA power amplifier with pulsed load modulation (PLM),” in *2010 IEEE Radio and Wireless Symposium (RWS)*, 2010, pp. 49–52. 5.2

[104] A. Grebennikov, *RF and Microwave Transmitter Design.* Hoboken, New Jersey: John Wiley & Sons, Inc., 2011. 5.2

[105] E. Mensink, E. Klumperink, and B. Nauta, “Distortion cancellation by polyphase multipath circuits,” *IEEE Transactions on Circuits and Systems I: Regular Papers*, vol. 52, no. 9, pp. 1785–1794, 2005. 5.2, C